

Planning and Energy Management of Energy Storage Systems in Active Distribution
Networks

By

Hussein Mohamed Hassan Abdeltawab

A thesis submitted in partial fulfillment of the requirements for the degree of

Doctor of Philosophy

in

Energy Systems

Department of Electrical and Computer Engineering

University of Alberta

© Hussein Mohamed Hassan Abdeltawab, 2017

Abstract

This thesis discusses the techno-economic planning and operation of energy storage systems in active distribution power systems. Energy storage systems (ESSs) can participate in multi-services in the grid, such as energy arbitrage, renewable energy time-shifting, peak shaving, power loss minimization and reactive power support. The main objective is to enable the owner (a consumer or distribution company) to maximize profit while maintaining the power quality and respecting the operational constraints.

In this thesis, energy storage planning is conducted by sizing and allocating both of stationary and mobile storage. With stationary storage sizing, the system operator owns the storage which increases the total profit by performing multi grid services including distribution system expansion, energy arbitrage, energy loss minimization, time shifting, and reactive power support. The optimization includes practical constraints for the battery dynamics, such as the state of charge, and the number of charging cycles. The power flow constraints are considered, and the bus voltage and branch ampacity are included. The sizing scheme includes other options, such as distributed generators, static VAr compensators, and other power-balancing services. The sizing scheme was tested by simulation on a real radial feeder in Ontario, Canada. The sizing problem was also investigated for mobile energy storage systems (MESSs).

The second part of the thesis discusses the use of predictive energy management systems (EMSs) for different applications. First, a predictive EMS for a hybrid wind-battery system is discussed. The EMS provides more profit for the owner by including a practical method that considers the battery expended-life cost. The EMS determines the optimal charging cycles and

state of charge that will achieve the maximum net profit for the hybrid system owner. A predictive EMS is also developed for a flywheel with a wind system. The flywheel regulates the hybrid system power and its rate to comply with the grid code. The EMS considers the flywheel power loss minimization as a factor in the optimization. A day-ahead EMS is designed for mobile storage to define the optimal dispatching buses and powers such that the distribution system owner's profit is maximized. This objective is achieved by simultaneously performing power loss minimization, reactive power support, and energy arbitrage. Finally, the thesis demonstrates multi ESS participation in day-ahead markets by defining the robust operating zones in the distribution system. The uncertainties of loads and renewable resources are considered to define the safe dispatch levels for the distributed storage.

Comparative case studies, conducted on a real active distribution system in Ontario, Canada, showed the effectiveness of the proposed planning and EMS algorithms.

Preface

This thesis is an original work by Hussein Abdeltawab. As detailed in the following, some Chapters of this thesis have been published or accepted for publication as scholarly articles in which Prof. Yasser A.-R. I. Mohamed was the supervisory author and has contributed to concepts formations and the manuscript composition.

Chapter 3 has been submitted as **H. H. Abdeltawab** and Y. A.-R. I. Mohamed, “Energy Storage Sizing and Allocation for Distribution Network Upgrade Cost Minimization,” *IEEE Transactions on Industrial Electronics*, Aug. 2016, 8-double-column pages, submitted.

Chapter 4 has been submitted as **H. H. Abdeltawab** and Y. A.-R. I. Mohamed, “Allocation and Sizing of Mobile Energy Storage in Active Distribution Systems,” *IEEE Transactions on Smart Grid*, Aug. 2016, 8-double-column pages, submitted.

Chapter 5 has been published as **H. H. Abdeltawab** and Y. A.-R. I. Mohamed, “Market-Oriented Energy Management of a Hybrid Wind-Battery Energy Storage System via Model Predictive Control with Constraints Optimizer,” *IEEE Transactions on Industrial Electronics*, vol. 62., no. 11, pp. 6658 - 6670, Nov. 2015.

Chapter 6 has been published as **H. H. Abdeltawab** and Y. A.-R. I. Mohamed, “Robust Energy Management of a Hybrid Wind and Flywheel Energy Storage System Considering Flywheel Power Loss Minimization and Grid-Code Constraints,” *IEEE Transactions on Industrial Electronics*, vol. 63 no. 7, pp. 4242 – 4254, Nov. 2016.

Chapter 7 has been submitted as **H. H. Abdeltawab** and Y. A.-R. I. Mohamed, “Robust Operating Zones Identification for Independent-Energy-Storage Market Participation,” *Sustainable Energy, Grids and Networks*. submitted, Aug. 2016. 12 double-column pages.

Chapter 8 has been published as **H. H. Abdeltawab** and Y. A.-R. I. Mohamed, “Mobile Energy Storage Scheduling and Operation in Active Distribution Systems,” *IEEE Transactions on Industrial Electronics*, in press. 12 double-column pages.

Acknowledgements

I would like to express my deep gratitude to my supervisor, Prof. Yasser A.-R. I. Mohamed, for his dedicated guidance and assistance during my research. I appreciate all his serious contributions of time and discussions during my Ph.D. program.

Further, I would like to express my thanks to the examiners committee for their valued time and interests in my thesis. I would also like to acknowledge the financial support provided by the Alberta Innovates – Technology Futures Graduate Student Scholarship.

Table of Contents

Chapter 1	1
1 Introduction.....	1
1.1 Research Motivations.....	1
1.2 Thesis Objectives	2
1.3 Thesis Contributions	3
1.4 Thesis Organization	5
Chapter 2	7
2 Literature Survey	7
2.1 ESS Planning in Active Distribution Networks.....	8
2.1.1 Stationary Energy Storage Systems Planning.....	8
2.1.2 Mobile Energy Storage Systems Planning.....	10
2.2 Energy Management of Storage Systems	10
2.2.1 Predictive EMS of Hybrid WECS-BESS System.....	11
2.2.2 Predictive EMS of Hybrid WECS-FESS System	13
2.2.3 Robust Dispatch of Multiple ESS in Active Distribution Systems.....	16
2.2.4 EMS of Mobile Storage System.....	20
Chapter 3	22

3	Stationary Energy Storage Systems Sizing and Allocation for Multi-Services in Active Distribution Systems	22
3.1	Introduction	22
3.2	Problem Formulation	24
3.2.1	ESS Dynamic Model.....	26
3.2.2	Distributed Generation	28
3.2.3	Static VAr Compensator (SVCs)	30
3.2.4	Power Imbalance Solutions.....	31
3.2.5	Power Flow Model	32
3.3	Case Study.....	38
3.4	Results Discussion	43
3.4.1	Economic Discussion	46
3.4.2	ESS/SVC Rating, Reactive Power Support Options.....	49
3.4.3	ESS and SVC Locations.....	50
3.4.4	ESS for T&D Deferral, Competitive or Not?.....	51
3.5	Conclusion.....	52
Chapter 4	53
4	Mobile Energy Storage Sizing and Allocation for Multi-Services Grid Support.....	53
4.1	Introduction	53
4.2	Problem Formulation	54

4.2.1 Mobile Storage System Structure.....	54
4.2.2 MESS Planning Cost Function.....	55
4.2.3 MESS Model.....	58
4.2.4 Final Optimization Problem.....	60
4.3 Proposed Algorithm.....	61
4.4 Case Study.....	65
4.5 Conclusion.....	71
Chapter 5.....	72
5 EMS of a Hybrid Wind-Battery Energy Storage System via Model Predictive Control...	72
5.1 Introduction.....	72
5.2 Hybrid WECS-BESS Description.....	73
5.2.1 Wind Energy Conversion System (WECS).....	74
5.2.2 Battery Energy Storage System (BESS).....	75
5.2.3 Hybrid System State-Space Model.....	77
5.3 Economic Perspective of Energy Management.....	78
5.3.1 Electricity Market Regulations for Renewables.....	78
5.3.2 Energy Storage Cost Calculation.....	79
5.4 Proposed Energy Management System Design.....	82
5.4.1 A Glance over MPC.....	83
5.4.2 Problem Formulation.....	84

5.4.3 MPC Constraints Optimizer	88
5.4.4 Constraints Optimizer Algorithm.....	90
5.5 Case study: Alberta Electricity Market	94
5.5.1 Comparative Simulation Results.....	95
5.5.2 Constraints Optimizer Sensitivity to Prediction Error	98
5.6 Conclusions	100
Chapter 6	101
6 EMS of a Hybrid Wind – Flywheel Energy Storage System via Model Predictive Control	
101	
6.1 Introduction	101
6.2 Problem Formulation	102
6.2.1 FESS Model	106
6.2.2 The Proposed Control Structure.....	110
6.3 The Proposed Control Algorithm.....	113
6.3.1 Hybrid System Linearization	113
6.3.2 Adaptive Hysteresis Controller (AHC).....	117
6.3.3 Uncertainty Modes	118
6.3.4 The Two-stage Controller	121
6.4 Case Study.....	123
6.5 Validation study	129

6.6 Conclusion.....	133
Chapter 7	135
7 Multi Energy Storage Robust Operation in Active Distribution Network	135
7.1 Introduction	135
7.2 Problem Formulation	135
7.3 Robust Operating Zones Generation	137
7.3.1 Stage A: Uncertainty Set Relaxation.....	143
7.3.2 Stage B: Worst-Case Uncertainty Detection.....	146
7.3.3 Stage C: ROZ Determination	149
7.4 Case Study.....	149
7.5 Conclusions	155
Chapter 8	156
8 Mobile Energy Storage Scheduling and Operation in Active Distribution Systems	156
8.1 Problem Description.....	156
8.1.1 Motivation	156
8.1.2 MESS Model.....	158
8.2 Energy Management System.....	161
8.2.1 Transit Delay Model	162
8.2.2 MESS Dynamic Model Considering the Transit Delay	165
8.2.3 Original EMS Problem.....	166

8.3 Two-Stage EMS	169
8.3.1 Stage 1 (Instantaneous Transit EMS).....	169
8.3.2 Stage 2 (PSO Profit Maximizer)	171
8.4 Case Study.....	174
8.5 Conclusion.....	185
Chapter 9	186
9 Conclusions.....	186
9.1 Thesis Summary.....	186
9.2 Future work	188
Bibliography.....	189

List of Tables

Table 3-1 Planning input data.	42
Table 3-2. Optimization Results with different ESS technologies, and services (T1:T4) (P1 is shown with white background whereas P2 is grey).	44
Table 3-3 Biggest five loads in the Radial feeder	50
Table 4-1 Optimization input parameters.....	67
Table 4-2. Optimization Results With different ESS Technologies.	68
Table 5-1 Simulation Results.	97
Table 5-2 Optimizer results in two different sample times.	98
Table 6-1 parameters of a single FESS unit.....	124
Table 7-1 Fuzzy expert rules.....	145
Table 7-2 RES, BESS rating.	150
Table 7-3. ROZ size and voltage violations in 100 scenarios.....	153
Table 8-1 Input data for the EMS.	177
Table 8-2 System performance comparison.....	181

List of Figures

Figure 1-1 Thesis structure.....	5
Figure 3-1 System model and interconnection between the technical system and the economic model for the planning optimization problem.	25
Figure 3-2 Linearized capability curves for a circle with a different number of linearizing lines.	35
Figure 3-3 Single line diagram for the distribution feeder under study.	38
Figure 3-4 PU distance of first year (365 realization) to the 10 scenarios (centroids) depicted as + sign, the mean distance of each scenario is shown as solid red line, while the confidence levels are depicted by black line with a confidence level shown as a box.	40
Figure 3-5. Yearly input data(a) PU load profile (b) PU PV generation (C) hourly market buy price (HOEP) (d) PU wind generation.	41
Figure 3-6 Sizing results for different ESS technologies in case of P1 (Q support) (a) different technologies cost share (b) different incomes from the investment.	47
Figure 3-7 Comparison between total ESS size (MVA) to SVC size (MVAR) in two case (A) ESS provides Q support (case P1) (B) SVC only provides Q support (case P2).....	49
Figure 4-1 MESS structure.....	54
Figure 4-2 Power conversion system cost versus rated power.....	57
Figure 4-3 Hybrid optimization scheme for MESS Sizing and allocation.....	64
Figure 4-4 Single line diagram for the distribution feeder under study.	66
Figure 4-5 MESS rated power verses Profit.	69

Figure 4-6. Summer day scenario results (a) Energy buy and sell prices (b) grid purchased power (after/before) MESS (c) MESS active and reactive Powers (d) MESS location (station). (e) Capacity and daily number of cycles.....	70
Figure 5-1 The hybrid system structure.	73
Figure 5-2 Simplified battery model.	76
Figure 5-3 The system open-loop model.	78
Figure 5-4 Relation between expended-life (EL), No. of cycles and DOD.	81
Figure 5-5 The constraints optimizer mechanism.	89
Figure 5-6 Flow chart of constraints optimizer and MPC operation.	92
Figure 5-7 Simulation results for 3 cases (A, B, C) to evaluate three different controllers (MPC1, 2, 3).	95
Figure 5-8 net profit change for each MPC controller in the three case studies.	96
Figure 5-9 Optimizer results at different sample times.....	99
Figure 6-1 Hybrid system structure.....	106
Figure 6-2 Hybrid system nonlinear model	109
Figure 6-3 Optimization objectives at different cost function weight.	111
Figure 6-4 Hybrid system time-variant linearized model.	114
Figure 6-5 Linearized model performance.....	115
Figure 6-6 Relation of actual wind power with expected, maximum power.	119
Figure 6-7 the proposed EMS structure.	122
Figure 6-8 Wind power prediction error distribution.....	124
Figure 6-9 Simulation results comparing the performance of the traditional EMS (C1) and the proposed MPC-based EMS (C2).	125

Figure 6-10 FESS internal dynamics- a comparison between (C1) and (C2).....	127
Figure 6-11 AHC limits for SOC.	128
Figure 6-12 Opal-RT (OP 5600) real-time simulator set-up (1- OPAI-RT OP5600 real-time simulator, 2- analog output module OP5330, 3- local host-PC, 4- a digital oscilloscope).....	129
Figure 6-13 System description and different process interfaces.	130
Figure 6-14 Real-time simulation results with time scales; a- wind power (100 kW/Div.); b- FESS power (20KW/Div.); c- SOC (5%/Div.) d- power loss (0.35 kW/div.).....	133
Figure 7-1(a) Different uncertainty sets definition techniques (b) proposed risk-based uncertainty definition technique.	141
Figure 7-2 ROZ generation framework.....	142
Figure 7-3 WCU detection flowchart.....	149
Figure 7-4 RES and load day-ahead profile with uncertainty.....	150
Figure 7-5 Voltage profile at base case.....	151
Figure 7-6 Desired BESS power profiles without ROZ.....	152
Figure 7-7 RES, load uncertainty distribution for 100 scenarios each has 24 hours sample (total 2400 uncertain sample points).....	152
Figure 7-8. ROZ limits for BESS1, 2 at 30% RES-penetrations.	154
Figure 8-1 Power Conversion System cost versus size.....	158
Figure 8-2 Radial feeder with multi-MESS stations.	158
Figure 8-3 Mobile energy storage system description.	160
Figure 8-4 System techno-economic model structure.....	161
Figure 8-5 Transit delay model generation.	163
Figure 8-6 Transition scenarios example for a three MESS station at sample k.	164

Figure 8-7 Stage 2 structure (PSO profit maximizer).....	167
Figure 8-8 Radial feeder under study.....	174
Figure 8-9 Day-ahead input data. (a) Load profile. (b) RESs profiles. (c) Wholesale market and sell prices. (d) Traffic congestion delay.....	176
Figure 8-10 EMS results (a)MESS Position (b) MESS active power and reactive power set (c) Grid power and (e) SOC and Number of cycles.	179
Figure 8-11 Voltage profile after and before using the MESS.	180
Figure 8-12 Worst case bus voltage comparison (a) Bus 41 load profile and WT3 generation (b) MESS active and reactive power (C) Bus 41volt with and without MESS reactive power support.....	182
Figure 8-13 Comparison between reliability-based EMS with economic EMS. (a) Station position of MESS. (B) MESS state of charge.....	184

List of Acronyms

BESS	Battery energy storage system
DFT	Discrete Fourier transform
DG	Distributed generator
Disco	Distribution company
Disco	Distribution company
DNC	Daily number of cycles
DNO	Distribution network operator
DOD	Depth of discharge
ELC	Expended-life cost
EMS	Energy management system
ESS	Energy storage system
EV	Electric vehicle
FESS	Flywheel energy storage system
HIL	Hardware-in-the-loop
ISO	Independent system operator
MESS	Mobile energy storage system
MPC	Model predictive control

NPV	Net present value
PV	Photovoltaic
RES	Renewable energy source
RO	Robust optimization
ROZ	Robust operating zone
SESS	Stationary energy storage system
SOC	State of charge
SVC	Static VAr compensator
T&D	Transmission and distribution
TSO	Transmission system operator
VPP	Virtual power plant
WECS	Wind energy conversion system

Chapter 1

Introduction

1.1 Research Motivations

The world is moving toward the extensive utilization of renewable energy as a solution to the energy crisis. Growing electricity demand, increasing fuel prices, and greenhouse gas emissions have led us to turn to renewable energy resources (RESs) to solve these problems.

Unfortunately, the intermittent nature of RESs leads to technical grid issues regarding the power quality, security, and reliability [1]. Due to the increasing penetration level of RESs, research shows that for every 10% wind penetration, a 2-4% balancing generation is needed for a stable operation [2]. Because most energy storage systems (ESSs) are green regulation sources with low carbon emission, they are a perfect tool for facilitating renewable energy integration in both distribution and transmission network, as well. ESSs can provide extra services for the grid, such as load shifting, energy arbitrage, power loss minimization, transmission, and distribution upgrade deferral (T&D upgrade deferral), and peak shaving [3], [4].

The future of RESs growing might appear to depend on the use of ESSs; however, most ESSs have a significant capital cost, as was recently reported in [5]. For ESSs to be a viable solution for different grid services, optimal techno-economic planning, and operating schemes are a must. This thesis begins by investigating the optimal sizing and siting of ESSs to achieve optimum planning, whereas ESS operation is investigated by using some proposed energy management schemes.

1.2 Thesis Objectives

This thesis aims at optimizing the planning and operation of some ESSs in the power system. On the one hand, the optimum sizing and allocation of an ESS prevent buying an oversized unit which reduces the capital cost. On the other hand, smart energy management decisions for ESSs increase their life spans and provide the optimum utilization of the system.

First, the thesis objectives for the planning stage are summarized as follows.

- I. The planning scheme is intended to maximize the owner's profit as long as the power system technical constraints are respected. The owner can be a utility company or a customer, depending on the application, whereas the technical constraints are the grid codes, which guarantee the power quality, system security, and reliability.
- II. Optimal sizing of the ESSs power and energy rating should be performed, and the best bus for each ESS should be allocated.
- III. ESSs should be designed to be multi-tasking by achieving different objectives simultaneously, such as energy arbitrage, energy arbitrage, reactive power support, energy losses minimization, and, finally, feeder upgrade cost deferral.
- IV. The planning scheme should consider adopting other technologies along with ESSs, such as static VAR compensators (SVCs) or distributed generators (DGs), and also consider load shedding and RES power curtailment as options.
- V. The planning scheme should consider the prediction error in the futuristic data, such as the load variations, renewable resources intermittency, and energy prices fluctuations. Considering various scenarios improves the reliability of the input data, which leads to more accurate planning results.

- VI. The planning scheme should optimize the ESS life span by considering the batteries state of charge and number of charging cycles.
- VII. The ampacity of the network branches should be kept below the rated values, and the voltage levels should remain within the allowable fluctuation level as permitted by the grid code.
- VIII. The previous objectives should be considered in planning mobile energy storage systems (MESSs) as well.

Second, an effective and robust energy management system (EMS) is essential for an ESS.

The thesis objectives for the EMS stage are as follows.

- I. To maximize the owner's profit while respecting the grid code and the ESS operating limits.
- II. To make the EMS robust against predictions error and severe uncertainties.
- III. To enable the EMS to satisfy the previous objectives while considering the ESS life time constraints.
- IV. To design an EMS for different applications that represent stationary energy storage systems (SESSs) and mobile ones (MESSs).
- V. To design an EMS for different applications in short duration storage (seconds, minutes) and long duration storage (hours).

1.3 Thesis Contributions

The main thesis contribution is divided into two main parts. First, in the field of planning ESSs, this thesis makes two main contributions:

- I. First, this thesis proposes a sizing and siting scheme for stationary ESSs (SESSs) for distribution system upgrade cost minimization. The T&D upgrade deferral is achieved along with other objectives, such as energy arbitrage, power loss minimization, and reactive power support.
- II. The second contribution is the novel planning scheme for mobile ESSs (MESSs) in the distribution system. This scheme includes MESSs for providing various grid services as well.

In the field of ESSs operation, different energy management schemes are developed.

- I. For long-term storage, a model predictive EMS scheme is designed for a hybrid system. This system consists of a battery ESS (BESS) with a wind energy conversion system (WECS). The BESS shifts the WECS power into more profitable hours while taking the BESS expended-life cost into consideration.
- II. For short-term storage, a model predictive EMS is designed for another hybrid system. A flywheel energy storage system (FESS) is added to a WECS to reduce the curtailed wind power while respecting the grid code (regarding the power limit and rate). The proposed solution has the advantage of considering the FESS power loss minimization during operation.
- III. The MESS operation is studied by proposing a day-ahead EMS scheme that regulates the dispatchability level and optimal locations for an MESS for an incoming day to provide voltage support and trade energy simultaneously.
- IV. Finally, the thesis proposes a robust coordination framework for distributed ESSs for day-ahead operation. The framework defines the maximum allowable active power

levels (charge and discharge powers) for each ESS at each sample time such that no power quality violation occurs (voltage level and ampacity).

1.4 Thesis Organization

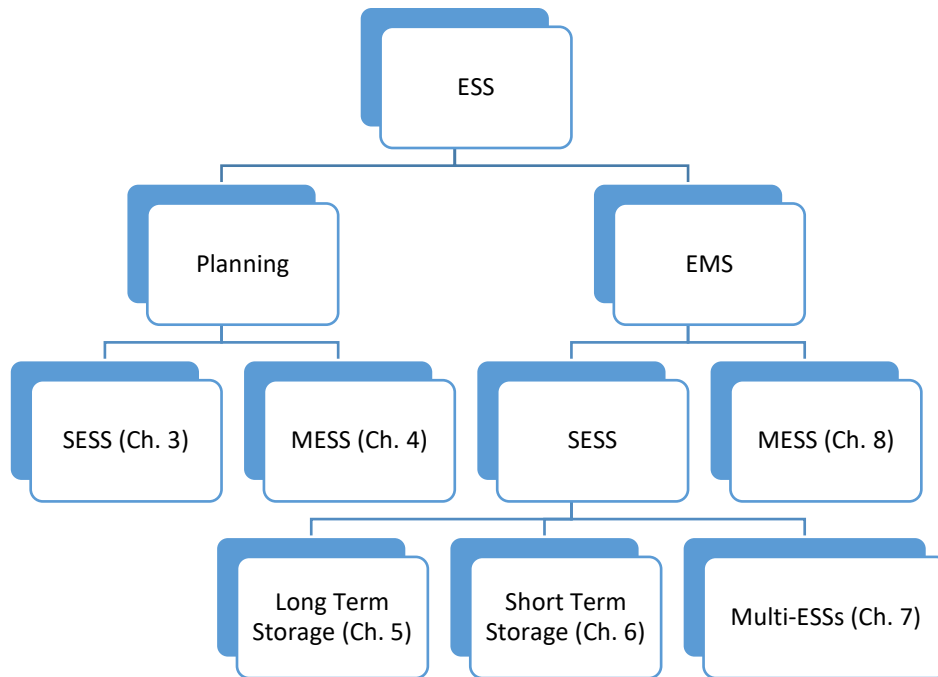


Figure 1-1 Thesis structure.

As shown in Figure 1-1, the body of this thesis begins in Chapter 3, while Chapter 2 discusses a current and up-to-date literature in the area of ESS planning and EMS. The thesis body is organized such that the planning topics are discussed before the EMS and operation topics. The planning of a stationary ESS for distribution system upgrade is discussed in Chapter 3, followed by Chapter 4, which discusses MESS planning.

The EMS topics are discussed in Chapters 4-8. Long duration storage is represented here by a BESS combined with a WECS for wind power time-shifting application. The EMS of such a system is explained in Chapter 5. For short duration storage, an example of a FESS with WECS is discussed in Chapter 6, where a model predictive EMS is designed. Chapter 7 deals with

multi-ESS operation in the distribution system. Finally, MESS operation for day-ahead is optimized in Chapter 8. Lastly, Chapter 9 draws the conclusion and suggestions for future work.

Chapter 2

Literature Survey

Optimal ESS sizing (power rating and energy capacity) is an important topic when it comes to adopting ESS for a certain grid service. ESS oversizing leads to unnecessarily high initial capital cost whereas under-sizing will not lead to the optimal profit desired for the ESS (due to the charging limitation or low capacity). Besides, optimal siting of ESSs is of high interest to enable effective reactive power support and efficient power loss reduction in the distribution system. Due to the foregoing reasons, the power research community has been investigating the ESS planning problem thoroughly and deeply in different ESS applications. The first part of this chapter demonstrates the current research effort in the area of ESS planning.

The optimal operation of an ESS is achievable by an EMS that satisfies the ESS owner objectives. These objectives are economic (profit from energy market), technical (improve power quality) or both. Utilizing the knowledge of RESs, load and market predictions lead to a better management of the ESS in achieving the long-term objectives. The second part of this chapter discusses the current research effort in the area of predictive EMSs for both short and long duration storage. Furthermore, a literature survey on MESS day-ahead EMS and multiple ESS management is presented.

2.1 ESS Planning in Active Distribution Networks

2.1.1 Stationary Energy Storage Systems Planning

The ESS planning has been widely discussed in the literature over different grid levels using various optimization techniques. In the transmission system level, the work of [6] used the Tabu search for optimal sizing of ESSs to maximize the revenue of the system considering the ESS life cost. On the other hand, the authors of [7] proposed a three-level technique to define the optimal ESS sizes and locations as well. Whereas the work in [6] and [7] presented deterministic optimization algorithms for ac networks, the research in [8] revisited the sizing problem using a stochastic optimization algorithm with a dc power flow model. On the distribution system level, the framework in [9] proposed a stochastic optimization technique for sizing and siting of ESSs in the power distribution system. The objective function in [9] depends on the power quality measurements (voltage deviation, power loss, and feeders loading factors) instead of the ESS cost. The ESS sizing problem was investigated in a microgrid system [10] where the deterministic sizing problem maximizes the profit in both islanded and grid-connected modes. A stochastic optimization version of [10] was discussed in [11] for an islanded microgrid as well. Further, the authors of [12] revisited the same problem after considering the battery exact efficiency model.

Recently, ESS sizing for frequency regulation services has been attracted much attention. The discrete Fourier transform (DFT) was used in [13] to decompose the power imbalance signal into different frequency ranges (acting as pass-band filters) to size different ESS capacities (intra-hour, intraday and real time). The same technique was applied in [14] for an islanded microgrid, where the imbalance power spectrum was shared between a diesel engine and a fast regulating ESS. Whereas [13]- [14] do not consider the ESS cost, the authors of [15]

and [16] designed a search algorithm that tunes the frequency regulation bandwidth such that the ESS cost is minimal. The partial DFT was also adopted in [17] to overcome some drawbacks of the DFT, such as redundant computation of zero power elements, especially for photovoltaic (PV) power.

To avoid ESS oversizing, the methods proposed in [18] and [19] use a multi-stage optimization to tune the optimal ESS size. On the one hand, the algorithm in [18] calculated the optimal ESS size based on hourly data, followed by a faster algorithm (with one minute-sampled data) that takes into account the wind and PV curtailment to obtain the desired ESS regulation capacity. On the other hand, the framework proposed in [19] tracked the minute-by-minute power imbalance regulating effect on the battery lifetime (as the total life cycles depend on their depth of discharge [20]). Regarding the parameters uncertainty, a probabilistic optimization was adopted to consider the wind power uncertainty distribution in the ESS sizing problem, such as in [21] and [22].

Recently, utilizing ESSs in transmission and distribution (T&D) deferral cost was proposed in [23] using a probabilistic optimization. The algorithm of [23] used a genetic algorithm to size the ESS such that the future distribution network upgrade cost is minimal by services, such as minimizing energy losses, adopting energy arbitrage and reducing the feeder upgrade capacity. However, the ESS was not used in either reactive power support or regulation services, which provide better utilization of ESSs and defer possible investments in capacitor banks or SVCs.

Chapter 3 in this thesis proposes a comprehensive planning technique for ESSs in distribution systems. This technique can be adopted by the distribution company (Disco) to judge the viability of using ESS as a mean of T&D cost deferral with other functions, such as energy arbitrage, reactive power support, and power loss reduction.

2.1.2 Mobile Energy Storage Systems Planning

Whereas the research has been focusing mainly only on the planning of stationary ESSs, the sizing, and planning of an MESS has not yet been thoroughly investigated. On the power industry and research levels, the MESS has witnessed some interest lately. First, an MESS project was conducted by the Electric Power Research Institute (EPRI) in the USA [24], [25]. The project discussed designing a prototype MESS with a utility-scale size that uses the lithium-ion technology for peak shaving. Some MESSs are also available commercially in 100, 1000 and 5000 kW units produced or rented by some companies [26] for peak shaving and improved reliability applications. An example of an MESS prototype project is a 500 kW/1000 kWh project for the tea industry peak shaving in China [27]. Another project under investigation is the design a 500 kW/776 kWh MESS. This MESS uses an SCiBTM lithium-ion battery bank for peak shaving and voltage regulation in the distribution system. The project is located in Spain and is supported by the New Energy and Industrial Technology Development Organization (NEDO) in Japan [28]. The work in [29] investigated the MESS sizing problem to improve the power system reliability; however, it does not introduce a multi-tasking EMS for the MESS, and it does not consider the load and RES uncertainty.

In Chapter 4, the problem of MESS sizing and allocation is investigated. Chapter 4 plans an MESS owned by a Disco. The Disco considers the operation of the MESS in multi-services, such as energy arbitrage, power loss reduction, and reactive power support services. The algorithm in Chapter 4 decides the MESS size and optimal buses to provide such services.

2.2 Energy Management of Storage Systems

After the optimal planning and successful installation of ESSs, the user has to decide the real-time operation strategy of the assets depending on their objectives and the storage type

(long- duration or short duration storage) and the storage technology (stationary or mobile). An ESS may be owned by either the customer or the utility. Detailed applications of ESS have reached 17 application categorized in [3]. These applications objectives vary from electric supply services, ancillary services, grid system services, end-user service and finally, RES integration. In this thesis, the focus is on the EMS development in the following ESS applications:

- Wind power time-shifting (Chapter 5) as a typical application for long-duration storage.
- Wind power grid integration (Chapter 6) as a typical application for short-duration storage.
- Multi-services of MESS (energy arbitrage, power loss reduction and voltage support) as explained in Chapter 8.

For ESSs integration, Chapter 7 defines the safe dispatching levels for multi-ESSs in the power distribution system. The following Subsections (2.2.1-2.2.4) provide a literature survey on each of the areas above.

2.2.1 Predictive EMS of Hybrid WECS-BESS System

There have been many concerns regarding the economic revenue of renewable sources in de-regulated markets. Energy markets are either regulated markets (with fixed tariffs) or de-regulated markets (with variable tariffs). In a de-regulated market, the energy price is high during peak hours, whereas it is low during off-peak hours. To maximize the WECS owner's profit, the owner may invest in adding a BESS to store the wind energy to sell it back during peak hours [30], [31]. This makes the system "hybrid" and capable of performing wind power

time-shifting. A predictive EMS utilizes the future knowledge of both the energy price and WECS generation to choose the optimal times to shift the WECS power.

Recently, predictive control of energy storage has gained research interest either on the lower control level (charging level) [32] or the energy management level [33], [34]. Further, the current development in the electrical vehicles industry [33], [35] has boosted this interest. The model predictive control (MPC) was proposed in several studies for energy management of hybrid systems. In [36], an EMS was proposed as an MPC for an isolated hybrid power system composed of a WECS and BESS. The MPC aims at dispatching the WECS by regulating the BESS power to the desired set-point. The problem was formulated as minimizing a quadratic cost function of the power regulation error. However, the regulation constraints were taken as the BESS power limits and the state of charge (SOC). No constraints on the BESS daily number of cycles (DNC) were considered which may lead to an overcharging and rapid shortage in the battery life. A decentralized MPC for a PV, WECS and BESS stand-alone system was designed in [37]. The controller aimed at minimizing a multi-objective cost function that includes the power imbalance, depth of discharge (DOD) and the PV power during the incoming 24-hour period. Unfortunately, the choice of the weights of this cost function is empirical, which lacks a systematic design approach for different systems. Further, as the design model is nonlinear, non-convex optimization techniques were used to solve this problem. Because reaching a feasible solution is highly related to the weights of the cost function and the initial system conditions, a stopping criterion was used to skip the algorithm after a fixed number of iterations if no feasible solution is reached. In [30], an EMS was designed as an MPC for a hybrid system (PV+BESS). The controller aimed at maximizing the profit by exploiting the market diurnal price difference. In the case of violating the pre-contracted power commitment, a penalty is paid

by the system owner. This penalty was taken into account as a cost in the MPC problem. The work in [30] neglected the storage cost; however, this cost value is nontrivial and can change the overall control strategy [38]. Moreover, although the SOC and the BESS power constraints were considered, the DNC constraint was not included. Recently, this point was considered in [31]. The authors of [31] considered that the optimal DNC is fixed at one cycle/day. The charge/discharge periods were optimized using a two-stage iterative algorithm. However, the unity DNC is only optimal with special wind power and market patterns, and this is not the general case due to the high volatility of the market [39] and the variable daily wind power patterns. Depending on these patterns, it may be more appropriate to allow the DNC to vary from one cycle/day.

To address the shortages above in the previous studies, Chapter 5 proposes an EMS for a hybrid power system composed of a WECS and BESS. The EMS is designed as a real-time MPC that maximizes the owner's profit by performing wind power time-shifting [40] while considering the exact BESS expended-life cost.

2.2.2 Predictive EMS of Hybrid WECS-FESS System

The short-term storage can improve the wind power integration by improving wind power quality which is achieved by limiting the wind power maximum magnitude and ramp rate. A FESS is an effective short-duration storage with a high power density that enables covering peak loads for short times [41]. FESSs start to replace uninterruptable power supply (UPS) units that are combined with a backup diesel generator. FESSs can replace an expensive 15-minutes UPS system to provide a fifteen second ride-through until the diesel engine is synchronized with the system; thus, FESSs fulfill the same task with a remarkably reduced cost and with higher lifetime than the UPS system [42]. Not only FESSs provide a wide range of services in power

systems, but also they have many applications in the medical, transportation and, air aviation fields [43], [44]. Further, a FESS has a fast response time that makes it a perfect tool for improving the power quality, such as voltage sag correction [45]. Furthermore, the FESS has a very long life that can reach 20 years or 100,000 cycles in commercial systems [46].

Because the FESS has a very long life and a rapid response, it is a perfect candidate for various power regulation services. In a DC microgrid, the authors of [47] used a flywheel for real-time model uncertainty compensation using active disturbance rejection control. The authors of [48] proposed a hybrid system composed of a FESS combined with a pumped hydro storage (PHS). The FESS provided a fast response by generating the high-frequency power signals components that cannot be accurately fulfilled by the slow PHS; thus, the total system accuracy was improved. On a higher level, some independent system operators (ISOs), such as the California ISO (CAISO), tested the FESS performance in regulating reserve services [49] and it showed a proven fast response time and an accurate tracking for the regulation signal. In the Pennsylvania-New Jersey-Maryland Interconnection (PJM), USA, the biggest FESS station with a 20 MW rated capacity is participating in the frequency regulation [50]. Recently, Temporal Power has started the commercial operation of a 2.0 MW FESS in Harriston, Ontario [51] as well.

Economically speaking, the FESS has proven to be a viable solution in frequency regulation because it has the lowest net present value (NPV) when compared with other technologies, such as lead-acid batteries and coal stations [50]. The final application of FESSs is in the integration of RESs. A FESS was used to smooth the RES power in an isolated power network [52], and in a grid connected system [53], [54].

Regarding the obstacles facing a FESS, the self-discharge losses (standby losses) may reach high levels [53] mainly due to windage losses [55]. Stand-by losses the main reason limiting the FESS to the short-period storage; however, with the rapid technology in magnetics, windage losses are reduced by using magnetic bearings carrying a shaft rotating in vacuum chambers at very high speeds [56]. A high-speed FESS, driven by induction machines, can operate in a very wide speed range (reaching 16,000 RPM in some practical systems [46]) via field weakening [57]. However, the FESS lifetime is depleted dramatically when the operating speed increases [58], [59]; therefore, a smart EMS is necessary to achieve optimum operation while considering such practical constraints. The work in [60] proposed a smart EMS for smoothing the output power of a wind turbine using a short-term prediction; however, the power loss minimization objective was not considered.

Indeed, the FESS can be depleted very quickly if a poorly-designed EMS is adopted; thus, the work in [53] addressed this problem by reducing the FESS losses used with a wind farm for power smoothing. In [53], an offline nonlinear optimization algorithm was used to derive a relationship between the moving average wind speed and the optimal FESS operation speed to extend the lifetime of the FESS. The main disadvantage of this technique is the sensitivity to the process parameters where any change in the wind energy conversion system parameters demands a new solution. The same research team developed a multiple-task EMS for a FESS in [54], where the FESS was used for both frequency control and active power smoothing (APS). The grid-interfacing converter was switched between the two modes via the frequency regulation error threshold value, whereas the reactive power was always controlled to regulate the ac-side voltage magnitude. A fuzzy controller was designed for APS to decide the active power setpoint depending on the filtered wind power and the FESS speed. On the other hand,

the frequency control was manipulated by a lag compensator with a traditional power versus frequency droop gain. The main drawback in [54] is the expert design criteria and the use of a basic frequency regulation technique without participation in the regulating market. Further, the wind predictions were not used to improve the EMS of the FESS or boost its lifetime.

To overcome the difficulties above, Chapter 6 proposes an EMS for a hybrid system composed of a WECS and a FESS in the transmission system. The FESS regulates the hybrid system output power such that the grid code is respected (maximum power and ramp rate limits) while minimizing the FESS standby losses and boosting its lifetime using the predicted wind power data.

2.2.3 Robust Dispatch of Multiple ESS in Active Distribution Systems

The lack of regulatory rules and grid codes for ESSs in different applications is one of the main challenges facing effective integration of ESSs in grid systems [3], [61]. Whereas an ESS acts as an electrical load or generator as viewed by the grid, the distribution network operator (DNO) needs to define the safe dispatchability zones of each ESS in the case of charge or discharge modes. Within these zones (named from now on as robust operating zone (ROZ)), the DNO should guarantee that system operational limits are respected under renewable generation and load uncertainties. On the other hand, because each ESS has a different stakeholder with different profit portfolios and dispatching agendas (e.g., energy arbitrage or renewable integration), the DNO should not interfere with the ESS commitment or impose a certain dispatching strategy on other assets. In addition to the challenges above, load and RES uncertainty makes the ROZ identification for ESS a complicated problem.

Recently, the dispatchability problem of ESSs in a power system with uncertain resources has gained a significant interest. Research effort in this area is divided into three groups.

Group-A: This group considers the ac power flow model in the dispatching problem; however, the RES or load uncertainty is neglected (deterministic optimal power flow (OPF)). Group A has investigated the ESS effect on the power flow. The authors of [42] designed an EMS for a multi-storage system, including the power flow constraints, to optimize the charge and discharge periods. In [62], an active-reactive OPF problem for the same system was solved using nonlinear programming for profit maximization; whereas in [63], a Lagrangian relaxation was proposed for solving the OPF with ESS. Further, the OPF in the presences of ESSs was solved with dynamic programming using the Bellman recursive technique in [64]. Although the power flow constraints were considered in [65]- [64], the load and RES uncertainty were neglected. Further, the system was assumed to be owned by the same stakeholder, which is not always the case in distributed power grids (as supported by [66], [67] which investigated the independent ESS operation). Furthermore, the participation of ESSs in the reserve market was not considered. However, recent research has proven that participation the regulating reserve is one of the most profitable applications for ESSs [68], and the combination of energy and spinning reserve market participation improves the profit margin [4].

On the other hand, the power flow has been investigated in ESSs planning for power system participation [69]- [70]. Whereas [69] focused on the planning of a dc lossless system [69], the authors of [70] proposed a multi-objective optimization for ESSs in an ac grid with a high penetration level of photovoltaic systems. The nonlinear optimization in [70] aimed at peak shaving and voltage regulation considering the ESS cost trade-off.

Group-B: This group uses different stochastic programming techniques to take into account the uncertainty of RESs and loads, but the ac power flow model is not considered. Further, the stochastic programming is based on the availability of stochastic data, and it requires a huge computational effort.

There is no doubt that the uncertainties of RESs and loads raise serious concerns on power grid security and its technical constraints; thus, Group-B uses the stochastic programming to consider these uncertainties in the optimization problem. The work in [71] focused on ESS and wind integrations for time shifting. The wind speed and price uncertainties were considered using stochastic dynamic programming. Another ESS application that adopts stochastic programming was reported in [72] where the ESS was used for both energy arbitrage and reserve markets participation. Although the uncertainty was considered in [71]- [72], the power flow model was not added to the optimization where a single owner for all assets was assumed. Recently, the work in [66] investigated independently-owned ESSs participating in energy and reserve markets using stochastic programming; however, the power flow model was not considered. Unlike [66], the authors of [73] considered the dc power flow in the study of a stochastic security-constrained unit commitment of ESSs (or hybrid vehicles' fleet) with wind energy. Unfortunately, unlike the dc power flow, the ac power flow models impose nonlinear constraints in the stochastic optimization. As a result, traditional linear programming techniques fail with such non-convex constraints. Another concern about the stochastic programming methods is related to the probabilistic nature of the optimization results [74] where many scenarios are needed to reach reliable results. Accordingly, these methods are computationally intensive [75]. Finally, the stochastic programming methods assume the availability of all probability density functions (PDFs) of system uncertainties which is not always the case.

Group C: This is the most recent group which tries to solve the stochastic programming problems by using robust optimization (RO). Unfortunately, RO faces the problem of giving conservative decisions. Further, no RO work considered the ac power flow during operation so far. Recently, RO has gained wide interest in the literature as a reliable tool for optimization problems with uncertain disturbances [74]- [75]. In [75], RO was used for the unit commitment problem in a wind facility with hydro storage. The authors considered the wind uncertainty but with a deterministic load. The work in [76] addressed this problem via a multi-stage RO that considered both RES and load uncertainties. Recently, an adaptive RO was considered in [74], which presented a general RO scheme for solving the unit commitment problem with any uncertainty at any bus. Further, in [77], an energy management system that uses RO for maximizing the social profit of a microgrid by manipulating a distributed storage and demand side management scheme was proposed. A contingency-constrained unit commitment using RO was discussed in [78]. Three observations related to current RO applications need to be highlighted here.

First, although the power balance and power rate limits were considered in [74]- [77], the power flow constraints were not considered because the problem is already bilinear due to the uncertainty polyhedral set constraints [74]; adding the power flow imposes additional nonlinear constraints leading to feasibility problems.

Second, RO is very sensitive to the uncertainty set choice [79] because the optimization is always inclined to satisfy the worst-case scenario which is allocated at an extreme boundary of the polyhedral uncertainty set [74]. Thus, a conservative choice for the uncertainty set leads to very conservative commitment results. The uncertainty budget is a good way to manipulate the uncertainty set size; however, there are not enough techniques in the literature addressing the

budget choice criterion. Finally, the work in [74]- [77] assumed a single stakeholder for all assets who has the right to decide the dispatch strategies of all assets.

To overcome the drawbacks of RO and stochastic programming, Chapter 7 proposes a framework to facilitate ESSs participation in day-ahead markets under distribution system uncertainty taking the power flow constraints into consideration.

2.2.4 EMS of Mobile Storage System

Like stationary ESSs, mobile ESSs, such as electric vehicles (EVs), can provide various services to the grid as well. For example, although the demand response can provide high energy cost reduction (via load shifting to the off-peak hours) [80], combining EVs with demand response has proven to improve the power balance and demand response management results [81]. Using EVs is an effective solution for the renewable sources intermittency problem in microgrids [82]. Besides, when EVs are controlled to regulate the PV power intermittency, it leads to a significant cost minimization in PV-powered-charging stations [83]. Aggregated EVs in parking lots can participate in the vehicle to grid (V2G) and grid to vehicle (G2V) programs to reduce the energy cost via energy arbitrage [84] and/or participating in the reserve market [85].

Unlike EVs, an MESS is a utility-scale storage bank (e.g., lithium-ion battery) owned and fully controlled by the utility company. The storage is mobilized by a truck and connected to the system at different stations. The advantage of transportability is the ability to deliver a localized reactive power support, power loss reduction, voltage regulation, dispersed RESs integration, and T&D upgrade deferral. Indeed, the MESS is a promising storage technology that will contribute to solve many problems in active distribution systems. Optimal scheduling and

energy management algorithms for an MESS in an active distribution system are not developed in the current literature; thus, Chapter 8 proposes a day-ahead EMS for an MESS owned by a Disco. The Disco uses the MESS for minimizing the day-ahead cost of the power imported from the grid. Further, the MESS provides a reactive power support for the system for voltage regulation at critical loads.

Chapter 3

Stationary Energy Storage Systems Sizing and Allocation for Multi-Services in Active Distribution Systems

3.1 Introduction

Energy storage systems (ESSs) provide various power and ancillary services at the distribution system level [3], [4]. One of these services is the transmission and distribution (T&D) cost deferral. When an ESS is dispatched for peak shaving, it defers the upgrade investments required to increase the network current carrying capacity (including feeders and substations). An ESS also makes a profit due to the diurnal energy price variation (energy arbitrage [3]). The T&D cost deferral using ESSs was investigated in a study conducted by SANDIA in [86]; the study showed the economic benefits of using an ESS in T&D upgrade. Besides, an ESS, if optimally allocated and sized in the distribution network, represents a strategic reactive power reservoir. Further, a significant power loss minimization is possible via an ESS, especially in heavily-loaded long feeders (high R/X ratio).

Still, this brings up the question of the viability of ESS services especially with the relatively high cost of some ESS technologies and shorter lifetime (e.g., batteries). Besides, in the case when an ESS is a viable T&D upgrade cost option, the optimal solution may combine different technologies; e.g., SVC, DG, and capacity upgrade along with the ESS option. This chapter is dedicated to investigating the sizing and allocation of these technologies to provide T&D upgrade deferral while providing multi-services for the distribution system owner (Disco).

The main contributions of the proposed planning scheme are as follow:

- 1- The uncertainty of parameters is considered by adopting different realistic daily time-series scenarios for load, the wind, and PV and market price profiles. Further, K-mean Clustering technique is utilized for scenarios minimization to reduce the computational effort.
- 2- Different technologies (ESS, DG, SVC, feeder's upgrade) are considered in the planning scheme as T&D solutions. Thus, our cost/benefit analysis is more comprehensive and fair.
- 3- The planning scheme respects the power system constraints regarding the voltage level and feeder's capacity which guarantees an acceptable power quality.
- 4- ESS life constraints are well modeled during the planning horizon, including the state of charge and the total/daily numbers of cycles.
- 5- ESS participates in Multi-tasks including; energy arbitrage, reactive power support, energy losses minimization, and finally feeder's upgrade cost deferral.
- 6- The comprehensive algorithm can compare different ESS technologies (portfolio) since it allows defining the ESS efficiency, the number of cycles, and its associated costs.

Chapter 3 is organized as follows. Section 3.2 presents the problem formulation, including the objective function, and its constraints. Section 3.3 validates the proposed method using a case study on a real distribution feeder. The case study uses realistic wind, PV, market and load data to show the main contribution of this work. A case study is discussed in Section 3.4. Finally, the conclusions are drawn in Section 3.5.

3.2 Problem Formulation

The distribution company (Disco) is an organization that makes a profit by delivering electrical energy from the transmission system to the final residential consumers via its distribution network. The main profit is the difference between the energy market wholesale buy price and the end-user sell price. A distribution network upgrade is required to adapt to the growing rate of loads and the increasing penetration of RESs. T&D upgrading includes increasing the current carrying capacity of feeders, substations upgrade (transformers), or even adding a reactive power source in case of weak grids. The assets upgrade represents a huge cost on the Disco which requires an unusual solution to bring the cost down. Adding an ESS can defer some T&D costs as reported in [86]. This work proposes an ESS sizing and allocation technique for upgrade cost minimization whereas ESSs are optimally dispatched for providing different services. The optimization aims at maximizing the Disco profit while maintaining an acceptable power quality level.

Before discussing the cost function and presenting the operational constraints, the symbols terminology is explained. For any parameter $x_b^a(i)$, x is the parameter/variable name (e.g., p : power, c : cost, v : rms voltage); a represents the technology description (e.g., ESS, DG, SVC), b is a time index (e.g., sc : scenario where a scenario here describes a daily profile for all exogenous inputs, y : year index, t : hour index); and finally, i is the location index (e.g., i : bus index, l : branch index). For example, $q_{sc,y,t}^{SVC}(i)$ is the reactive power injected by the SVC located at bus i at the hour t of a day (scenario) sc of the planning year y . The cost function presents the Disco profit during the planning horizon as given in (3.1).

$$\begin{aligned} & \text{Maximize (pro)} \\ \text{pro} = & inc - c^{grid} - c^{ES} - c^{SVC} - c^{DG} - c^{T\&D} - c^{imb} \end{aligned} \quad (3.1)$$

The Disco profit (*pro*) results from the income resulting from selling energy to the end-users. The expenses include the energy purchasing cost from the grid, the storage cost, SVC and DG investment costs, future T&D upgrade costs for the substations and feeders, and finally, the power imbalance cost that includes RESs curtailment or load shedding. As shown in Figure 3-1, the techno-economic model is an inter-connected system. The optimization decision variables are the SVC, DG, and ESS sizes/locations plus the power set points for SVC, DG, ESS, load shedding and wind/PV curtailment. The input data includes the wind, PV, and load expected powers. The power flow model calculates the branches' powers which affect the T&D upgrade cost and the grid power needed; having all the previous inputs beside the cost of all assets results in the profit calculation as shown in (3.1). The following section demonstrates the models, constraints and cost models of different system components.

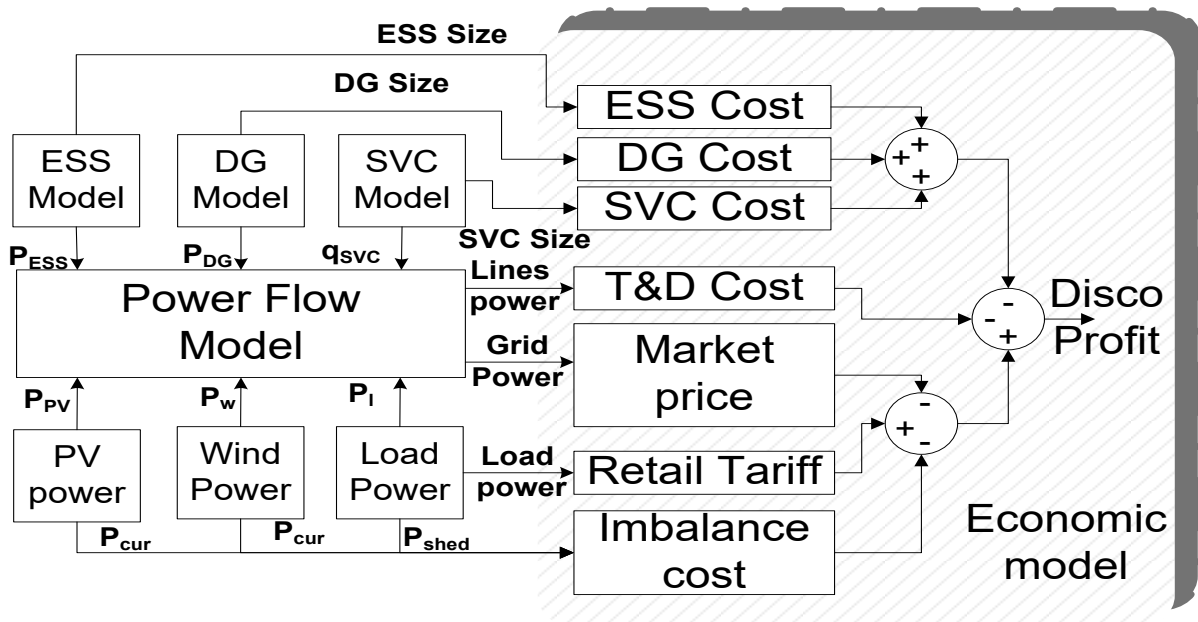


Figure 3-1 System model and interconnection between the technical system and the economic model for the planning optimization problem.

3.2.1 ESS Dynamic Model

At any sample t , the ESS is either charging power ch or discharging power dc . The ESS power p^{ES} is the sum of these two powers as expressed in (3.2). The discharge power is negative whereas the charge power is positive; both are limited by the ESS rated apparent power \mathbb{S}^{ES} as expressed in (3.2)-(3.4). The binary variable $ce_{y,sc,t}^{ES}(i)$ guarantees that the discharge and charge powers are mutually exclusive at each sample time for each ESS. Further, when charging is enabled $ce_{y,sc,t}^{ES}(i) = 1$, the first constraints of (3.3), $0 \leq ch_{y,sc,t}^{ES}(i) \leq \mathbb{S}^{ES}(i)$, is dominant because $\mathbb{S}^{ES}(i) \leq \overline{\mathbb{S}^{ES}}$. When charging is disabled $ce_{y,sc,t}^{ES}(i) = 0$, the second constraint of (3.3) is dominant. A similar logic applies to the discharging constraint (3.4). Decomposing the constraints in this way (instead of $0 \leq ch_{y,sc,t}^{ES}(i) \leq \mathbb{S}^{ES} ce_{y,sc,t}^{ES}(i)$) enables the inclusion of both the operational and planning constraints in a mixed-integer linear forms instead of nonlinear ones.

$$p_{y,sc,t}^{ES}(i) = ch_{y,sc,t}^{ES}(i) + dc_{y,sc,t}^{ES}(i) \quad (3.2)$$

$$0 \leq ch_{y,sc,t}^{ES}(i) \leq \mathbb{S}^{ES}(i) \quad 0 \leq ch_{y,sc,t}^{ES}(i) \leq \overline{\mathbb{S}^{ES}} ce_{y,sc,t}^{ES}(i) \quad (3.3)$$

$$-\mathbb{S}^{ES}(i) \leq dc_{y,sc,t}^{ES}(i) \leq 0 \quad -\overline{\mathbb{S}^{ES}}(1 - ce_{y,sc,t}^{ES}(i)) \leq dc_{y,sc,t}^{ES}(i) \leq 0 \quad (3.4)$$

The ESS instantaneous energy $E_{y,sc,t}^{ES}$ is calculated dynamically from the ESS power whereas both the charge and discharge efficiencies are considered as in (3.5) such that ($\eta^{ch} < 1, \eta^{dc} > 1$). The notation η^{dc} represents the reciprocal of the per-unit discharge efficiency. It is worth mentioning that an hourly sample rate is considered; thus the power equals the energy. The ESS energy is limited by its rated capacity in (3.6). The number of cycles N^{ES} is another expression used to count the absorbed and injected power from the ESS daily (in Watt-hours) as in (3.7). When a rated capacity \mathbb{E}^{ES} is absorbed and injected by an ESS, N^{ES} is incremented by $1 \times \mathbb{E}^{ES}$. N^{ES}

is daily controlled by (3.8) which limits the daily cycles to a \overline{DN}^{ES} cycle/day. The total number of cycles $\overline{TN}^{ES}\mathbb{E}^{ES}(i)$ represents the total energy traded during the ESS service life as in (3.9). For example, if each year is presented by four daily scenarios (one for each season), the probability of each scenario is 25% of the year days ($\rho_{sc} = 91 \text{ days}$). At the end of each scenario ($t = 24\forall sc\forall y$), the number of cycles $N_{y,sc,t=24}^{ES}$ reflects the stored kWh from/to the system. Summing these amounts for all scenarios during all operation years leads to the total exchanged energy with the grid during the storage service time which is limited by the storage nominal number of cycles \overline{TN}^{ES} .

$$E_{y,sc,t+1}^{ES} = E_{y,sc,t}^{ES} + (\eta^{ch}ch_{y,sc,t}^{ES} + \eta^{dc}dc_{y,sc,t}^{ES}(i)) \quad (3.5)$$

$$0 \leq E_{y,sc,t}^{ES} \leq \mathbb{E}^{ES}(i) \quad (3.6)$$

$$N_{y,sc,t+1}^{ES} = N_{y,sc,t}^{ES} + \frac{(\eta^{ch}ch_{y,sc,t}^{ES} - \eta^{dc}dc_{y,sc,t}^{ES}(i))}{2} \quad (3.7)$$

$$0 \leq N_{y,sc,t=24}^{ES}(i) \leq \overline{DN}^{ES}\mathbb{E}^{ES}(i) \quad (3.8)$$

$$\sum_y \sum_{sc} \rho_{sc} N_{y,sc,t=24}^{ES}(i) \leq \overline{TN}^{ES}\mathbb{E}^{ES}(i) \quad (3.9)$$

For ESSs allocation and sizing, a binary location variable $z^{ES}(i)$ models the existence of an ESS station at certain bus i . The maximum desired number of ESS establishments is limited by (3.10). On the other hand, the maximum power and capacity ratings are upper bounded by (3.11)-(3.12). This sizing/allocation model has been adopted before in [9].

$$\sum_i z^{ES}(i) \leq \overline{z}^{ES}, i \in \mathcal{N}^{ES} \quad (3.10)$$

$$0 \leq \mathbb{S}^{ES}(i) \leq z^{ES}(i)\overline{\mathbb{S}}^{ES} \quad (3.11)$$

$$0 \leq \mathbb{E}^{ES}(i) \leq z^{ES}(i)\overline{\mathbb{E}}^{ES} \quad (3.12)$$

Because ESSs will participate in reactive power support in the proposed planning framework, the reactive power is constrained by the power converter thermal capacity expressed in (3.13). Because (3.13) is a nonlinear constraint (a sphere domain with a variable radius \mathbb{S}^{ES}), it is linearized by a set of linear vectors f^{ES} that defines the ESS thermal capability domain $\varphi^{ES}(i)$ as explained in (3.14). Further details on the linearized domain are given in [9].

$$p_{y,sc,t}^{ES}(i)^2 + q_{y,sc,t}^{ES}(i)^2 \leq \mathbb{S}^{ES^2} \quad (3.13)$$

$$f^{ES}(p_{y,sc,t}^{ES}(i), q_{y,sc,t}^{ES}(i), \mathbb{S}^{ES}(i)) \in \varphi^{ES} \quad (3.14)$$

The ESS initial capital cost in (3.15) includes its fixed cost FC^{ES} (land, installation cost, etc.); ESS power conversion system cost C^{ES}/MW ; and ESS storage cost C^{ES}/MWh that stands for the battery bank price. The operation and maintenance costs $O\&M^{ES}$ are calculated and transferred to the first year considering the interest rate IR during the project life y [9]; all operational future costs are referred to the year of investment as a common time reference for a correct judgement on the project cost/benefit analysis. If the inflation rate is significant, it can be included to calculate the effective interest rate as explained in [23]. It is worth mentioning that the energy constraint (3.6) allows a full battery discharge which may reduce its life time. As a compensation, an extension for the ESS capacity can be added by setting α^{TN} (e.g., set $\alpha^{TN} = 0.2$ for getting an equivalent life of \overline{TN}^{ES} at 20% minimum SOC).

$$c^{ES} = \sum_i z^{ES}(i)FC^{ES}(i) + C^{ES}/MVA \mathbb{S}^{ES}(i) + C^{ES}/MWh(1 + \alpha^{TN})\mathbb{E}^{ES}(i) + \frac{\sum_y \sum_i z^{ES}(i)O\&M^{ES}(i)}{(1 + IR)^{y-1}} \quad (3.15)$$

3.2.2 Distributed Generation

Distributed generators (DGs), e.g., a micro turbine empowered by natural gas or a diesel generator, are another possible investment option for T&D cost deferral. DGs power limit and allocation are stated in (3.16)-(3.19). When a DG is connected to the grid via a voltage-source

converter (e.g., fuel cell), the capability curve is linearized in a way similar to (3.14). If a DG is directly connected via an ac machine, the capability curve includes the rotor and stator current limits, and the stator ends iron heating limits. The capability curve is linearized as explained in [9] and the resulting linear vectors are expressed as f^{DG} in (3.19).

$$\sum_i z^{DG}(i) \leq \overline{z^{DG}}, i \in \mathcal{N}^{DG} \quad (3.16)$$

$$0 \leq \mathbb{S}^{DG}(i) \leq z^{DG}(i) \overline{\mathbb{S}^{DG}} \quad (3.17)$$

$$0 \leq p_{y,sc,t}^{DG}(i) \leq \mathbb{S}^{DG}(i) \quad (3.18)$$

$$f^{DG}(p_{y,sc,t}^{DG}(i), q_{y,sc,t}^{DG}(i), \mathbb{S}^{DG}(i)) \in \varphi^{DG}(i) \quad (3.19)$$

Unlike ESSs, the DG cost includes a nontrivial running cost plus the capital cost; the installation FC^{DG} , and the DG price C^{DG}/MVA as in (3.20). The DG running cost is a quadratic function in the active power as expressed in (3.21).

In (3.21), at certain time t , if the DG is on, then $SS_{y,sc,t}^{DG}(i) = 1$. An initial running cost $\theta_y^{\$}$ is considered regardless of the DG power whereas the DG power (and quadratic power) affects the fuel consumption depending on the DG parameters $(\theta_y^{\$/MW^2}, \theta_y^{\$/MW})$. These parameters may vary yearly with the fuel average yearly price as well. Summing the operation costs for each sample t in each scenario Sc and after considering the scenario yearly probability of occurrence (ρ_{sc}) will result in the yearly DG running cost. Finally, repeating the same process for each year gives the DG total running cost during the planning period.

A piece-wise linearization for the DG cost is possible by dividing the operating power domain into g slices in (3.22)-(3.23) and linearizing each slice as in [87]. In the case of cost

linearization, the constraints in (3.23) are added to define the different linearization domains limits.

$$c^{DG} = \sum_i z^{DG}(i)FC^{DG}(i) + C^{DG/MVA}\$^{DG}(i) + \frac{\sum_y \sum_i z^{DG}(i)O\&M^{DG}(i) + OC_y^{DG}(i)}{(1 + IR)^{y-1}} \quad (3.20)$$

$$OC_y^{DG}(i) = \sum_y \sum_{sc} \rho_{sc} \sum_t \theta_y \$/MW^2 (p_{sc,y,t}^{DG}(i))^2 + \theta_y \$/MW p_{y,sc,t}^{DG}(i) + \theta_y \$ SS_{y,sc,t}^{DG}(i) \quad (3.21)$$

$$OC_y^{DG}(i) \cong \sum_y \sum_{sc} \rho_{sc} \sum_t \sum_g \beta_y \$/MW p_{y,sc,t}^{DGg}(i) + \beta_y \$ SS_{y,sc,t}^{DG}(i) \quad (3.22)$$

$$p_{sc,y,t}^{DG}(i) = \sum_g p_{y,sc,t}^{DGg}(i), 0 \leq p_{y,sc,t}^{DGg}(i) \leq SS_{y,sc,t}^{DG}(i) \overline{p^{DGg}} \quad (3.23)$$

For a viable DG investment, the Levelized cost of its production (\$/MWh) must be less than the grid price; otherwise, the optimization process will not consider such investment as a cost-saving one. In some cases, DGs are owned by the consumers, which became allowed by most of the Discos. In such a case, the DG generation schedule is considered as an input for the power flow model without including DGs as an investment option in the planning scheme. It is worth mentioning that such a detailed model for the DG cost introduces many variables to the planning problem; thus, it is practical to consider such a model with a few number of DGs. When the number of DGs is large, modeling simplifications (such as considering a linear operating cost and neglecting start-up cost) are acceptable for the sake of problem simplification.

3.2.3 Static VAr Compensator (SVCs)

The SVCs can provide an efficient voltage regulation service by installing them at the far end buses in case of weak grids. Improving the voltage profile reduces the power loss and increases

the feeder current carrying capacity. The allocation and rating of SVCs are governed by (3.24)-(3.26) whereas the SVC cost (capital and O&M) is stated in (3.27).

$$\sum_i z^{SVC}(i) \leq \overline{z^{SVC}}, i \in \mathcal{N}^{SVC} \quad (3.24)$$

$$0 \leq \mathbb{Q}^{SVC}(i) \leq z^{SVC}(i) \overline{\mathbb{Q}^{SVC}} \quad (3.25)$$

$$-\mathbb{Q}^{SVC}(i) \leq q_{y,sc,t}^{SVC}(i) \leq \mathbb{Q}^{SVC}(i) \quad (3.26)$$

$$c^{SVC} = \sum_i z^{SVC}(i) FC^{SVC}(i) + C^{SVC}/MVR \mathbb{Q}^{SVC}(i) + \frac{\sum_y \sum_i z^{SVC}(i) O\&M^{SVC}(i)}{(1+IR)^{y-1}} \quad (3.27)$$

3.2.4 Power Imbalance Solutions

The power imbalance results from unexpected changes in loads or variations in the power generated by RESs. The system operator can use many tools to rebalance the power, like load shedding, RES curtailment, or up and down regulation by exporting/importing extra energy from grid/ESS/DGs. The load shedding is constrained by each bus load power as in (3.28) whereas the RES curtailment is limited by the RES power in (3.29). To avoid excessive load shedding, the constraint in (3.30) keeps the disconnected load energy below a certain level $\overline{\mathbb{E}^{shd}}$ that agrees with the power quality and reliability standards.

$$0 \leq p_{y,sc,t}^{shd}(i) \leq p_{y,sc,t}^{load}(i), i \in \mathcal{N}^{load} \quad (3.28)$$

$$0 \leq p_{y,sc,t}^{cur}(i) \leq p_{y,sc,t}^{res}(i), i \in \mathcal{N}^{RES} \quad (3.29)$$

$$\sum_y \sum_{sc} \rho_{sc} \sum_t \sum_i p_{y,sc,t}^{shd}(i) \leq \overline{\mathbb{E}^{shd}} \quad (3.30)$$

The cost associated with load shedding c^{shd} in (3.31) represents a loss of energy sale priced at $sp_{sc,y,t}$, plus a penalty $spen_{sc,y,t}$ paid by the Disco to the consumer for the loss of service, $spen_{sc,y,t}$ is a time-variant penalty because the shedding time affects the customer comfort level

differently. Regarding the RES curtailment cost c^{cur} , it may be modelled to include the levelized generation cost of the RES plus an environmental penalty for curtailing a clean power source ($cpen$) as in (3.32).

$$c^{shd} = \sum_y \sum_{sc} \rho_{sc} \sum_t (sp_{y,sc,t} + spen_{y,sc,t}) \sum_i p_{y,sc,t}^{shd}(i) \quad (3.31)$$

$$c^{cur} = \sum_y \sum_{sc} \rho_{sc} \sum_t (cpen) \sum_i p_{y,sc,t}^{cur}(i) \quad (3.32)$$

Finally, the total power imbalance cost is defined as in (3.33).

$$c^{imb} = c^{cur} + c^{shd} \quad (3.33)$$

3.2.5 Power Flow Model

The power flow model for a radial distribution network consists of a single slack bus and a set of PQ-buses $i \in \mathcal{N}^{bus}, i \neq 0$ that connects a group of branches $l: (i \rightarrow j) \in \psi$. In the power flow model, the change in buses active and reactive power $\Delta p_{y,sc,t}^{bus}(i), \Delta q_{y,sc,t}^{bus}(i)$ leads to a change in each node voltage amplitude and angle. For a set of buses \mathcal{N}^{bus} , the power is represented as the sum of RESs (after curtailment), load (after shedding), DGs, SVC and ESS powers as in (3.34)-(3.37). The injected power has a negative sign whereas the absorbed one is positive. The ESS discharge power is negative as well. The loads are assumed as a constant power type with a power factor pf ; thus the load reactive power is a constant ratio of the active power as $q_{y,sc,t}^{Load} = \lambda_{y,sc,t}^{Load} p_{y,sc,t}^{Load}$, $\lambda_{y,sc,t}^{Load} = \tan(\cos^{-1} pf)$. Further, the RES reactive power can be modeled by tuning $q_{sc,y,t}^{res}$ but in such a case, an apparent power for RES has to be added.

$$p_{y,sc,t}^{bus}(i) = (p_{y,sc,t}^{Load}(i) - p_{y,sc,t}^{shd}(i)) - (p_{y,sc,t}^{res}(i) - p_{y,sc,t}^{cur}(i)) - p_{y,sc,t}^{DG}(i) + p_{y,sc,t}^{ES}(i) \quad (3.34)$$

$$q_{y,sc,t}^{bus}(i) = (\lambda_{y,sc,t}^{Load} p_{y,sc,t}^{Load}(i) - \lambda_{y,sc,t}^{Load} p_{y,sc,t}^{shd}(i)) - q_{y,sc,t}^{res}(i) - q_{y,sc,t}^{DG}(i) + q_{y,sc,t}^{ES}(i) - q_{y,sc,t}^{SVC}(i) \quad (3.35)$$

$$\Delta p_{y,sc,t}^{bus}(i) = -p_{y,sc,t}^{shd}(i) + p_{y,sc,t}^{cur}(i) - p_{y,sc,t}^{DG}(i) + p_{y,sc,t}^{ES}(i) \quad (3.36)$$

$$\Delta q_{y,sc,t}^{bus}(i) = -\lambda_{y,sc,t}^{load} p_{y,sc,t}^{shd}(i) - q_{y,sc,t}^{DG}(i) + q_{y,sc,t}^{ES}(i) - q_{y,sc,t}^{SVC}(i) - q_{y,sc,t}^{res}(i) \quad (3.37)$$

In a distribution system with a low voltage-angle difference, many studies discussed the power flow relaxation and convexification [88], [89]. One of the power flow approximations in distribution systems uses the second-order cone programming as adopted before in [9] and [90]. Another simple linear technique depends on calculating the voltage Jacobian from the power flow (voltage sensitivity to active and reactive power) [91]. The advantage of the sensitivity technique is the resulting linear equality constraints that simplify the optimization problem, especially with a huge number of variables and constraints, like the present planning problem. The power loss sensitivity can be calculated as well [92], [93]. Before optimization, the initial total power loss $ip_{y,sc,t}^{loss}$, $iq_{y,sc,t}^{loss}$ are calculated and the instantaneous loss sensitivity to the active and reactive power matrices $\left. \frac{dp^{loss}}{dP^{bus}} \right|_{y,sc,t}$, $\left. \frac{dq^{loss}}{dQ^{bus}} \right|_{y,sc,t}$ are obtained. The total power loss is expressed as a sum of the initial power loss and the resulting losses due to any power change at any bus as in (3.38)-(3.39). Finally, the grid power (slack bus) is the sum of all buses power plus the total power loss [6] as shown in (3.40)-(3.41).

$$p_{y,sc,t}^{loss} = ip_{y,sc,t}^{loss} + \left. \frac{dp^{loss}}{dP^{bus}} \right|_{y,sc,t} \Delta P_{y,sc,t}^{bus} + \left. \frac{dq^{loss}}{dQ^{bus}} \right|_{y,sc,t} \Delta Q_{y,sc,t}^{bus} \quad (3.38)$$

$$q_{y,sc,t}^{loss} = iq_{y,sc,t}^{loss} + \left. \frac{dq^{loss}}{dP^{bus}} \right|_{y,sc,t} \Delta P_{y,sc,t}^{bus} + \left. \frac{dq^{loss}}{dQ^{bus}} \right|_{y,sc,t} \Delta Q_{y,sc,t}^{bus} \quad (3.39)$$

$$p_{y,sc,t}^{grid} = p_{y,sc,t}^{bus}(i=0) = \sum_{i,i \neq 0} p_{y,sc,t}^{bus}(i) + p_{y,sc,t}^{loss} \quad (3.40)$$

$$q_{y,sc,t}^{grid} = q_{y,sc,t}^{bus}(i=0) = \sum_{i,i \neq 0} q_{y,sc,t}^{bus}(i) + q_{y,sc,t}^{loss} \quad (3.41)$$

Because the total power loss is represented in the grid power expression, the branches power is calculated by the power balance expression in (3.42)-(3.43) which indicates that the branch power equals the branch output bus power plus the power transferred to other branches

connected to it [90]. The branch capacity is limited by (3.45), where the apparent power of the feeder $s_{sc,y,t}^f(l)$ is limited by the nominal feeder thermal capacity $\mathbb{S}^f(l)$ after considering a reserve capacity fr to account for uncertainties. A feeder extension is possible by adding a capacity extension \mathcal{C}^{fm} that is associated with the feeder upgrade method m ; each method has a different capacity extension that is enabled by the variable $z^{fm}(l)$.

A linearized version of the constraint (3.45) is given in (3.46). It is worth mentioning that linearizing (3.44) leads to convexifying the optimization problem at the price of adding more variables and less accuracy for the capability function. For instance, Figure 3-2 compares the constraint domain of the original capability curve (circle as in (3.44)); when this nonlinear function is linearized around more operating points (twenty instead of eight for example), the linearized constraints almost coincide with the circle. However, the number of constraints increases from eight into twenty. As a result, this trade-off should be considered when linearizing any nonlinear function. A similar concept applies to the constraints (3.14), (3.19).

$$p_{y,sc,t}^f(l) = p_{y,sc,t}^{bus}(j) + \sum_{k:(j \rightarrow n) \in \psi} p_{y,sc,t}^f(k), \quad l: (i \rightarrow j) \quad (3.42)$$

$$q_{y,sc,t}^f(l) = q_{y,sc,t}^{bus}(j) + \sum_{k:(j \rightarrow n) \in \psi} q_{y,sc,t}^f(k), \quad l: (i \rightarrow j) \quad (3.43)$$

$$s_{y,sc,t}^f{}^2(l) = p_{y,sc,t}^f{}^2(l) + q_{y,sc,t}^f{}^2(l), \quad l: (i \rightarrow j) \quad (3.44)$$

$$\|s_{y,sc,t}^f(l)\| \leq \mathbb{S}^f(l) + \sum_m z^{fm}(l) \mathcal{C}^{fm} / (1 + fr^f) \quad (3.45)$$

$$f^l(p_{y,sc,t}^f(l), q_{y,sc,t}^f(l)) \leq \mathbb{S}^f(l) + \sum_m z^{fm}(l) \mathcal{C}^{fm} / (1 + fr^f) \quad (3.46)$$

Regarding the voltage level, the initial voltage $iv_{sc,y,t}$ is first calculated before optimization.

After calculating the voltage sensitivity $\left. \frac{dv(i)}{dP^{bus}} \right|_{y,sc,t}$, $\left. \frac{dv(i)}{dQ^{bus}} \right|_{y,sc,t}$, the nodal voltage magnitude is

given and limited in (3.47)-(3.48) as a function of the buses power change. Finally, the Disco

income inc from selling energy depends on its retail selling tariff $sp_{y,sc,t}$ as in (3.49). Some companies adopt a fixed monthly tariff like EPCOR-Alberta, and others have an on-peak/off-peak tariff, such as Hydro One-Ontario.

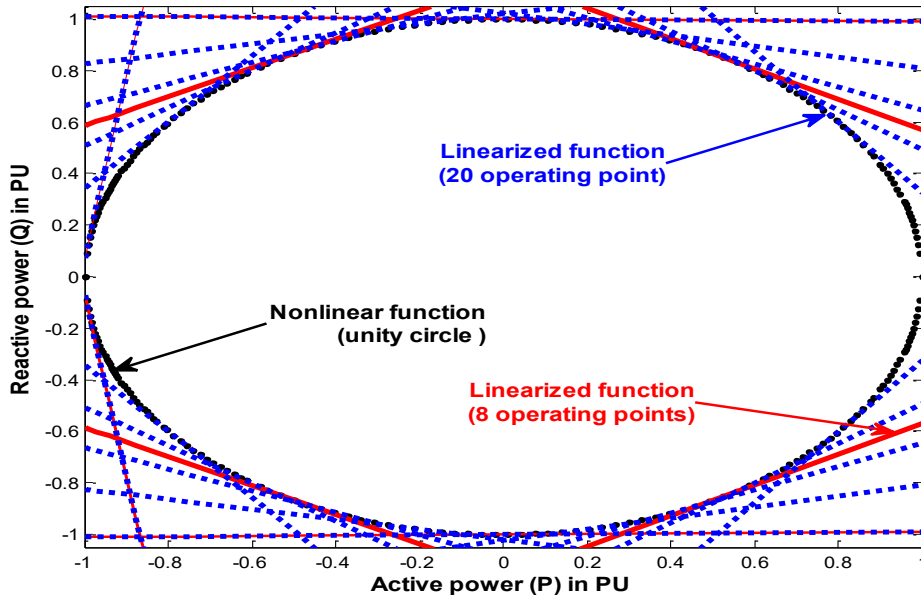


Figure 3-2 Linearized capability curves for a circle with a different number of linearizing lines.

$$v_{y,sc,t}(i) = iv_{y,sc,t} + \left. \frac{dv(i)}{dP^{bus}} \right|_{y,sc,t} \Delta P_{y,sc,t}^{bus} + \left. \frac{dv(i)}{dQ^{bus}} \right|_{y,sc,t} \Delta Q_{y,sc,t}^{bus} \quad (3.47)$$

$$\underline{v} \leq v_{y,sc,t}(i) \leq \bar{v} \quad (3.48)$$

On the other hand, the Disco buys energy from the wholesale energy pool with a market price $bp_{y,sc,t}$ expressed in (3.50). The T&D cost $c^{T\&D}$ includes the sum of each feeder l (with a length le^f) upgrade cost $UC^{f_m/KM}$ to a higher capacity model m . Further, the substation is upgraded to a rating similar to its connected feeder $l=l$ but with a different upgrade cost as in (3.51).

$$inc = \sum_y \sum_{sc} \rho_{sc} \sum_t sp_{sc,y,t} \sum_i p_{sc,y,t}^{Load}(i) \tau \quad (3.49)$$

$$c^{grid} = \sum_{sc} \rho_{sc} \sum_y \sum_t bp_{sc,y,t} p_{sc,y,t}^{grid} \tau \quad (3.50)$$

$$c^{T\&D} = \sum_m z^{fm}(1) UC^{subm} + \sum_l \sum_m z^{fm}(l) le^f(l) UC^{fm/KM} \quad (3.51)$$

By subtracting the income from the grid energy cost ($inc - c^{grid} = \sum_{sc,y,t} \rho_{sc} (sp_{sc,y,t} - bp_{sc,y,t}) \sum_i p_{sc,y,t}^{Load}(i) \tau - bp_{sc,y,t} p_{sc,y,t}^{loss}$), the optimization aims at reducing the energy losses cost automatically when it maximizes the Disco profit.

Indeed, ESSs are apparently sized/allocated to participate in different services simultaneously: energy arbitrage that takes advantage of the diurnal price difference ($bp_{sc,y,t}$); energy losses minimization depending on its purchase value $bp_{sc,y,t} p_{sc,y,t}^{loss}$; reactive power support (imposed by the constraint (3.48)); T&D upgrade reduction (in order to minimize $c^{T\&D}$), and finally, regulating reserve services (for reducing c^{imb}). The final upgrade problem is represented as a mixed-integer quadratic problem as stated in (3.52) whereas the profit is presented in (3.1).

$$\begin{aligned} & \max_{\mathbb{S}, \mathbb{Z}, x_{sc,y,t}} \text{pro} & (3.52) \\ \text{s. t. } & \left\{ \begin{array}{l} \text{ESS dynamical model: (3.2) - (3.12)\&(3.14)} \\ \text{DG power constraints: (3.16) - (3.19)} \\ \text{SVC power constraints; (3.24) - (3.26)} \\ \text{power imbalance: (3.28) - (3.30)} \\ \text{Power flow model: (3.34) - (3.43)\&(3.46) - (3.48)} \end{array} \right. \end{aligned}$$

The optimization variables consist of the rating set \mathbb{S} (contains any technology rating $\mathbb{S} = \{\mathbb{S}^{ES}, \mathbb{S}^f, \mathbb{S}^{DG}, \mathbb{Q}^{SVC}\}$), the allocation binary set that includes the locations, on/off decisions in the entire problem $\mathbb{Z} = \{\mathbb{Z}^{ES}, \mathbb{Z}^{DG}, \mathbb{Z}^{SVC}, \mathbb{Z}^f\}$, and any dispatch variable of the form $x_{sc,y,t}$, such as power or voltage.

For each year y , the daily scenario changes from season to season, from month to month and even from working days to weekends (e.g., as depicted in Figure 3-5 for the first-year daily scenarios).

Considering 365 daily scenarios per year or even more than 365 by assuming an k possibility for each daily scenario such that $\sum_y \sum_{SC} \sum_k \rho_{k,sc} = 1$, the previous assumptions will lead to an enormous problem size. As a result, and without loss of generalization, this work uses a scenarios minimizations technique using the k -means method similar to the one adopted in [9]. First, each day n is represented by a realization Re_n that consists of PV, load, wind and price normalized data where $(Re_n, n = 1:n)$ dimension is 1×96 in case of hourly sampled data. By setting the number of desired scenarios to J , the k -means clustering approximates all the n realizations by a J centroids $(c_{sc}, sc = 1:J)$. The Euclidian distance of each realization is $d_{Nsc} = \|Re_N - c_{sc}\|_2$ defines the belonging factor (the membership value) of each realization Re_N to a certain centroid c_J . Finally, d_{Nsc} is used to calculate the probability of each centroid ρ_{sc} .

Regarding the quality of this approximation, Figure 3-4 shows the per unit (pu) Euclidean distance of each realization of the first year (shown in Figure 3-5) with the ten approximating scenarios. The sum of all distances from a realization to all scenarios is equal to one. Although four scenarios (1, 4, 6, and 9) can approximate the realizations accurately because they are very close to most of the scenarios (their mean pu distance to all realization is less than 0.05 pu and consequently they have a higher probability ρ_{sc}), these scenarios, still, have a long distance to some special realizations (e.g., days with an unusual load profile or volatile market). Such uncommon realizations are well fitted by the other scenarios that have a very close distance to them while they are far away from most of common realizations.

3.3 Case Study

This section validates the proposed planning scheme by testing it for upgrading a real rural radial feeder in Ontario-Canada, owned by Hydro One (the Disco) [94] as shown in Figure 3-3.

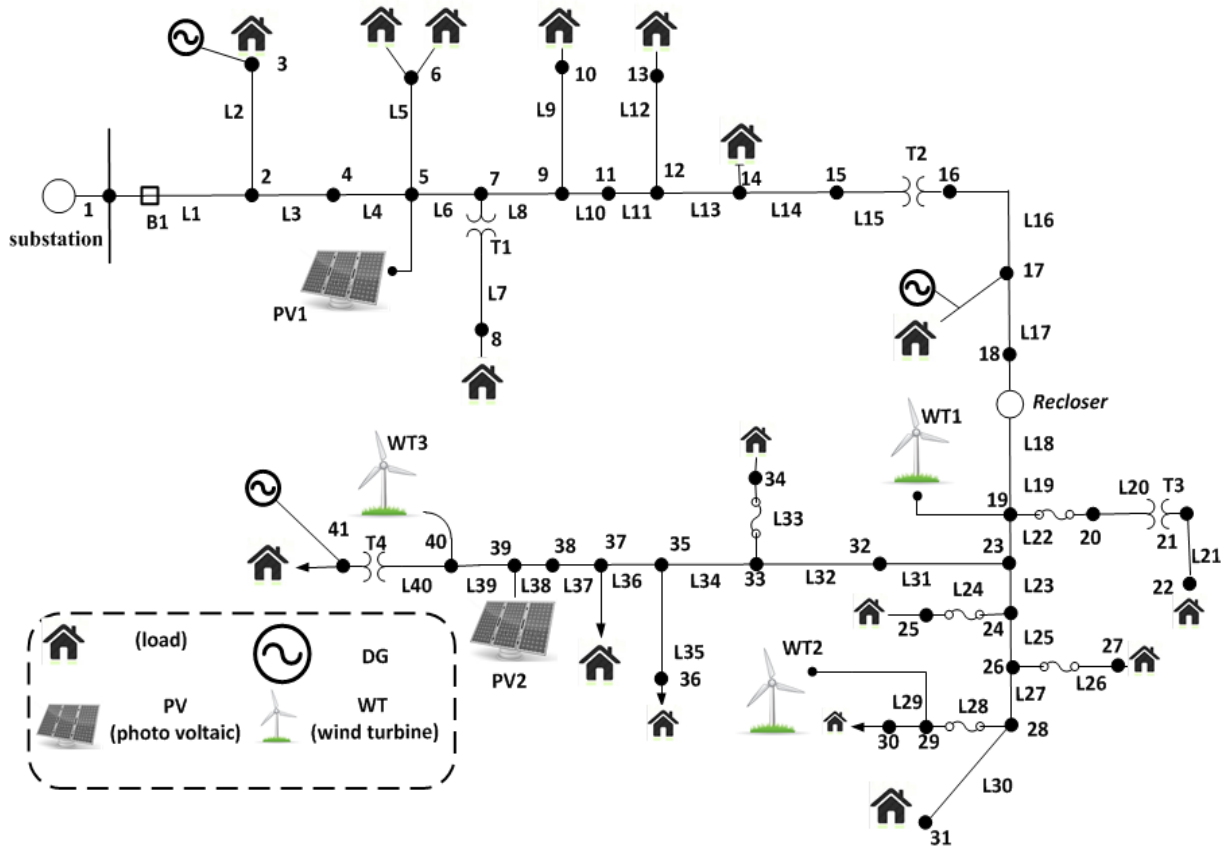


Figure 3-3 Single line diagram for the distribution feeder under study.

The 30 kilometers feeder has a substation capacity of 16 MVA; it consists of 41-buses with 16 kV voltage-level. Per Hydro One rules, the customers can have their own DGs up to 10 MVA [94], thus the Disco here is not investing in the DGs; however, the DG expected generation will be considered as an input in the planning process. Three Diesel generators (customer-owned) that operate daily during peak-hours (5:8 pm) are assumed. The rated power for DGs and RESs is given in Table 3-1 whereas the feeder impedances are given in [94]. A realistic residential load profile (as measured by the PJM in 2014 [95]) is used to simulate the

load as depicted in Figure 3-5-a; each season has a unique load profile with higher peak during summer. A 4% yearly load growth is assumed during this study; thus, the nominal load is expected to reach 22.77 MVA in ten years. Two PV plants are added to the system with a real PV radiation taken from [96], shown in Figure 3-5-b with longer generation hours during summer that reduce gradually while moving toward winter. The PV generation is assumed to have the same growth rate as the load [9] whereas the wind generation capacity is fixed. Three wind facilities are dispersed on the feeder to make the total RES penetration of this feeder 37% calculated as a ratio between the maximum RES output to peak load. A real wind generation is considered [97] as depicted in Figure 3-5-d. It is worth mentioning that winter days are windier than summer days, especially during late night hours. The buy price of Ontario (HOEP: hourly Ontario Energy Price) is provided by the Independent Electricity System Operator (IESO) in [98] and depicted in Figure 3-5-c. It is very important to notice that some days have a very high price difference which indicates that energy arbitrage will be a successful investment in such a market.

It is assumed that the Disco considers an energy billing price 20% more than the HOEP average price. Due to the enormous problem size and number of states, the yearly realizations are minimized to ten scenarios per year; this results in a total hundred scenarios for the whole planning horizon. The wind generation curtailment is penalized by 100\$/MWh and load shedding by 150\$/MWh with maximum 30-minute load shedding period/year. These high values are chosen by trial and error to avoid over-curtailment and over-load shedding during the optimization process; otherwise these options, which remarkably affect the system reliability in a negative way, would be preferred by the optimization algorithm than the upgrade ones.

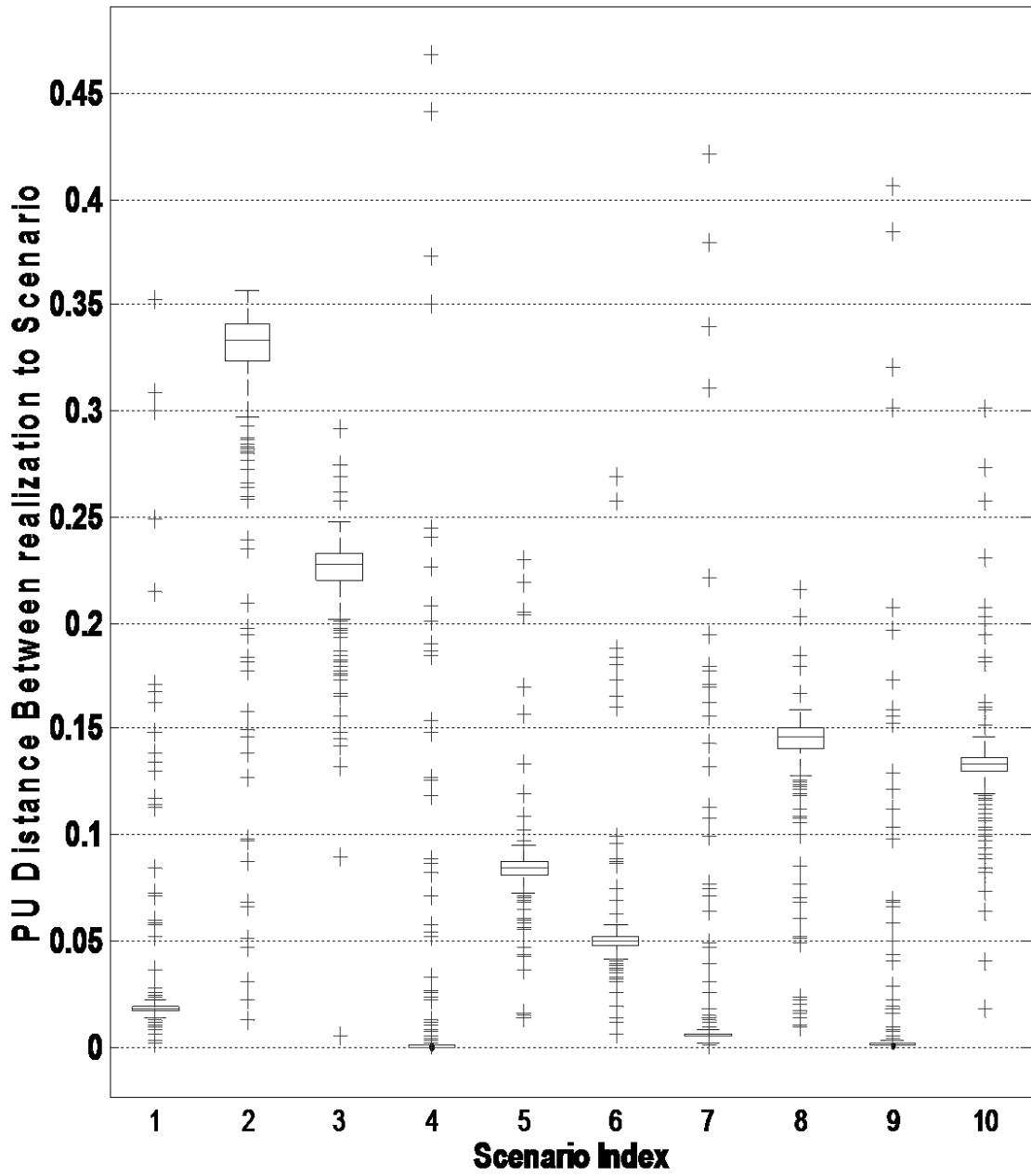


Figure 3-4 PU distance of first year (365 realization) to the 10 scenarios (centroids) depicted as + sign, the mean distance of each scenario is shown as solid red line, while the confidence levels are depicted by black line with a confidence level shown as a box.

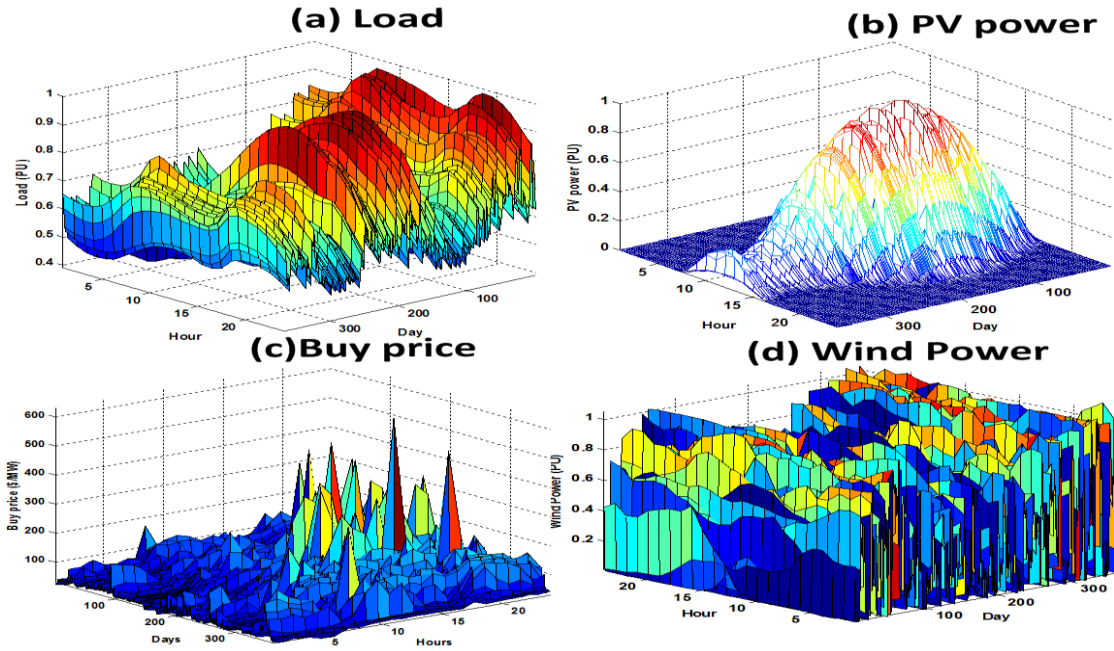


Figure 3-5. Yearly input data(a) PU load profile (b) PU PV generation (C) hourly market buy price (HOEP) (d) PU wind generation.

For T&D upgrade, five upgrade models are considered with a capacity upgrade difference of one MVA. The substation and feeders cost is taken from [23]. A 20% feeder capacity is added as a reserve. Regarding the SVC cost, it varies dramatically depending on the voltage level [99]; a medium-voltage level cost is adopted as reported by Hydro One in [99]. Four battery technologies, with the cost details reported in [100], are considered to decide the best ESS portfolio. The number of cycles/day for an ESS depends on the minimum to maximum buy price ratio [20]. For example, if the ESS charged energy levelized cost is 50\$/kWh, the energy arbitrage is profitable only if the energy price difference is greater than 50\$. In this example, it is assumed that 250 cycles/year are profitable for energy arbitrage, which results in 2500 life cycles needed during the planning period. If the battery technology has less life cycles, a replacement cost is calculated, and if the technology has more life, the battery value is calculated as a second-use one after the service time. Regarding the ESS converter replacement,

a DC-AC converter has a long lifetime that may reach 12 years [101] due to switches low failure rate and the use of reliable film capacitors. As a result, no ESS converter replacement cost is considered in this 10 years planning project.

It is also possible to just define the maximum number of cycles during the planning period without imposing a daily number of cycles (by omitting constraint (3.8)). In such a case, the optimization decides the optimal daily number of cycles according to the market profile. Further, the total number of cycles constraint may be omitted as well; however, a life cycle dependent ESS cost model should be considered in the objective function [20] (nonconvex optimization needed). One may argue that ten years' market predictions are not that accurate; thus, it is safer to assume a maximum one daily number of cycles and the total life cycles instead of possible ESS oversizing that may result from misleading long-horizon predictions. In both cases, it is the designer choice according to their philosophy (optimistic or conservative) and their trust of provided predictions.

As a general case, all buses are considered as candidates for ESSs and SVCs ($\mathcal{N}^{ES} = \mathcal{N}^{SVC} = \mathcal{N}^{bus}$). However, in this study, ten buses along the feeders are chosen as candidates for ESSs and SVCs as shown in Table 3-1.

Table 3-1 Planning input data.

RES, DG rating	$p^{wt1} = 2MW, p^{wt2} = p^{wt3} = 1.5MW, p^{DG1} = 1 MW$ $p^{pv1} = p^{pv2} = 0.5 MW, p^{DG2} = p^{DG3} = 0.5 MW$			
ESS	Lead-Acid	Na-S	Zn-Br	Li-ion
C^{ES}/MVA	\$/ MVA installed 400	350	400	400

C^{ES}/MWh	\$/ MWh installed 330	350	400	600
η	80%	75%	70%	85%
Life cycles	2000 cycles	3000	3000	4000
$\underline{v} = 0.95, \bar{v} = 1.05, sp = 0.9\$/KWh, \tau = 1, IR = 3\%, Y = 10, Sc = 10,$ $\overline{S}^{ES} = 3 MVA, \overline{E}^{ES} = 15MWh, FC^{ES} = FC^{SVC} = 5000\$, C^{SVC}/MVAR = 143K\$$ $\overline{DN}^{ES} = 1, \overline{TN}^{ES} = 2500, \overline{z}^{ES} = 4, \overline{z}^{SVC} = 5, O\&M^{ES} = O\&M^{SVC} = 500\$/y$ $UC^{subm} = [300,400,500,600,700] K\$, UC^{fm}/KM = [151,152,153,154,155]K\$$ $m = 5, fr^f = 20\%, c^{fm} = [1,2,3,4,5] KVA, \mathcal{N}^{ES} = \{4,6,9,12,22,25,28,35,39,40\}$				

3.4 Results Discussion

Four battery technologies (T1 to T4) are compared in this study. To show the importance of considering the reactive power support of ESSs in the upgrade scheme, two cases are compared: P1: planning ESS with Q support, and P2: planning ESS without Q support (as in [23]). The optimization results are shown in Table 3-2 and depicted in Figure 3-6 for eight case studies (four technologies each with and without Q support). The problem was solved with the Gurobi solver [102] using a 3.30 GHz AMD six-core processor. The solver gap from the global optimal is recorded as 1.98%. Each problem was solved in about 670,000 iterations that lasted for 9 hours and 12 minutes.

The cost and planning data provided in Table 3-1 Planning input data is the main drive for the optimization algorithm under different technologies. First, the converter cost is almost the same for the four batteries; thus it only affects the compromise between having a higher ESS power rating verses having a higher SVC rating for reactive power support (this point will be discussed in details later). Second, the storage cost is the main factor for considering the energy arbitrage investment. The energy arbitrage is also affected by the price difference volatility as shown in Figure 3-5-c. For achieving the desired 2500 cycles/10 years, a replacement cost for

the lead-acid ESS is required which makes this technology remarkably expensive. For the Na-S ESS, 500 cycles are still available for the battery, which results in a second-use battery income which can be transferred as a discount in the price as well. The third ESS technology (Zn-Br) has a higher storage cost than the Na-s ESS; further, the Zn-Br ESS has the lowest charging efficiency among the four cases. The final competitor is the Li-ion ESS with the highest charging efficiency; although it has the highest life time as well, the Li-ion ESS has an extremely expensive storage cost (almost double the lead-acid ESS for double lifetime and higher efficiency).

The advantage of enabling Q support is providing some deferral cost for the SVC option but at the price of occupying a part of the ESS converter capacity. The terminologies used in Table 3-2 are defined as follows. First, the T&D deferred cost is the difference between the T&D upgrade cost for the 10th year maximum load without considering other technologies and the T&D upgrade cost for the 10th year load with considering ESS/SVCs. Second, the arbitrage benefit is the total ESS time-shifted energy value $\sum bp_{sc,y,t} p_{sc,y,t}^{ES}$. Third, the maximum load reduction represents the grid power reduction after solution compared to the original one. Finally, the losses saving is the value difference between the energy purchased from the grid and the total energy sold to customers.

Table 3-2. Optimization Results with different ESS technologies, and services (T1:T4) (P1 is shown with white background whereas P2 is grey).

	T1:Lead-Acid	T2: Na-S	T3: Zn-Br	T4: Li-ion
ESS	Bus [28]	[4,28,40]	[28,39,40]	[28,39,40]
Buses, Power	0.016 MW \cong 0	[1.11,0.57, 1.38] MW	[0.016,0.26,0.07] MW	[0.016,0.15, 0.22] MW

(MW),		Total: 3.06	Total: 0.346	Total: 0.386
Capacity	0.017 MWh \cong 0	[2.23, 1.5,	[0.03,0.54,0.17]	[0.03,0.37,
(MWh)		4.07] MWh	MWh	0.56] MWh
		Total: 7.8	Total: 0.74	Total: 0.96
	Bus [28]	[28,40]	[28,39,40]	[28,39]
	0.016 MW \cong 0	[0.016,	[0.23,0.37,0.1]	[0.21,0.39] MW
		1.075] MW	MW	Total: 0.6
		Total: 1.09	Total: 0.7	
	0.017 MWh \cong 0	[0.05,3.35]	[0.8,1.12,0.29]	[0.86,1.35]
		Total: 3.4	Total: 2.21	Total: 2.21
ESS Cost	21.5K\$	3.35M\$	409 K\$	538 K\$
	21K\$	1.379 M\$	1.04 M\$	1.08 M\$
SVC	Buses:[4,9,28,39,40]	[4,9]	[4,9,28,40]	[4,9,28,40]
Buses,				
Power	[5,1.5,0.53,06,1.3]M	[5,0.54]	[5,1.6,0.55,1.1]	[5,1.61,0.55,1]
(MVar)	VAr	MVar	MVar	MVar
	Total: 8.44	Total: 5.54	Total: 8.25	Total: 8.16
	[4,9,28,39,40]	[4,9,28,39,40]	[4,9,28,39,40]	[4,9,28,39,40]
	[5,1.52,0.55,0.06,1.3]	[5,1.75,0.56,0.03,1.29]	[5,1.58,0.51,0.01,1	[5,1.6,0.55,0.01,1
	Total: 8.45	Total: 8.63	.31] Total: 8.41	.36] Total: 8.52
SVC Cost	1.224 M\$	0.812 M\$	1.194 M\$	1.185 M\$
	1.227 M\$	1.25 M\$	1.22 M\$	1.33 M\$
T&D	3.233 M\$	2.646 M\$	2.921 M\$	2.979 M\$
COST	3.233 M\$	2.745 M\$	2.848 M\$	2.919 M\$
T&D	339K\$/9.5%	927K\$/26%	652/18.24%	594K\$/16.6%
deferred	339K\$/9.5%	827K\$/20%	714KS/20%	654 K\$/18.3%
cost				

Losses	3.97M\$/66%	4.4M\$/68.5%	4.05M\$/67.38%	4.06M\$/67.5%
min. value	3.97M\$/66%	4.23M\$/68 %	4.04 M\$/67.2%	4.1M\$/67.75%
Arbitrage	6.1K\$	2.313M\$	222 K\$	312 K\$
benefit	6.3 K\$	0.95 M\$	565.3K\$	650 K\$
Peak-load	10%	18.9%	13.47%	13.87%
reduction	10%	18.83%	13.43%	14.14 %
profit	46.12M\$	46.819 M\$	46.36 M\$	46.4 M\$
	46.11M\$	46.2 M\$	46.26 M\$	46.24 M\$

3.4.1 Economic Discussion

The ESS investment share depends on its MWh cost as shown in Figure 3-6-a; more than three million Dollars are invested in the Na-S ESS (T2) compared to twenty thousand in the lead-acid ESS (T1) (almost none). A higher investment in the ESS leads to a higher ESS rated power thus to cope with the higher capacity. A smaller SVC size is required when the ESS rated power increases. For example, a total 5.54 MVar-SVC is needed in T2 as compared to 8.44 MVar-SVC in T1 (about 3 MVar difference). This result is interesting especially when noticing that the ESS converter size in T2 is higher by approximately 3 MVA than that in the T1 case. Regarding the T&D cost, ESSs with higher capacities can achieve better peak shaving and consequently lead to lower T&D costs as shown in Figure 3-6-a, and higher T&D deferral as in Figure 3-6-b.

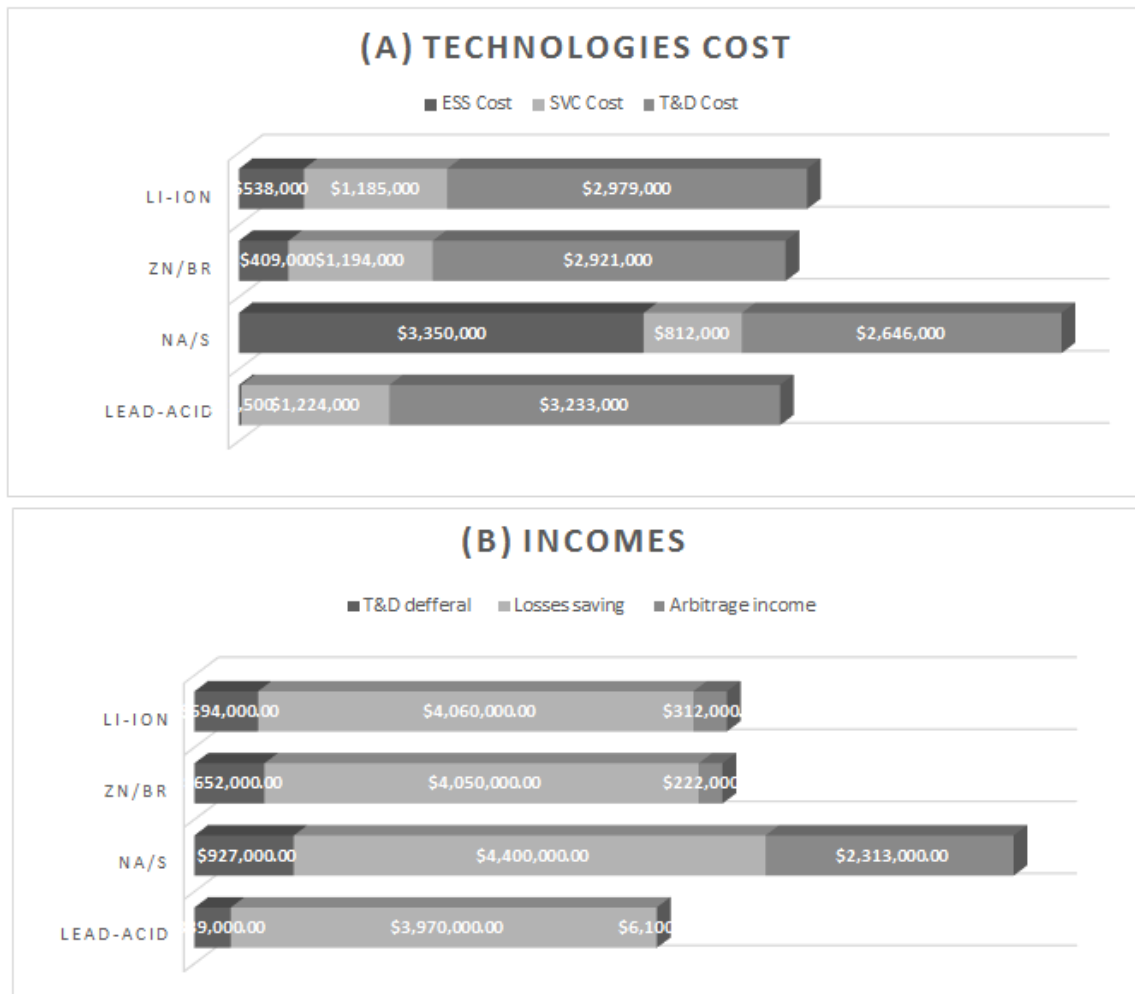


Figure 3-6 Sizing results for different ESS technologies in case of P1 (Q support) (a) different technologies cost share (b) different incomes from the investment.

Regarding the power loss saving, a non-significant difference is noticed between ESS technologies. In fact, the power loss minimization is dependent on the voltage profile. Because the voltage deviations are kept within $\pm 5\%$ in all cases, the power loss savings with different ESS technologies are very close. On the other hand, the energy arbitrage income depends on the ESS capacity (MWh); whereas T2 has 7 MWh more capacity (more or less) compared to other

technologies, T2 harvests two million Dollars extra income from energy arbitrage (shown in Figure 3-6-b).

The T&D upgrade should not convey a profit in the first place; this is the case with T1 (lead-acid) where the total cost exceeds the income. This means that the Disco will pay a part of their energy trading profit ($inc - c^{grid}$) to cover the T&D upgrade costs. This is not the case with other technologies (T2-4) where the Disco is actually making a profit from sources like energy arbitrage and losses saving.

A key result here is that energy arbitrage is the main element for considering the ESS option in the first place. Actually, the ESS cost may exceed the feeder upgrade cost; however, the energy arbitrage income still makes the ESS a competitive solution. Let us consider a flat price market; in such a case, the energy arbitrage income will be zero, and no ESS will be invested (e.g., case T1) except of course if the ESS cost is diminished dramatically. Further, the correlation between the peak load and the peak market price is vital because it facilitates the operation of an ESS for peak shaving (needed for T&D deferral) and energy arbitrage (needed for extra income) simultaneously. Luckily, this correlation was proven in [67] where the ESS was found, in most of the time, performing peak shaving automatically although it was managed for energy arbitrage.

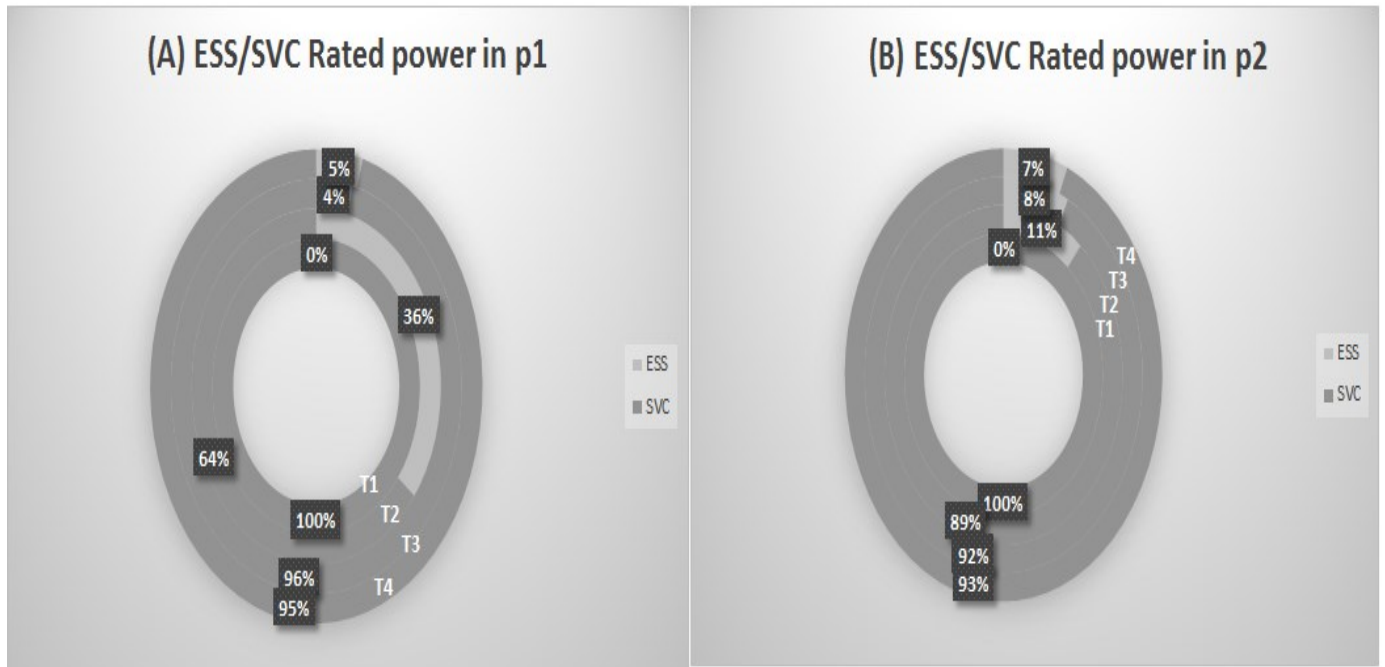


Figure 3-7 Comparison between total ESS size (MVA) to SVC size (MVAR) in two case (A) ESS provides Q support (case P1) (B) SVC only provides Q support (case P2).

3.4.2 ESS/SVC Rating, Reactive Power Support Options

It is worth noticing that the MVA cost of any ESS is more than double of the SVC-MVAR cost. As a result, the profitable energy arbitrage ESS technologies will require a bigger converter size and consequently, it will participate more in Q support. This appears clearly in the case of the lead-acid ESS (T1); in both P1, and P2, a full Q support source from an SVC is considered due to the high cost of the lead-acid battery (unattractive in energy arbitrage). For T3, T4, the ESS MWh cost is still high leading to a lower MVA size. On the contrary, the Na-S ESS (T2) represents 36% of the installed power rating (sum of the MVAR of SVCs plus the MVA of ESSs) in the network (in case of P1). This confirms the viability and effectiveness of using ESSs for Q support when ESSs are equipped with batteries providing a profitable income

(e.g., such as energy arbitrage, here). For T2, in case of P2 (no reactive power support), the ESS size is reduced to be 11% of the installed capacity because all reactive power support comes from the SVCs. Although the ESS MVA cost gets lower, the total profit of the Disco is 619,000\$ higher when the ESSs participate in Q support. This is clear in the profit of T3 and T4 as well where the profit in case P1 is always greater than P2.

3.4.3 ESS and SVC Locations

Before discussing the results of the ESSs/SVCs chosen locations, it is worth mentioning that the sizing and siting problem is power flow-based in the first place, which means it depends on the feeder impedances, loads and RESs characteristics and distribution. The case study feeder has two major loads at the feeder beginning and one at the feeder end as shown in Table 3-3, other loads are less than 500 kW. Also, there are also two large wind farms near the feeder ends (bus 40 and bus 29).

Table 3-3 Biggest five loads in the Radial feeder

Bus index (<i>i</i>)	3	8	41	6	36
Rated $p^{load}(i)$ MW	6.4	3.18	2.16	0.9	0.8
Power factor - lagging	0.976	0.947	0.951	0.87	0.8

For the case T1, an SVC is located at the feeder start (bus 4) close the heaviest load and PV1 station; another large SVC is needed near the feeder end (bus 40) which is heavily loaded and has a wind turbine WT3. A smaller SVC exists at the other feeder end as well (bus 28) close by the other wind turbine (WT2). It is noticed that the SVC locations are the same whenever the

ESS does not participate in Q support (P2 policy); however, this is not the case in P1 (ESS provides Q support).

In case of P1, the SVCs were located mainly at the feeder start where the ESS units were sited at the feeder end. This is an important result here because ESSs provide peak shaving service during energy arbitrage, and they are best located at the feeder end to defer more feeder upgrade cost. This is the case of T2, T3 and T4 where a storage is always located at bus 28 whereas the other is located at bus 40 (or 39). In all cases, a 5 MVAR SVC is always needed at the feeder start (Bus 4).

It very important to emphasize again that assets allocations change with the feeder topology and loads distribution and SVC/ESS converter cost; thus a total different results may occur with a meshed system for instance.

3.4.4 ESS for T&D Deferral, Competitive or Not?

Due to its reasonable cost and moderate efficiency, the Na-S ESS was proven to be a competitive T&D upgrade deferral technology. Conducting energy arbitrage is a key factor for providing extra income from the market and achieving peak shaving simultaneously. The strong correlation between peak shaving and energy arbitrage was proven before in [67]. Further, this result agrees with the current International Renewable Energy Agency (IRENA) report [103]. The report showed that the Na-S ESS has the highest capacity worldwide (400 MW). The Li-ion ESS comes in the second place followed by advanced lead-acid (higher lifetime).

Adopting the Na-S ESS increased the profit by 1.5 % (708,000\$) compared to just using SVCs with feeder upgrade (e.g., compared to case T1). On the one hand, the profit increase may look trivial and indecisive for the Disco to take the risk of adopting a new technology. On the

other hand, this profit can increase dramatically with the reduced ESS cost in the future. As supported by the IRENA report [103], it is expected that the Li-ion storage cost will drop to 200 \$/kWh by 2020; the thing that will make the Li-ion ESS the first candidate for different transmission and distribution services. Further future scenarios, such as copper price increase, can significantly increase the potential of ESSs because the feeder upgrade cost will be outrageous, especially for long radial feeders.

3.5 Conclusion

A comprehensive sizing and allocation scheme for ESSs, SVC and DGs for distribution system upgrade was presented in this chapter. The proposed optimization algorithm aimed at maximizing the utility profit by allowing ESSs to participate in multiple grid support functions that include minimizing the T&D deferral cost, conducting energy arbitrage, minimizing the power loss, and providing reactive power support. A case study on a real radial feeder was conducted using realistic power and market price data. The study compared different ESS technologies. Given the current cost of ESSs, the energy arbitrage income was found to be a key factor in considering the ESS investment. Combined with other services, such as reactive power support, the energy storage option represented a profitable T&D deferral tool. The Na-S battery proved to be a competitive system upgrade option.

Chapter 4

Mobile Energy Storage Sizing and Allocation for Multi-Services

Grid Support

4.1 Introduction

A mobile (transportable) energy storage system (MESS) is a localizable storage device that can provide various services at different buses of the system. Controlling the MESS active power is used for load leveling, load shifting, losses minimization or energy arbitrage. Controlling the MESS reactive power is used for voltage regulation at different grid locations. Because bulk power converters have cheaper per-unit cost, an MESS may cost less than multi-SESSs. Further, the mobility of MESSs enables a single unit of functioning as multiple stationary units. The problem of sizing an MESS and locating its seasonal stations (buses) is not investigated in the literature. Chapter 4 of this thesis proposes an MESS sizing and allocation technique taking variables variations into account (load variations, renewable resources intermittency, and market prices fluctuations). The sizing problem has a mixed-integer nonlinear form; thus, a hybrid optimization technique is developed based on both the particle swarm algorithm (PSO) and mixed integer convex programming. Besides, a dynamic model for the MESS is adopted for the capacity and lifetime constraints. A network power flow (for voltage level and feeders' ampacity) is considered in the problem formulation as well. To validate the proposed solution, a case study is conducted on a real 41-bus radial feeder in Ontario, Canada and using real renewable, load, and market data. This Chapter starts with the problem formulation in Section 4.2. The proposed sizing algorithm is explained in Section 4.3.

A case study comparing stationary and mobile storage is investigated in Section 4.4. Final conclusions are drawn in Section 4.5.

It is worth mentioning that this chapter has similar objectives and tools as Chapter 3, however, the main difference is the movability of the MESS and modeling it.

4.2 Problem Formulation

4.2.1 Mobile Storage System Structure

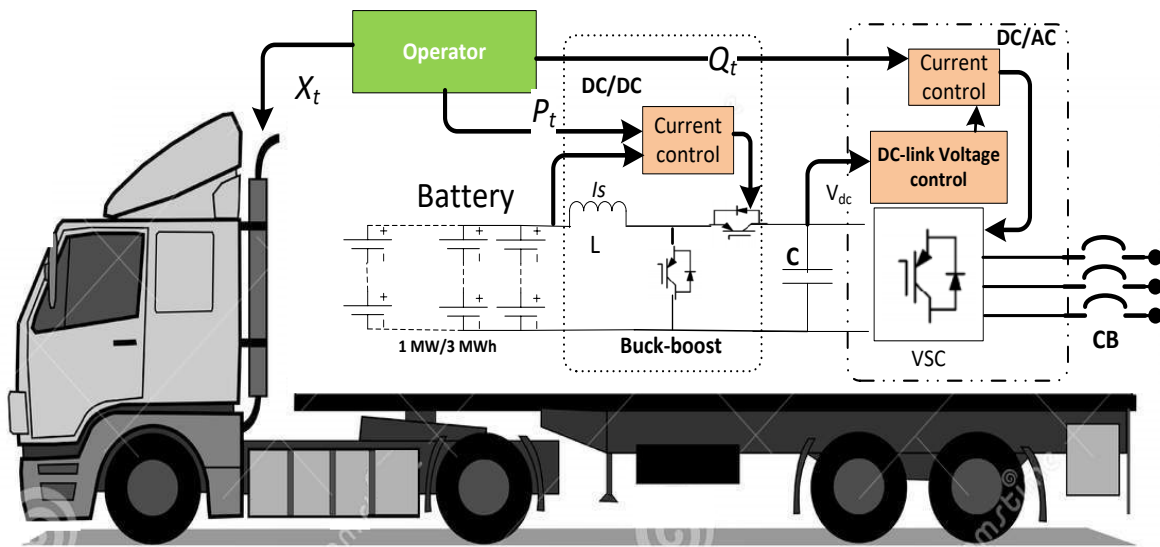


Figure 4-1 MESS structure.

Before discussing the sizing problem, the MESS structure is explained briefly. As shown in Figure 4-1, an MESS consists of an ESS carried on a truck. On the one hand, the ESS is an array of battery cells (e.g., lithium-ion) which can connect to the grid via a dc/dc/ac bidirectional VSC. The dc/dc converter is a current-controlled buck-boost controller. The current controller regulates the bidirectional power according to the set point provided by the operator via changing the dc/dc current controller set point. On the other hand, the dc/ac converter transfers the power to (from) the grid via regulating the dc-link voltage [104]. In the

dq -frame, the dc-link voltage controller generates the VSC-direct current set point whereas the operator tunes the reactive power via changing the quadrature current set point, which can also be controlled autonomously to regulate the terminal voltage, without the operator interference. Further details on the design of the current and dc-link voltage controllers can be found in [104]. On the other hand, the operator must define the truck desired bus (station x_t) at each sample so that the driver moves the MESS to this station. It is worth mentioning that the direct connection of an MESS to a medium voltage network involves special commissioning procedures; thus, it is preferred to be connected to a low-voltage network or equipping each MESS station with a low-voltage terminal via a distribution transformer. An MESS is an investment conducted by a Disco. The Disco aims at profit maximization while maintaining an acceptable power quality level (e.g., voltage level). To fulfill this objective, the optimization problem must consider the participation of the MESS in the following grid-support services: 1) Energy arbitrage. 2) Power loss minimization. 3) Voltage regulation.

4.2.2 MESS Planning Cost Function

The cost function presents the Disco profit during the planning horizon as given in (4.1). The cost function pro is calculated for each time sample t indexed in an operation year y in a certain operation scenario sc . Each operation scenario sc has a certain probability ρ_{sc} such that $\sum_{sc} \rho_{sc} = 1$. A scenario represents a different load, PV, wind and load power and market prices combinations.

$$Max(pro = inc - c^{grid} - c^{MES}) \quad (4.1)$$

$$inc = \sum_{sc} \rho_{sc} \sum_y \sum_t sp_{sc,y,t} \sum_i p_{sc,y,t}^{Load}(i) \tau \quad (4.2)$$

$$c^{grid} = \sum_{sc} \rho_{sc} \sum_y \sum_t bp_{sc,y,t} p_{sc,y,t}^{grid} \tau$$

$$c^{MES} = C^{truck} + \sum_i z^{MES}(i) FC^{MES}(i) + C^{MES/MVA} (\mathbb{S}^{ES}) \mathbb{S}^{ES} \quad (4.3)$$

$$+ C^{MES/MWh} (1 + \alpha^{TN}) \mathbb{E}^{MES} + \sum_y \frac{O\&M_y^{MES}}{(1 + IR)^{y-1}}$$

(4.4)

The Disco profit results from the income inc coming from selling energy to the end-users as in (4.2). This income results from selling the load power $p_{sc,y,t}^{Load}$ with a sell price $sp_{sc,y,t}$ that depends on the Disco tariff. Each Disco buys the power $p_{sc,y,t}^{grid}$ from the energy market for a variable wholesale buy price $bp_{sc,y,t}$ that witnesses a big change from off-peak to peak hours, depending on the market volatility. An MESS can perform a load shifting to reduce the cost of the purchased energy c^{grid} to increase the profit as in (4.3). Maximizing the profit means reducing the power loss cost as will be explained later. Finally, c^{MES} is the MESS capital and running cost that consists of five parts as in

(4.4):

1. The truck capital cost (TC).
2. The MESS stations cost FC^{MES} that includes a fixed cost for each station constructed and preparation at a certain bus i .
3. The energy storage (ES) power cost $C^{MES/MVA}$ that represents the capital cost for purchasing the power conversion system of the battery. This cost varies with the

converter size with a nonlinear function as shown in Figure 4-2. The data are adapted from the average power conversion source cost provided in the EPRI report [105].

4. The ESS battery bank cost that represents the storage element cost C^{MES}/MWh . It is worth mentioning that if an extension is desired for the battery, its cost can be considered by setting the parameter α^{TN} ; this maybe the case to reach a certain number of cycles TN because the battery life is a function in the minimum state of charge (SOC) [20].
5. The MESS operation and maintenance costs $O\&M^{MES}$ are calculated yearly and transferred to the first year depending on the interest rate IR during the project life y [9]. If the inflation rate is significant, it can be included to calculate the effective interest rate as explained in [23]. The maintenance cost includes the expected truck and ESS periodical maintenance cost, whereas the operation cost includes the MESS driver stipend and the truck yearly commute cost (gasoline cost, oil change cost, etc.).

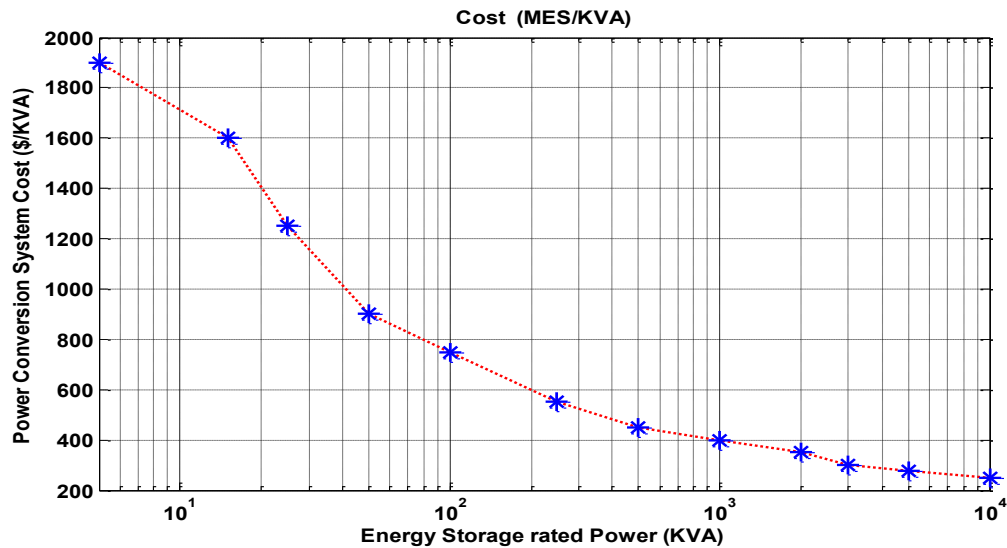


Figure 4-2 Power conversion system cost versus rated power.

4.2.3 MESS Model

The MESS modeling is different from the stationary ESS in that it should be allocated at a single station as given in (4.5). The constraint in (4.5) states that at any instant t in a planning year y of a particular scenario sc , the location of the MESS $x_{sc,y,t}^{MES}(i)$ is unique at a single station of the MESS stations that belongs to the buses set \mathcal{N}^{MES} . Another important factor is the number of daily trips DT conducted by the MESS which is expressed in (4.6). If an MESS stayed the whole day at the same station $i=a$, then $\sum_{t=1}^{24} x_{sc,y,t}^{MES} - x_{sc,y,t-1}^{MES} = 0 \forall i$ which means that no trips are made. On the other hand, if the MESS moved from a station a to another one b at a time α , then $|x_{sc,y,\alpha+1}^{MES}(a) - x_{sc,y,\alpha}^{MES}(a)| = |x_{sc,y,\alpha+1}^{MES}(b) - x_{sc,y,\alpha}^{MES}(b)| = 1$ which means that DT is accumulated by one each time a transition is made. The daily number of trips is upper bounded in (4.7). It is worth mentioning that there is a transit or delay each time the trip is made, however; adding an exact delay model significantly complicates the problem; thus, an instantaneous transition is assumed and the delay effect is investigated later.

$$\sum_i x_{sc,y,t}^{MES}(i) = 1 \forall i \in \mathcal{N}^{MES} \quad (4.5)$$

$$DT_{sc,y,t=24} = \frac{\sum_{t=1}^{24} \sum_i |x_{sc,y,t}^{MES}(i) - x_{sc,y,t-1}^{MES}(i)|}{2} \quad (4.6)$$

$$DT_{sc,y,t=24} \leq \overline{DT} \quad (4.7)$$

The stations location and sizing of an MESS is expressed in (4.8)-(4.10). The binary variable $z^{MES}(i)$ indicates that the bus i is chosen to host an MESS station. The number of stations is limited in (4.8), whereas the station maximum power $\overline{\mathbb{S}}^{MES}$ is upper bounding the MESS rated power \mathbb{S}^{MES} in (4.9). The MESS maximum allowable capacity $\overline{\mathbb{E}}^{MES}$ is expressed in (4.10).

$$\sum_i z^{MES}(i) \leq \overline{z^{MES}} \quad \forall i \in \mathcal{N}^{MES} \quad (4.8)$$

$$0 \leq \mathbb{S}^{MES} \leq z^{MES}(i) \overline{\mathbb{S}^{MES}} \quad (4.9)$$

$$0 \leq \mathbb{E}^{MES} \leq z^{MES}(i) \overline{\mathbb{E}^{MES}} \quad (4.10)$$

The MESS power consists of two mutually exclusive terms; the charging power $ch_{sc,y,t}^{MES}$ (positive) and discharging power $dc_{sc,y,t}^{MES}$ (negative) as shown in (4.11). The MESS is only allowed to charge or discharge at a certain station i if it exists at this station and within the rated power limit as in (4.12)-(4.13). The reactive power injected/absorbed at any bus for voltage regulation purposes is similarly constrained in (4.14). Finally, the converter thermal limit is defined in (4.15). It is worth mentioning that the constraints (4.12)-(4.15) are nonlinear because both \mathbb{S}^{MES} and $x_{sc,y,t}^{MES}(i)$ are decision variables.

$$p_{sc,y,t}^{MES}(i) = ch_{sc,y,t}^{MES}(i) + dc_{sc,y,t}^{MES}(i) \quad (4.11)$$

$$0 \leq ch_{sc,y,t}^{MES}(i) \leq \mathbb{S}^{MES} x_{sc,y,t}^{MES}(i) \quad (4.12)$$

$$-\mathbb{S}^{MES} x_{sc,y,t}^{MES}(i) \leq dc_{sc,y,t}^{MES}(i) \leq 0 \quad (4.13)$$

$$-\mathbb{S}^{MES} x_{sc,y,t}^{MES}(i) \leq q_{sc,y,t}^{MES}(i) \leq \mathbb{S}^{MES} x_{sc,y,t}^{MES}(i) \quad (4.14)$$

$$p_{sc,y,t}^{MES}(i)^2 + q_{sc,y,t}^{MES}(i)^2 \leq x_{sc,y,t}^{MES}(i) \mathbb{S}^{MES^2} \quad (4.15)$$

Regarding the capacity sizing, the MESS capacity at any time sample is defined as an integrator of the power injected/absorbed at any station i . Both the charging and discharging efficiencies η^{ch}, η^{dc} are considered as well in (4.16). The MESS capacity is upper-bounded by its rated value in (4.17). The number of cycles N^{MES} is another integrator that counts the MESS energy at/from any bus i as in (4.18). When a rated capacity \mathbb{E}^{MES} is totally absorbed and

injected by the ESS, N^{MES} is incremented by $1 \times \mathbb{E}^{MES}$. The total ESS number of cycles \overline{TN}^{MES} is imposed by (4.19).

$$E_{sc,y,t+1}^{MES} = E_{sc,y,t}^{MES} + \sum_i (\eta^{ch} ch_{sc,y,t}^{MES}(i) + \eta^{dc} dc_{sc,y,t}^{MES}(i))\tau \quad (4.16)$$

$$0 \leq E_{sc,y,t}^{MES} \leq \mathbb{E}^{MES} \quad (4.17)$$

$$N_{sc,y,t}^{MES} = N_{sc,y,t-1}^{MES} + \frac{\sum_i (\eta^{ch} ch_{sc,y,t}^{MES}(i) - \eta^{dc} dc_{sc,y,t}^{MES}(i))\tau}{2} \quad (4.18)$$

$$\sum_{sc} \rho_{sc} \sum_y \sum_t N_{sc,y,t=24}^{ES} \leq \overline{TN} \mathbb{E}^{MES} \quad (4.19)$$

4.2.4 Final Optimization Problem

Regarding the power flow, the same constraints in (3.34)-(3.48) are adopted here. Further, in the case of using DGs, SVCs or power imbalance solution, the operation constraints can be easily added from Section 3.2.

To focus on the MESS sizing problem. It is considered as the only technology under study. The final optimization problem is shown in (4.20).

$$\begin{aligned} & \max_{\mathbb{S}^{MES}, \mathbb{E}^{MES}, \mathbb{Z}^{MES}, \mathbb{X}^{MES}, \mathbb{P}, \mathbb{Q}, \mathbb{V}} (pro) \\ s.t. & \begin{cases} \text{MESS dynamical model: (4.5) - (4.19)} \\ \text{Power flow model: (3.34) - (3.48)} \end{cases} \end{aligned} \quad (4.20)$$

The decision variables of this problem include the MESS rated power and capacity $\mathbb{S}^{MES}, \mathbb{E}^{MES}$, and the MESS stations set \mathbb{Z}^{MES} . Other variables that result from the optimization process represent the system operation nature during the different scenarios, years and samples. These variables help the operator to study the system performance under the planning decision results. These variables include the instantaneous MESS location set $\mathbb{X}^{MES} = \cup_{sc,y,t,i} \mathcal{X}_{sc,y,t}^{MES}(i)$ and similarly, the active, reactive power, and voltage sets: $\mathbb{P}^{MES} =$

$U_{Sc,y,t,i} p_{sc,y,t}^{MES}(i), Q^{MES} = U_{Sc,y,t,i} q_{sc,y,t}^{MES}(i) v_{sc,y,t}^{MES} = U_{Sc,y,t,i} v_{sc,y,t}^{MES}(i)$, and the battery dynamics, such as the capacity and number of cycles. The final sizing problem (4.20) is a mixed integer nonlinear problem due to the MESS constraints (4.12)-(4.15). Further, the cost function is a nonlinear function of the storage rated-power-dependent cost as shown in Figure 4-2. Next, Section 4.3 presents the proposed algorithm to solve this problem.

4.3 Proposed Algorithm

To convert the problem (4.20) from a mixed-integer nonconvex problem (due to constraints (4.12)-(4.15) and the nonlinear converter cost) into a convex one, the following technique is proposed. First, the particle swarm optimization is utilized to detect the optimal MESS rated power (S^{ES}) and stations optimal locations (z^{MES}). Using all these variables into (4.20), the problem will be converted into a mixed-integer convex programming problem which can be solved easily to find the optimal capacity. This technique mixes the artificial intelligence method with the gradient-based optimization. The PSO is a smart iterative search method that changes the decision variables (swarm positions) to optimize (minimize or maximize) a certain criterion [106]. In this chapter, the PSO changes the MESS rated power and locations such that the profit is maximized. The proposed algorithm is described in the following steps.

The PSO generates a random initial population of particles $Y(j=0)$ which is defined by M particles size as in (4.21). Each particle at certain iteration j , $y(j)$ consists of the MESS rated power $S_m^{MES}(j)$ with its associated cost and a proposed locations set $z_m^{MES}(j)$ as in (4.22).

$$Y(j) = [y_1(j), y_2(j), \dots, y_m(j), \dots, y_M(j)] \quad (4.21)$$

$$y_m(j) = [S_m^{MES}(j), z_m^{MES}(j)] \rightarrow c_m^{MES/MVA}(j) \quad (4.22)$$

To maintain the particles limits, the following constraints in (4.23)-(4.24) are imposed on all particles to keep the rated power within the allowable range and define the locations binary sets.

$$0 \leq \mathbb{S}_m^{MES}(j) \leq \overline{\mathbb{S}^{MES}} \quad (4.23)$$

$$\mathbb{Z}_m^{MES}(j) \in \{0,1\} \quad (4.24)$$

For each particle, the associated profit is calculated by solving the mixed-integer convex problem in (4.25). The problem is the same as the one in (4.20) after the following modifications. A) The MESS location set becomes a parameter decided by each particle. B) The nonlinear constraints (4.12)-(4.15) become convex (linear or quadratic) after considering the MESS rated power a constant parameter. C) The rated power cost is calculated from an interpolation table follows Figure 4-2. Now, this problem can be efficiently solved by solvers as GUROBI [102]. The resulting capacity is also saved for each solution after solving (4.25) as expressed in (4.26)

$$\begin{aligned} & \max_{\mathbb{E}^{MES}, \mathbb{x}^{MES}, \mathbb{P}, \mathbb{Q}, \mathbb{V}} (\text{pro}_m(j) = \text{pro}(y_m(j), c_m^{MES}/MVA(j))) \quad (4.25) \\ \text{s. t. } & \left\{ \begin{array}{l} \text{MESS dynamical model: (5) - (7), (10), (11), (16) - (19)} \\ \text{Power flow model: (3.34) - (3.48)} \\ \mathbb{Z}^{MES} = \mathbb{Z}_m^{MES}(j) \\ 0 \leq ch_{sc,y,t}^{MES}(i) \leq \mathbb{S}_m^{MES}(j)x_{sc,y,t}^{MES}(i) \\ -\mathbb{S}_m^{MES}(j)x_{sc,y,t}^{MES}(i) \leq dc_{sc,y,t}^{MES}(i) \leq 0 \\ -\mathbb{S}_m^{MES}(j)x_{sc,y,t}^{MES}(i) \leq q_{sc,y,t}^{MES}(i) \leq \mathbb{S}_m^{MES}(j)x_{sc,y,t}^{MES}(i) \\ p_{sc,y,t}^{MES}(i)^2 + q_{sc,y,t}^{MES}(i)^2 \leq x_{sc,y,t}^{MES}(i)\mathbb{S}_m^{MES}(j)^2 \\ \mathbb{E}_m^{MES}(j) = \left\{ \mathbb{E}^{MES} \left| \arg\{\max_{\mathbb{E}, \mathbb{x}}(\text{pro}_m(j))\} \right. \right\} \end{array} \right. \quad (4.26) \end{aligned}$$

At each iteration J ; the local and global best positions are updated as follows:

$$y^{loc}(j = J) = \{y_\beta(j) | \text{pro}_\beta(j) > \text{pro}_m(j) \forall m\} \quad (4.27)$$

$$y^{Glo}(J) = \{y_\alpha | \text{pro}_\alpha > \text{pro}_m(j) \forall m, \forall j \leq J\} \quad (4.28)$$

Depending on the iteration J , the new inertia ω and speed vectors V are found from (4.29)-(4.30), the speed is inclined to both the local and global best positions depending on the factors c_1, c_2 . Finally, the speed is used to update all particles positions as shown in (4.32) after checking its limits in (4.31)

$$\omega(j) = \omega_{max} - \frac{\omega_{max} - \omega_{min}}{\bar{j}} j \quad (4.29)$$

$$V_m(j+1) = \omega(j)V_m(j) + c_1 r_1 (y^{loc}(j) - y_m(j)) + c_2 r_2 (y^{Glo}(j) - y_m(j)) \quad (4.30)$$

$$-\overline{V}_m \leq V_m(j+1) \leq \overline{V}_m \quad (4.31)$$

$$y_m(j+1) = V_m(j+1) + y_m(j) \quad (4.32)$$

Step 2 is repeated as long as the stopping criterion is not triggered. There are two stopping criteria. First, if the maximum number of iterations \bar{j} reached. Second, if the profit percentage change stayed within a pre-calculated tolerance zone ε for a certain number of iterations γ as explained in (4.34).

$$j \geq \bar{j} \quad (4.33)$$

$$\Delta pro^{Glo}(j:j+\gamma) \leq \varepsilon, j+\gamma \leq \bar{j} \quad (4.34)$$

Finally, if the stopping criterion is achieved, an optimum sizing and allocation decision is reached. Figure 4-3 shows the flowchart of the proposed optimization framework.

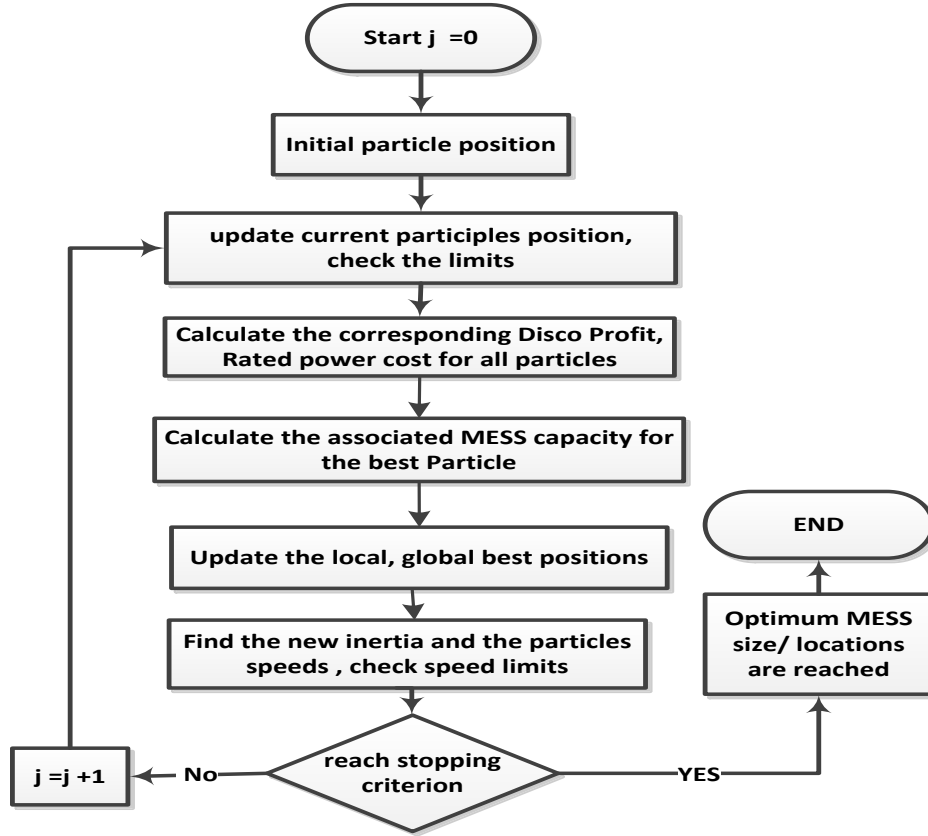


Figure 4-3 Hybrid optimization scheme for MESS Sizing and allocation.

It is worth mentioning that the resulting profit is not the actual profit. In reality, the MESS transit period is not zero, and every time the MESS moves from a station a at instant λ heading to another station b at time k , it will stay in transit for a period τ_{abk} (depends on the station locations and transit time) until it reaches its destination at instant $\lambda + \tau_{ab\lambda}$. The set of time \mathcal{N}^{tr} expressed in (4.35) indicates that the MESS is in transit. If the MESS is in transit, that means that the Disco has to buy (or sell) the MESS scheduled energy from the grid till the MESS reaches its next destination (b). Thus, the grid purchased cost is adjusted and the real profit $\mathcal{R}pro$ is calculated as in (4.36).

$$\mathcal{N}^{tr} = \{[\lambda, \lambda + \tau_{ab\lambda}] | x_{sc,y,t}^{MES}(a) = x_{sc,y,t+1}^{MES}(b) = 1 \forall a \neq b, a, b \in \mathcal{N}^{MES}\} \quad (4.35)$$

$$\mathcal{R}pro = pro - \sum_{sc} \rho_{sc} \sum_y \sum_{t \in \mathcal{N}^{tr}} bp_{sc,y,t} p_{sc,y,t}^{MES} \tau \quad (4.36)$$

4.4 Case Study

The MESS sizing algorithm is applied to the system described in Section 3.3 and shown in Figure 4-1. There exist three DG units that operate daily during peak-hours (5:8 pm). The rated power for DG units and RESs is given in Table 4-1. A daily realistic residential load profile is adopted (as measured by PJM [95]) and depicted in Figure 4-4 (a). Two PV plants (PV1, PV2) have a generation profile used from [96] as shown in Figure 4-4(b), whereas three wind facilities (WT1, WT2, WT3) are dispersed on the feeder. The energy price is taken from [107]. Typical wind profiles in [108] are used and shown in Figure 4-4(d). The total RES penetration of this feeder reaches 37%. The energy sell price is assumed to a fixed monthly tariff as adopted by the distribution utility company (e.g., [109], [110]). Twelve years' historical market, power data are used as real scenarios (realizations) to cover the whole planning horizon, scenarios are derived as explained in Section 3.2.

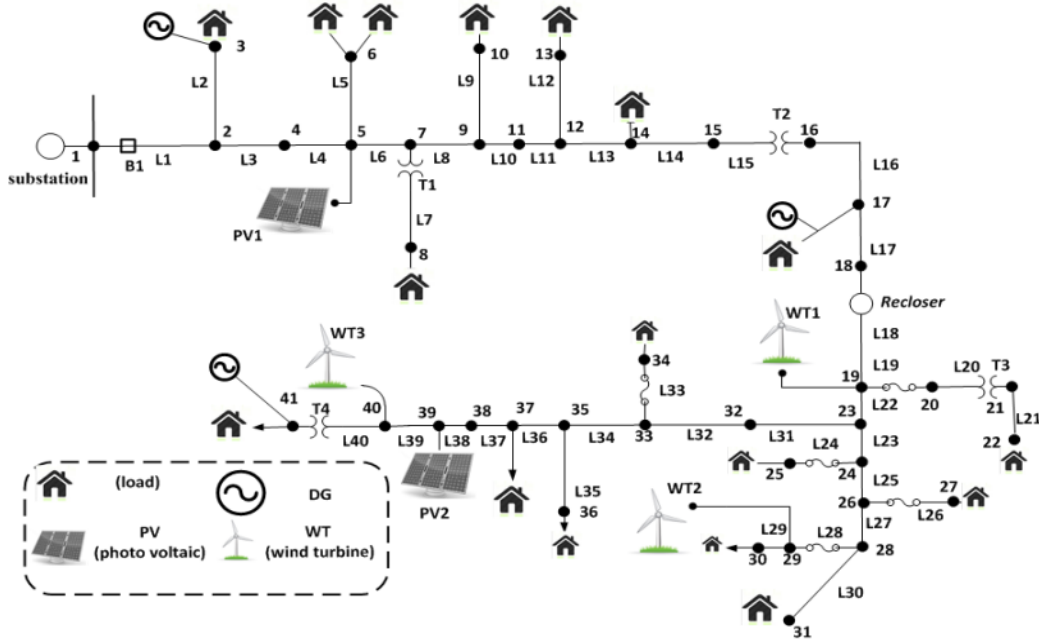


Figure 4-4 Single line diagram for the distribution feeder under study.

Regarding the MESS, the lithium-ion battery is adopted due to its high energy intensity, high efficiency, and long life. The battery technical and economic data are taken from [100]. The storage life cycles are 3000 life cycles during the planning period. The power conversion cost follows Figure 4-2, whereas the yearly operation and maintenance cost is assumed 12 k\$/year (assuming a part-time driver with two hours duty daily), and the truck capital cost is assumed 50 k\$. For MESS stations allocation, ten buses are chosen as candidates as given in Table 4-1; only three buses are allowed as MESS stations. The PSO parameters are set using a trial and error approach, and the population size was found to provide an adequate computational time for this particular problem. For defining the MESS daily number of trips \overline{DT} , the minimum value is desirable given that it achieves the maximum profit and guarantees a feasible solution. Here, \overline{DT} was found to be four. The sizing problem of the MESS using the proposed algorithm is solved by the Gurobi solver in 6 hours and 35 minutes using a 3.30 GHz AMD six-core processor. The solver gap from the global optimal is recorded as 0.39%.

Table 4-1 Optimization input parameters.

RES, DG units rating	$p^{wt1} = 2MW, p^{wt2} = p^{wt3} = 1.5MW, p^{DG1} = 1 MW$ $p^{pv1} = p^{pv2} = 0.5 MW, p^{DG2} = p^{DG3} = 0.5 MW$ $\mathcal{N}^{MES} \text{ candidates} = \{4, 6, 9, 12, 22, 25, 28, 35, 39, 40\}$
MESS Data	$\underline{v} = 0.95, \bar{v} = 1.05, \tau = 1, IR = 3\%, Y = 12, Sc = 48,$ $\overline{S}^{MES} = 5 MVA, \overline{E}^{ES} = 15MWh, FC^{MES} = 5000\$,$ $C^{truck} = 50K\$, \overline{DT} = 4, \alpha^{TN} = 20\%$ $\overline{DN}^{MES} = 1, \overline{TN}^{MES} = 3000, \overline{z}^{MES} = 3, O\&M^{MES} = 12k\$/y$ $C^{MES}/MWh = 600 K\$, \eta = 0.85$
PSO Data	$\bar{J} = 200, c_1 = c_2 = 2, \omega_{max} = 0.9, \omega_{min} = 0.1$ $M = 10, \gamma = 8, \varepsilon = 0.25\%, \overline{V}_m = [0.5 * ones(10,1); 1]$

Two cases are compared in Table 4-2 during the whole operation period, which includes the MESS and stationary ESSs (SESSs). The SESS sizing and allocation is same as the MESS with changing the size, allocation constraints with theses used in [9]. Because the MESS is a centralized ESS, it has a higher power rating which yields a less per unit power-converter cost. It is interesting how the SESS has a higher converter total cost although its aggregated power rating is less than that in the MESS. The saving in the power converter cost alone reached 200 k\$ which is the main reason in the profit privilege of the MESS. Because the optimal MESS size is higher than the equivalent SESS size, the MESS has managed to gain greater arbitrage benefit and was capable of achieving higher losses reduction because it improves the voltage profile. Further, a significant maximum load reduction is reached which may defer the substation or feeder upgrade cost as well. The MESS has achieved 1.38 times the equivalent SESS profit.

Regarding the MESS stations allocations, three locations are selected by the optimization algorithm; one near the feeder substation {bus 9}, while the other two at the end of each lateral (buses 28, 40). This result makes sense because the MESS is supposed to provide a reactive

power support for voltage regulation at the weakest buses. Regarding the optimality of the resulting MESS sizing, Figure 4-4 compares the profit with different MESS power ratings. It can be concluded that the proposed algorithm has managed to define an optimum solution.

Table 4-2. Optimization Results With different ESS Technologies.

	MESS	Stationary-ESSs
Rated power	3250 kVA	727, 595, 1500 kVA: 2822 kVA (Total)
Capacity	6381.3 kWh	1455, 1190, 3000 kWh: 5645 kWh (Total)
Optimal locations	9 (St.1), 28 (St.2), 40 (St.3)	28, 39, 40
Power converter cost	418,220\$	618,300\$
Battery bank cost	3,828,780\$	3,387,000\$
Total Storage cost	4,247,000 \$	4,005,300 \$
Losses reduction	47.22%	45.17 %
Max. Load reduction	4.38%	4.39 %
Saved losses	2,092,500 \$	1,985,600 \$
Arbitrage profit	2,919,800 \$	2,570,800 \$
Total profit	10,138,000\$	9,923,500 \$
Profit increase	765,400 \$	550,900 \$

To monitor the dynamic performance of the MESS that results from the sizing discussion, a winter day scenario is shown in Figure 4-6. During this scenario, the MESS shifts late night energy to the afternoon peak hour to achieve arbitrage profit as shown in Figure 4-6 (b). Regarding the MESS location transitions, first, the MESS provides a leading reactive power support at the far end of the feeder (Station 3 or bus 40) then it moves to bus 9 to start charging. The reason for this transition is reducing the power loss by choosing a charging location near the main substation. The second transition is made to bus 28 (Station 2) near WT3 where the

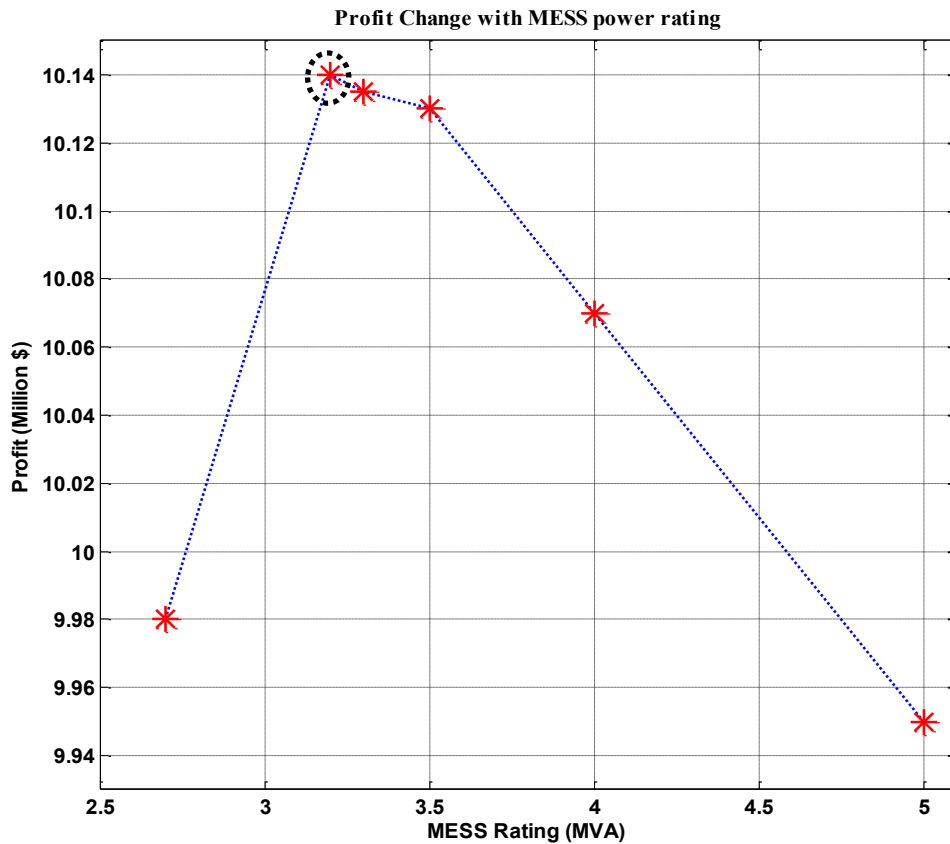


Figure 4-5 MESS rated power versus Profit.

Extra wind power is saved for peak hours. After charging the surplus wind energy, the MESS moves to the feeder end (at Station 3 located at bus 40) where the MESS performs voltage regulation with energy arbitrage (discharging stored off-peak energy during the peak hour).

The number of the MESS trips is kept four as given in the optimization constraints and depicted in Figure 4-6(d). Besides, the capacity is upper-bounded by the rated value, and the number of charging cycles is one as shown in Figure 4-6(e).

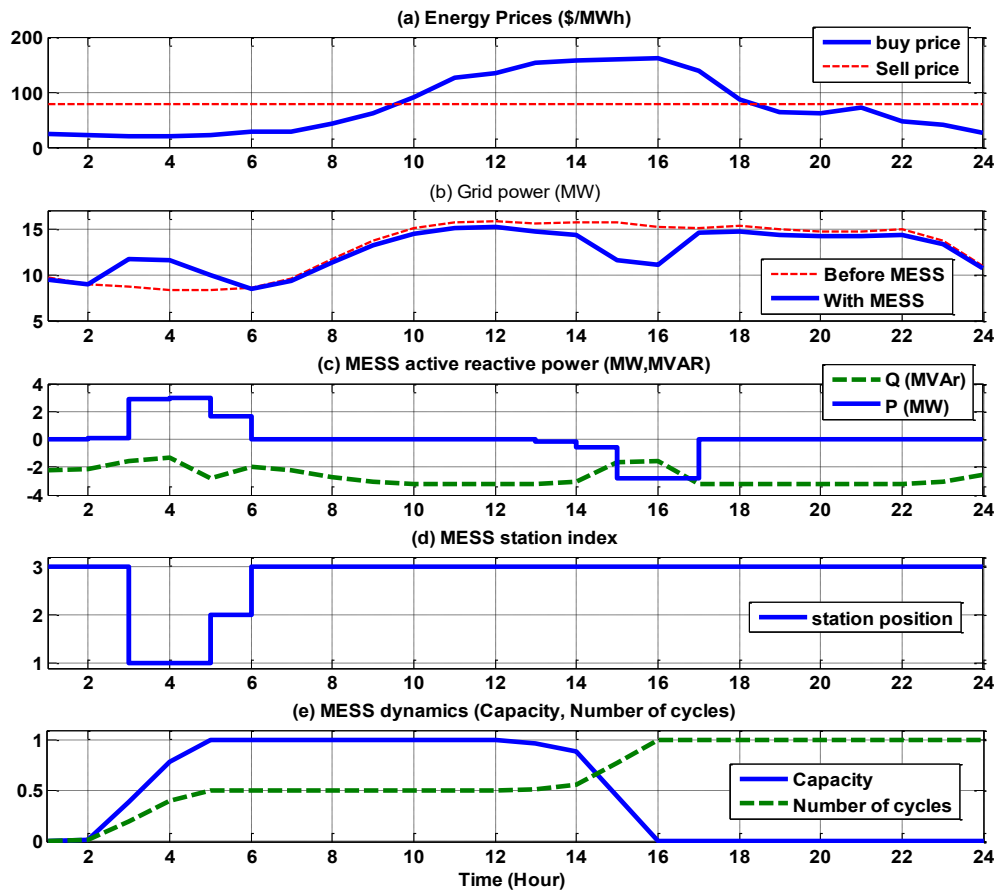


Figure 4-6. Summer day scenario results (a) Energy buy and sell prices (b) grid purchased power (after/before) MESS (c) MESS active and reactive Powers (d) MESS location (station). (e) Capacity and daily number of cycles.

It is worth mentioning that MESS positioning strategy will change if it does not participate in voltage regulation (omit constraint (48) and instead, add SVCs or capacitors); this is all up to the DNO who may prefer different energy management strategies for the MESS. It should be noted that these results are mainly due to the advantage of cheaper bulk power converter cost and generally speaking, it cannot always be generalized that the MESS is a better investment option than the SESS. In fact, a separate cost-benefit analysis for each technology should be conducted to decide the optimal option for a given system. Further, the MESS has some

reliability disadvantage due to its transition from a station to another (transition delay). Finally, the MESS cannot always guarantee a successful replacement for a large number of SESSs, as more than one MESS can be required to have different positions in enormous power systems. This point will be investigated in future research.

4.5 Conclusion

This chapter proposed a sizing and allocation algorithm for a mobile energy storage system in the distribution system. The optimization aimed at maximizing the utility profit by considering the participation of the MESS in multi grid-support services including energy arbitrage, voltage regulation, and power loss minimization. The sizing constraints included the battery life cycles and dynamic capacity, and the feeder voltage levels and ampacity. Load and renewable energy variations were modeled via considering different scenarios in the sizing scheme. Further, a size-dependent cost for the power converter was adopted which is more realistic and practical. The sizing algorithm was tested by a case study on a real radial feeder using realistic power and market price data. The study results showed that using the MESS may yield a higher profit than stationary ESSs due to its low bulk power conversion cost while providing multi-tasking as in multi-stationary ESSs. Future research will consider the same problem with multi mobile storage units with more sophisticated transit delay models.

Chapter 5

EMS of a Hybrid Wind-Battery Energy Storage System via Model Predictive Control

5.1 Introduction

This chapter presents a market-oriented energy management system (EMS) for a hybrid power system composed of a wind energy conversion system (WECS) and a battery energy storage system (BESS). The EMS is designed as a real-time model predictive control (MPC) system. The EMS dispatches the BESS to achieve the maximum net profit from the deregulated electricity market for the owner (RES energy time shifting). For net profit maximization, the EMS aims at expanding the BESS lifetime by applying typical and practical constraints in the MPC problem on both the daily number of cycles (DNC) and depth of discharge (DOD). These constraints are vital because the BESS life is a function in both the DNC and the DOD. The MPC constraints optimizer is designed to tune these lifetime constraints optimally to achieve the maximum market revenue with a minimal expended-life cost. The effectiveness of this work is verified by comparison with a conventional MPC used in previous works. A simulation study is conducted using a real wind power and market data in Alberta, Canada. The new contributions of this work to the research field are:

- 1) A detailed storage cost is calculated and considered in the optimization problem. Further, the expended-life cost, which is a function in the DNC and DOD, has also examined for obtaining an accurate and practical economic cost function.

- 2) The trade-off between the DNC and DOD constraints and the daily profit is investigated.
- 3) An MPC constraints optimizer is designed to tune the DNC and DOD constraints such that the net profit is maximized. The optimizer is maneuvered by the compromises between the battery expended-life cost and the expected profit from the market.
- 4) Adding the expended-life cost (ELC) converts the optimization into a non-convex problem and the proposed constraints optimizer manages in convexifying the problem.
- 5) The applicability of the proposed EMS is valid for all types of BESSs and is extendable to other areas, such as microgrids, hybrid vehicles storage planning or vehicle to grid (V2G).

5.2 Hybrid WECS-BESS Description

In this section, the hybrid system is briefly described including the structure of the power and control circuits. The system under investigation is composed of a WECS and a lead-acid BESS as depicted in Figure 5-1.

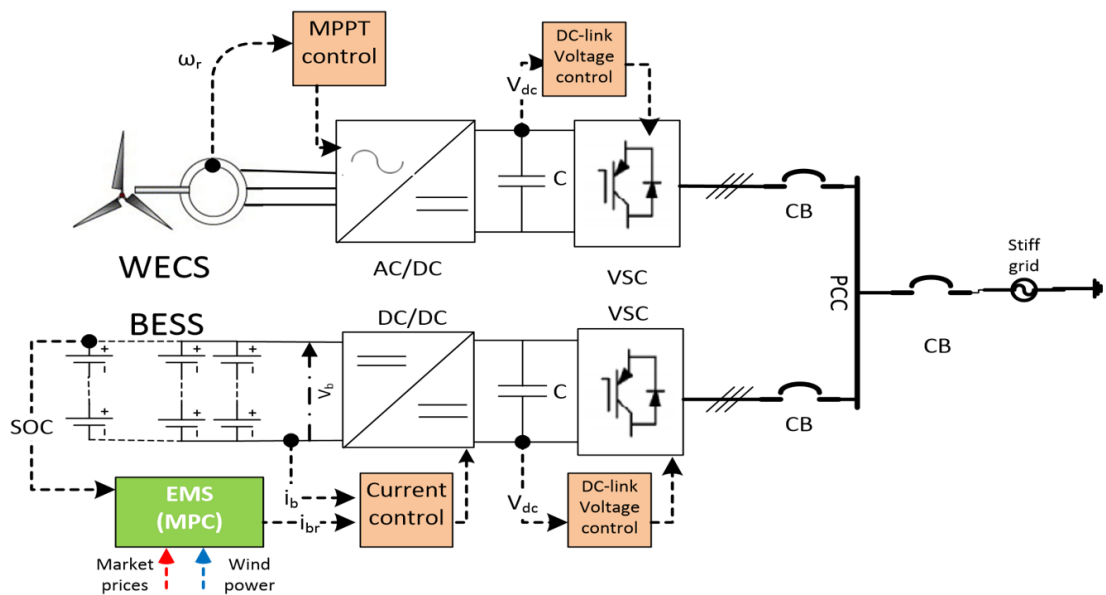


Figure 5-1 The hybrid system structure.

5.2.1 Wind Energy Conversion System (WECS)

The WECS is assumed to be a directly connected permanent-magnet synchronous generator (PMSG). The PMSG is connected to the grid via an ac/dc/ac converter composed of two voltage-source converters (VSCs) coupled by a dc-link [104]: the stator-side (ac/dc) converter and the grid-side converter (dc/ac). The stator-side VSC controls the electrical torque of the PMSG to achieve the maximum power point tracking (MPPT). Another task for the stator-side VSC is flux regulation via control of the generator direct-axis current. Flux regulation may be used for magnetizing the PMSG in the case of demagnetization (due to aging, temperature, etc.). In this system, the direct-axis current is regulated to zero to reduce the Ohmic losses.

On the other hand, the grid-side VSC transfers the harvested power from the dc-link to the grid by regulating the dc-link voltage to the nominal value. Another task for the grid-side VSC is reactive power compensation. In this work, the unity power factor is set, and no reactive power injection to the grid occurs; however, the system owner can exploit the reactive power control for ancillary services brought to the grid (e.g., for voltage regulation in case of weak grids). In the EMS, the WECS is modeled as an exogenous input that can be predicted from the wind speed. By neglecting the fast electrical dynamics of the generator and assuming an ideal MPPT, the WECS power is calculated as a first-order filter as follows [111], [112];

$$P_w = \frac{P_m \eta_w}{\tau_{wnd} s + 1} \quad (5.1)$$

$$P_m = 0.5 \rho c_p(\lambda) A \bar{V}_w^3 \quad (5.2)$$

where P_w , P_m , s , η_w , τ_{wnd} , ρ , c_p , λ , A , \bar{V}_w are the WECS harvested electrical power, WECS mechanical power, Laplace transform operator, WECS efficiency (including shaft and gears, generator, power converter and cable efficiencies), the drivetrain time-constant (e.g., ratio

between the shaft inertia and friction), air density, power coefficient, tip speed ratio, rotor disk area and the effective wind speed across the rotor disk. Further details are explained in [111]. The dominant dynamics of the WECS are modeled as a first-order filter with p_m representing the input disturbance to the system [112] τ_{wnd} is assumed to be 1.5 s and $\eta_w = 0.9$.

5.2.2 Battery Energy Storage System (BESS)

The BESS consists of an array of lead-acid cells. The array terminal voltage is determined by the number of series cells in the same string, whereas the total current is the sum of the parallel strings currents. The reader is referred to the IEEE Standard 485 [113] for more information on the BESS sizing. The BESS is connected to the grid via a dc/dc/ac bidirectional VSC. The dc/dc converter is a current-controlled buck-boost controller. The current controller regulates the charging (discharging) power according to the set point provided by the EMS. On the other hand, the ac/dc converter transfers the power to (from) the grid via regulation of the dc-link voltage [104]. Further, the system owner can exploit the reactive power control for ancillary services brought to the grid for reactive power support; however, the proposed work does not investigate the participation in these services, which may require certain BESS rating requirements [40]. All controllers above (current, MPPT and voltage controllers) are relatively fast (have very wide bandwidth) with respect to the EMS speed. Thus, the internal dynamics of all these are constant from the EMS point of view. As a result, the battery storage dynamics are only considered in the EMS design model.

Any battery has a non-linear time-variant model due to sophisticated parasitic chemical losses and the unmodeled temperature-dependent dynamics [114], [115]. The authors of [115] derived a system identification model for the lead-acid battery using experimental measurements over ten years of experimental results. The resulting model is a third-order state

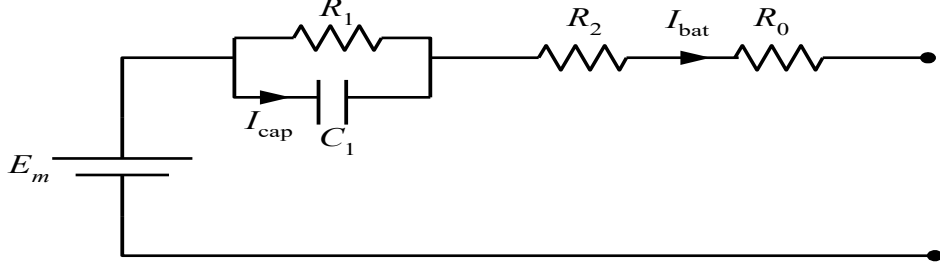


Figure 5-2 Simplified battery model.

space model (the states are the ambient temperature, the battery current, and the battery charge). The authors of [36] used the model given in [115] assuming an ambient temperature operation and zero parasitic losses. The resulting battery model is a third-order linearized model, and the simplified battery is shown in Figure 5-2. A comparison with the nonlinear battery model shows SOC error below 5% [36] and voltage error between 5% and -9% . As a result, the derived BESS model in [36] is accurate enough to represent realistic BESS dynamics, particularly for supervisory energy management controllers, and, therefore, it is adopted in this work.

$$\left\{ \begin{array}{l} \begin{array}{l} \dot{x}_1 \\ \dot{x}_2 \\ \dot{x}_3 \end{array} = \begin{bmatrix} -\frac{1}{\tau_1} & 0 & 0 \\ 0 & 0 & 0 \\ 0 & 1 & 0 \end{bmatrix} \begin{bmatrix} x_1 \\ x_2 \\ x_3 \end{bmatrix} + \begin{bmatrix} 1 \\ 1 \\ 0 \end{bmatrix} u \\ Y = \begin{bmatrix} P_b \\ SOC \end{bmatrix} = \begin{bmatrix} R_1 \bar{x}_2 & E_m - (R_0 + R_1 + R_2) \bar{x}_2 & 0 \\ 0 & 0 & \frac{1}{Q} \end{bmatrix} \begin{bmatrix} x_1 \\ x_2 \\ x_3 \end{bmatrix} \\ \begin{bmatrix} x_1 \\ x_2 \\ x_3 \end{bmatrix} = \begin{bmatrix} I_{cap} \\ I_{bat} \\ \int I_{bat}(t) dt \end{bmatrix} \\ u = \frac{dI_{bat}}{dt} \\ \tau_1 = R_1 C_1. \end{array} \right. \quad (5.3)$$

In (5.3), I_{cap} , I_{bat} , P_b , SOC , Q , \bar{x}_2 and E_m are the capacitor current, the battery current, the battery power, the state of charge ($SOC=1-DOD$), the battery rated charge and the open circuit voltage, operating point current, respectively. On the other hand, R_0 , R_1 , R_2 , C_1 , τ_1 are battery-

based parameters derived for the equivalent electrical model for the lead-acid battery [36]. The reader is referred to [36] for the proof and further details. Further, the work in [116] derives an accurate Li-ion battery model.

5.2.3 Hybrid System State-Space Model

The total power injected to the grid (P_g) is the sum of the WECS and BESS power (negative in case of discharge):

$$P_g(t) = P_w(t) - P_b(t). \quad (5.4)$$

A complete state-space model for the hybrid system is now reached after discussing the BESS and WECS models. The discrete version of the resulting model is presented as follows, assuming a sampling time T_s :

$$\begin{aligned} X_t(k+1) &= AX_t(k) + BU(k) + B_d U_d(k) \\ Y_t(k) &= CX_t(k) + D_d U_d(k) \\ U_d(k) &= [P_m] \\ Y_t(k) &= [DOD, P_g, P_b]' \\ X(0) &= X_0. \end{aligned} \quad (5.5)$$

As shown in (5.1) and (5.3), the hybrid system is modeled as a fourth-order state-space linearized model with a state vector (k). The controlled input (k) is the battery charging current rate provided by the EMS, whereas the exogenous input (k) is the wind power. The outputs are the DOD and the battery and grid powers. The system is completely controllable and observable because the controllability and observability matrices have full ranks. The open-loop system model is depicted in Figure 5-3.

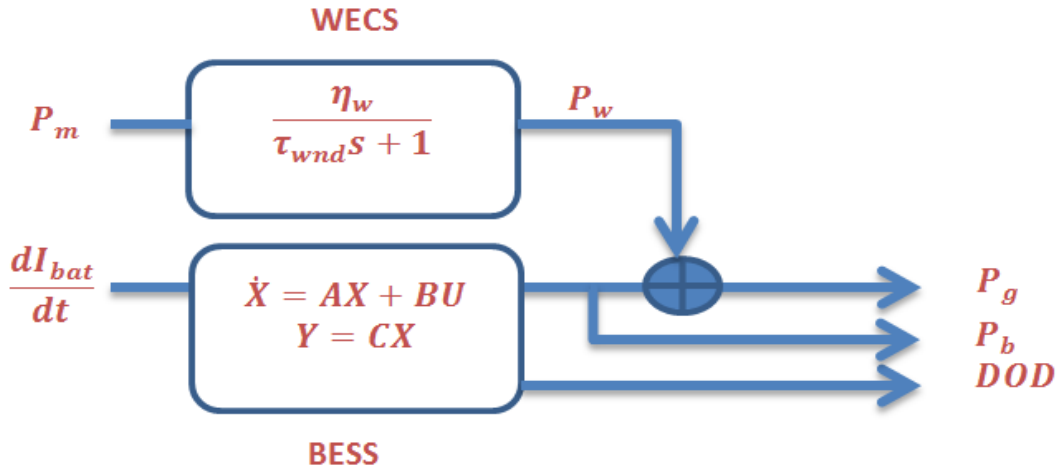


Figure 5-3 The system open-loop model.

5.3 Economic Perspective of Energy Management

5.3.1 Electricity Market Regulations for Renewables

Electricity market analysis is a key research topic of its own. We will briefly focus here on the renewable energy regulations in both regulated and de-regulated markets. As mentioned earlier, the regulated market is a fixed tariff system; however, renewable sources may get a fixed tariff in de-regulated markets, because some governments have started to motivate investors by providing incentives for renewable sources like photovoltaic (PV) and WECSs. For instance, there was a fixed feed-in-tariff issued in 2010 by the Ontario power authority, Canada, by adopting a fixed feed-in tariff rate of 0.44 CAD/kWh for renewable resources [117]. This policy helped the investors to easily anticipate the projected profits and payback periods of their investments. As a result, the PV installed capacity has increased by 218% in Ontario within just one year [117].

In contrast, in other deregulated markets where renewable sources have no fixed tariff, the energy price depends on the difference between the supply and demand. Sometimes, the

electricity market can be very volatile and highly unanticipated [39]. Further, the de-regulated market behavior changes during different seasons and between working days and weekends [118]. Some countries have a daily de-regulated market where the market closes on a day-ahead energy commitment. In contrast, other countries run a continuous market with gate closure where an energy commitment is made periodically each fixed time before the actual delivery. After gate closure, no other bids are allowed, and the committed energy must be delivered to the participants [30]. Gate closure has distinct values from one country to another. For instance, a gate closure occurs each five minutes in Australia and Nord Pool Spot, each hour in the United Kingdom and some United States regions, each four hours in Spain [30] and each two hours in Alberta, Canada. The failure of energy commitment after gate closure leads to power-system imbalance; thus, the system operator must compensate this imbalance using the available spinning reserve. The compensation cost is collected as a penalty from the participants who failed to fulfill their energy commitment (mainly PV and WECS facilities). In Alberta, different regulations exist for WECS integration [119], [120]. A WECS does not bid in the market because it is non-dispatchable; thus, the wind energy is traded with the current existing price market (price-taker) [119]. Further, each WECS must declare its system wind power limit (SWPL) to the Alberta Electric System Operator (AESO). The SWPL is updated to the AESO each 20 minutes [119] and the exported wind power should not exceed 115% of the stated SWPL [120]. An EMS controls the SWPL by wind energy curtailment techniques [120].

5.3.2 Energy Storage Cost Calculation

The storage cost study should be comprehensive to include all initial and running costs. This study was investigated before in [38]; however, it assumed a fixed DOD and DNC operation. Thus, in this section, we will modify the rules of [38] by adding the BESS expended-life

constraints in [121]. Here, the cost is divided into two categories: first, a fixed storage cost (SC) that includes power converters, balance of operation, replacement cost and maintenance costs; second, a BESS expended-life cost (ELC) that depends on the depletion in the storage unit cost due to the EMS. For ensuring a profitable hybrid power system, an optimal sizing for BESS is required to determine the rated power and capacity of the BESS. The optimal sizing of a Lead-acid BESS was discussed before in [122]. By adopting the technique in [122], or any other technique, it is possible to determine the power and capacity of the BESS; these values determine the annual capital cost of the project (excluding storage cost) as follows [38]:

$$ACC = (PCS + BOP)CRF \quad (5.6)$$

$$BOP = BOP_u Q \quad (5.7)$$

$$PCC = PCC_u P_r \quad (5.8)$$

$$CRF = \frac{ir(1 + ir)^y}{(1 + ir)^y - 1} \quad (5.9)$$

where ACC , PCC , PCC_u , BOP , BOP_u , CRF , y , P_r , and ir are the annual capital cost, power converter (total \$ and per-unit \$/kW) cost, balance of plant (total \$ and per-unit \$/kWh) cost, capital recovery rate, the project lifetime in years, BESS rated power, and the interest rate, respectively. The expended-life (EL) of a lead-acid BESS is a function in both the DOD and DNC and calculated as follows [121]:

$$EL(N, DOD) = \frac{N}{N_t(DOD)} \quad (5.10)$$

$$N_t(DOD) = a * DOD + b \quad (5.11)$$

where N_t is the battery total number of cycles as a function of the DOD, and a and b are constants depending on the battery type, characteristics and the total number of cycles at the nominal DOD (taken 3200 cycle here) [121]. The DOD has different forms for other types of batteries (Lithium-Ion or NiMH batteries) which are stated in [121]. The relation between the expended-life with the DOD and DNC is depicted in Figure 5-4.

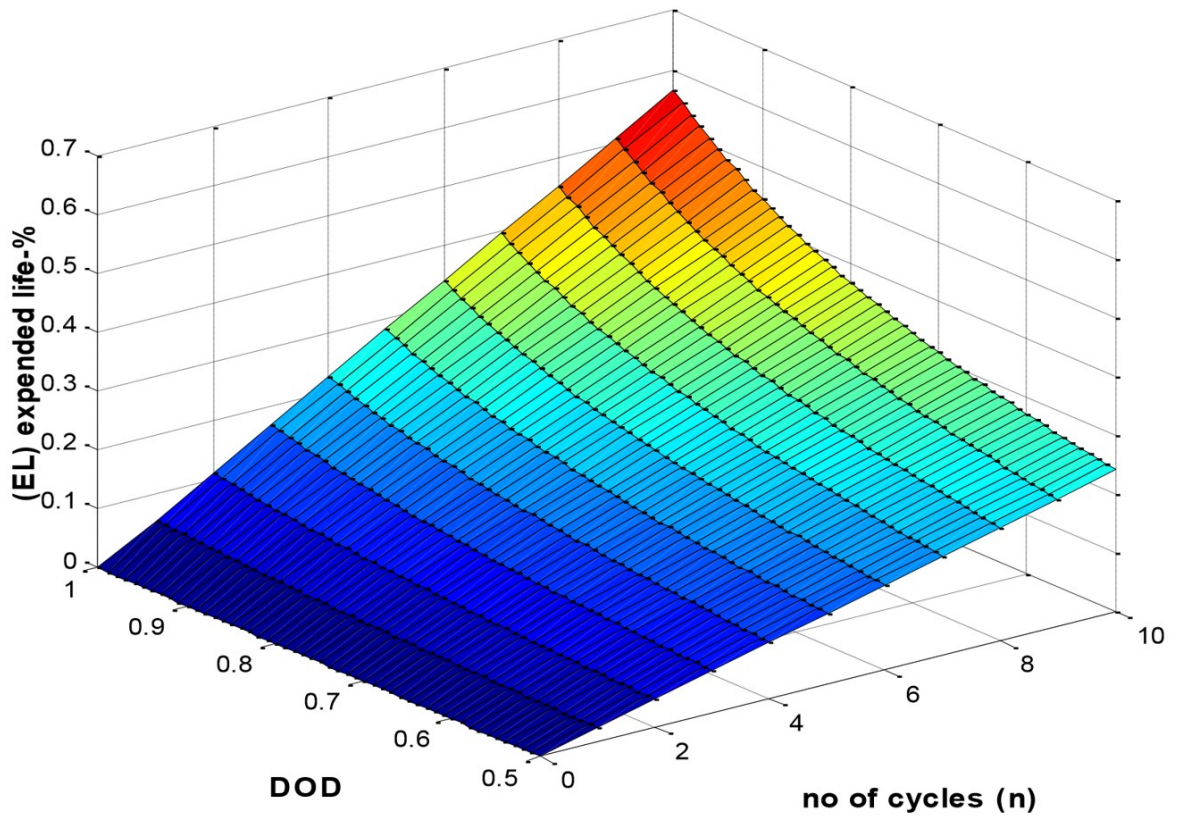


Figure 5-4 Relation between expended-life (EL), No. of cycles and DOD.

The expended-life cost (ELC) for the BESS, using it N - cycles with DOD , is estimated as:

$$ELC(N, DOD) = SUC * \frac{N}{N_t(DOD)} (\$) \quad (5.12)$$

$$SUC = SUC_u * Q \quad (5.13)$$

where S and SUC_u are the storage unit total \$ and per-unit \$/kWh cost, respectively. Note that the ELC is calculated on a daily basis and depends on the achieved DNC and DOD. The yearly expended-life (YEL) is estimated in (5.14) assuming D working days yearly, with the yearly average number of cycles N_{avg} given as

$$YEL = \frac{N_{avg}D}{N_t(DOD_{avg})} (pu/year). \quad (5.14)$$

Assuming a fixed yearly number of cycles, given the YEL , the battery replacement times (BRT) during the project lifetime (y years) is predictable from the desired period of service and the depletion period for the battery bank. Further, the wearing period of the BESS (WP) is estimated easily as the time of years to reach 100% depletion as in (5.16).

$$BRT = YEL * y - 1 \quad (5.15)$$

$$WP = \frac{1}{YEL} (years) \quad (5.16)$$

In the case of a non-integer BRT , it is rounded up and the project lifetime is extended. In such a case, y is updated and equation (5.9) is re-calculated. After deciding the BRT , the annual replacement cost (ARC) is calculated, given the future BESS cost (FBC) [38]:

$$ARC = CRF * FBC * Q * \sum_{j=1}^{BRT} (1 + ir)^{-j*WP} \quad (5.17)$$

Finally, the storage cost is obtained from the ACC , ARC and the annual operation and maintenance cost ($O\&MC$), given the annual discharged energy (ADE) [38]:

$$SC = \frac{ACC + O\&MC + ARC}{ADE} (\$/KWh) \quad (5.18)$$

$$ADE = QN_{avg}D \quad (5.19)$$

5.4 Proposed Energy Management System Design

This section explains the proposed EMS, which is designed to achieve multiple objectives. First, the primary objective of the EMS is to maximize the profit of the hybrid system owner from the deregulated market. The EMS utilizes the available forecast of wind power and market prices for profit maximization (energy arbitrage). In this work, the prediction horizon is taken as an hourly forecast for the incoming 24 hours; however, different time frames and

sampling intervals are also applicable depending on the data availability and the market operation. Second, the EMS must dispatch the BESS within acceptable safe power and energy constraints. Third, the EMS must maximize the BESS lifetime by adopting the minimal DNC and DOD as long as a feasible solution exists. Finally, the EMS is only allowed to increase the DOD or DNC if a potential profit higher than the ELC exists. For real-time utilization of the changing market price and wind power forecast, an MPC is utilized to design the EMS. The motive of using the MPC will be briefly explained in the upcoming subsection, and then the problem formulation is discussed. Finally, the proposed constraints optimizer is designed.

5.4.1 A Glance over MPC

A finite horizon MPC is used as an EMS [123]. The MPC is a control technique that is helpful in case of knowing the controlled output desired trajectory for the incoming prediction horizon (n_p).

Thus, the controller predicts the output of the system for this horizon (iteratively using the state-space model) at the current instant, assuming ideal modeling, as follows:

$$\mathbf{y} = [Y(k|k), Y(k+1|k), \dots, Y(k+n_p|k)] \quad (5.20)$$

It should be noted that \mathbf{y} is a function in the control action vector (\mathbf{u}) and the predicted state vector (\mathbf{X}). The MPC generates the control action for the incoming control horizon n_c as follows:

$$\mathbf{u} = [U(k|k), U(k+1|k), \dots, U(k+n_c|k)] \quad (5.21)$$

It is worth mentioning that the control horizon must be less than, or equal to, the prediction horizon. The MPC is an optimal controller which decides the value of \mathbf{u} that optimizes a certain

objective function. The calculations of (\mathbf{y}, \mathbf{w}) from the state-space model in (5.4) are explained in [123]. The main motives for using MPC in this work are formulated in the following [123]. It utilizes the knowledge of the future trajectory (e.g., market price and wind power predictions) in optimizing the short-term control decision (e.g., BESS power). Furthermore, the MPC is an optimal controller that minimizes a particular cost function over the incoming time window (n_p or n_c), (e.g., the net profit). The cost function serves multiple objectives (output tracking, control effort minimizing, etc.). The constraints of the optimization process may include the states, input, input rate and output limits; thus, the MPC guarantees a safe operation for the plant with allowable operating margins and a bounded input–output stability (e.g., the energy, DNC and power constraints in this work). The MPC has been proven to be robust and effective in many industrial applications [124]. On the other hand, the MPC is very sensitive for unmodeled dynamics and process disturbances. An effective way to overcome this issue is to adopt the receding horizon policy [123]. The receding horizon policy states that the control action is only implemented in the current instant. The prediction horizon window is then shifted by one step when new measurements are available and this process is repeated for each sample.

5.4.2 Problem Formulation

The market price forecast and expected wind power are assumed to be predictable for the incoming prediction horizon (n_p):

$$\mathbf{c}(k) = [\bar{\mathcal{C}}(k|k), \bar{\mathcal{C}}(k+1|k), \dots, \bar{\mathcal{C}}(k+n_p|k)] \quad (5.22)$$

$$\mathbf{w}_a(k) = [\bar{\mathcal{U}}_a(k|k), \bar{\mathcal{U}}_a(k+1|k), \dots, \bar{\mathcal{U}}_a(k+n_p|k)] \quad (5.23)$$

where (k) is the market prediction at the instant kT_s . Using the upper accent (e.g., $\bar{\mathcal{C}}(k|k)$) indicates that the expected price and wind power contains a prediction error. In fact, the actual price and wind power can be formulated as follows:

$$C(k) = \bar{C}(k) + \tilde{C}(k) \quad (5.24)$$

$$U_d(k) = \bar{U}_d(k) + \tilde{U}_d(k) \quad (5.25)$$

where $C(k)$, $U_d(k)$ are the energy prices and wind power prediction errors at instant (k), respectively. Because there is no way to estimate the wind power and the market behavior exactly, we assume that the prediction error is a Gaussian white noise (with zero mean value), and the estimated values are the expected values:

$$E(C(k)) = \bar{C}(k) \quad (5.26)$$

$$E(U_d(k)) = \bar{U}_d(k), \quad k \rightarrow \infty \quad (5.27)$$

The EMS objective is to maximize the gross profit, which equals the net of energy bought by (or sold from) the grid during the incoming horizon, minus the storage cost during this horizon:

$$Pro = \sum_{k=T_o}^{T_o+n_p T_s} \bar{C}(k) P_g(k) T_s - \sum_{k=T_o}^{T_o+n_p T_s} P_{bd}(k) T_s SC \quad (5.28)$$

$$NET.Pro = Pro - ELC \quad (5.29)$$

where Pro , $NET.Pro$, P_{bd} , and T_o are the projected gross profit, the net profit for the incoming horizon, the discharged power from the BESS and the initial time index, respectively. The BESS energy is negative if it is exported to the grid, whereas it is positive if it is imported. The gross profit is a convex problem solved efficiently by the branch and bound solver. On the other hand, the net profit acts as a non-convex problem because it includes the ELC (a nonlinear function in the DNC and DOD). Thus, optimizing the net profit represents a challenging optimization problem that may lead to feasibility problems. As a result, the gross profit is optimized whereas the net profit is taken into consideration by designing the constraints optimizer which will be discussed next. The discharged power is expressed as follows:

$$P_{bd}(k) = \frac{|P_b(k)| - P_b(k)}{2} \quad (5.30)$$

Equation (5.30) gives zero in case of battery charging or standby operations ($(k) \geq 0$), whereas it gives the absolute value of the battery power in case of discharging only. In the case of using a one-hour sampling time and the energy price is given in \$/kWh, one can replace T_s by one as follows:

$$Pr_o = \sum_{k=T_o}^{T_o+n_p T_s} \bar{C}(k) P_g(k) - \sum_{k=T_o}^{T_o+n_p T_s} P_{bd}(k) SC \quad (5.31)$$

The problem constraints are on the BESS power, DOD and DNC. First, the BESS power must be within the allowable limits during charging or discharging. This constraint is formulated as follows:

$$\underline{P}_b(k) \leq P_b(k) \leq \overline{P}_b(k) \forall k \in [T_o, T_o + n_p T_s] \quad (5.32)$$

where $\overline{P}_b(k)$, $\underline{P}_b(k)$ are the upper and lower limits of the power at instant k . It is very important to define the available rating of the BESS at each sample in the incoming prediction horizon. If a scheduled maintenance for the full BESS is carried out from $[T_{ms}, T_{me}]$ (e.g., maintenance for the main circuit breaker), the BESS power limits $\overline{P}_b(k)$, $\underline{P}_b(k)$ must be set to zero during this period. On the other hand, if a partial maintenance for some strings of the array (e.g., partial capacity test) from $[T_{ms}, T_{me}]$ is required, the BESS working power must be modified in this period. The second constraint is on the DOD in order to charge (or discharge) the battery with the permissible capacity.

$$\underline{DOD}(k) \leq DOD(k) \leq \overline{DOD}(k) \forall k \in [T_o, T_o + n_p T_s] \quad (5.33)$$

The DOD has a lower limit \underline{DOD} that is probably zero, which means the BESS has a full capacity. On the other hand, the upper limit is recommended by the manufacturer (usually 70–80%). The lower limit prevents the BESS overcharging whereas the upper limit restrains the deep discharge of the BESS. It should be noted that battery lifetime is very sensitive to the DOD as given in (10). As a result, the value of max. DOD is optimized later in this section. The final constraint is on the DNC , and this constraint is formulated as follows. First, the battery status (BS) is calculated as a sign function for the BESS power:

$$\begin{aligned}\mathbb{B}s &= [\text{sign}(P_b(k)), \dots, \text{sign}(P_b(k + n_p))] \\ \mathbb{B}s &= [BS_1, BS_2, \dots, BS_{n_p}]\end{aligned}\tag{5.34}$$

The output of the sign function is 1, 0, and -1 if the BESS is charging, in the standby mode, or discharging, respectively. The change of the BESS state is detected by calculating the difference of (5.34).

$$\Delta\mathbb{B}s = [BS_2 - BS_1, \dots, BS_{n_p} - BS_{n_p-1}]\tag{5.35}$$

The sum of all elements of the vector $\Delta\mathbb{B}s$ equals the number of states change (NSC) between the charge and discharge states. It should be noted that if the BESS is in standby, this does not affect the NSC when taking the sum of (35). The number of cycles (N) equals half the NSC . The DNC is bounded by an upper limit (\bar{N}) in (5.37).

$$N = 0.5 \sum_{j=1}^{n_p-1} |\Delta BS_j|\tag{5.36}$$

$$N \leq \bar{N}\tag{5.37}$$

Now, the final MPC optimization problem is stated after defining the cost function in (28) and the operational constraints in (5.32)-(5.33), and (5.37). Given the initial states value, the

market price prediction (5.22) and the expected wind power horizon (5.23), and all the constraints limits over the incoming prediction horizon, the final problem (λ) optimizes the gross product as in (5.38):

$$\lambda \left\{ \begin{array}{l} \text{Max}_{\text{un}}(Pro) \\ \text{s. t.} \left\{ \begin{array}{l} X_t(k+1) = AX_t(k) + BU(k) + B_d U_d(k) \\ Y(k) = CX_t(k) + D_d U_d(k) \quad X_t(0) = X_0 \\ \underline{P}_b(k) \leq P_b(k) \leq \overline{P}_b(k) \\ \underline{DOD}(k) \leq DOD(k) \leq \overline{DOD}(k) \\ N \leq \overline{N} \\ \forall k \in [T_o, T_o + n_p T_s] \end{array} \right. \end{array} \right. \quad (5.38)$$

This problem is solved in real time, i.e., for each T_s , when all the predictions and constraints are updated. The receding horizon policy is adopted; thus, only ($k|k=1$) is applied in the real process.

The question arising now is how to choose the DNC and DOD constraints of the MPC problem (λ) such that it achieves the optimal profit and lifetime saving (maximum net profit).

5.4.3 MPC Constraints Optimizer

The net profit, as given in (5.29), is divided into two parts. First, the gross profit, which includes all income subtracted from the fixed cost is a linear function that increases with the DOD and DNCs. On the contrary, the second part, which represents the depleted lifetime (ELC), is minimized with the minimal DNC and DOD as stated in (5.10). Further, the ELC needs a non-traditional nonconvex optimization, causing a feasibility problem. Although the ELC has a significant value, eliminating it from the optimization problem improves feasibility. To overcome this problem, an MPC constraints optimizer is proposed. As given in (5.12), the ELC is only a function in DNC and DOD. Thus, employing an upper limit on the DNC and DOD inherently leads to imposing an upper ELC limit. If one can find the optimal operating

limits (max DOD and max DNC) that result in the worst ELC $ELC \leq ELC(\overline{DOD}, \overline{N})$ and always guarantee maximal net profit, then we can optimize the gross profit instead of the net profit. Therefore, the MPC constraints optimizer is a search algorithm for max DOD and max DNC or by other means (\overline{ELC}) that leads to the maximum net profit. This process is done offline (given the day-ahead predictions). When optimal max DOD and max DNC are detected, the real-time MPC uses them to optimize the gross profit, but now it is inherently guaranteed that the worst case ELC is considered. Figure 5-5 shows the tuning mechanism of the optimizer and its effect on the net profit.

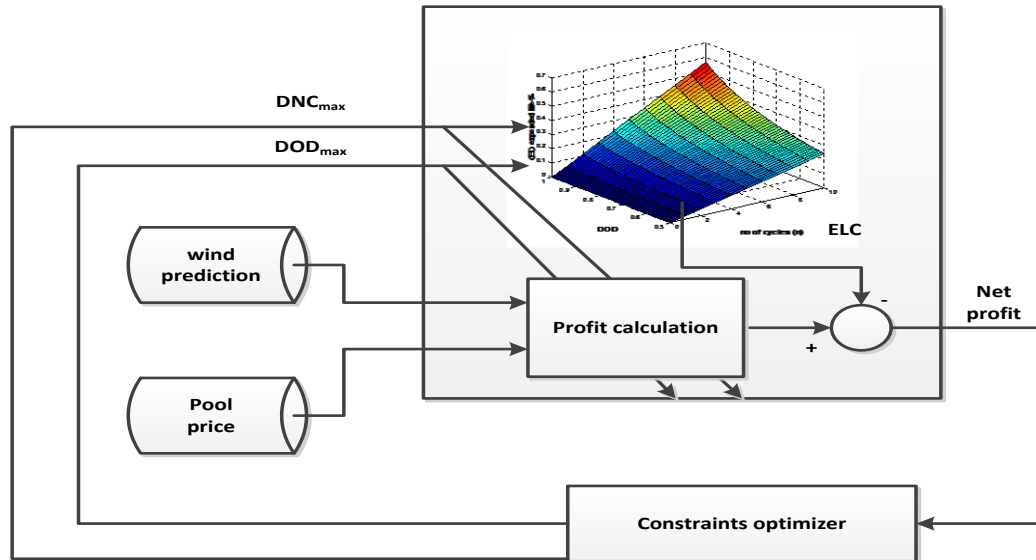


Figure 5-5 The constraints optimizer mechanism.

There is no doubt that the optimal lifetime occurs with the minimal DNC and DOD, as stated in (5.10). For achieving such a goal, the upper limit on both the DOD and DNC must be tightened as much as possible. On the other hand, by tightening the constraints \overline{DOD} and \overline{N} , not only the gross profit is minimized, but the feasible solution set is also narrowed and the global optimal profit may be allocated outside this set, which is not optimal.

This chapter proposes an MPC constraints optimizer for both \overline{DOD} and \overline{N} that continues tightening the constraints as long as the gross profit reduction is less than the expended-life cost. In other words, the optimizer is a profit-oriented trainer for the constraints that aims at detecting the constraints that maximize the net profit; these constraints are used later in the real-time MPC. At each iteration, the optimizer fixes the DNC and DOD constraints and measures the net profit. Second, it changes one of the constraints and reads the new net profit; the gradient of the net profit surface guides the optimizer to the direction of the optimal constraints over the permissible constraints plain. Assuming that the optimal constraints set ψ_{opt} belongs to a 2D plain composed of 2 sets (\mathbb{N}, \mathbb{D}):

$$\overline{DOD}_{opt} \in \mathbb{D}, \mathbb{D} = [\overline{DOD}_{min}, \overline{DOD}_{max}] \quad (5.39)$$

$$\overline{N}_{opt} \in \mathbb{N}, \mathbb{N} = [\overline{N}_{min}, \overline{N}_{max}] \quad (5.40)$$

$$\psi_{opt} = (\overline{N}_{opt}, \overline{DOD}_{opt}) = \psi(\max(NET.PRO)) \quad (5.41)$$

The constraints optimizer detects ψ_{opt} via this two-stage algorithm (A, B). These stages represent the offline training that is repeated daily as soon as the day-ahead market prices are announced.

5.4.4 Constraints Optimizer Algorithm

Stage A (Detecting \overline{N}_{opt})

1. At $k=T_0=0$; given the predictions $\mathbb{C}(k), \mathbb{W}_a(k)$, and the battery initial SOC_0 ; set $\psi = (\overline{N}_{max}, \overline{DOD}_{max})$.
2. Calculate the storage cost by calculating SC in (5.18). Solve the MPC problem (λ) in (5.38) to find the gross profit. By calculating the corresponding ELC from (5.12), the net profit is reachable as in (5.29).

3. Skip to step (8) if \bar{N}_{opt} is reached; otherwise continue.
4. If this is the first i^{th} iteration, then skip to step (7), otherwise continue.
5. If the problem is feasible, and $i \leq i_{max}, i_{max} = \bar{N}_{max}$, go to step (6). Otherwise, either $\bar{N} = 0$ or the problem is stuck at an infeasible solution. In both cases, the previous choice is the best available one ($\bar{N}_{opt} = \bar{N}(i - 1)$), then stage B is initiated.
6. Calculate the difference in the net profit, if this difference is positive, we skip to step (7); this means that tightening the DNC improves the net profit. On the other hand, if the difference is negative, then the previous solution provides the maximum net profit, and set ($\bar{N}_{opt} = \bar{N}(i - 1)$) then skip to stage B (go to step 8).
7. Tighten the DNC constraints as follows: $\bar{N}(i) = \bar{N}(i) - 1$, update the constraints set ψ_{ij} , then jump to step (2)

Stage B (spotting max optimal \overline{DOD}_{opt})

8. Set the MPC constraints at $\psi = (\bar{N}_{opt}, \overline{DOD}_{max})$, back to step (2).
9. If this is the first j^{th} iteration, then skip to step (12), otherwise continue.
10. If the problem is feasible, and $j \leq j_{max}$ ($j_{max} = \frac{\overline{DOD}_{max} - \overline{DOD}_{min}}{\alpha}$, where α is the \overline{DOD} search sensitivity (resolution)), go to step (11). Otherwise, the algorithm reached $\overline{DOD} = \overline{DOD}_{min}$ or it is stuck at an infeasible solution and, in both cases, the previous choice is the best available one ($\overline{DOD}_{opt} = \overline{DOD}(j - 1)$) and ψ_{opt} is reached.

11. Calculate the difference in the net profit, if this difference is positive, skip to step (12); this means that tightening the DOD improves the net profit. On the other hand, if the difference is negative, then the previous solution provides the maximum net profit and $(\overline{DOD}_{opt} = \overline{DOD}(j - 1))$ is set. Accordingly, $t \psi_{opt}$ is reached.
12. Tighten the DOD constraints as follows: $(\overline{DOD}(j) = \overline{DOD}(j - 1) - \alpha)$. α -choice is considered a tradeoff between the computational effort and the accuracy of reaching the optimal value (e.g., the smaller the α , the more precise \overline{DOD}_{opt} but with a higher number of iterations). Update the constraints set ψ_{ij} , then jump to step (2).

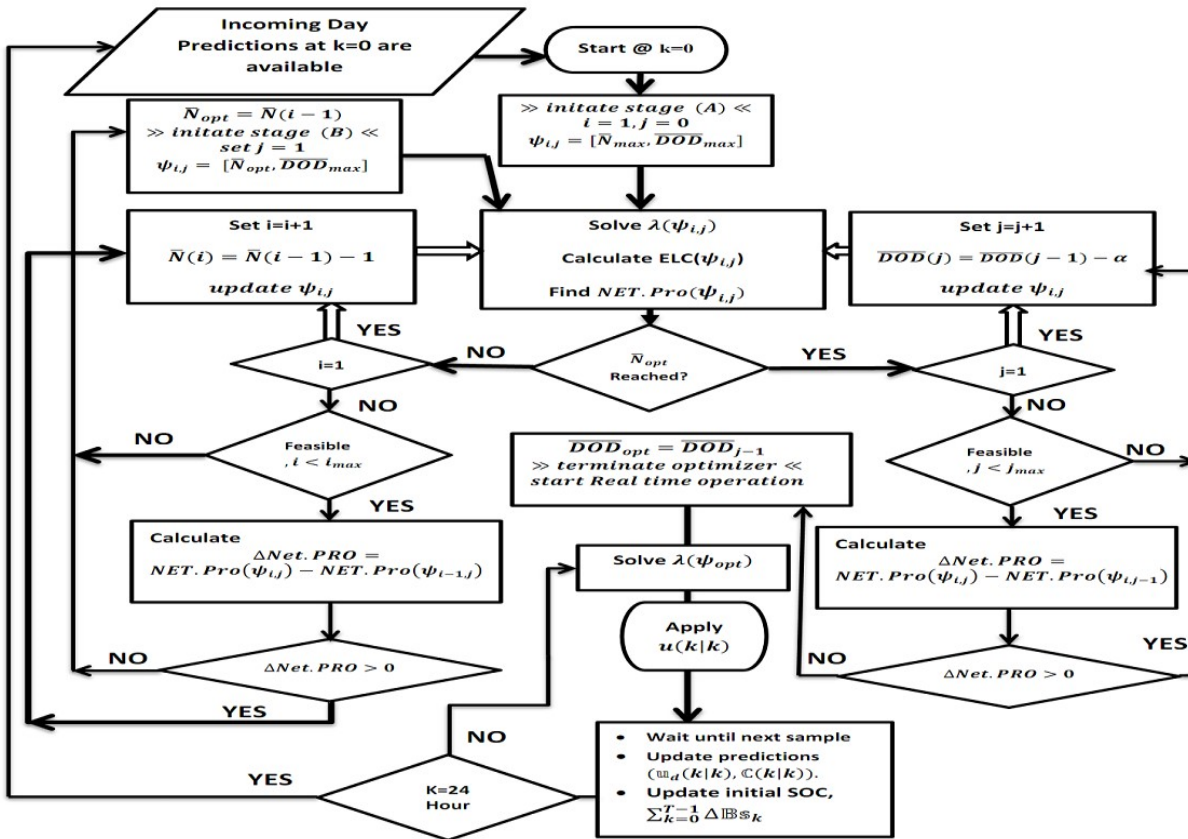


Figure 5-6 Flow chart of constraints optimizer and MPC operation.

As discussed earlier, the search for the optimal constraints is like the search for the coordinations of the set ψ_{opt} in a 2D space. Stage A represents a vertical search for \overline{N}_{opt} . While \overline{N}_{opt} is detected, Stage B is initiated by adopting a horizontal search for \overline{DOD}_{opt} . Once ψ_{opt} is reached, it is used to initiate the real-time MPC that enforces the optimal constraints $\lambda(\psi_{opt})$.

Real-Time Operation

To deal with disturbance changes (prediction error in the wind and market data), in each new sample, the MPC is applied with the pre-tuned constraints (ψ_{opt}) and the receding control policy is applied as follows. The new predictions for market and wind data are first updated; these data have less prediction error as they are short-term forecasts. At each new sample k , the prediction horizon is decided such that it finishes at the end of the day; (e.g., $n_p = \frac{24*60*60}{T_s} - K$) where T_s is in seconds. Knowing the initial number of changes from charge to discharge $\Delta\mathbb{B}s$ already done from the day start ($\sum_{k=0}^{T-1} \Delta\mathbb{B}s_k$) and the current SOC, the MPC updates its initial conditions and manages to keep the desired optimal operation (ψ_{opt}) until the end of the day ($k=24$ hr). The flowchart in Figure 5-6 explains the MPC constraints optimizer.

The optimality of the MPC constraints optimizer is guaranteed as both the ELC and gross profit are monotonically increasing functions in DNC and DOD. Thus, the resulting net profit surface (which is the difference between the ELC and gross profit) has a single maximum that can be easily detected by the proposed searching technique, without being trapped in the local optimum. Another big concern is the constraints optimizer robustness. In other words, *how much the wind and pool price prediction errors will affect the optimizer decisions*. Actually, with a reasonable prediction error (e.g., 10–15%), it is found that the optimizer has low sensitivity to such uncertainty.

5.5 Case study: Alberta Electricity Market

This study simulates a 5.0 MW WECS connected with 1.0 MW / 3.0 MWh BESS, as shown in Figure 5-1, in Alberta, Canada. The BESS rating is chosen to be 20% of the WECS power [122], the capacity is chosen to store up to the rated BESS power for up to three hours. With a series (2.135 V – 500 Ah) battery, the BESS bank consists of 562 in 5 parallel strings to get the desired rated capacity; the system has a 1200 voltage dc-link [36]. With the sample time chosen as one hour because the pool price provided by Alberta Electric System Operator (*AESO*) is the average hourly price [125]. In this work, an agreement between the market participant (system owner) and the grid operator (here; *AESO*) of updating the market predictions hourly is assumed; however, the system owner can adjust the sample time to adapt to the existing update rate of the prediction data as provided by the grid operator. At the end of the day, the system owner is paid the difference between the generation and consumption by the system operator according to each hour price.

Further, the prediction horizon (equals the control horizon) is taken for the next 24 hours. As a result, the problem λ is solved 24 times a day as long as new pool prices, wind power predictions and initial conditions are updated at each sample. The battery maximum DOD is 70% to achieve 3200 total number of cycles/life whereas the maximum DNC is set to 4 cycles/day in the constraints optimizer.

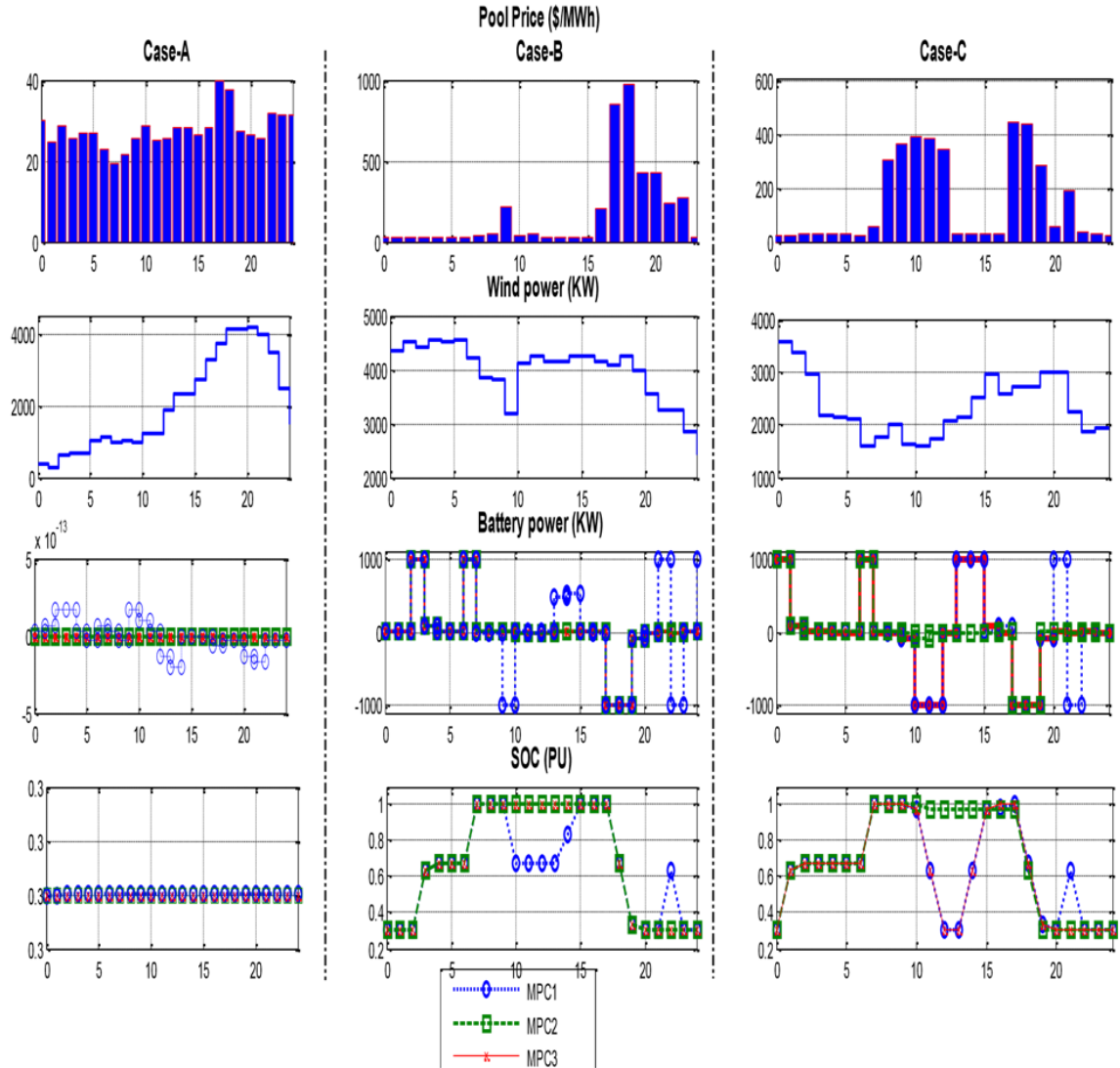


Figure 5-7 Simulation results for 3 cases (A, B, C) to evaluate three different controllers (MPC1, 2, 3).

5.5.1 Comparative Simulation Results

A comparison between three different MPC approaches used in energy management of hybrid systems is conducted to evaluate the effectiveness of the proposed algorithm:

- **MPC1:** An MPC without DNC constraints and fixed SOC constraint (e.g., same management strategy as proposed in [36] and [30]). It should be noticed that MPC1 is a modified version of the MPC in [36] as it maximizes the profit instead of

minimizing the power fluctuations; however, MPC1 has the same constraints and model as in [36].

- **MPC2:** An MPC with fixed single DNC and fixed SOC constraint (e.g., strategy used in [31]). MPC2 emulates the same energy management strategy used in [30].
- **MPC3:** The proposed MPC with constraints optimizer. The simulation is conducted on real pool price data taken from the Alberta electricity market in Canada [125]. The test data represents three days with different market patterns and their associated wind power during the second week of December 2010.

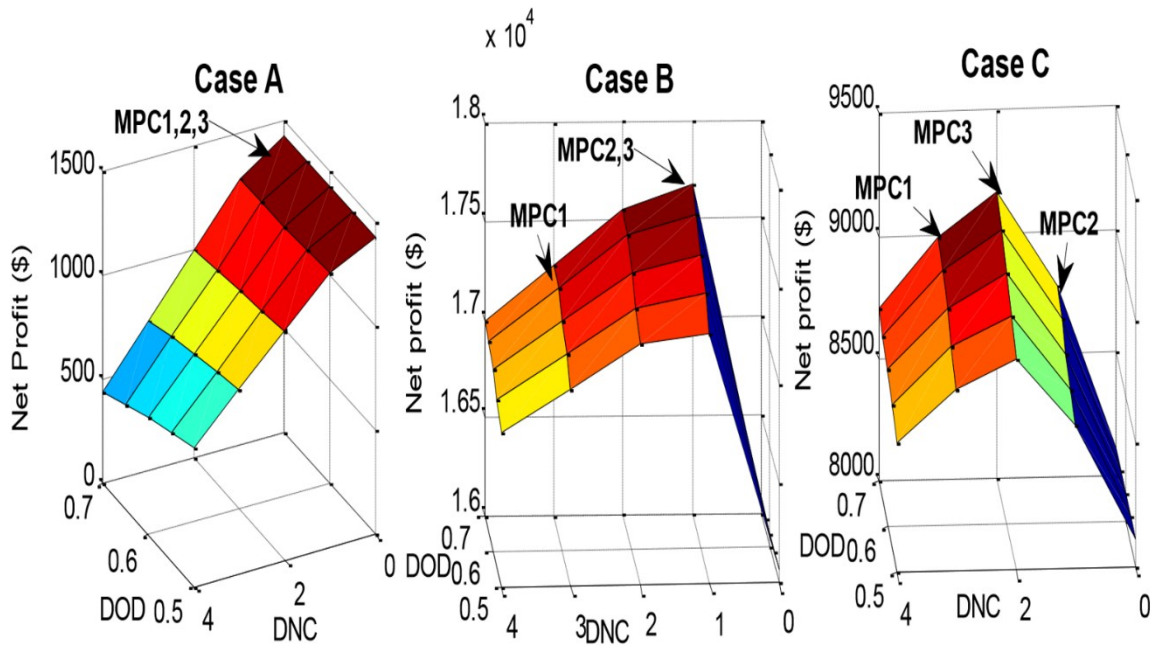


Figure 5-8 net profit change for each MPC controller in the three case studies.

Three cases are investigated to evaluate the performance of the three MPC controllers. Simulation results are shown in Figure 5-7, whereas a results summary is given in Table 5-1. All controllers respect the BESS power and SOC limits.

Table 5-1 Simulation Results.

		MPC1	MPC2	MPC3
Case A	DNC	0	0	0
	Net-profit (\$)	1,420\$	1,420\$	1,420\$
Case B	DNC	3	1	1
	Net-profit (\$)	17,276.8\$	17,678.2\$	17,678.2\$
Case C	DNC	3	1	2
	Net-profit (\$)	8,992\$	8,777.7\$	9,167\$

Case A: This case represents a flat market profile with a low maximum to minimum pool price ratio. The performance of all controllers is the same in this case.

All controllers have decided to stop BESS operation (DNC=0) as the market revenue cannot cover the operation cost.

Case B: This case represents a single-peak market pattern; however, there is a smaller peak for just a single hour at $t=8$. MPC1 targets the maximum profit without considering the ELC. Thus, it charges the battery three times and achieves the minimum net profit because it has a large ELC. On the other hand, MPC2 is constrained by a maximum daily single cycle, which luckily fits that market pattern. As a result, it achieves the maximum net profit. Finally, MPC3 is manipulated by the constraints optimizer that detects the maximum net profit at a single cycle. The constraints optimizer has compared the revenue of discharging at the small peak at

$t=8$; however, the revenue does not cover the cost of the extra cycle. Thus, the optimal DNC is chosen as one.

Case C: This is a double-peak market pattern. For MPC1, blinded from the DNC cost, it detects a fake maximum profit with three cycles. On the contrary, MPC2 is limited by the maximum single cycle constraint. As a result, it reaches a local maximum profit less than the profit associated with two cycles. Finally, MPC3 is guided again by the constraints optimizer which has achieved the maximum net profit of the three controllers (4.4% greater than MPC2, 2% higher than MPC1). Figure 5-8 shows the net profit surface versus the DNC and DOD.

Considering the computational effort, the constraints optimizer computational time is suitable for the sampling time. It is found that the average iteration time for solving the MPC problem λ using MATLAB is 0.486 s on a 3.3 GHz-6 core processor; then the maximum iterations time equals $i_{max} * j_{max} * 0.486$. In our case, with $\alpha = 0.01$ and $N_{max} = 4$, the maximum time is about 136 s, which is about 4% from the sampling time.

5.5.2 Constraints Optimizer Sensitivity to Prediction Error

This study compares the behavior of the constraints optimizer to gauge its sensitivity to pool price and wind prediction errors. Two cases are compared. The first assumes a 1-hr sampled data, whereas the second case assumes the same set sampled at 15-min. The inter-samples error range is 30%, as shown in Figure 5-9.

Table 5-2 Optimizer results in two different sample times.

Net Profit	$\bar{N}= 1$	$\bar{N}= 2$	\bar{N}_{opt}
$T_s= 60 \text{ min}$	17,678\$	17,077\$	1
$T_s= 15 \text{ min}$	17,409\$	16,836\$	1

Figure 5-9 shows that, even with such a big difference in the data set, both cases have the same number of cycles. This is also supported by the results in Table 5-2, which shows that the optimizer has considered the same maximum DNC in both cases (which is one). Because the net profit has decreased (when \bar{N} moved from one to two), \bar{N}_{opt} is found to be one in both cases. Thus, the optimizer shows low sensitivity to such a prediction error.

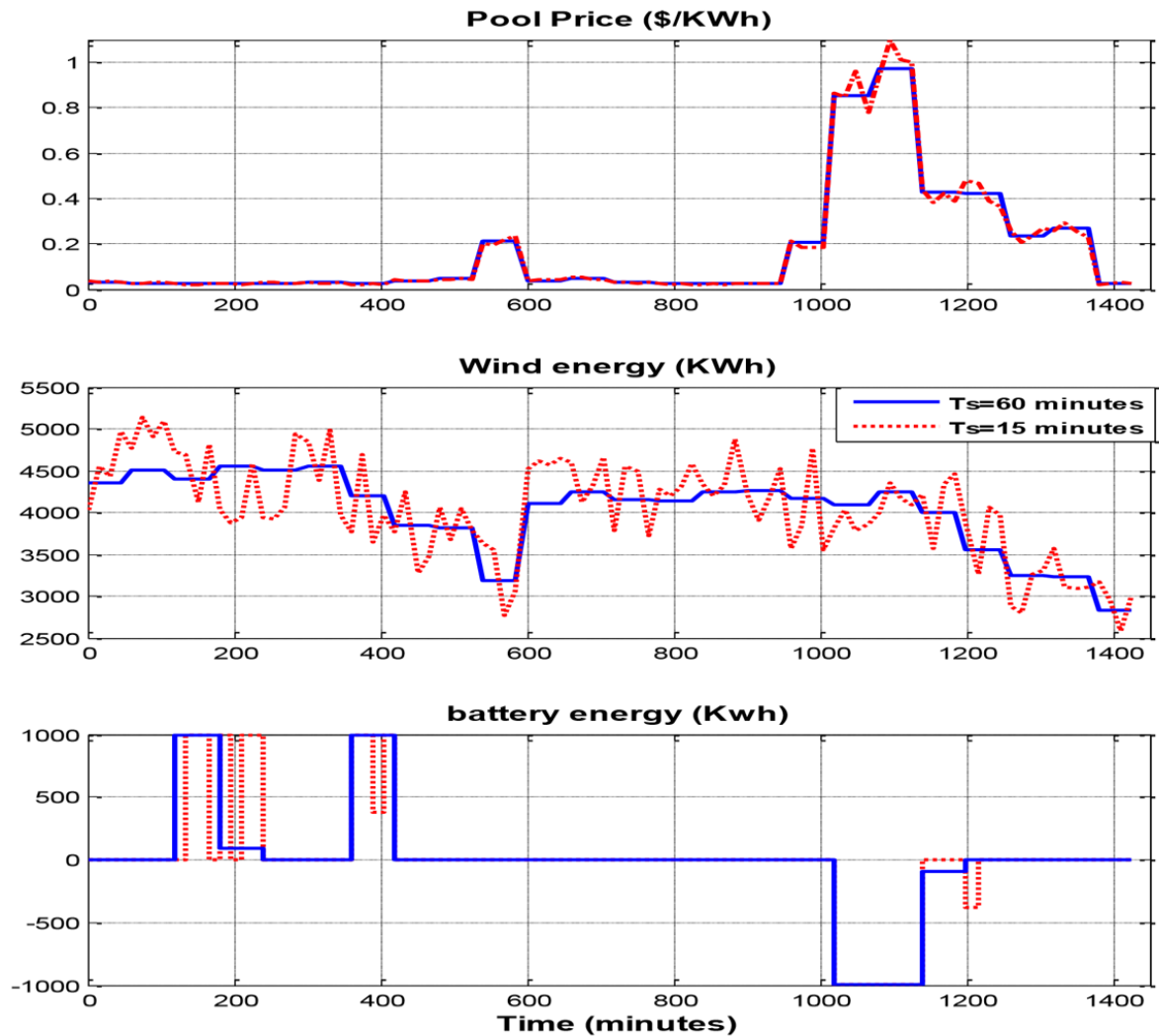


Figure 5-9 Optimizer results at different sample times.

5.6 Conclusions

This chapter addressed the development of a comprehensive market-oriented EMS via MPC for a hybrid power system (WECS with BESS). The MPC aimed at maximizing the daily profit by dispatching the BESS. The real-time optimization process was based on receiving the market price and wind power predictions in each new sample. For expanding the BESS lifetime, constraints on the power rating, the DOD and the DNC were included. The MPC constraints optimizer tightened the DNC and DOD constraints to achieve the maximum profit with the minimal expended-lifetime cost. Real wind power and market data of the Alberta province showed that the proposed MPC constraints optimizer had reached the optimal profit with the minimal sacrifices in the BESS life. Comparison with other two MPC techniques showed that the proposed MPC always managed to achieve the maximum net profit for the system owner.

Chapter 6

EMS of a Hybrid Wind – Flywheel Energy Storage System via Model Predictive Control

6.1 Introduction

The maximum power and power ramp rate are important grid codes for renewable energy resources (e.g., wind farms) in transmission systems. The RES power curtailment regulates the RES maximum power and ramp rate; however, adding an energy storage system (ESS) can time shift surplus wind energy instead of curtailing it. The flywheel energy storage system (FESS) has the advantages of high efficiency and long lifetime; however, it has non-negligible standby losses and its lifetime is reduced exponentially as the rotating speed increases. Considering such practical constraints, this chapter presents an EMS for a hybrid power system composed of a wind farm with a FESS. The FESS time shifts the surplus wind energy to respect the grid codes and reduce wind curtailment; meanwhile, the EMS aims at minimizing the FESS standby losses and boosting its lifetime using the predicted wind power data.

The proposed EMS is composed of two cascaded controllers. The first controller is a linear model predictive controller that defines the long-term FESS power set-point. The second controller is a real-time adaptive hysteresis controller that compensates for the wind power prediction error. Simulation results showed that the proposed EMS manages to minimize the losses significantly as compared to a conventional EMS. Further, a hardware-in-the-loop test is used to validate the results in a real-time environment. The contributions of this study to the research field are:

- Designing a multi-objective MPC-based algorithm that aims at maximizing the power imported from the hybrid system to the grid under typical grid code constraints while reducing FESS losses and boosting its lifetime.
- Converting the MPC optimization problem from a mixed-integer nonlinear programming (MINLP) problem into a convex one with global optimum and guaranteed feasibility; the latter is more suitable for real-time control and optimization without loss of accuracy.
- Developing an adaptive online hysteresis controller that is tuned by the MPC algorithm to compensate for the prediction error; therefore, a robust MPC optimization with robustness against prediction error is yielded.
- The proposed two-stage EMS is a multi-sample-rate algorithm that serves the optimization goals while compensating inter-samples and predictions errors.

6.2 Problem Formulation

This work aims at designing an EMS for a hybrid system composed of a large wind farm with a FESS. The hybrid system must respect the grid code regarding the maximum output power and its rate. Instead of an excessive wind curtailment, a FESS facilitates short-term storage for this energy to increase the hybrid system generation while respecting the grid code. The wind turbines are controlled via a maximum power point tracking (MPPT) algorithm to harvest the maximum wind power. Assuming an ideal MPPT and a zero pitch angle, the steady-state wind turbine power is calculated as follows [111]:

$$P_w(t) = 0.5 \eta_w \rho c_p(\lambda_o) A v_w(t)^3 \quad (6.1)$$

where $P_w, t, \eta_w, \rho, c_p, \lambda_o, A, V_w$ are the WECS harvested electrical power, time index, WECS efficiency (including shaft and gears, generator, power converter and cables efficiencies), air

density, power coefficient, optimal tip speed ratio, rotor disk area and the effective wind speed across the rotor disk, respectively.

Many transmission system operators (TSOs) demand the WECS owners to commit in advance a maximum generated power ($\bar{P}_w(t)$), with a rate ($\Delta\bar{P}_w$). This commitment is updated periodically depending on the market. For example, in Alberta-Canada, the WECS owner updates the maximum power to the TSO every 20 minutes [120]. Other markets, such as the Spanish market [30], require an advance commitment and impose a penalty as well in case of violation. The power transferred to the grid according to the grid code ($P_{gc}(t)$) is

$$P_{gc}(t) = \{P_w(t) | P_w(t) \leq \bar{P}_w(t), -\Delta\bar{P}_w \leq \Delta P_w(t) \leq \Delta\bar{P}_w\} \quad (6.2)$$

$$\Delta P_w(t) = P_w(t) - P_w(t-1) \quad (6.3)$$

As given in (6.2)-(6.3), the wind power magnitude and rate are limited by the grid code regulations [126]. The power curtailment is used to achieve this target by limiting the up-ramp rate and maximum magnitude. Extra energy is exported from the grid in case of sudden wind power drop. The curtailed power is calculated as:

$$P_c(t) = P_{gc}(t) - P_w(t) \quad (6.4)$$

An effective way to reduce $P_c(t)$ is to add a FESS. An EMS controls the FESS active power set-point as shown in Figure 6-1. A conventional EMS defines both the curtailed wind power and the FESS active power, given the wind generation as follows:

$$Max(P_g(t)) \quad (6.5)$$

$$P_g(t) = P_w(t) - P_f(t) + P_c(t) \quad (6.6)$$

$$-P_{re} \leq P_g(t) \leq \bar{P}_w(t) \quad (6.7)$$

$$-\Delta\bar{P}_w \leq \Delta P_g(t) \leq \Delta\bar{P}_w \quad (6.8)$$

$$-P_{wr} \leq P_c(t) \leq 0 \quad (6.9)$$

$$-\bar{P}_f \leq P_f(t) \leq \bar{P}_f \quad (6.10)$$

$$0 \leq SOC(t) \leq 1$$

$$SOC(t) = SOC(t-1) + \frac{P_f(t)}{\eta_f \bar{E}_f} \quad (6.11)$$

$$\bar{E}_f = 0.5J(\bar{\omega}_r^2 - \underline{\omega}_r^2) \quad (6.13)$$

where $P_g(t), \Delta P_g(t), P_{re}, P_{wr}, P_f(t), SOC(t), \eta_f, J, \bar{\omega}_r, \underline{\omega}_r$ are, respectively, the hybrid system total power exported to the grid measured at the point of common coupling (PCC) and its change; the reserve power imported from grid; the WECS rated power; the FESS output power; the FESS state of charge; the FESS overall round trip efficiency; the FESS inertia; and the FESS maximum and minimum mechanical speeds.

The problem (6.5) shows the EMS strategy that aims at hybrid system power maximization. Equation (6.6) represents the power balance equation measured at the PCC with the grid. The power exported (or imported) from or to the grid $P_g(t)$ equals the available wind power minus the curtailed wind power ($P_w(t) + P_c(t), P_c(t) \leq 0$) minus the FESS power $P_f(t)$, it is worth mentioning that the FESS has a negative and positive power during the discharge and charge modes, respectively. In the stand-by mode, the power equals zero. The grid code is embedded in constraints (6.7) and (6.8) that define the maximum system generated power and its rate, respectively. The curtailment power is constrained in (6.9) as a negative power up to the wind farm rated power P_{wr} . The FESS is represented as an integrator. It has two constraints that

represent the power limits in (6.10) and the state-of-charge (SOC) in (6.11). The SOC is the integration of the per-unit power as given in (6.12) taking into consideration the FESS efficiency η_f (including converter and cables losses), whereas (6.13) calculates the FESS rated capacity \overline{E}_f that depends on the FESS inertia (J) and the FESS maximum and minimum mechanical speeds ($\overline{\omega}_r, \underline{\omega}_r$). Problem (6.5) charges the FESS up to its limits when wind power exceeds the constraints (6.7) and (6.8). On the other hand, it fully discharges the FESS when the wind power is less than the expected value. It is a linear programming problem (LP) that can be easily solved online in a real-time fashion (with a sample time in the range of seconds); however, it does not take into consideration the following points:

- 1- minimizing the standby losses of the FESS;
- 2- utilizing the knowledge of predicted short-term wind speed in the management decisions to improve the overall hybrid system performance;
- 3- taking into consideration the FESS number of cycles as the FESS life is affected significantly by its operating speed.

This chapter presents an improved EMS that considers these points. To address these problems, a detailed model for the FESS is required.

6.2.1 FESS Model

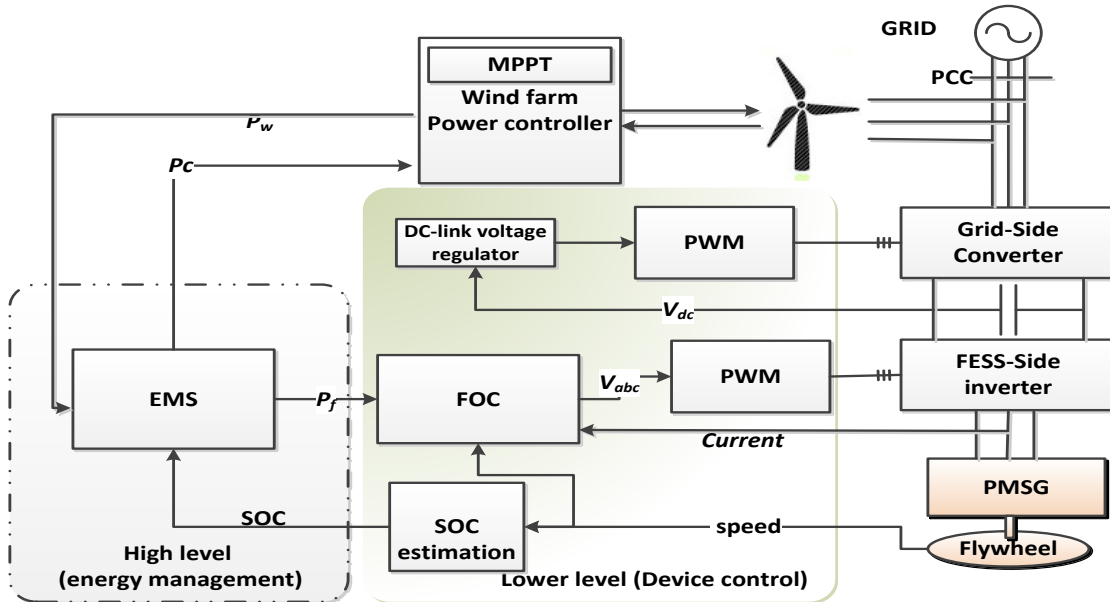


Figure 6-1 Hybrid system structure.

The storage station is composed of a number of smaller FESS units connected in parallel. There have been already commercial FESS units with up to 250-kW power and 15-min commitment time for each unit [46] (62.5 kWh). A commercial 20-MW station is already in service for frequency regulation in the PJM system [46]. In the case of wind power smoothing, the sizing of the FESS is taken no more than 10% of the WECS size [53]. As the FESS is a relatively expensive technology, a maximum 10% of WECS rating is a reasonable choice [18]. A FESS unit has a permanent-magnet synchronous machine (PMSM) with high speed. Each unit is connected via a back-to-back converter to the PCC as shown in Figure 6-1. The grid-side converter is controlled to regulate the dc-link voltage. Further, the reactive power can be controlled for voltage control at the PCC in the case of a weak grid [104]. On the other hand, the EMS defines the active power set-point for the FESS-side inverter. The FESS-side inverter is current-controlled in the dq -frame as explained in [53]. The direct-current set-point is set to

zero to reduce losses [104], while the quadrature current set-point is controlled to manipulate the electric torque as follows:

$$T_e^* = \frac{3p}{2} \frac{\psi_{pm} i_{sq}^*}{\omega_r} = \frac{P_f^*}{\omega_r} \quad (6.14)$$

where T_e , p , ψ_{pm} , i_{sq}^* , P_f^* , ω_r are the FESS electric torque set-point; PMSM number of pole pairs; PMSM flux and the stator quadrature current set-point; the FESS power set-point; and the FESS mechanical speed, respectively. The current controller is a proportional-integral (PI) controller that defines a quadrature stator voltage set-point. A pulse-width modulation (PWM) scheme embeds the voltage set-point into switching pulses for the inverter. Neglecting the fast inverter switching dynamics, the inverter acts as an amplifier with a gain equals half the dc-link voltage. Further details are given in [104]. Since this work focuses on EMS that works with a sample time in range of several seconds, all the current closed-loop dynamics is modeled as a low-pass filter [27] as expressed in (6.15).

$$I_{sq}(s) = \frac{I_{sq}^*(s)}{\tau_i s + 1} \quad (6.15)$$

where I_{sq} , s , τ_i are the stator quadrature current; Laplace transform variable; and the time-constant of the closed-loop current control dynamics. The electric torque manipulates the machine mechanical speed according to the following shaft dynamic equation [53] as given in (6.16).

$$\frac{T_e(s) - T_l(s)}{\omega_r(s)} = \frac{1}{Js + B} \quad (6.16)$$

where B , T_l are the friction and mechanical torque, respectively. The output power (P_f) is the difference between the air-gap power (P_{gab}) and the power loss (P_{loss}) [53]. It is worth

mentioning that the power loss in the FESS are mainly due the windage losses that produces a drag force proportional to the square of rotational speed. Further, eddy currents produce another drag force which is proportional to the rotational speed [55]. The hysteresis loss is neglected here as it decays exponentially with the speed [55] because current FESSs operate at very high speeds. The stator copper loss is also addressed and it depends on the quadrature current (as the direct current is zero at steady state) and the stator resistance r_s . Total power loss is stated in (6.18). A practical way to measure the losses constants c_1, c_2 can be done by a simple technique as follows; the FESS operates at different speeds, and at each operating speed, the power loss is measured in steady state (as the difference between the gap and output powers). By mapping the power loss in the desired speed domain, a simple quadratic curve fitting technique can be adopted to estimate c_1, c_2 (e.g., least square error). The power loss calculation depends on the mode of operation (standby, charging or discharging) which is modeled here by the sign of the FESS power set-point (i). If the FESS is accelerating, then the output power is reduced by P_{loss} as shown in (6.17). In the standby mode, there is still a windage loss in the machine. Finally, in the discharge mode, the output power is still reduced by the power loss. Therefore, the power flow in the FESS can be described as follows:

$$P_f = P_{gab} - iP_{loss} + (1 - i)P_{loss} \quad (6.17)$$

$$P_{loss} = c_1\omega_r^2 + c_2\omega_r + 1.5r_s i_{sq}^2 \quad P_{gab} = T_e\omega_r \quad (6.18)$$

$$i: \begin{cases} 1, P_f^* \geq 0 \\ 0, P_f^* < 0 \end{cases} \quad (6.19)$$

The SOC is calculated using (6.20), whereas the number of charging cycle (N) is defined by (6.21). N will increase by one each time the FESS fully charges and discharge the full capacity(\bar{E}_f).

$$SOC(t) = SOC(t-1) + \frac{P_f(t)}{E_f} = \int \frac{P_f(t)}{E_f} dt \quad (6.20)$$

$$N(t) = N(t-1) + \frac{i(t) P_f(t) - (1-i(t)) P_f(t)}{2\bar{E}_f} = \int \left| \frac{P_f(t)}{2\bar{E}_f} \right| dt \quad (6.21)$$

The hybrid system model is shown in Figure 6-2.

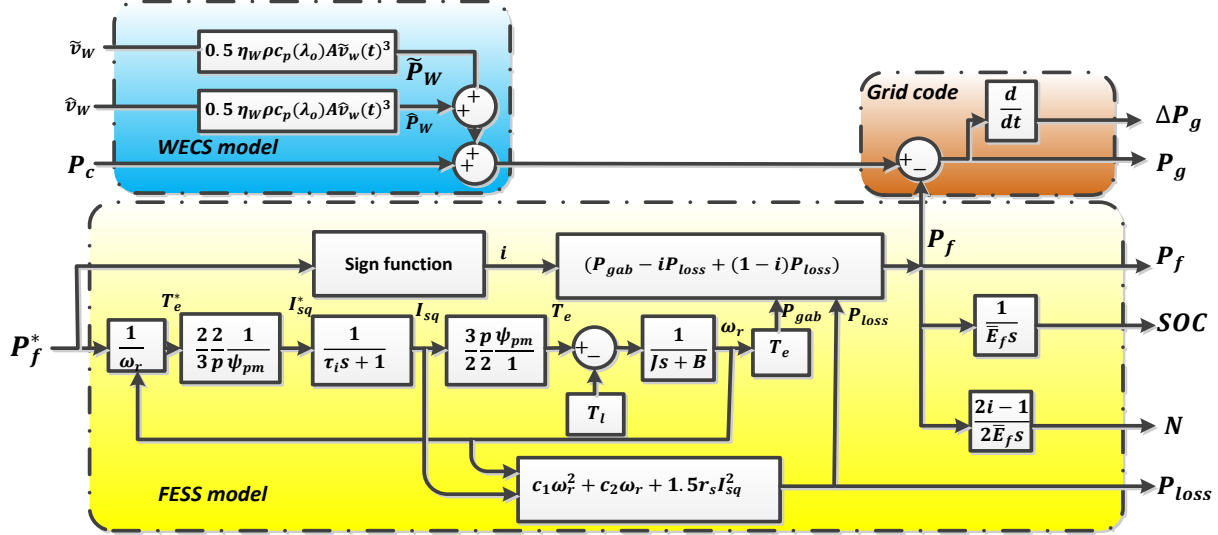


Figure 6-2 Hybrid system nonlinear model

The system can be presented as a state-space fourth-order model from (6.14)-(6.21). The control inputs are the FESS power set-point P_f^* and the curtailed wind power P_c . The expected wind speed \hat{v}_w is considered as a known forecasted input, whereas the prediction error \tilde{v}_w is an unknown disturbance. The model outputs include the grid power value and its rate, FESS output power P_f , FESS power loss P_{loss} , SOC, and N .

$$\dot{X} = F(X, i, U) \quad (6.22)$$

$$Y = H(X, i, U, U_d) \quad (6.23)$$

$$X = [i_{sq}, \omega, SOC, N]^T \quad (6.24)$$

$$U = [P_f^*, P_c] \quad (6.25)$$

$$U_d = [\tilde{v}_w] \quad (6.26)$$

$$Y = [P_g, \Delta P_g, P_f, P_{loss}, SOC, N] \quad (6.27)$$

6.2.2 The Proposed Control Structure

To utilize the knowledge of future expected wind speed \bar{v}_w , a finite-horizon model predictive controller is used to optimize the future controlled inputs P_f^*, P_c according to a certain objective function. Because the maximum wind power is updated each commitment period T_{com} , the prediction horizon is chosen as $n_p = \frac{T_{com}}{T_{s1}}$ where T_{s1} is the sampling time of the expected wind speed. T_{s1} is in the range of minutes to provide a long prediction period with low number of samples. Now, the operational control problem can be formulated as

$$\text{Min} \left(\alpha \sum_{k=1}^{n_p} P_{loss}(kT_{s1}) - \sum_{k=1}^{n_p} P_g(kT_{s1}) \right) \quad (6.28)$$

$$X(kT_{s1} + T_{s1}) = F(X(kT_{s1}), i(kT_{s1}), U(kT_{s1}), U_d(kT_{s1})) \quad (6.29)$$

$$Y(kT_{s1}) = H(X(kT_{s1}), i(kT_{s1}), U(kT_{s1}), U_d(kT_{s1})) \quad (6.30)$$

$$Y(kT_{s1}) \leq \bar{Y} \begin{cases} P_{re} \leq P_g(kT_{s1}) \leq \bar{P}_w(T_{com}) \\ -\Delta\bar{P}_w \leq \Delta P_g(kT_{s1}) \leq \Delta\bar{P}_w \\ 0 \leq SOC(kT_{s1}) \leq 1 \\ N(T_{com}) \leq \bar{n} \end{cases} \quad (6.31)$$

$$Y(kT_{s1}) \leq \bar{Y} \begin{cases} -\Delta\bar{P}_w \leq \Delta P_g(kT_{s1}) \leq \Delta\bar{P}_w \\ 0 \leq SOC(kT_{s1}) \leq 1 \\ N(T_{com}) \leq \bar{n} \end{cases} \quad (6.32)$$

$$U(kT_{s1}) \leq \bar{U} \begin{cases} -\bar{P}_f \leq P_f^*(kT_{s1}) \leq \bar{P}_f \\ -P_{wr} \leq P_c(kT_{s1}) \leq 0 \end{cases} \quad (6.33)$$

$$U(kT_{s1}) \leq \bar{U} \begin{cases} -\bar{P}_f \leq P_f^*(kT_{s1}) \leq \bar{P}_f \\ -P_{wr} \leq P_c(kT_{s1}) \leq 0 \end{cases} \quad (6.34)$$

$$v_w(kT_{s1}) \subseteq [v_w(jT_{s2}), v_w(jT_{s2} + SR)], SR = \frac{T_{s1}}{T_{s2}}, j = k \times SR \forall k \quad (6.35)$$

$$v_w(kT_{s1}) \subseteq [v_w(jT_{s2}), v_w(jT_{s2} + SR)], SR = \frac{T_{s1}}{T_{s2}}, j = k \times SR \forall k \quad (6.37)$$

The objective function given in (6.28) is a multi-objective function that maximizes the exported power to the grid under typical grid code constraints while minimizing the flywheel losses. The setting of the weight α defines the EMS inclination to power loss minimization by reducing the FESS activity or total system power generation. By increasing α , the EMS focuses more on losses minimization and vice versa as shown in Figure 6-3.

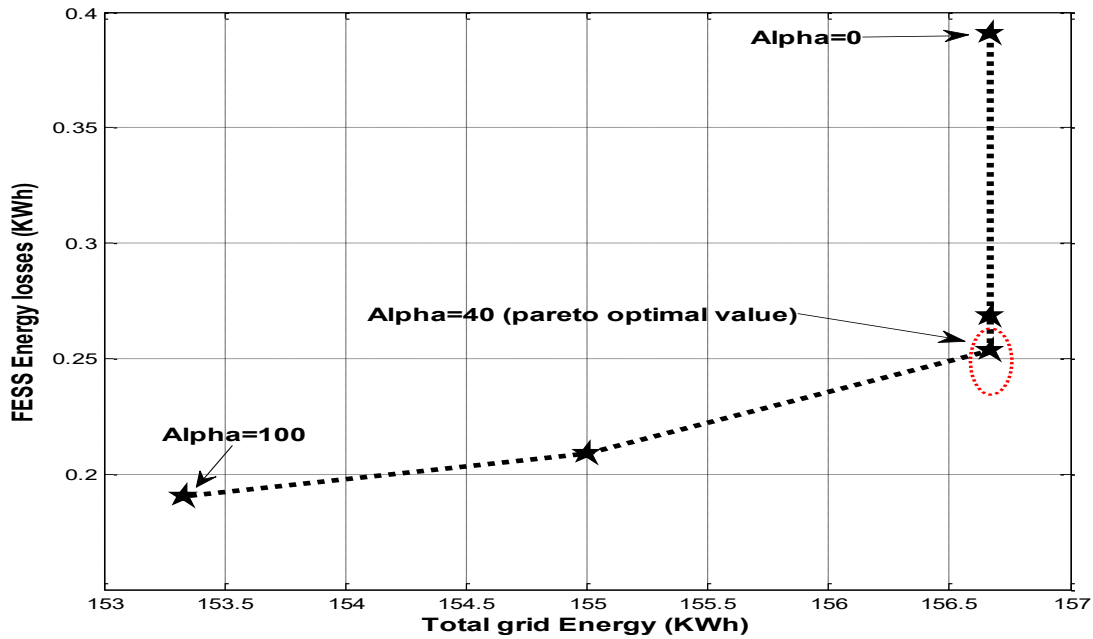


Figure 6-3 Optimization objectives at different cost function weight.

Figure 6-3 shows the relation between the energy losses in a 100 kW/6.6 kWh FESS unit and a 1.0-MW WECS for a 20-min time window. The values of $\alpha = 0$ to $\alpha = 100$ are tested with an increment of 10. The optimal value (Pareto-point) is the one that gives the minimum losses while yielding the maximum output power. This value is found as $\alpha_{op} = 40$. It is worth noting that the optimal value of α depends on the expected wind power during the incoming horizon. Thus, the operator can conduct a periodic test for $\alpha, \alpha \in [\underline{\alpha}, \bar{\alpha}]$ in each commitment period T_{com} . A simple recursive search can detect the optimal weight that achieves the

maximum exported power such that the losses is minimal or $\alpha_{op} = \{\alpha \in [\underline{\alpha}, \bar{\alpha}] | \{\bar{P}_g | \underline{P}_{loss}\}\}$.

Another simpler suboptimal technique is that the operator makes a constant choice for α that reflects the operator's preferences for power minimization.

The state-space model is discretized with a sampling time T_{s1} as given in (6.29), (6.30). The inequalities (6.31)-(6.34) represent the output constraints whereas (6.35)-(6.36) are the input constraints. In (6.31), the power exported to the grid is upper bounded by the maximum WECS power committed with the grid at this time (T_{com}), and the down limit is the maximum allowed grid support in case of wind down-ramp that cannot be handled by the FESS. Equation (6.32) defines the grid code rising and falling power ramp rates. The SOC limits are given by (6.33), and the number of cycles at the end of the commitment period is given by (6.34). The FESS power constraint is expressed by (6.35). Finally, the curtailed wind power is defined as a negative power up to the rated WECS P_{wr} as given by (6.36). The optimization problem (6.28) is a nonconvex problem that is solved in this work by two model modifications. First, the nonlinear state-space model converts the optimization into a nonlinear mixed integer problem that faces feasibility problems and has no guaranteed global minimum. This problem is solved later in this chapter by converting the system into a time-variant linear model without loss of accuracy. Second, the wind speed data has a prediction error which affects the results optimality (that is why many works do not include weather forecasts in EMS decisions, e.g., [127]). Further, the predicted wind speed data is discretized using a large sample rate (e.g., 5 minutes); in reality, the wind speed changes significantly during this time window. Equation (6.37) models this change as the wind speed $v_w(kT_{s1})$ is defined as a set of wind speeds during the same time window if a smaller sample time T_{s2} is considered (e.g., 1 s). In other words, $[v_w(jT_{s2}), v_w(jT_{s2} + SR)]$ is the inter-samples wind speed set during the bigger time window

kT_{s1} , where SR is defined as the sample times ratio. Such uncertainty-related problems are addressed by a faster online adaptive hysteresis controller

6.3 The Proposed Control Algorithm

6.3.1 Hybrid System Linearization

To convert the optimization problem into a convex one suitable for online operational control, a linear state-space model is required. The nonlinear model has an integer state represented by the sign of the FESS operation mode. To obtain a linear model, the integer state is converted to a constant, and then a time-variant linearized model is driven. The integer state (i) depends on the absolute value of (P_f^*) as given in (6.19). To find a constant integer that indicates the FESS mode of operation, the following approach is proposed. It is known that the FESS is only allowed to operate in the charge mode when the wind power is greater than the maximum allowable power. On the contrary, the FESS is allowed to operate in the discharge mode when the expected generated wind power is below the maximum grid power. As a result, the relation between the expected wind power and the maximum one (both known for the incoming horizon) gives a sufficient relation to identify the FESS operating mode, and in such a case, the integer variable i is generated as in (6.38). equation (6.38) models the FESS state as a charging when the expected wind power is higher than the maximum power, and vice versa.

$$i(t): \begin{cases} 1, \hat{P}_w(t) \geq \bar{P}_w(t) \\ 0, P_w(t) < \bar{P}_w(t) \end{cases} \quad (6.38)$$

Now, a linear model of (6.22) and (6.23) can be reached by linearizing the power loss relation in (6.18). The system identification technique is adopted for this purpose because it is practical, reliable and accurate modeling method [128].

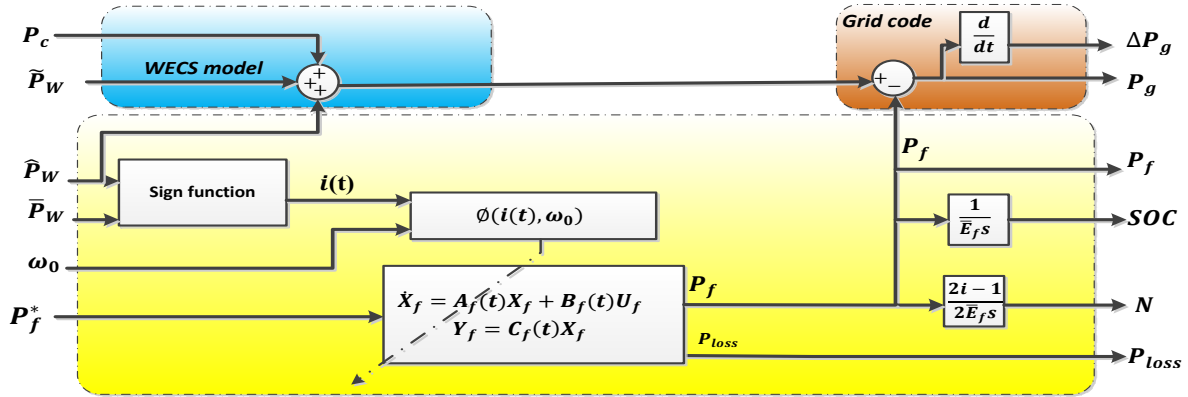


Figure 6-4 Hybrid system time-variant linearized model.

The system identification process is implemented by exciting the system using a time-series consisting of two thousand random inputs with a magnitude between the maximum and minimum FESS power $P_f^* \in [-\bar{P}_f, \bar{P}_f]$. Because the EMS dynamics is in the range of minutes, a sample-time of one second is used in the identification process. The identification data set is divided into training data (70% of the data set), and system validation data (30% of the data set) [128]. The identification process is repeated at different initial FESS speeds ω_0 to derive different models. It is found that the dc-gain of the linearized system transfer-function changes in these models; however, the system dynamics (poles and zeros) are the same; this finding makes sense because the model has static nonlinearities in the output (Wiener model) [31]. Thus, the power loss can be easily determined by tuning the model gain as a function of the initial FESS speed.

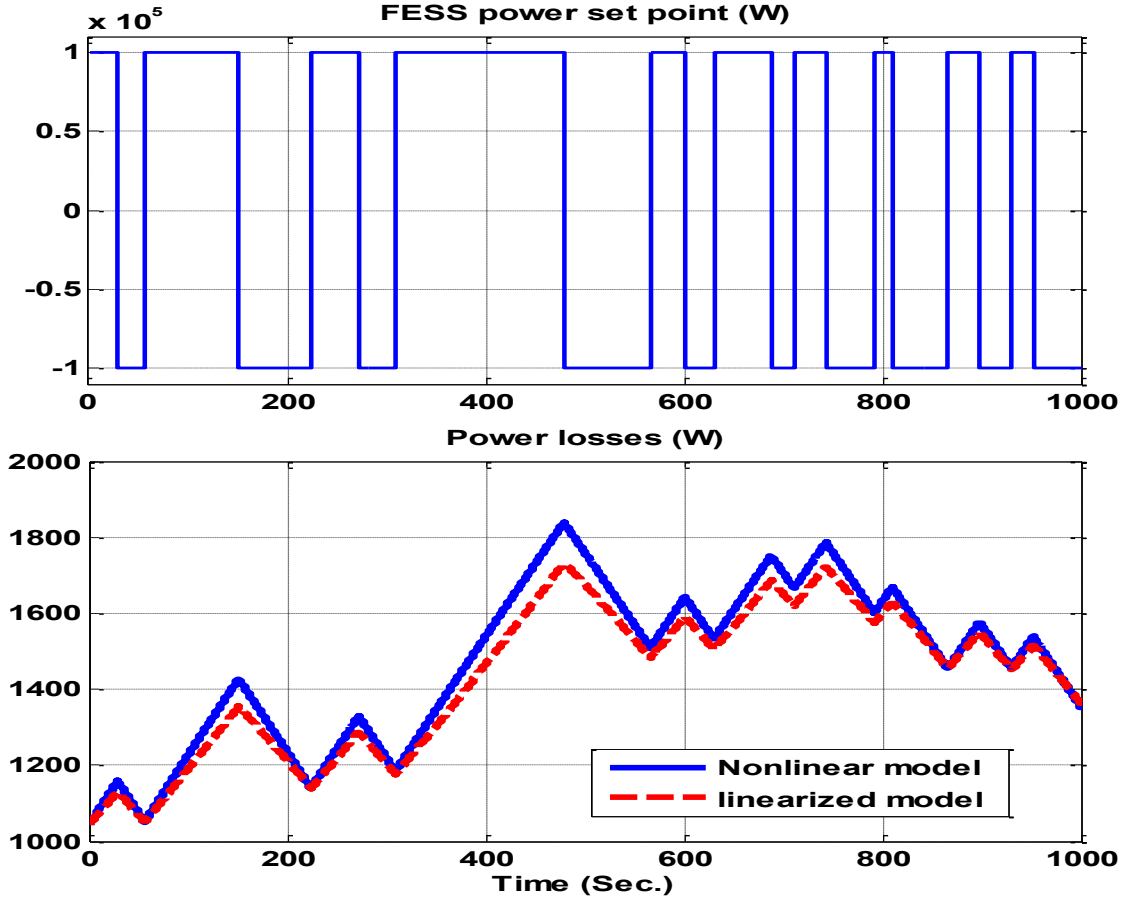


Figure 6-5 Linearized model performance.

The FESS resulting system can be easily formulated as a time-variant linear model that depends on ω_0 and i values as in (6.39)-(6.43).

$$P_{gc}(t) = P_c(t) + P_w(t) \quad (6.39)$$

$$\dot{X}_f = A_f(t)X_f + B_f(t)U_f \quad (6.40)$$

$$Y_f = C_f(t)X_f \quad (6.41)$$

$$\{A_f, B_f, C_f\}(t) = \Phi(i(t), \omega_0) \quad (6.42)$$

$$U_f = P_f^* \quad Y_f = [P_f \ P_{loss}] \quad (6.43)$$

where \emptyset is a look-up table array that generates the system linearized model depending on the mode of operation and initial speed. By considering the wind power instead of the wind speed, the overall system can be expressed as a linear model as shown in Figure 6-4. By comparing different identification models performances, it is found that a third-order model gives the best fitting with a fitting accuracy of 93.1%. Figure 6-5 compares the results of the linearized model (6.40) and the nonlinear model (6.22). After augmenting the other linear states with the linearized FESS model, a complete state-space model is reached.

The linearized model converts the MPC into a convex problem as shown by (6.44). First, given the expected and maximum WECS power, n_p linearized models are calculated for each sample in the coming horizon as shown by (6.45), (6.46). Further, the prediction error is assumed zero as this error is compensated by a faster controller that will be explained later. Because the MPC control action compensates for the expected disturbance \hat{P}_w , the generated MPC set-points are designated as follows $\hat{U} = [\hat{P}_f^*, \hat{P}_c]$. Further modifications for the input constraints are also considered, where the curtailment is only allowed if the expected WECS power is greater than the maximum as given by (6.54). The FESS is allowed to charge in case of over maximum WECS power and vice versa; however, it can operate in the standby mode in both cases as expressed in (6.51),(6.52).

$$\text{Min}_{\hat{P}_f^*, \hat{P}_c} (\alpha \sum_{k=1}^{n_p} P_{loss}(kT_{s1}) - \sum_{k=1}^{n_p} P_g(kT_{s1})) \quad (6.44)$$

$$X(kT_{s1} + T_{s1}) = A(kT_{s1})X(kT_{s1}) + B(kT_{s1})U(kT_{s1}) \quad (6.45)$$

$$Y(kT_{s1}) = C(kT_{s1})X(kT_{s1}) + DU(kT_{s1}) \quad (6.46)$$

$$Y(kT_{s1}) \leq \bar{Y} \begin{cases} P_{gs} \leq P_g(kT_{s1}) \leq \bar{P}_w(T_{com}) \\ -\Delta\bar{P}_w \leq \Delta P_g(kT_{s1}) \leq \Delta\bar{P}_w \\ 0 \leq SOC(kT_{s1}) \leq 1 \\ N(T_{com}) \leq \bar{n} \end{cases} \quad (6.47)$$

$$- \Delta \bar{P}_w \leq \Delta P_g(kT_{s1}) \leq \Delta \bar{P}_w \quad (6.48)$$

$$0 \leq SOC(kT_{s1}) \leq 1 \quad (6.49)$$

$$N(T_{com}) \leq \bar{n} \quad (6.50)$$

$$\hat{U}(kT_{s1}) \leq \bar{U} \begin{cases} -\bar{P}_f(1 - i(kT_{s1})) \leq \hat{P}_f^*(kT_{s1}) \leq \bar{P}_f i(kT_{s1}) \\ -P_r i(kT_{s1}) \leq \hat{P}_c(kT_{s1}) \leq 0 \end{cases} \quad (6.51)$$

$$-P_r i(kT_{s1}) \leq \hat{P}_c(kT_{s1}) \leq 0 \quad (6.52)$$

6.3.2 Adaptive Hysteresis Controller (AHC)

For prediction and WECS inter-samples error compensation, a change in the control action $\Delta U(jT_{s2}) = [\Delta P_f^*, \Delta P_c]$ is required. Adaptive control for an ESS was discussed before in [34] for distributed storage of a dc microgrid to achieve SOC balance. The adaption was applied for the droop coefficients. In this study, an additive corrective control action is proposed. This update in the control action is generated by the AHC; however, as this controller works with a faster sampling rate, it may affect the original MPC constraints and optimal solution. To overcome this problem, the condition (6.54) must be fulfilled.

$$U(jT_{s2}) = \begin{bmatrix} P_f^*(jT_{s2}) \\ P_c(jT_{s2}) \end{bmatrix} = \hat{U}(kT_{s1}) + \Delta U(jT_{s2}) = \begin{bmatrix} \hat{P}_f^*(kT_{s1}) \\ \hat{P}_c^*(kT_{s1}) \end{bmatrix} + \begin{bmatrix} \Delta P_f^*(jT_{s2}) \\ \Delta P_c^*(jT_{s2}) \end{bmatrix} \quad (6.53)$$

$$s.t. Y(jT_{s2}) \in [Y(kT_{s1}), Y((k+1)T_{s1})] \in HYS, k = \frac{j}{SR} \quad (6.54)$$

As given in (6.53), the final control action consists of two parts: the main part is from the MPC long-term controller $\hat{U}(kT_{s1})$, and the second part is a compensation for WECS

prediction error generated by AHC $\Delta U(jT_{s2})$. In case the compensation error is zero, the condition (6.54) is always satisfied, and the AHC generates zero.

Condition (6.54) guarantees that the AHC correction will not significantly change the outputs of process, since the outputs at any intersample jT_{s2} should be located between the previous and next value as expected by the MPC problem (6.44) known here as the hysteresis limits. For example, at $jT_{s2} = 630$ s ($T_{s2} = 1$ s), the AHC can produce a control action such that the current outputs are within the MPC hysteresis values; $Y(jT_{s2}) \in [Y(10T_{s1}), Y(11T_{s1})]$, $T_{s1} = 1$ min. If this is not the case, then a different control action is required to bring the current output within the hysteresis limits again as will be explained later. It is worth mentioning that the hysteresis can be given some flexibility which means that the output can diverge slightly from the optimal solution given by the MPC. This is possible by modifying the condition (6.54) to be as follows:

$$Y(jT_{s2}) \in [Y(kT_{s1}) - \lambda, Y((k+1)T_{s1}) + \lambda] \in HYS(kT_{s1}) \quad (6.55)$$

As noticed, the output is allowed to diverge outside the optimal MPC solution by a tolerance (λ). The next step is how to design the AHC that guarantees that $Y \in HYS$. This section is composed of two parts. First, Section 6.3.3 investigates different uncertainty modes and how $\Delta U(jT_{s2})$ is calculated. Second, Section 6.3.4 discusses how the AHC satisfies the MPC constraints by fulfilling (6.54).

6.3.3 Uncertainty Modes

The actual wind power can have six different positions, defined here as six modes if compared to the expected value of wind power $P_w(t)$ and the maximum wind power $\bar{P}_w(t)$ as shown in Figure 6-6.

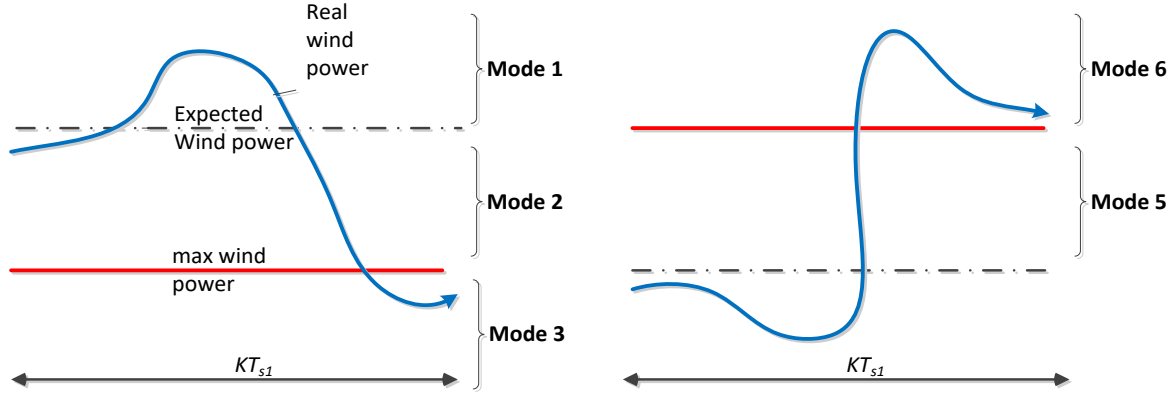


Figure 6-6 Relation of actual wind power with expected, maximum power.

In the first mode (M1), the real wind power P_w is greater than the expected wind power \hat{P}_w and the maximum wind power \bar{P}_w . In such a case, the extra wind power (e.g. the prediction error \tilde{P}_w) is stored in the FESS, as described by (6.56).

$$M = \{M1 \forall P_w(jT_{s2}) > \hat{P}_w(KT_{s1}) > \bar{P}_w(KT_{s1})\} \quad (6.56)$$

$$\Delta P_{f1}^*(jT_{s2}) = \tilde{P}_w(jT_{s2}) = P_w(jT_{s2}) - \hat{P}_w(KT_{s1})$$

In the second mode (M2), the real wind power is less than the expected wind power but it is still greater than the maximum wind power. In such a case, the FESS is required to be charged to a level less than the nominal value. If the difference between the real wind power and the maximum wind power is less than the nominal FESS set-point, then a reduction in the charge power is required. This process is described by (6.57).

$$M = \{M2 \forall \bar{P}_w(KT_{s1}) < P_w(jT_{s2}) < \hat{P}_w(KT_{s1})\} \quad (6.57)$$

$$\Delta P_{f2}^*(jT_{s1}) = \left(\tilde{P}_w(jT_{s2}) \middle| \hat{P}_f^*(KT_{s1}) > \bar{P}_w(KT_{s1}) - P_w(jT_{s2}) \right)$$

In the third mode (M3), the real wind power is less than the expected wind power and the maximum wind power. In such a case, the FESS is required to change from the charge to

discharge mode till the total hybrid system power is maximum. This process is described by (6.58).

$$\begin{aligned} M &= \{M3 \forall P_w(KT_{s1}) < \bar{P}_w(KT_{s1}) < \hat{P}_w(KT_{s1})\} \\ \Delta P_{f3}^*(jT_{s2}) &= -\hat{P}_f^*(kT_{s1}) - [\bar{P}_w(KT_{s1}) - P_w(jT_{s2})] \end{aligned} \quad (6.58)$$

In the fourth mode (M4), the real wind power is less than the expected wind power and the maximum wind power. In this case, the expected wind power is less than the maximum wind power. Thus, the FESS is in the discharge mode. In M4, The FESS can discharge more till the hybrid system power reaches its maximum. This process is described by (6.59).

$$\begin{aligned} M &= \{M4 \forall P_w(jT_{s2}) < \hat{P}_w(KT_{s1}) < \bar{P}_w(KT_{s1})\} \\ \Delta P_{f4}^*(KT_{s2}) &= \tilde{P}_w(jT_{s2}) \end{aligned} \quad (6.59)$$

In the fifth mode (M5), the real wind power is less than the maximum wind power but more than the expected wind power. In this case, the expected wind power is less than the maximum wind power. Thus, the FESS is in the discharge mode. In M5, The FESS can discharge less till the hybrid system power reaches its maximum. This process is described by (6.60).

$$\begin{aligned} M &= \{M5 \forall \hat{P}_w(KT_{s1}) < P_w(jT_{s2}) < \bar{P}_w(KT_{s1})\} \\ \Delta P_{f5}^*(jT_{s2}) &= \left(\tilde{P}_w(jT_{s2}) \middle| P_f^*(KT_{s1}) < \bar{P}_w(KT_{s1}) - P_w(jT_{s2}) \right) \end{aligned} \quad (6.60)$$

Finally, in the sixth mode (M6), the real wind power is more than both the maximum and expected wind powers. In this case, the expected wind power is less than the maximum wind power. Thus, the FESS is in the discharge mode. In M6, the FESS changes its mode to charge the extra wind power. This process is described by (6.61).

$$\begin{aligned} M &= \{M6 \forall P_w(jT_{s2}) > \hat{P}_w(KT_{s1}) > \bar{P}_w(KT_{s1})\} \\ \Delta P_{f6}^*(jT_{s2}) &= [P_w(jT_{s2}) - \bar{P}_w(KT_{s1})] - P_f^*(KT_{s1}) \end{aligned} \quad (6.61)$$

6.3.4 The Two-stage Controller

Only one of modes (6.56)-(6.61) is enabled at any time. The total FESS is calculated and limited by the FESS thermal limit in (6.35). However, ΔP_f^* may lead to undesired changes in the controlled outputs Y . It is very important to make sure that the outputs will be within the predefined limits determined by the MPC controller to guarantee optimum solution. Generally speaking, the outputs change $\Delta Y(jT_{s2})$ due to the AHC correction $\Delta P_f^*(jT_{s2})$ at steady-state depends on the system dc gain $\mathbb{H}(kT_{s1})$ as in (6.63) which depends on the linearized FESS model.

$$\Delta Y(jT_{s2}) = \mathbb{H}(kT_{s1})\Delta P_f^*(jT_{s2}) \quad (6.62)$$

$$\mathbb{H}(kT_{s1}) = \lim_{z \rightarrow 1} D(kT_{s1}) + C(kT_{s1})(zI - A(kT_{s1}))^{-1} B(kT_{s1}) \quad (6.63)$$

where A , B , C and D are extracted from (6.42), assuming zero disturbance and I is a unity matrix. The AHC applies the following rule to guarantee overall system operation within MPC optimal constraints:

$$\begin{cases} Y(KT_{s1}) + \Delta Y(jT_{s2}) > HYS: \{P_f(jT_{s2}) = \hat{P}_f^*(kT_{s1}) \\ Y(KT_{s1}) + \Delta Y(jT_{s2}) \in HYS: \{P_f(jT_{s2}) = \hat{P}_f^*(kT_{s1}) + \Delta P_f^*(jT_{s2}) \forall \mathbb{H} \\ Y(KT_{s1}) + \Delta Y(jT_{s2}) < HYS: \{P_f(jT_{s2}) = \hat{P}_f^*(kT_{s1}), \mathbb{H} < 0 \end{cases} \quad (6.64)$$

The control law (6.64) means that the compensating control action $\Delta P_f^*(jT_{s2})$ is applied if and only if all the resulting controlled outputs are within their allowable domain or hysteresis limit $(Y(KT_{s1}) + \Delta Y(jT_{s2})) \in HYS$ or if this control action will direct the outputs back to HYS depending the output sensitivity to this input. For example, without loss of generality, let us consider that Y is the SOC and the input is $\Delta P_f^*(jT_{s2})$ which has positive sensitivity (positive DC gain) with respect to the SOC . In case $SOC < HYS$, the allowed control action is charging to

increase the SOC. In this case, the SOC is within the allowable *HYS*, and vice versa in case of discharging.

Finally, both charging and discharging are allowed if $SOC \in HYS$. The number of cycles also has a positive sensitivity with the charging power and it follows the same rules. After the final FESS power is calculated by (6.64), the curtailed power value is used to respect the maximum grid code power given in (6.2) after replacing P_w by $P_w - P_f$. The final curtailment power is calculated as follows:

$$P_c(jT_{s2}) = P_{gc}(jT_{s2}) - [P_w(jT_{s2}) - P_f(jT_{s2})] \quad (6.65)$$

Figure 6-7 shows the proposed EMS block diagram in the two-stage control framework.

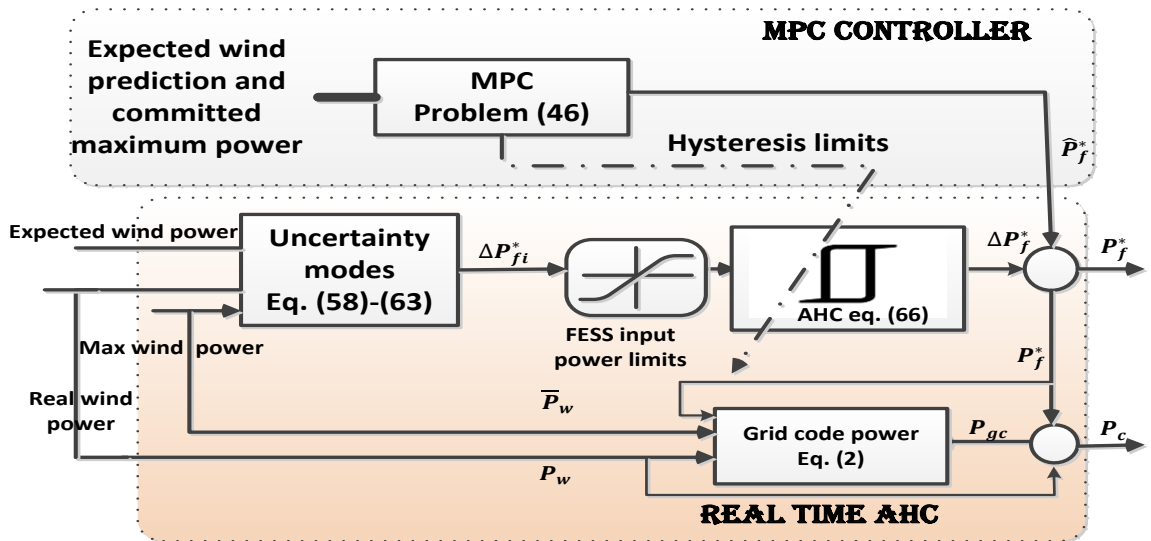


Figure 6-7 the proposed EMS structure.

6.4 Case Study

In this case study, a 150 MW wind farm is participating in the power market in the Alberta transmission system- Canada. The Alberta system operator (AESO) requires that the wind facility updates its maximum power limit every 20 minutes. Further, the ramp-rate should not exceed 10% of the rated plant power per minute [129], [120]. The prediction horizon is taken as 20 minutes (each commitment period). A typical wind speed profile is generated by TurbSim [130], a wind simulator developed by the National Renewable Energy Laboratory (NREL). A Great Plains Low-Level Jet (GP-LLJ) turbulence model is used with a mean wind speed of 7 m/s-normal turbulence intensity sampled each 6 seconds [130]. The resulting wind profile is applied on a doubly-fed induction generator-based wind farm Simulink model developed by Hydro-Quebec [131]. The resulting wind power profile represents the real wind power profile. By averaging this profile each 1 minute, the expected wind power is calculated, and this data is assumed to be known for the MPC. The prediction error is the difference between the real wind power and this averaged value. Distribution for prediction error is shown in Figure 6-8 for a data set of 400 samples. As shown in Figure 6-8, the prediction error range is about $\pm 15\%$. For the MPC, the prediction horizon is taken as $T_{s1} = 60$ s, $n_p = 20$, when the AHC works at a sample rate $T_{s2} = 6$ s.

A 15 MW/1 MWh FESS station is added to the system which is composed of 100 kW units. To enhance the lifetime of the FESS, it is only allowed to have one cycle each commitment period $\bar{N}=1$, which means 72 cycle per day. The FESS model parameters are taken from [53] with a higher inertia as shown in Table 6-1.

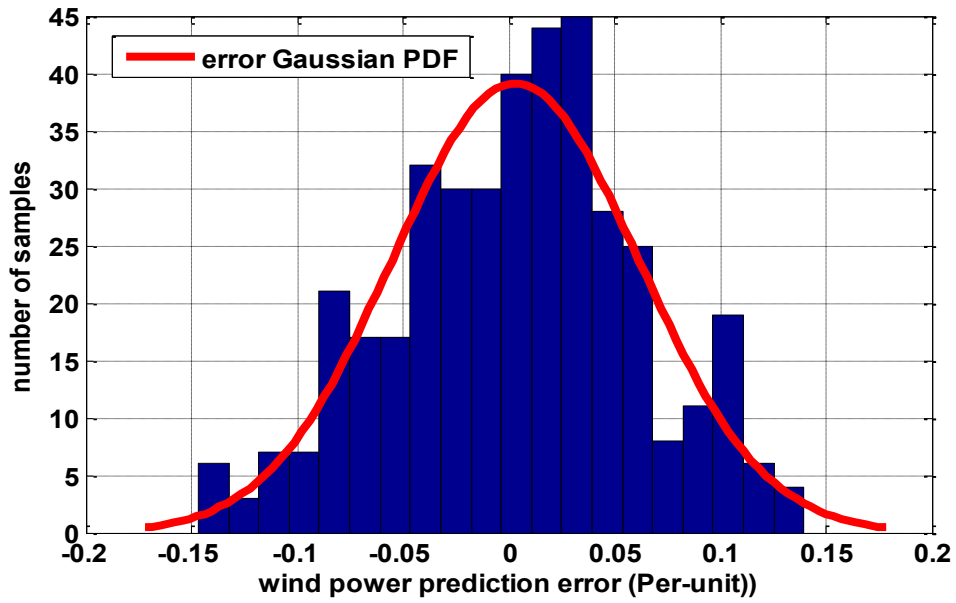


Figure 6-8 Wind power prediction error distribution.

The FESS can operate up to the charge/discharge rated power continuously for 4 minutes for providing energy coverage of 20% of the commitment period.

Table 6-1 parameters of a single FESS unit

$\bar{\omega}_r = 31 \text{ Krpm}$	$\underline{\omega}_r = 15.5 \text{ Krpm}$
$J = 6.076 \text{ Kgm}^2$	
$r_s = 8m\Omega$	
$P_r = 100 \text{ Kw}$	$c_1 = 9 \times 10^{-5} \text{ ws}^2/\text{rad}^2$
$c_2 = 0.175 \text{ ws}/\text{rad}$	

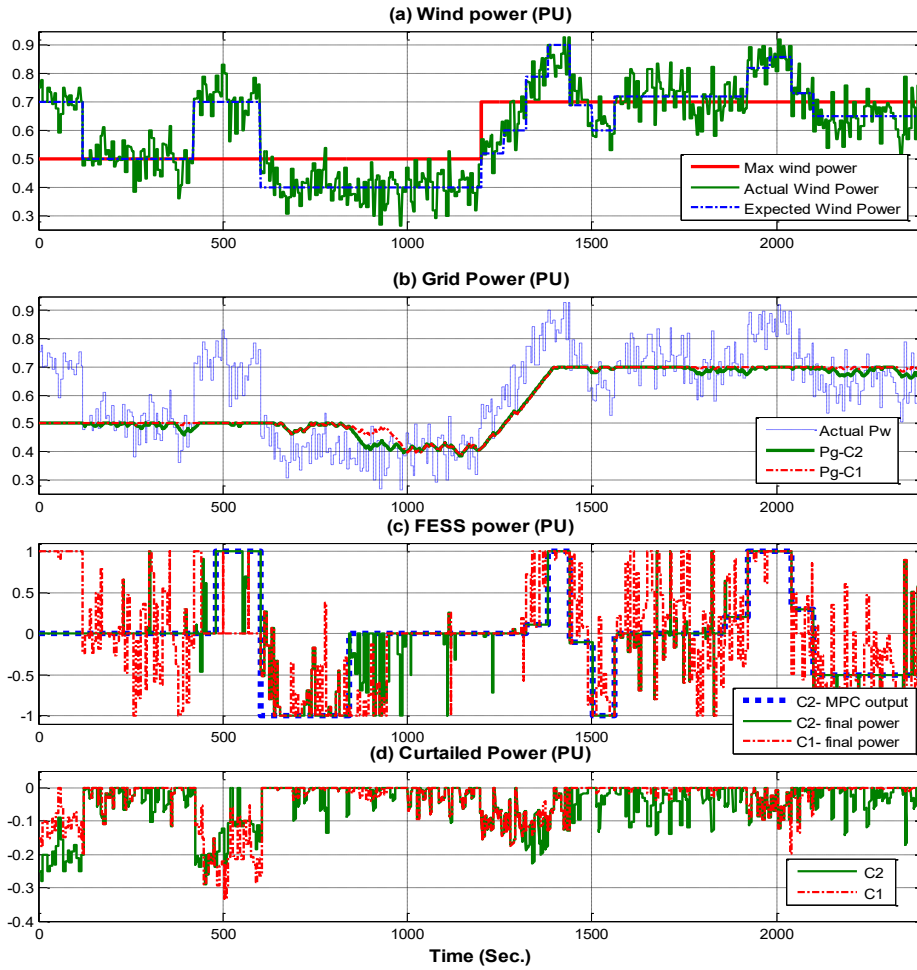


Figure 6-9 Simulation results comparing the performance of the traditional EMS (C1) and the proposed MPC-based EMS (C2).

The AHC updates its hysteresis limits from the MPC each minute and generates 10 corrections per minute. The hysteresis setting gives a tolerance $\lambda = 2\%$ for deviation from the optimal solution.

To show the advantages of the proposed MPC-based EMS, it is compared to the traditional EMS that is calculated in a real-time fashion based on the formulation in (6.5)-(6.13). Figure 6-9 shows the performance of the traditional EMS (C1) and the proposed MPC-based EMS (C2). Different powers are shown in Figure 6-9. In Figure 6-9(a), the expected wind power is plotted

by the blue dotted line whereas the maximum WECS is plotted by the red line. The simulation is conducted for two commitments periods (40 minutes), and actual wind power is measured each 6 s. It should be noted that the wind power has a high ramp rate at $t = 1200$ s which is followed by a sudden drop in power. Furthermore, in the first commitment period, the wind has two peaks exceeding the maximum, typically at $t = 0$ and 300 s. Similarly, in the second commitment period, two peaks occur at $t = 1200$ and 1800 s. The controller $C1$ has managed to maximize the power exported to the grid slightly than the controller $C2$ as shown in Figure 6-9(b) during the starting period of the commitment period; however, $C2$ decided to keep the FESS idle (standby) during this early period. The main reason for this performance is the lifetime constraints embedded in $C2$ where it aims at maximizing the power without over-acting on the FESS. Figure 6-9(c) shows that the proposed controller ($C2$) charges the FESS late at $t = 300$ s to discharge this energy back at the wind power gap at $t = 600$ s. On the other hand, the traditional controller ($C1$) keeps charging and discharging to regulate the WECS power to the maximum.

Further, this can be noted in Figure 6-9(d) which shows that the curtailed wind power is higher in ($C2$) than ($C1$) due to the higher activity of the FESS in case of $C1$. However, this difference is only 1% regarding the energy exported to the grid.

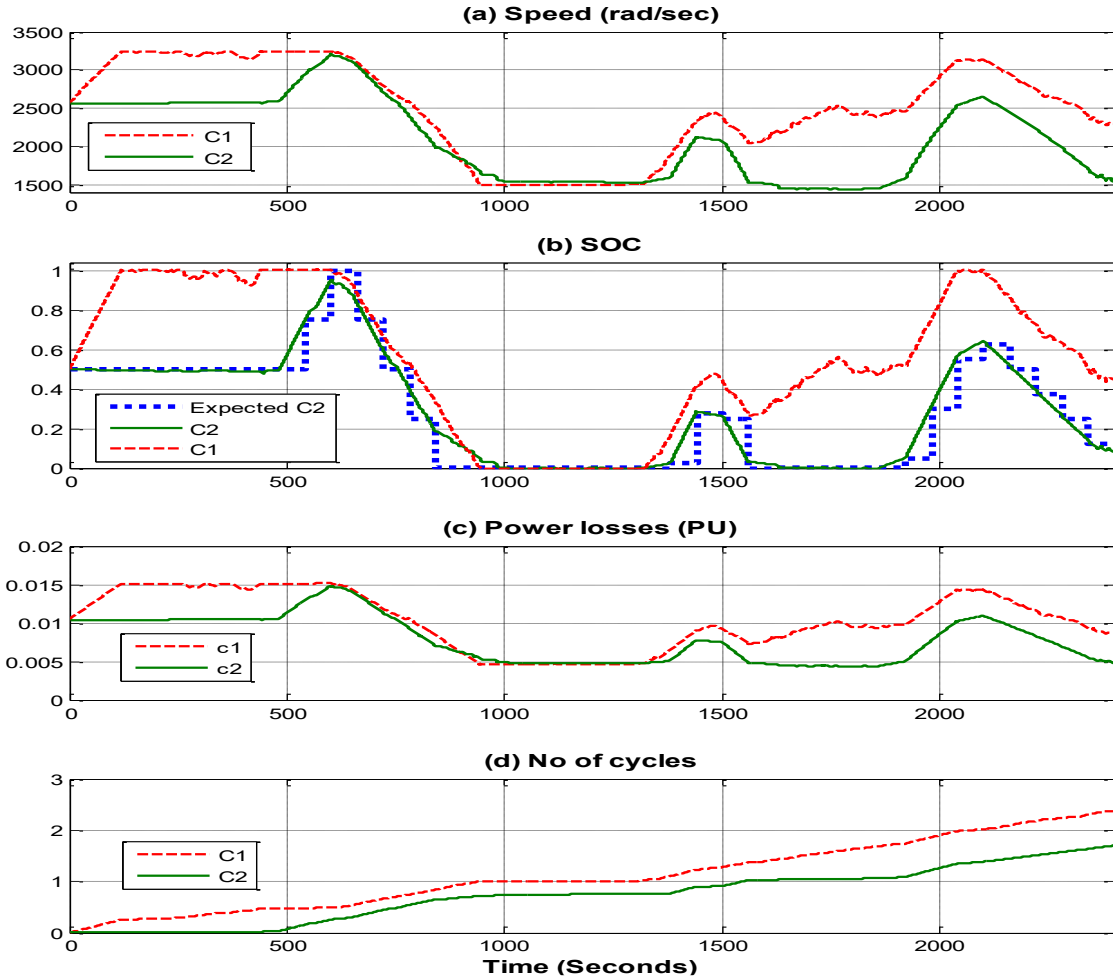


Figure 6-10 FESS internal dynamics- a comparison between (C1) and (C2).

Figure 6-10 shows the internal dynamics for the FESS in both cases. As C1 keeps operating the FESS all the time, it leads to early acceleration for the FESS (fast actuator saturation) as depicted in Figure 6-10 (a). As a result, the FESS has reached its maximum capacity earlier in C1 than C2; this is observed in Figure 6-10(b) where C1 starts charging at $t=0$, whereas C2 starts charging 500 s, later. The power loss has increased dramatically in C1 as compared to C2 as shown in Figure 6-10(c). The latter keeps the FESS in the idle mode till the second peak of the wind power. Further, the number of cycles with C1 exceeds the two cycles limit with 20% whereas C2 keeps it 20% below the limit as shown in Figure 6-10(d). A similar performance

occurs in the second commitment period when *C2* managed to pick-up the ideal charging and discharge times given the operational constraints. On the other hand, *C1* keeps operating the FESS in all cases. The energy loss has dropped from 155.7 kWh with *C1* to 117.3 kWh with *C2*. That is 24.7% reduction in the losses.

The AHC has changed the MPC power as depicted in Figure 6-9(c) according to the prediction error. The AHC is limited by output variables, such as the SOC that is depicted in Figure 6-11. For instance, in the idle periods (e.g., $t = [0, 300]$ s), no control action is allowed by the hysteresis controller to keep the SOC and N within limits. Figure 6-10 (b) shows that the AHC managed to direct the FESS SOC to follow the set-points produced by the MPC. Further, in other time periods, compensation for prediction error is allowed as shown in the period $t = [2100, 2400]$ s. To sum up, the proposed EMS managed to reduce the FESS losses and boost its lifetime while dealing with prediction errors and compensating for their effect without diverging from the optimal solution generated by the MPC algorithm.

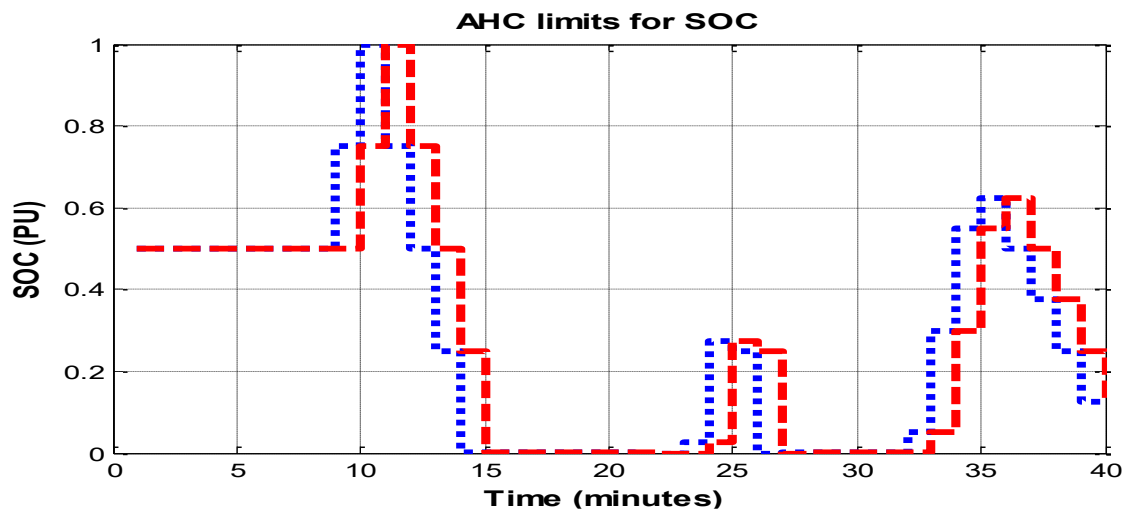


Figure 6-11 AHC limits for SOC.

6.5 Validation study

To show the effectiveness of the control algorithm and its applicability in a real-time environment, an HIL setup, for the hybrid system shown in Figure 6-2 is used. The OPAL-RT (OP 5600) real-time simulator [111] is used in this study. The simulator can adequately model different RESs and ESSs dynamics [132], [133], and [134]. Figure 6-12 shows the laboratory set-up. The HIL simulates a 1.0 MW wind farm connected with a 100 kW/0.69 kWh FESS. A lower FESS capacity is adopted to capture the significant system dynamics during a relatively short experimental period.

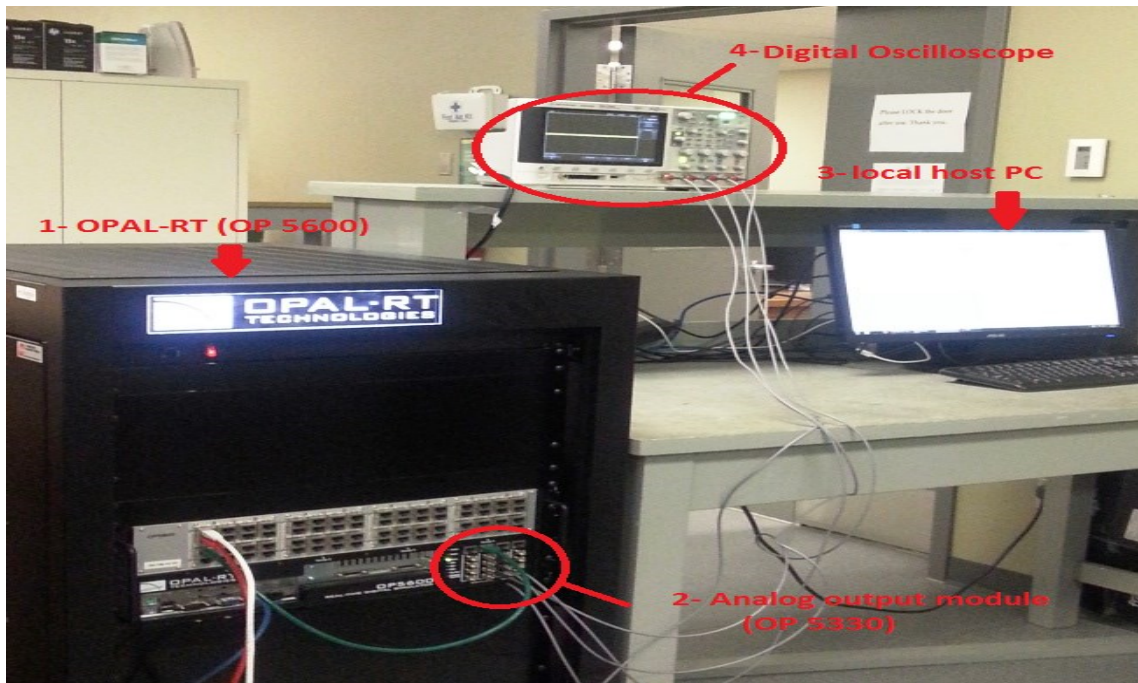


Figure 6-12 Opal-RT (OP 5600) real-time simulator set-up (1- OPAL-RT OP5600 real-time simulator, 2- analog output module OP5330, 3- local host-PC, 4- a digital oscilloscope).

The HIL test system is divided into four subsystems. The WECS is represented by the aerodynamic and the electro-mechanical models. A dedicated processor in the OPAL-RT simulator calculates the WECS power. The power is sent as an input to the controller with a

time step of 5 ms. The average power electronic converter model is used, which is very suitable for EMS studies [133]. The controller consists of two parts, the MPC, and the AHC. The MPC has a 125 s prediction horizon. The MPC optimization is solved by the Matlab solver on the local PC to fulfill the long-term optimization objectives. The MPC results are sent to the real-time simulator via a Simulink interface with the RT-LAB. The MPC results include the SOC hysteresis-limits to the AHC. Second, The AHC is solved by a dedicated master processor on the OPAL-RT with a time step of 100 ms. The AHC calculates the power set point for the FESS. The FESS is modeled on a third slave processor with a 5 ms sample rate to calculate the FESS dynamics with an average power converter model. These dynamics are used as feedback signals for the AHC and given as measurements for different interfaces, such as Simulink data sinks or digital oscilloscopes. Both the FESS and WECS dynamics are calculated in a real-time fashion due to the high processing speed of the simulator. Figure 6-13 depicts different subsystems in the HIL setup.

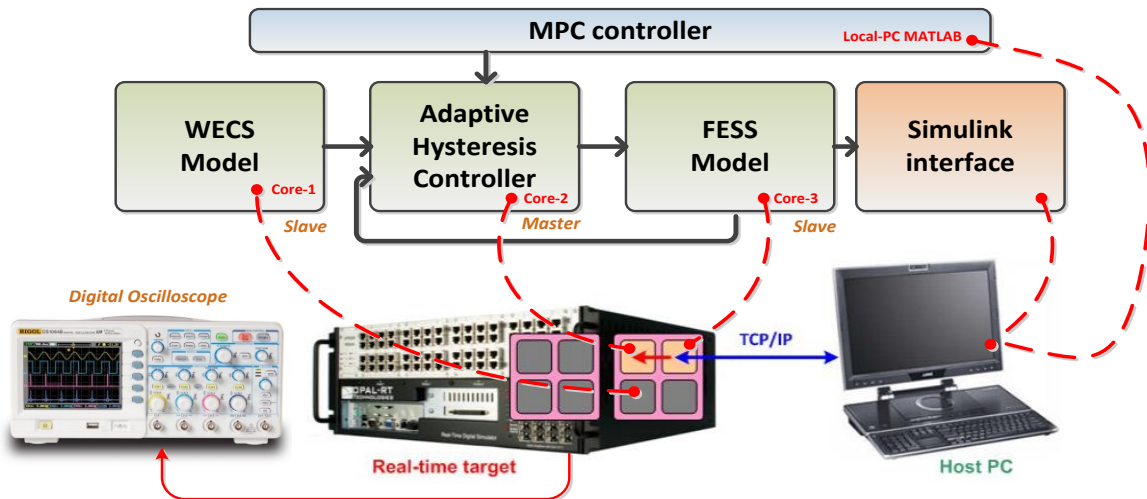


Figure 6-13 System description and different process interfaces.

The standard vector control scheme is adopted in the PMSM drive system of the FESS, which facilitates fast control characteristics over the drive system torque. The closed-loop torque response is dictated by the closed-loop current response. The system responses are measured by a four-channel digital oscilloscope (Agilent DSOX2004A). Key system variables are shown in Figure 6-14.

The wind profile generated in a 25-s period as illustrated in figure 6-14(a). The expected and maximum wind power profiles are also shown in Figure 6-14(a). The output power of the FESS is provided in Figure 6-14(b). The hysteresis limits for the SOC, which are generated by the MPC algorithm, are shown in Figure 6-14(c). The hysteresis limits are desired to be bounded between SOC_{min} , $5\% < SOC_{min} < 7\%$ and SOC_{max} , $20\% < SOC_{max} < 35\%$, which are depicted by the red and blue lines in Figure 6-14(c), respectively. The resulting real-time SOC profile is shown by the green line in Figure 6-14(c). Knowing the SOC limits and the difference between real and expected wind powers, the AHC generates the FESS power set point in real-time, which is used to generate the torque command of the PMSM drive system. The resulting FESS power loss profile is shown in Figure 6-14(d).

As shown in Figure 6-14(b), the wind power starts with a value that is less than the maximum wind power; i.e., $P_w < \bar{P}_w$. Because the initial SOC lies within the SOC limits, the AHC allows the FESS to discharge till point (0) where $P_w > \bar{P}_w$. In such a case, the AHC charges the FESS with this surplus wind power ($P_w - \bar{P}_w$). At point (1), the wind power decreases below the maximum value ($P_w < \bar{P}_w$); thus the FESS is discharged till point (2). Although $P_w < \bar{P}_w$, the AHC prevents further discharge for the FESS to stay inside the SOC limits provided by the MPC to satisfy the optimization problem in (6.44). The FESS stays in the stand-by mode until a

jump in the wind power occurs again; i.e., $P_w > \bar{P}_w$. In this case, the FESS is fully charged with this excessive wind power until it reaches point (3). Between points (3) and (4), a drop in the wind power occurs. As a result, the EMS changes the FESS mode from charge to discharge during this period. From point (4) to (5), the wind power climbs up to the maximum limit again. Thus, the FESS mode is changed by the EMS back to the charge mode. Although $P_w > \bar{P}_w$ after point (5), the AHC keeps the FESS in the stand-by mode to respect the SOC upper limit. After the upper limit is updated and the wind power drops below the maximum power as well, the FESS starts discharging again. The proposed EMS managed to track the wind power changes in real-time, while keeping the FESS dynamics within the optimal operational region provided by the MPC to minimize the FESS losses while respecting the grid integration codes.

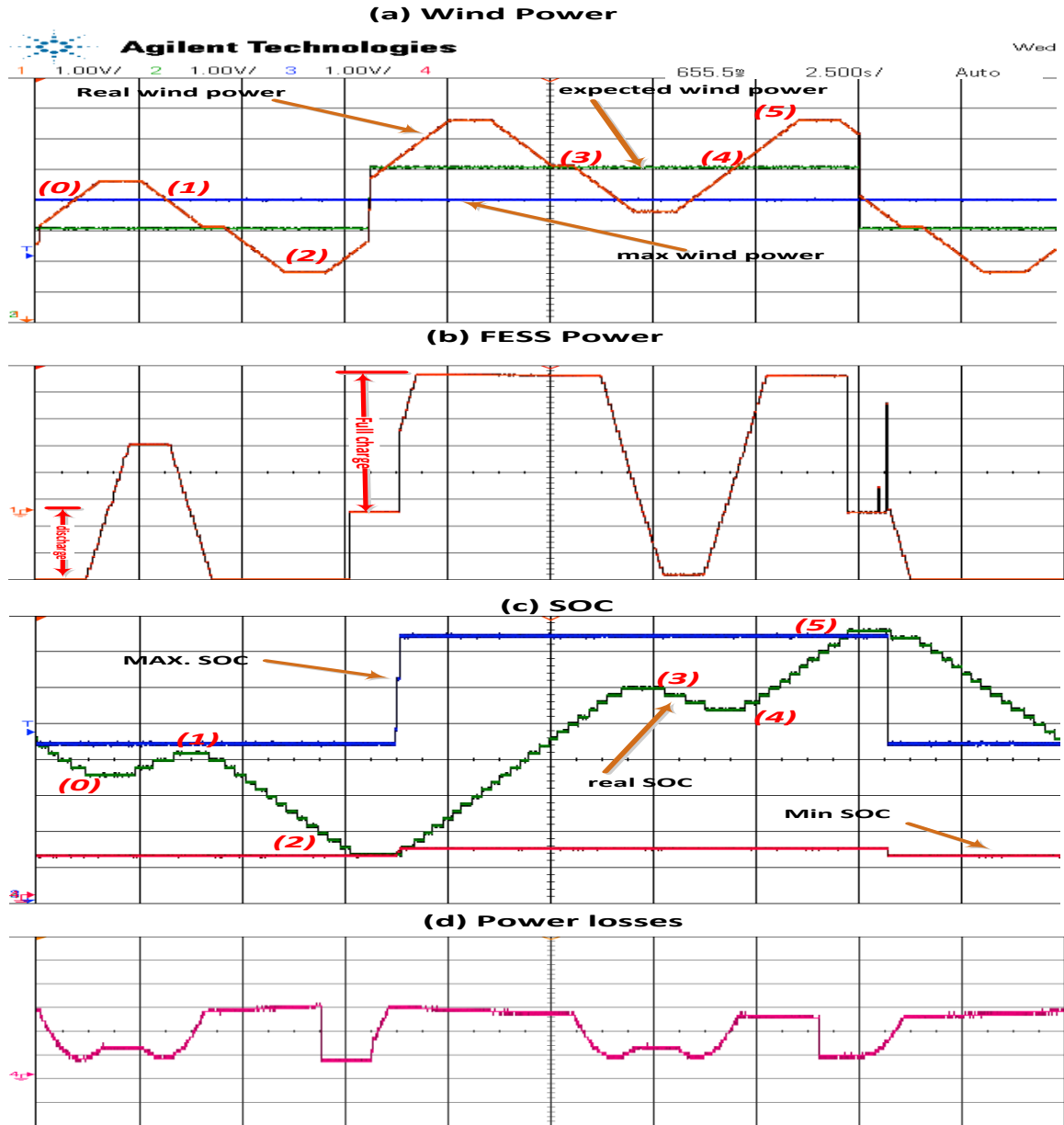


Figure 6-14 Real-time simulation results with time scales; a- wind power (100 kW/Div.); b- FESS power (20KW/Div.); c- SOC (5%/Div.) d- power loss (0.35 kW/div.)

6.6 Conclusion

This chapter presented a two-stage real-time EMS for a hybrid system composed of a FESS connected with a WECS. The EMS used an MPC-based algorithm to respect typical grid codes while minimizing the FESS losses and boosting its lifetime. The proposed technique converted

the MPC optimization problem from a nonlinear mixed integer into a linear convex problem without loss of accuracy. The AHC realized the second stage. The AHC was tuned by the MPC to ensure optimum operation under uncertainties associated with wind power prediction errors. The proposed EMS was compared with a traditional EMS on a typical 150-MW WECS. Furthermore, the real-time performance of the proposed EMS was validated in an HIL test bench. The proposed EMS managed to reduce the FESS losses by 25% as compared to the conventional EMS while compensating for the prediction errors and respecting the grid integration codes.

Chapter 7

Multi Energy Storage Robust Operation in Active Distribution Network

7.1 Introduction

This chapter discusses the day-ahead operation of multi ESSs in a distribution system with RESs. The chapter presents a tool to robustly allocate the allowable operating zones of active power margins for multi ESSs without violating typical distribution system constraints. This tool helps ESSs to manage their energy independently without violating the power system constraints. The main contribution is considering the power uncertainties (loads and renewable energy) without taking very conservative decisions. For defining robust operating zones (ROZ) for ESSs; first, a fuzzy expert relaxes the uncertainty domain. Second, a particle swarm optimization (PSO) algorithm detects the worst-case power uncertainty. Finally, the ROZ for each ESS that maintains safe system operation limits (voltage limits and branches ampacity) is obtained.

7.2 Problem Formulation

The typical energy management problem for any ESS ES is as follows:

$$\text{Max}_{p_{sk}}(\mathbb{F}(p_k^{ES})) \quad (7.1)$$

$$s. t. \begin{cases} \theta_{k+1}^{ES} = \mathbb{S}(\theta_k^{ES}, p_k^{ES}), \|\theta_k^{ES}\| \leq \overline{\theta}_k^{ES}, ES \in \mathcal{N}_s, k \in \mathcal{N}_k & (7.2) \\ 0 = \phi_k(p_k^{ES}, \theta_k^g, \mathbb{P}_{ex}), \|\theta_k^g\| \leq \overline{\theta}_k^g & (7.3) \end{cases}$$

As shown in (7.1), the ESS aims at optimizing a certain cost function $\mathbb{F}(p_k^{ES})$ which can be the ESS owner profit maximization by means like energy arbitrage, load shifting or even renewable energy integration [3]. Optimizing $\mathbb{F}(p_k^{ES})$ depends on choosing the optimal future ESS dispatch power p_{sk} . The future horizon can be minutes, hours, or even days. Without the loss of generality, we assume day-ahead operation example. The optimization problem has two constraints sets. First the ESS dynamical model $\mathbb{S}(\theta_k^g)$ in (7.2) that includes the storage states θ_k^g , such as (energy and power level, state of charge (SOC) and number of charging cycles). Energy storage states are limited in (7.2) (e.g., the state of charge is less than one, and the power is less than the converter rating). The second model is the grid power flow model ϕ_k . The power flow model is a static model that relates each bus active and reactive power to the nodal voltage and angle. The grid controlled variables (expressed here as θ_k^g and include the buses voltages and branches currents) depend on the storage power plus other exogenous power \mathbb{P}_{ex} , such as RES and load power. The grid variables are limited as in (7.3) to keep the voltage and current levels within limits.

Two main problems face the optimization problem (7.1). First, the exogenous power \mathbb{P}_{ex} is uncertain due to RESs and load prediction errors. Second, the problem (7.1) is solved by each ESS independently; in case of different ESS owners, this will require a complete knowledge of the distribution system model \mathbb{G} and other resources day-ahead dispatch (\mathbb{P}_{ex}) which is not very practical assumption. The proposed framework proposes the following.

- 1- Assuming that the system operator (DNO) has predictions of the RESs and load profiles, it will robustly calculate, for each ESS, the maximum power limits (for the day ahead) such that condition (7.3) is robustly fulfilled. These limits are defined here as the ROZ.

2- Each ESS owner can manage the asset independently by solving (7.4) with no need to know the whole system model (by only knowing the ROZ as provided in (7.6)).

$$\text{Max}_{p_{sk}}(\mathbb{F}(p_k^{ES})) \quad (7.4)$$

$$(7.5)$$

$$s. t. \begin{cases} \theta_{k+1}^{ES} = \mathbb{S}(\theta_k^{ES}, p_k^{ES}), \|\theta_k^{ES}\| \leq \overline{\theta}_k^{ES} \\ \underline{ROZ}_k^{ES} \leq \|p_k^{ES}\| \leq \overline{ROZ}_k^{ES}, k = 1: 24 \end{cases} \quad (7.6)$$

3- The owners of ESSs and RESs can co-operate together in time-shifting services or energy arbitrage under the proposed framework.

7.3 Robust Operating Zones Generation

From the previous discussion, the target is to find the ROZ which is defined in (7.7) and (7.8). The ROZ represents a supremum and infimum limits for the ESS power imposed by the grid model such that the grid states (voltage level and branches current) are within limits. For example, \overline{ROZ}_{sk}^{ES} may represent the maximum ESS discharge power such that the voltage level does not exceed 1.05 pu.

$$\overline{ROZ}_k^{ES} = (\sup p_k^{ES} \mid \|\theta_k^g\| \leq \overline{\theta}_{gk}) \quad (7.7)$$

$$\underline{ROZ}_k^{ES} = (\inf p_k^{ES} \mid \|\theta_k^g\| \leq \overline{\theta}_{gk}) \quad (7.8)$$

Assuming the power uncertainty $\tilde{p} \in [\underline{p}, \overline{p}]$ has a Gaussian probabilistic distribution (driven from the historical prediction error data). For defining the uncertainty lower and upper limits (ULL: \underline{p}) and (UUL: \overline{p}), if an uncertainty cumulative distribution function (ψ) is available, ULL and UUL may be taken at a (95%) confidence level (CL) with values $UUL = \arg(\psi_k^b = 95\%)$, $ULL = \arg(\psi_k^b = 5\%)$. These values for (UUL, ULL) are widely used in risk-based decisions [135]; however, other ranges are also considered, such as 99.9%-CL or 90%-CL, etc. The power at each bus b and future time k (p_k^b) is expressed in (7.9)-(7.11). The uncertain bus

power is expressed in (7.10) whereas the certain part is given in (7.11). Assuming a constant power load, the load reactive power is expressed as $\hat{q}_k^l = \lambda_l \hat{p}_k^l$ where $\lambda^l = \tan(\cos^{-1} \text{power factor})$. If a RES is assumed to operate at unity power factor, then λ_r equals zero. However, if a RES is desired to participate in voltage control, another control variable is added to the process q_k^{res} . Finally, if distributed generators (DGs) exist in the system, they can be added as a control variable as p_k^{DG}, q_k^{DG} . Without loss of generality and to focus on ESSs in this work, it is assumed that RESs have a unity power factor $\lambda^{res} = 0$, and the system has no DGs.

$$p_k^b = \hat{p}_k^b + \tilde{p}_k^b \quad q_k^b = \hat{q}_k^b + \tilde{q}_k^b \quad (7.9)$$

$$\hat{p}_k^b = p_k^{ES} + \hat{p}_k^{load} + \hat{p}_k^{res} \quad \hat{q}_k^b = q_k^{ES} + \lambda^l \hat{p}_k^{load} + \lambda_r \hat{p}_k^{res} \quad (7.10)$$

$$\tilde{p}_k^b = \tilde{p}_k^{load} + \tilde{p}_k^{res} \quad \tilde{q}_k^b = q_k^{ES} + \lambda^l \tilde{p}_k^{load} + \lambda_r \tilde{p}_k^{load} \quad (7.11)$$

$$\forall b = s = l = r, b \in \mathcal{N}_b, s \in \mathcal{N}_s, k \in \mathcal{N}_k, l \in \mathcal{N}_l, r \in \mathcal{N}_r$$

Let us define the uncertainty domain \mathcal{D} that combines the uncertainty in each bus power.

$$\mathcal{D} = \left\{ \tilde{p}_k^b \in \mathbb{R}^{n_b \times n_k} \mid \tilde{p}_k^b \in \left[\underline{p}_k^b, \overline{p}_k^b \right] \forall b \in \mathcal{N}_b, \forall k \in \mathcal{N}_k \right\} \quad (7.12)$$

The system power flow is a network that links a set of buses $b \in \mathcal{N}_b$ by a set of branches $t \in \mathcal{N}_t$ as explained in Section 3.2.5. Given the uncertainty domain D , RESs and load expected values, two optimization problems (7.13, 7.17) define the ROZ. These problems are solved for each sample $k \in \mathcal{N}_k$.

$$\begin{array}{l}
\overline{ROZ}_k^{ES} = p_k^{ES} \left| \begin{array}{l}
\max_{p_k^{ES}, q_k^{ES}} \left(\sum_{ES=1}^{n_s} \frac{p_k^{ES}}{C^{ES}} \right) \quad (7.13) \\
(7.9) - (7.12), \phi_k(\mathcal{D}) : \{ (3.42) - (3.48) \} \quad (7.14) \\
s. t. \left\{ \begin{array}{l}
p_k^{ES^2} + q_k^{ES^2} \leq C^{ES^2} \quad (7.15) \\
0 \leq p_k^{ES} \leq C^{ES} \quad (7.16)
\end{array} \right. \\
\hline
\underline{ROZ}_k^{ES} = p_k^{ES} \left| \begin{array}{l}
\min_{p_k^{ES}, q_k^{ES}} \left(\sum_{ES=1}^{n_s} \frac{p_k^{ES}}{C^{ES}} \right) \quad (7.17) \\
(7.9) - (7.12), \phi_k(\mathcal{D}) : \{ (3.42) - (3.48) \} \quad (7.18) \\
s. t. \left\{ \begin{array}{l}
p_k^{ES^2} + q_k^{ES^2} \leq C^{ES^2} \quad (7.19) \\
-C^{ES} \leq p_k^{ES} \leq 0 \quad (7.20)
\end{array} \right.
\end{array} \right.
\end{array}
\end{array}$$

The objective function (7.13) aims at maximizing the per-unit discharge power participation of all ESSs. The resulting ESS active power represents the ROZ upper limits. The reason for dividing each ESS active power on the apparent power (C^{ES}) is the fair participations of reactive power support from different ESSs as they have different sizes; otherwise, the large ESS units will have higher weights in the objective function. However, it should be noted that reactive power support is also location-based where one cannot guarantee equal VAR participation from different ESSs. Whereas (7.14) represent the power system model which is uncertain in the bus power as in (7.12), the constraint (7.15) defines the apparent power limit C^{ES} of each ESS, and (7.16) guarantees the operation of ESS in the discharge mode. Similarly, the maximum ESS charging power (\underline{ROZ}_k^{ES}) is driven by solving (7.17). Unlike problem (7.13), the constraint (7.20) enforces the ESS to operate in the charging mode. Problem (7.13) considers the ESS as a generator from the power flow point of view (that is why it is a maximization problem). On the other, problem (7.17) considers the ESS as a load, and this is the reason for minimizing the power to reach the maximum allowable charged power without violating the power system constraints.

Problems (7.13) and (7.17) are still uncertain because the power flow, model ϕ_k is a function in the uncertainty set \mathcal{D} that offers infinite uncertainty combinations for each bus power. The choice of different uncertainty sets dictates the choice of \tilde{p}_k^b in (7.9) and hence the *ROZ* results. Different choice criteria for \tilde{p}_k^b are depicted in Figure 7-1-a. If deterministic optimization is applied, then the uncertainty is neglected $\tilde{p}_k^b = 0$. On the other hand, techniques, such as robust optimization can include the worst case uncertainty (WCU), such as 99.9% of the uncertainty domain. The WCU provides a robust solution for all the other uncertainty combinations within \mathcal{D} and is located at one of the \mathcal{D} vertices [74]; however, the WCU represents a conservative solution. One possible solution is to reduce the uncertainty domain size from \mathcal{D} to a less conservative (relaxed) one \mathcal{D}_f via an uncertainty budget. An example for uncertainty budget is reducing the confidence level from 99.9% into 95% as shown in Figure 7.1(a); however, this technique is still not immune against all uncertainty possibilities.

The proposed framework relaxes the uncertainty domain according to its resulting risk on the system as shown in Figure 7.1(b). This solution acts more conservatively (e.g., like robust optimization) with the risky uncertainty, whereas it relaxes the uncertainty domain when the uncertainty does not represent any harm on the system constraints. For instance, risky over-generated power uncertainty that shifts the voltage level more than 1.05 pu or the current level over the ampacity limit is fully considered. The *ROZ* generation is formalized in a three-stage framework as explained in the following.

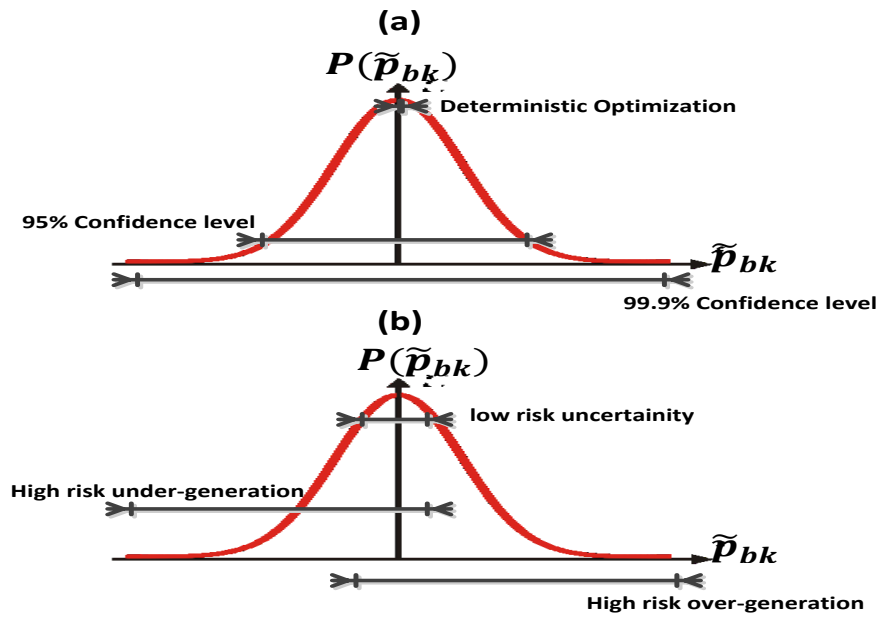


Figure 7-1(a) Different uncertainty sets definition techniques (b) proposed risk-based uncertainty definition technique.

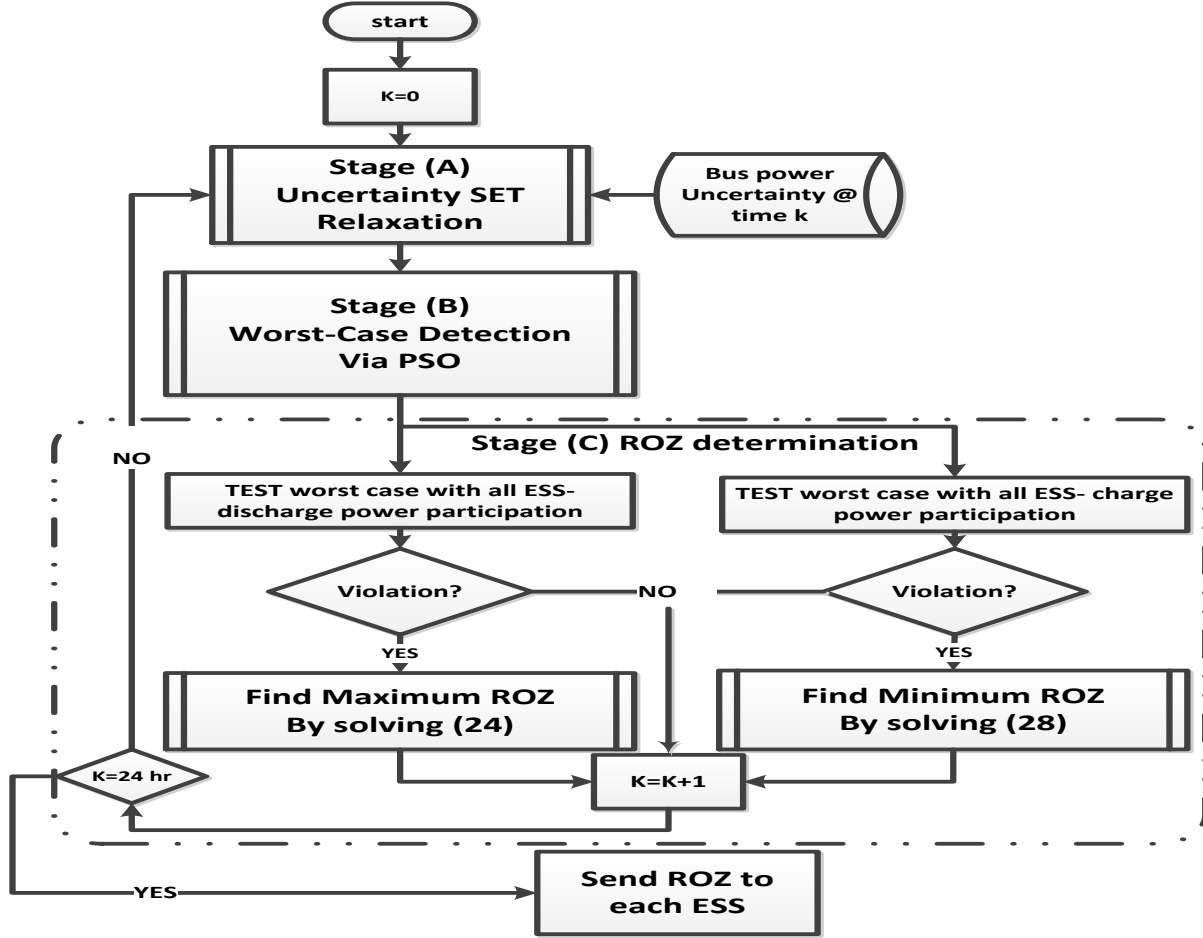


Figure 7-2 ROZ generation framework.

The proposed framework finds the ROZ in three stages as depicted in Figure 7-2. In Stage (A), given the uncertainty domain \mathcal{D} , it is relaxed to \mathcal{D}_f . In Stage (B), the PSO detects the worst case uncertainty within \mathcal{D}_f . Finally, in Stage (C), the full active power participation of all ESS in both full charge and discharge scenarios with the WCU are tested. In case of no grid code violation, each ESS can be fully discharged $\overline{ROZ}_k^{ES} = C^{ES}$ and fully charged $\underline{ROZ}_k^{ES} = C^{ES}$. Otherwise, the ROZ are defined by solving (7.13) and (7.17) after knowing the WCU to calculate \tilde{p}_k^b .

7.3.1 Stage A: Uncertainty Set Relaxation

In this stage, the uncertainty budget is calculated. It is considered as a weight for the uncertainty set for reducing the conservatism of results due to extreme case uncertainty. An uncertainty budget here is evaluated according to the uncertainty associated risk. In other words, the less risky the uncertainty is, the more relaxed the uncertainty domain is. Further, the risk probability is another factor in this process. This technique emulates the popular risk management strategies that depend on two main factors to make decisions: *the risk level and the risk probability*. The risk of the uncertainty focuses on its effect on voltage level, and a risk-based-budget value is assigned, accordingly. For instance, if we study a bus voltage variation for a wind turbine (with $\mp 20\%$ power variation), normally it is windy with light load during late night. As a result, extra wind generation is riskier on the bus voltage. Thus a high budget is assigned for the UUL and lower for the ULL, and vice versa during peak hours (under-voltage hours). On the other hand, for load uncertainty, the uncertainty budget maximizes the ULL during overvoltage times, and vice versa during peak load hours (under-voltage). To quantify the risk of uncertainty on the voltage level, the power with voltage relation is driven from the famous voltage sensitivity matrix (the power flow inverse Jacobian). Assuming unity power factor RES and constant power factor load, relation (7.21) is driven.

$$\begin{aligned}\partial v_k^b &= \Lambda_{bp} \partial p_k^b + \Lambda_{bq} \partial q_k^b \quad \forall b \in \mathcal{N}_b, \forall k \in \mathcal{N}_k \\ \partial v_k^b &= \partial p_k^b (\Lambda_{bp} + \Lambda_{bq} \lambda_l)\end{aligned}\tag{7.21}$$

For studying the active power uncertainty at a bus b and a time k , critical power uncertainty (CPU) limits $[\underline{\partial p_k^b}, \overline{\partial p_k^b}]$ are calculated in (7.22). It is worth noting that CPU is a function in both the bus voltage in the deterministic case $v_{bk}(0) = \arg(\Phi_k(\mathcal{D} = 0))$ and bus voltage

sensitivity. The upper CPU $\overline{\partial p_k^b}$ leads to a maximum overvoltage at the bus b , while the lower CPU $\underline{\partial p_k^b}$ leads to under voltage limits in load buses sets and vice versa for lower CPU.

$$\overline{\partial p_k^b} = \frac{\bar{v} - v_k^b(0)}{\Lambda_{bp} + \Lambda_{bq}\lambda_l} \quad \underline{\partial p_k^b} = \frac{v - v_k^b(0)}{\Lambda_{bp} + \Lambda_{bq}\lambda_l} \quad (7.22)$$

The uncertainty risk is calculated by comparing CPU and the uncertainty set limits. Further, if different uncertainties PDFs are available, the risk probability is reachable. Calculating the uncertainty budget from the uncertainty risk and the risk probability is not a straightforward process; however, it is a logic process that can be efficiently solved by using logic rules. Therefore, a fuzzy expert is proposed to tune the uncertainty budget limits using the risk and its probability. The proposed fuzzy inference system has four inputs;

- First; the UUL risk $R_{UUL_k}^b$. It is the difference between the UUL and the maximum CPU. If the uncertainty is higher than the critical power, the risk has a higher positive value which means a higher risk, and vice versa.

$$R_{UUL_k}^b = \overline{p_k^b} - \overline{\partial p_k^b} \quad (7.23)$$

- The second input is ULL-risk $R_{ULL_k}^b$. It is the difference between ULL and minimum CPU. Both inputs are represented in per-unit.

$$R_{ULL_k}^b = \underline{p_k^b} - \underline{\partial p_k^b} \quad (7.24)$$

- Finally, the third and fourth inputs are the risk probabilities' values. As both $\overline{\partial p_k^b}$, $\underline{\partial p_k^b}$ are deterministic, the risk probabilities are calculated from their CDF as follows; $\psi(R_{UUL_{bk}}) = \psi(\overline{p_k^b})$ and $\psi(R_{ULL_k}^b) = \psi(\underline{p_k^b})$. If an uncertainty CDF is available for the uncertainties, then the risk probabilities exist; otherwise, these probabilities are assumed as one (which means they are unconsidered) and in such a case, the rule size shrinks from nine to three. That means that

the expert can still work without an exact CDF data. Each input is represented in the domain of discourse by three membership functions [136], while the outputs are the uncertainty budget limits $\overline{\Gamma}_k^b, \underline{\Gamma}_k^b$ which have five Gaussian membership functions, each within [0,1]. The expert system has 18 rules given in Table 1 (first three rows are for the upper limit $\overline{\Gamma}_k^b$, whereas the last three rows are for the lower limit $\underline{\Gamma}_k^b$).

Table 7-1 Fuzzy expert rules.

$R_{UUL_k}^b$	positive	zero	Negative
$\psi(R_{UUL_k}^b)$			
Low probability	V-Low	Low	Medium
Medium probability	Low	Medium	High
High probability	Medium	High	V-High
$R_{ULL_k}^b$	negative	zero	Positive
$\psi(R_{ULL_k}^b)$			
Low probability	V-Low	Low	Medium
Medium probability	Low	Medium	High
High probability	Medium	High	V-High

An easy way to define uncertain variable ξ (given its uncertainty range $[\underline{\xi}, \overline{\xi}]$ and its average $\hat{\xi}$) is by using a triangular membership function centered at $\hat{\xi}$, which expands by two linear lines to the points $(\underline{\xi}, \overline{\xi})$: however, if the CDF is given, other non-uniform presentations are possible. Further details for deriving a membership function for an uncertain variable is given in [137], while fuzzy risk management applications in power system restoration is discussed in [138]. The expert outputs are the weights of uncertainty budgets, which relax the original uncertainty set \mathcal{D} to get a filtered or un-conservative new set \mathcal{D}_f .

$$\mathcal{D}_f = \left\{ \tilde{p}_k^b \in \mathbb{R}^{n_b \times n_k} \mid \tilde{p}_k^b \in [\underline{\Gamma}_k^b \underline{p}_k^b, \overline{\Gamma}_k^b \overline{p}_k^b] \forall b \in \mathcal{N}_b, \forall k \in \mathcal{N}_k \right\} \quad (7.25)$$

It is worth mentioning that the derived surface from Table 7-1 is a non-unique and sub-optimal solution; however, it is derived using logic rules and empirical trials. As a future work, a learning algorithm will be investigated to train the membership function parameters. It should be noticed that other criterion rather than voltage level may be adopted to study the uncertainty risk, such as voltage stability as adopted in [139], however, it is assumed that RES penetration is not so high such that it threatens the voltage stability.

7.3.2 Stage B: Worst-Case Uncertainty Detection

Stage-B aims at defining the WCU over the relaxed uncertainty set \mathcal{D}_f using PSO. Not only does PSO have a long history with power system applications, but also it has the following advantages [140]. First, the fitness function is the gauge of the solution quality without the need for complex calculations, such as gradient or matrix inversion calculations that may be infeasible. This reduces the computational complexity and relaxes the continuity and convexity conditions needed in gradient-based methods. Second, PSO is easily merged with other optimization techniques (such as semi-definite programming in this chapter). Further, it can escape local minima, as the scattered population results guide the solution. Finally, PSO is preferred over other evolutionary algorithms for its simplicity, low memory requirement, and fewer parameters tuning. On the other hand, like other heuristic algorithms, the solution may have long calculation times depending on the population size and the initial position; however, with the current developments in high-performance computing tools, less computational time is achievable. Due to the aforementioned reasons, PSO is adopted as a WCU detector (d^*) at uncertainty domain \mathcal{D}_f hyper-plane. Each particle of the swarm-population $X_k^j(\tau)$ is a vector with dimension $1 \times n_b$ represents the power uncertainties combination j calculated at future

sample time k at the PSO iteration τ . The total population size equals $J \times K$. \mathcal{D}_f represents the population search domain or the particles limits:

$$X_k^j(\tau) = \vec{d}_k^b = [\tilde{p}_{1k}^{bj}(\tau), \dots, \tilde{p}_{kn_b}^{bj}(\tau)], X_k^j(\tau) \in \mathcal{D}_f \quad (7.26)$$

To detect the worst power uncertainty, the PSO maximizes a fitness function that represents the sum of voltage deviation at all buses (penalty function fV_k) in (7.27).

$$fV_k = \sum_{b=1}^{n_b} \frac{1}{1 + e^{-\alpha(v - v_k^b)}} + \frac{1}{1 + e^{\alpha(\bar{v} - v_k^b)}} + \beta (v_k^b - v_r)^2 \quad (7.27)$$

$$\max(fV_k) \forall k \quad (7.28)$$

The penalty function consists of three parts: two sigmoid functions represent a very high penalty for violating the desired voltage range and, the third part is a quadratic function that penalizes the voltage deviation from the nominal 1.0 pu. Two remarks need to be highlighted here. First, the choice of voltage deviation penalty function is not unique; however, the selection of the function in such a shape assigns the voltage deviation a low penalty within the permissible voltage zone but a much higher penalty for working outside this zone. Second, other penalty functions are added easily, such as the branch ampacity limits (represented by the sum of sigmoid functions centered at each branch maximum current or the power loss.

At a certain iteration τ , after the penalty function is calculated for all J -particles, the local and global best positions are updated and the new velocity vector is calculated for each particle as in (7.29). For solution quality, PSO must fulfill two important criteria: first, a high exploration at the start of the search, and second, a deep exploitation to avoid trapping in a local-suboptimal later [140]. Thus, a high speed for particles exploration is gained via high initial inertia that reduces monotonically with the iterations progress to achieve higher exploitation later as in

(7.30). Next, the particles positions are updated as in (7.31). The reader is referred to [141] for further details about PSO.

$$\omega_k(\tau) = \omega_{max} - \frac{\omega_{max} - \omega_{min}}{Max.Iter} \tau \quad (7.29)$$

$$V_k^j(\tau + 1) = \omega_k(\tau)V_k^j(\tau) + c_1 r_1 (Pbest_k^\tau - X_k^j(\tau)) + c_2 r_2 (Gbest_k^\tau - X_k^j(\tau)) \quad (7.30)$$

$$X_k^j(\tau + 1) = V_k^j(\tau + 1) + X_k^j(\tau) \quad (7.31)$$

Finally, the stopping criterion is achieved in two cases; first, the convergence case happens if the fitness function settles at a certain value within the predefined tolerance zone. This must happen for a predefined number of iterations to guarantee convergence and avoid trapping in a local minimum. Second, in an emergency case, it happens if the number of iterations exceeds the maximum number ($\tau \geq \bar{\tau}$). After a stopping criterion is reached, the WCU is defined as the global best position as $WCU_k = Gbest_k$.

Figure 7-3 depicts an example of a two -bus system with uncertain powers $\tilde{p}_{1k}, \tilde{p}_{2k}$ the probabilistic distribution of the uncertainty is presented by two different Gaussian distributions. The uncertainty domain \mathcal{D} is explained in the uncertainty space as follows $\mathcal{D} = \{(\tilde{p}_{1k}, \tilde{p}_{2k}) \in \mathcal{R}^{2 \times 1} \mid \tilde{p}_{bk} \in [\underline{p}_{bk}, \overline{p}_{bk}] \forall b \in \{1, 2\}\}$. After applying stage A to define the uncertainty risk via fuzzy expert, the domain is relaxed to $\mathcal{D}_f = \{(\tilde{p}_{1k}, \tilde{p}_{2k}) \in \mathcal{R}^{2 \times 1} \mid \tilde{p}_{bk} \in [\underline{\Gamma}_b p_{bk}, \overline{\Gamma}_b \overline{p}_{bk}] \forall b \in [1, 2]\}$. Stage (B) detects the worst case uncertainty (WCU) and found it at one of the vertices as depicted in Figure 7-3. This point is less conservative than the original WCU.

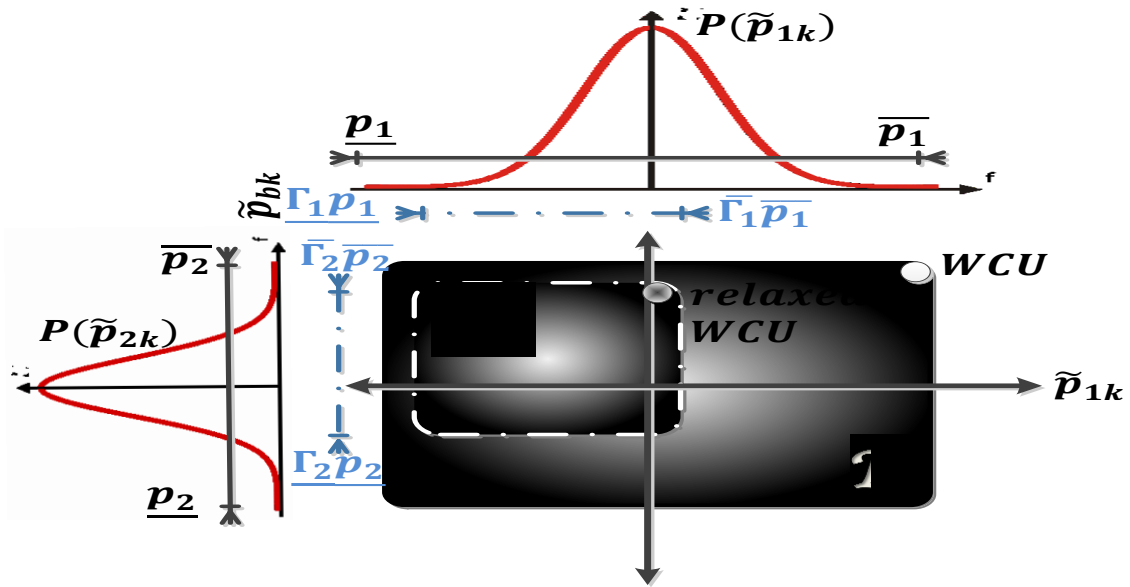


Figure 7-3 WCU detection flowchart.

7.3.3 Stage C: ROZ Determination

After detecting the WCU, a power flow test with full ESS discharge power participation is conducted with the WCU. If any of the power system constraints is violated, the WCU is set in (7.9) as $\tilde{p}_{bk} = WCU_k$. Next, problem (7.13) is solved to define the maximum discharge ROZ. Similarly, the maximum charge power is found from solving (7.17). To guarantee the feasibility of these problems, the reactive power reservoir from ESSs must manage to keep the voltage within allowable margins. If a non-feasibility problem is faced, then the ESS cannot provide adequate reactive (and active) power support for the network and the system operator must start a load shedding scheme; renewable energy curtailment plan or add extra VAR support in the network.

7.4 Case Study

The case study investigates the effect of RES uncertainty on ESS ROZ shape. In this study, we consider the radial feeder described in Section 3.3. The RES profiles are historical data

from Alberta system Operator (AESO). All BESS and, RES ratings are given in Table 7-2. Different RES and load operating profiles are shown in Figure 7-4 as per unit of each asset rating, whereas Figure 7-5 shows the voltage surface in the base case (no BESS participation and zero RES uncertainty).

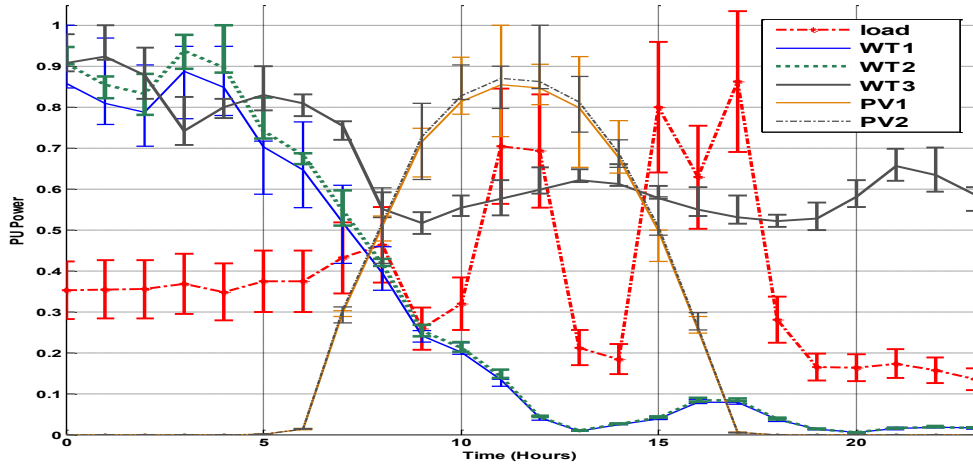


Figure 7-4 RES and load day-ahead profile with uncertainty.

Table 7-2 RES, BESS rating.

Rat ings	$p_{WT1} = 2MW, p_{WT2} = 1.5MW, p_{WT3} = 1.5MW,$ $p_{pv1} = 0.5MW, p_{pv2} = 0.5MW,$ $p_{BESS1} = 1MW/3MWh, p_{BESS2} =$ $2MW/6MWh$
-------------	--

Simulations study the effect of uncertainty domain choice \mathcal{D} on the ROZ and voltage violation. Four cases with different conservatism degrees are compared here:

- a. **Deterministic case (\mathcal{D}_1):** the RES and load uncertainty are unconsidered (as in [65]-[64]); $UUL_1 = ULL_1 = 0$

- b. **Uncertainty budget (\mathcal{D}_2)**; in this case, the fuzzy expert defines the uncertainty budget, given ULL, and UUL as $UUL_2 = \arg(\varphi_{ik} = 95\%)$, $ULL_2 = \arg(\varphi_{ik} = 5\%)$, $\mathcal{D}_2 = \mathcal{D}_f$
- c. **No-budget case (\mathcal{D}_3)**, same as (\mathcal{D}_2) without uncertainty budget $UUL_3 = \arg(\varphi_{ik} = 95\%)$, $ULL_3 = \arg(\varphi_{ik} = 5\%)$,
- d. **Six-sigma case (\mathcal{D}_4)**; most conservative but highest robustness case considering 99.99% of the uncertainty domain under the famous six-sigma rule. No uncertainty budget is assumed here. This emulates the robust optimization techniques used in Group-c: $UUL_4 = \arg(\varphi_{ik} = 99.99\%)$, $ULL_4 = \arg(\varphi_{ik} = 0.01\%)$.

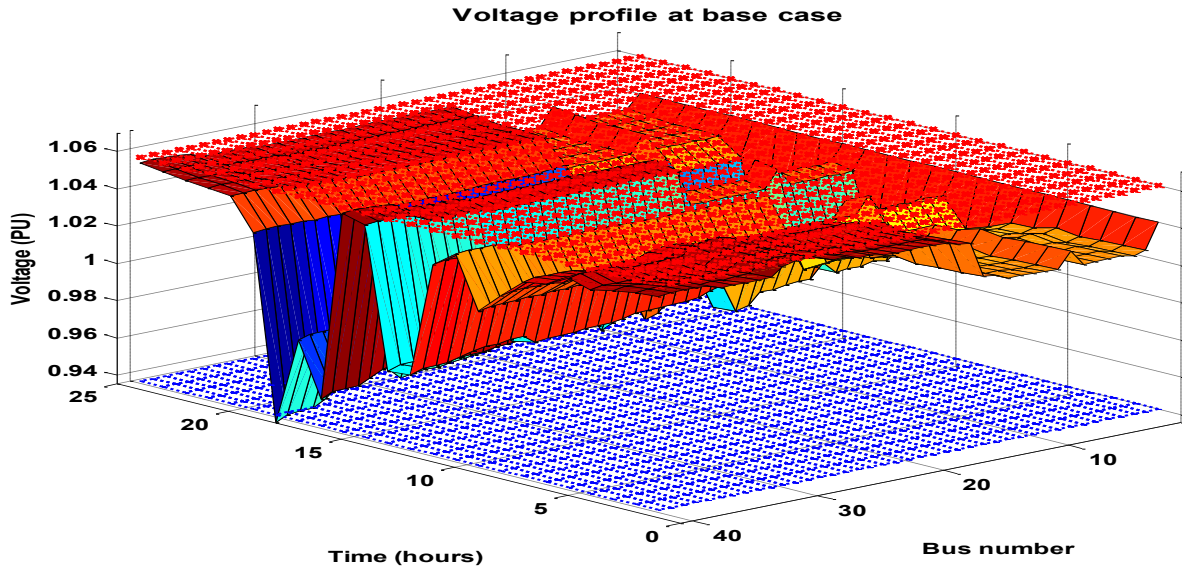


Figure 7-5 Voltage profile at base case.

To validate the resulting ROZ (four sets corresponding to the domains above), it has been tested on one hundred different uncertainty scenarios. In each scenario, both BESS1 and BESS2 obeyed the ROZ as given by the system operator and shown in Figure 7-8, in all simulations. In these simulations, the BESS owners desire to have the following profiles shown in Figure 7-6

where BESS1 acts as hybrid system combined with PV1. It time-shifts PV1 peak noon-power to sell it during peak hour. BESS2 trades energy arbitrage it fully charges at a cheaply priced energy at ($k=5:7$) to discharge it back during peak hours.

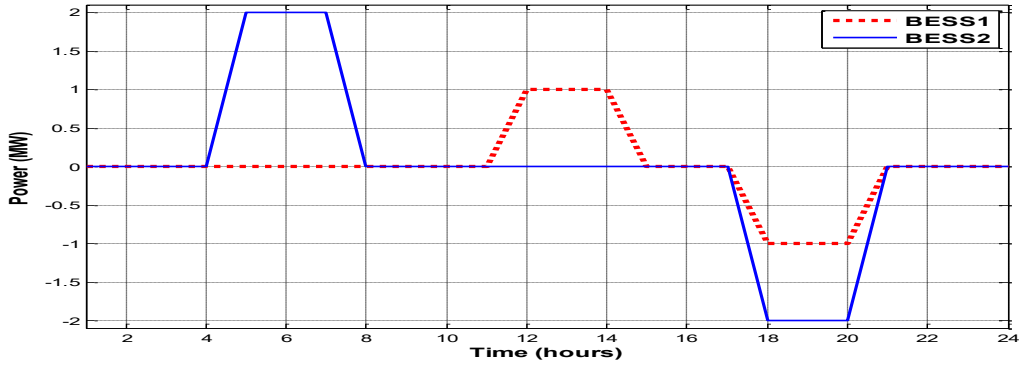


Figure 7-6 Desired BESS power profiles without ROZ.

The previous two dispatches are conducted within a hundred different uncertainty power flow scenarios, with distributions shown in Figure 7-7. The system operator does not have to know the exact CDF. However, the uncertainty limits are required to define \mathcal{D} .

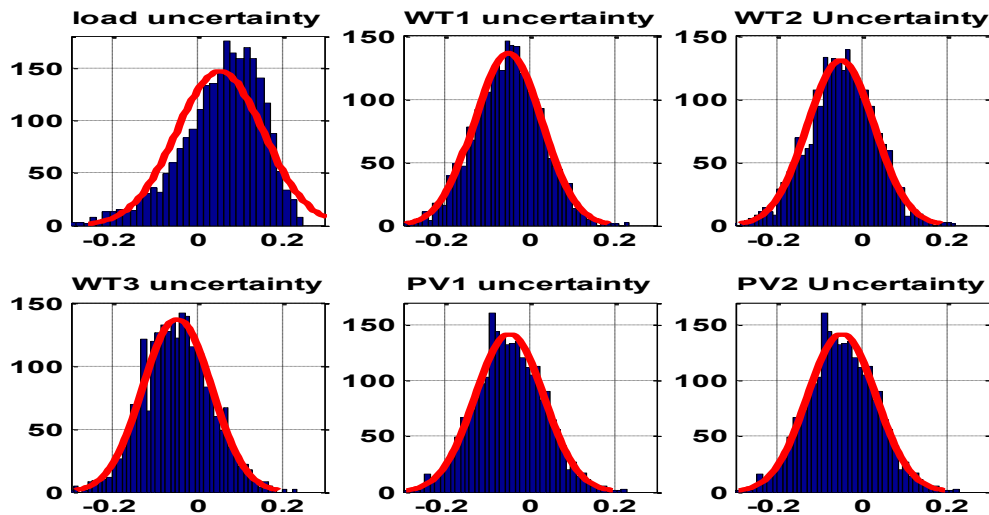


Figure 7-7 RES, load uncertainty distribution for 100 scenarios each has 24 hours sample (total 2400 uncertain sample points).

Given $\mathcal{D}_i, i = 1: 4$, we calculate ROZ from (24) and (28) for each case of the different four strategies. These ROZ are compared Figure 7-8. ROZ at each case is send to the ESSs to upper limit the desired dispatch power depicted in Figure 7-6.

A comparison is conducted between the four cases by testing the hundred different uncertainty scenarios generated from Figure 7-7. Further, the comparison is repeated at various RES penetration levels (20, 30 and 40%). No contingency is assumed in all simulations. The results are investigated from two perspectives. First, the network sound operation represented here by buses' voltage violations. This is represented here by the count of [over-voltage (OV) or under-voltage (UV)] during the 100 scenarios. No ampacity violation occurs; thus they are not included in the comparison. On the other hand, The ESS-owner cares about the ROZ size, as a higher ROZ-size means a higher operation margin and profit. The ROZ-size is calculated

$$ROZS_s = \frac{\int_{k=0}^{n_k} (\overline{p_{sk}} - p_{sk}) dk}{\int_{k=0}^{n_k} 2S_s dk} \forall s \in \mathcal{N}_s.$$

A comparison between the gross violations (OV, UV) over the 100 different scenarios is shown in Table 7-3. It compares the four ROZ cases corresponding to the various uncertainties.

Table 7-3. ROZ size and voltage violations in 100 scenarios.

	20%-RES			30%-RES			40%-RES		
	OV	U V	ROZ ₂	OV	UV	ROZ ₂	O V	U V	ROZ ₂
\mathcal{D}_1	133	47	98.2%	88	45	98%	43	41	97.6%
\mathcal{D}_2	7	3	95.7%	7	1	95.7%	6	1	95.3%
\mathcal{D}_3	6	2	95%	6	0	95.3%	5	1	94.9%
\mathcal{D}_4	0	0	92.9%	0	0	92.9%	0	0	92.1%

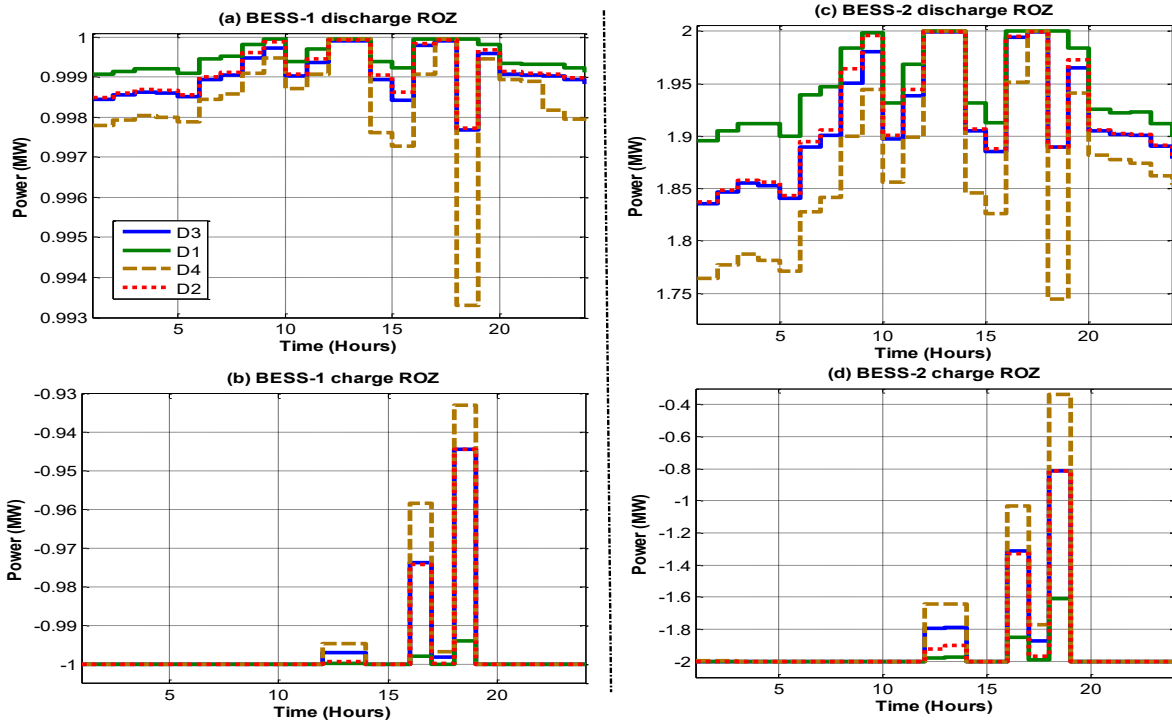


Figure 7-8. ROZ limits for BESS1, 2 at 30% RES-penetrations.

As expected, the deterministic case \mathcal{D}_1 achieves the highest ROZ size but with the highest number of violations on all penetrations (all apparent power is committed as active power while reactive power support is not enough for voltage regulation to heal the uncertainty effect). On the other hand, the six-sigma case \mathcal{D}_4 results in a zero voltage violations but it achieves the lowest ROZ size for all ESSs. As a result, the ESSs cannot fully operate to its up active power, to provide the needed reactive power support. For the proposed uncertainty budget \mathcal{D}_2 and the no-budget case \mathcal{D}_3 , the number of violations is very small (a maximum of ten times violations occur during the 100 scenarios in a 41-bus system); however, the ROZ size in the case of \mathcal{D}_2 is always greater than in \mathcal{D}_3 . As a result, the proposed framework has managed to boost the ROZ size without big sacrifices in the power system security. On the other hand, the RES penetration effect is clear on the ROZ-size, for a higher RES penetration, higher reactive power support is

required from the ESSs. As a result, the active power limits decreases (ROZ size diminishes with RES penetration).

7.5 Conclusions

This chapter presented a framework to define the ROZ for the power converters interfacing distributed energy storage units. The technical constraints included permissible voltage level and branches ampacity. The main work contribution is considering the power uncertainty while reducing the results conservatism. The ROZ was calculated in three stages. First, a fuzzy-based technique relaxes the uncertainty domain. Second, a PSO-based detection algorithm was designed to determine the worst case uncertainty. Finally, a convex power flow problem defined the ROZ. The proposed framework was tested on a real 41-bus radial feeder using different uncertainty scenarios. Four uncertainty sets with different conservatism levels were compared. The results showed that the proposed technique managed to boost the ESS participation with a very low voltage and ampacity violations.

Chapter 8

Mobile Energy Storage Scheduling and Operation in Active Distribution Systems

A mobile (transportable) energy storage system (MESS) can provide various services in distribution systems including load leveling, peak shaving, reactive power support, renewable energy integration and transmission deferral. Unlike stationary energy storage units, a mobile energy storage system can move between different buses by truck to provide various local services within the distribution feeder. This chapter proposes a day-ahead EMS for an MESS that aims to minimize the cost of the power imported from the grid. The MESS does not only shift renewable energy power to load peak hours but also can provide localized reactive power support. Given day-ahead predictions for load and RES power, the EMS decides the optimal MESS stations in the feeder and its operating power. Next, a particle swarm optimization-based algorithm is developed to tune the moving time of the MESS according to a transit delay model. The applicability of the proposed scheduling and operation algorithms is tested on a radial distribution feeder.

8.1 Problem Description

8.1.1 Motivation

Still, with the increasing number of RESs dispersed in the system, a large number of ESSs is needed to support the grid stability and reliability. This may result in an infeasible investment from the economic point of view for two main reasons. First, the high cost of most of ESSs and

its relatively low lifetime. Second, the ESS cost diminishes with its rating; thus, a significant number of ESSs is way much expensive than a single unit with the same ratings. According to [105], the ESS power conversion system per-unit cost varies from (1,800\$/kW) for a 5 kW station compared to (300\$/kW) for a 2 MW one as shown in Figure 8-1. As a result, a significant saving is achievable if a single bulk ESS can replace a large number of smaller ESSs. However, distributed ESSs provide some localized services that a single centralized ESS cannot provide, such as voltage regulation or power loss minimization. An MESS solves this problem because an MESS is a single ESS that can be plugged into the system at different locations during different times, it can provide different localized grid services in a way much cheaper than multi stationary ESSs (SESSs). The advantage of transportability is the ability to deliver a localized reactive power support for voltage regulation, power loss reduction, dispersed RESs integration, and last but not least, transmission and distribution upgrade deferral.

Indeed, aggregated EVs look like a cheaper similar solution for providing grid services exactly like the MESS. A similar solution where the network operator does not have to invest any initial cost, however; aggregated EVs in parking lots have both power and energy uncertainty due to their uncontrollable availability time [84] which question the reliability of the service. Besides, it requires a high number of EVs to give the same power rating equivalent to a single MESS truck. Finally, not all the EVs owners will be willing to participate in grid services [83].

This study does not claim by any mean that an MESS will always prove to be financially attractive than aggregated EVs or SESSs. Rather, a feasibility study that compares all the

different technologies should be conducted for a given system to select the best option from the technical and economic perspectives.

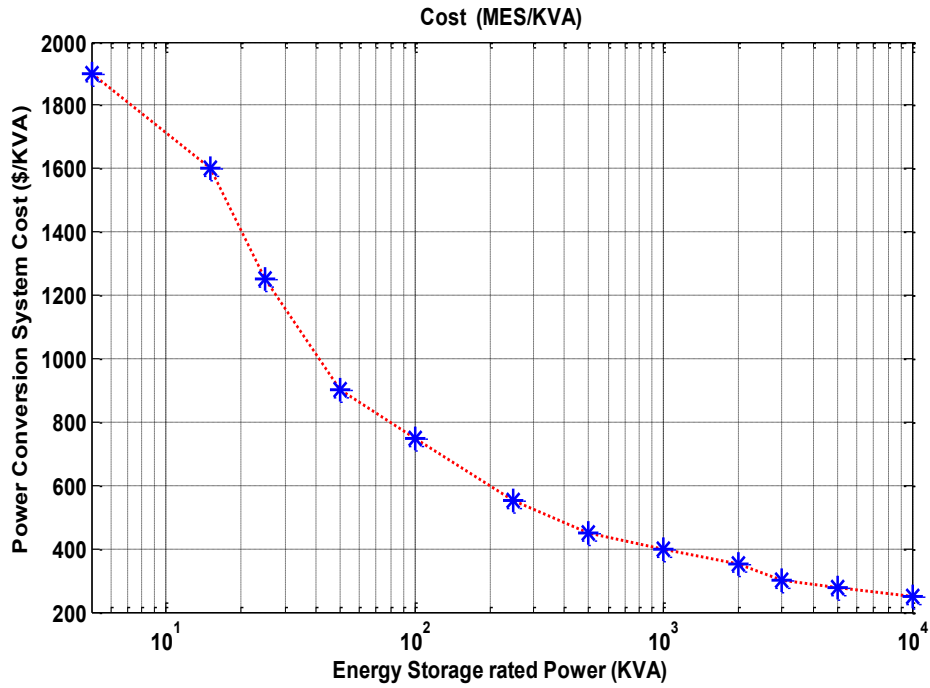


Figure 8-1 Power Conversion System cost versus size.

8.1.2 MESS Model

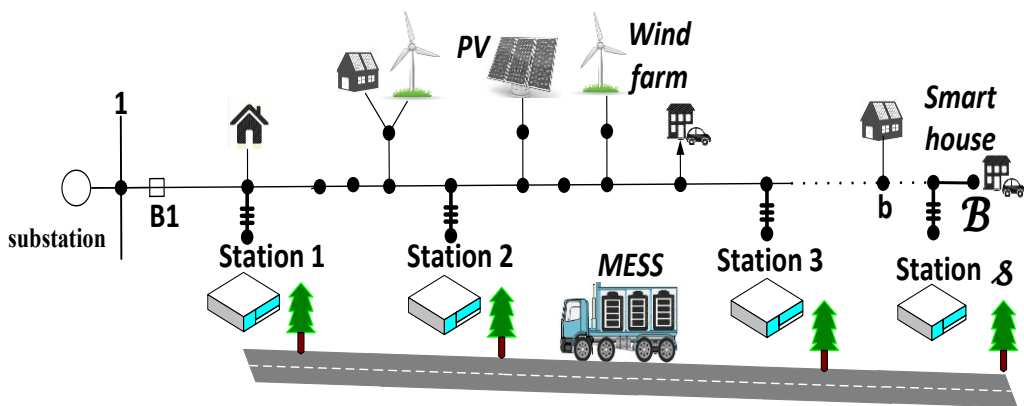


Figure 8-2 Radial feeder with multi-MESS stations.

Figure 8-2 shows an example of a radial feeder. The feeder has RESs set \mathcal{N}_r at different locations of the feeder, such as wind energy conversion systems (WECS) and photovoltaic (PV). Furthermore, other dispatchable resources (such as microturbines, small diesel engines, etc.) may exist at different buses and defined by the set \mathcal{N}_g . Moreover, the feeder has a load set \mathcal{N}_l with some smart houses (net-zero houses) that may use a rooftop PV, heat pumps, electric storage, and electric vehicle. RESs have different profiles that can be forecasted efficiently using both numerical and physical techniques (e.g., [65]). Moreover, electrical loads can be accurately predicted for the day-ahead operation planning [142], [143]. It should be emphasized that even with a 10-15% power prediction error, a day-ahead EMS cannot reach an optimal solution; rather, day-ahead EMS provides a sub-optimal solution. To compensate for the forecast error, a real-time controller is required to adjust the EMS solution depending on actual system measurements. For instance, a day-ahead EMS decides the reactive power setpoint; however, due to unpredictable real-time changes (sudden load change, faults or outages, RES intermittency, etc.), the actual reactive power is tuned by a real-time on-line voltage controller that measures the bus voltage and tunes the reactive power accordingly. This multi-level control scheme has been adopted widely in the literature, such as in [28]. In power system dispatch, the system operator adopts the same strategy when it comes to frequency control. The operator measures the frequency deviation and the power imbalance to decide the area control error (ACE), then the operator starts adjusting its day-ahead schedule by dispatching its reserve resources in real-time accordingly to compensate the ACE [29].

The DNO can schedule an MESS to move between different positions for multi-services. Different MESS positions ($\mathcal{N}_s = \{1, 2, \dots, s\}$) define the buses at which the MESS can be connected to the system which will be designated as the *MESS-stations*. Figure 8-3 depicts the

structure of an MESS which consists of two parts: the ESS and the truck. The ESS consists of an array of battery cells (e.g., lithium-ion).

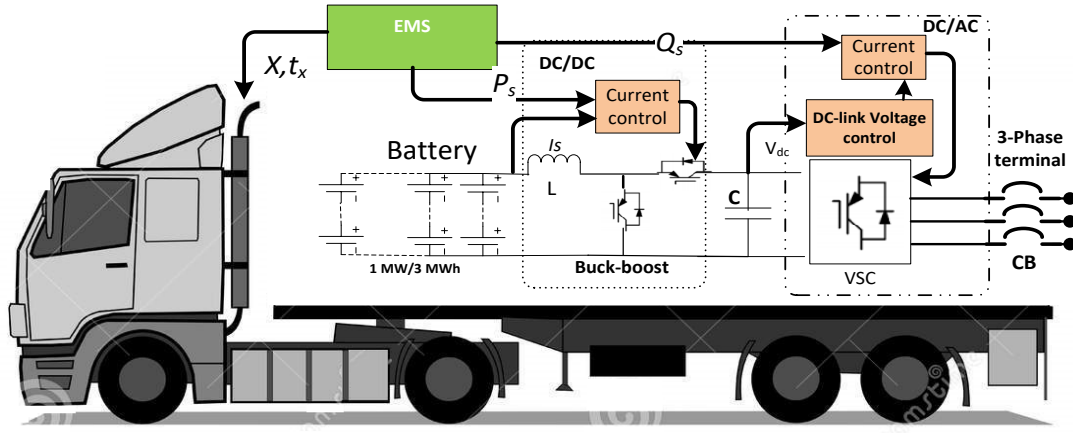


Figure 8-3 Mobile energy storage system description.

While the battery bank terminal voltage is determined by the number of series cells in the same string, the total current is the sum of the parallel strings currents. The reader is referred to IEEE standards 485 [113] for further sizing details. The ESS is connected to the grid via a dc/dc/ac bidirectional VSC. The dc/dc converter is a current-controlled buck-boost controller. The current controller regulates the charging (discharging) power according to the set point provided by the EMS. When the EMS sends the active power set point at time k (P_{sk}) to the dc/dc current controller, the controller calculates the current set point I_{srefk} by dividing the power on the battery bank voltage (V_{sk}); $I_{srefk} = \frac{p_{sk}}{V_{sk}}$. The current controller is a proportional-integral (PI) controller that regulates the battery current by manipulating the modulation index of the buck-boost converter [104]. On the other hand, the dc/ac converter transfers the power to (from) the grid via regulating the dc-link voltage [104]. In the dq -frame, the dc-link voltage controller decides the VSC-direct current set point whereas the EMS controls the reactive power q_{sk} via changing the quadrature current set point. Further details on the design of the current

and dc-link voltage controllers can be found in [104]. A fast charging module is also available in some commercial versions [144]. The truck path is also controlled via the EMS. The driver requires a schedule for the MESS stations that include the station number s and the transition time to this station t_s . To sum up, the DNO needs to design an EMS system for an MESS that generates two set of outputs. Firstly, the EMS calculates the ESS active and reactive power at each sample. Second, the EMS defines the desired station at each time and the transition time to this station. Next, the EMS design is explained in details.

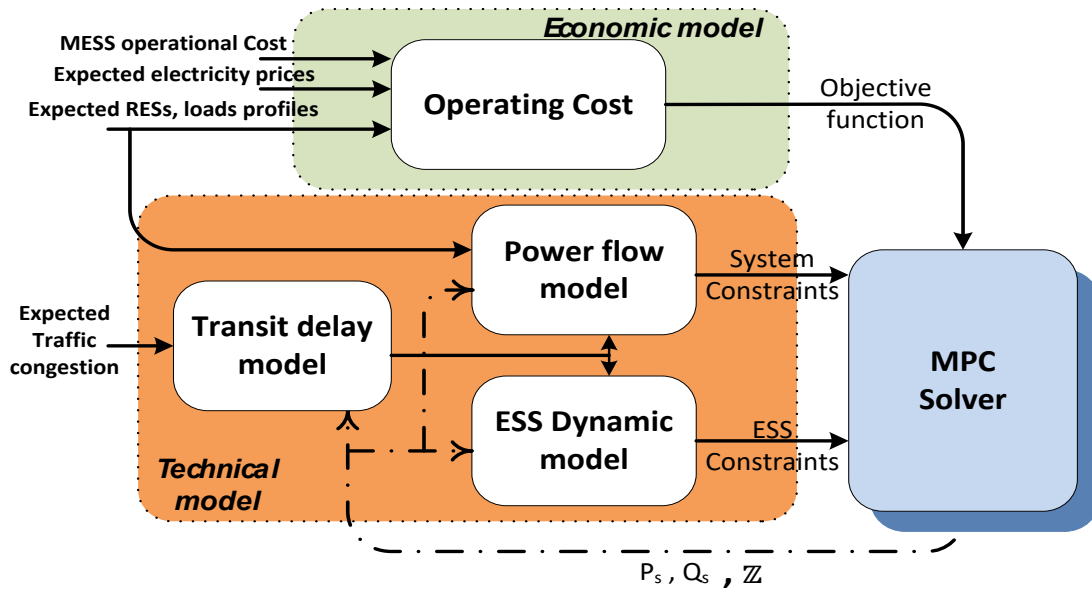


Figure 8-4 System techno-economic model structure.

8.2 Energy Management System

To design the EMS for an MESS, a complete techno-economic model, as depicted in Figure 8-4, is required. The technical model is composed of three subsystems:

- 1) the transit delay model that describes the commute time between two stations;

2) the power flow model that relates (the buses voltage, line current, and power loss) to the MESS power and positions (e.g., as in Section 3.2.5);

3) the ESS dynamic model that represents the battery dynamics. The economic model defines different costs of all resources that are reflected in the EMS objective function.

8.2.1 Transit Delay Model

The delay model depends on both time and stations positions. For a set of stations \mathcal{N}_s , the distance between stations is defined by the distance matrix $Dist$ with a zero diagonal, any element $d_{ij} \forall i, j \in \mathcal{N}_s$ define the distance between stations (i, j) . In case $d_{ij} = d_{ji}$, then the MESS uses the same road between two stations (i, j) .

$$Dist = \begin{bmatrix} 0 & \cdots & d_{1s} \\ \vdots & \ddots & \vdots \\ d_{s1} & \cdots & 0 \end{bmatrix} \quad (8.1)$$

The traffic congestion delay tc_{ijk} is a time and location dependent index can give an indicator [145] for the traffic delay. τ_{ijk} is the commute time (in samples) from a station i to j at time $k \in \mathcal{N}_k$ which is composed from three parts: the commute time, traffic congestion delay and installation time

$$\tau_{ijk} = round\left(\frac{tc_{ijk} + d_{ij}V_{avg} + t_{ins}}{T_s}\right) \forall i, j \in \mathcal{N}_s, k \in \mathcal{N}_k, i \neq j \quad (8.2)$$

In (8.2), V_{avg} is the average truck speed, t_{ins} is the MESS installation time (the connection of an MESS to the grid at the station). T_s is the sample time in minutes. For the sake of the modeling, let us define the Boolean matrix $\mathbb{Z} \in \mathcal{R}^{s \times \mathcal{K}}$, where each element z_{ik} equals one if the MESS exists at station i at sample time k . Next, let us define the Boolean vector $\mathbb{Y} \in \mathcal{R}^{\mathcal{K}}$ that represents the delay model. If the MESS is in transit at a sample T due to moving from a station

i to reach another one j after an τ_{ijT} samples of transition delay: $z_{iT} = z_{jT+\tau_{ijT}} = 1, i \neq j \forall i, j \in \mathcal{N}_s$. Then $y_{k+l} = 1, l \in [1, \tau_{ijT}], k = T$ In order to define y_k , all previous transit conditions that will lead to a future transit delay are modelled. By this way, y_k is expressed as a sum of minimum terms that represent all possible previous transits as shown in Figure 8-5.

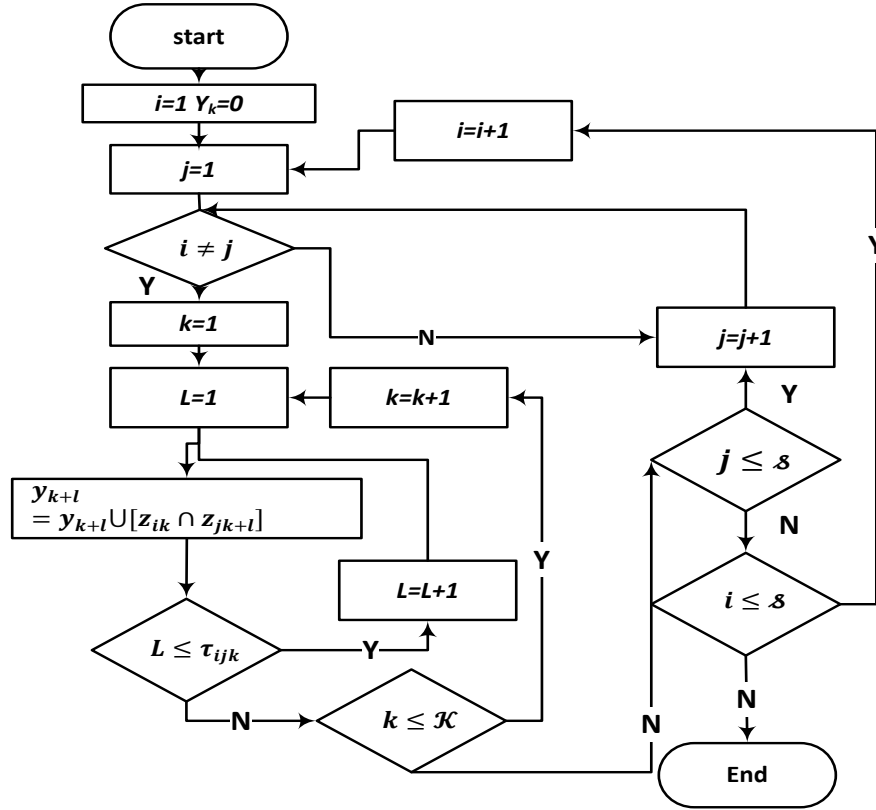


Figure 8-5 Transit delay model generation.

An example for defining y_k for three stations is depicted in Figure 8-6. In this example, three MESS stations exist; thus at any transit instant T , the nonzero transitions depend on the current MESS station and the next MESS destination with the following transition delay $\tau_{12T} = 1 \tau_{23T} = 2 \tau_{13T} = 3 \tau_{ijT} = \tau_{jiT}$. As shown in Figure 8-6, there are six possible transition scenarios at this sample time (2 possible transitions from each current station). Any transition

scenario occurs if both the current and destination stations equal one ($z_{ik} = z_{jk+l} = 1 \rightarrow z_{ik} \cap z_{jk+l} = z_{ik+1}z_{jk} = 1$). Finally, the aggregation of all possible transitions for a certain transit time T is defined as follows $y_{T+1} \cup y_{T+2} \cup y_{T+3} = (z_{1T}z_{2T+1} \cup z_{2T}z_{1T+1}) \cup (z_{2T}z_{3T+2} \cup z_{3T}z_{2T+2}) \cup (z_{1T}z_{3T+3} \cup z_{3T}z_{1T+3})$. These six possible transitions are depicted by the dotted lines in Figure 8-6. Further, when applying the same concept during each time $0 \leq k \leq \mathcal{K}$ and aggregating all the results, this will lead to a complete transition delay model.

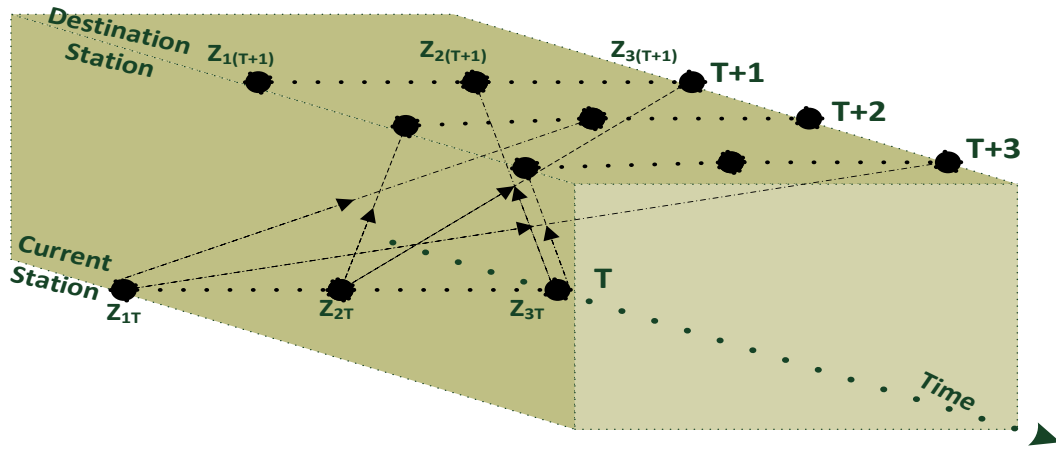


Figure 8-6 Transition scenarios example for a three MESS station at sample k .

The delay model is described as follows:

$$\mathcal{N}_s, k \in \mathcal{N}_k \begin{cases} \sum_i z_{ik} = 1 & (8.3) \\ \frac{\sum_i \sum_k |z_{ik} - z_{ik-1}|}{2} \leq N_{trips} & (8.4) \\ \mathbb{Y} = \{y_1, y_2, y_k, \dots, y_{\mathcal{K}}\} & (8.5) \end{cases}$$

Equation (8.3) states that the MESS truck can only be at one station i at any sample k . In case of multiple MESS units, the right-hand side of (8.3) is replaced by N_{mess} which is the total number of MESS trucks; this case will be investigated in future studies. Equation (8.4) constraints the maximum number of trips that an MESS can make per day (N_{trips}) which equals

half the number transitions. In case the MESS moved at time k from a station i to be at station j , then $z_{ik} = 0, z_{ik-1} = 1, z_{jk} = 1, z_{jk-1} = 0$ and the sum of the difference at sample k is calculated as $\sum_i \frac{|z_{ik} - z_{ik-1}|}{2} = 1$, which means one trip is made. However, if the MESS stays at station i at samples k and at $k-1$, then $\sum_i \frac{|z_{ik} - z_{ik-1}|}{2} = 0$ which means no trips are made. Finally, (8.5) is a set of equalities that represent the transit flag y_k .

The power flow model is given by equations (3.34) to (3.48). It is worth mentioning that other linearization techniques for the power flow are also possible as long as it provides a convex constraint; otherwise, nonconvex optimization is needed to solve the EMS problem.

8.2.2 MESS Dynamic Model Considering the Transit Delay

The final part of the technical model is the ESS dynamics including the ESS power, total number of cycles N , and the state of charge (SOC) which are expressed in (8.6)-(8.8).

In this model, we assume that anytime, there is always an ESS at each station s ; however, the constraint in (8.3) states that the MESS can be located at one unique station. Thus, the condition for injecting discharge ($p_{dh_{sk}}$) or importing charge power ($p_{ch_{sk}}$) at a certain bus s at time k is that the MESS exists at this station ($z_{sk} = 1$), and the MESS is not at transit state ($y_k = 0$). These conditions are modelled by (8.6). Equation (8.7) expresses the SOC as an integrator. The SOC equals one if the accumulated charge reaches the rated energy of the storage \bar{E}_s . The charge and discharge efficiency is considered as η_{ch}, η_{dh} , respectively. As one MESS is assumed at each bus, the total SOC is the sum of all stations ESS SOC at a certain time. A similar technique is used for calculating the number of cycles N_k that is assumed as an integrator as well. The number of cycles is incremented by one each time a full charge is absorbed by the MESS and injected again to the grid as expressed in (8.8).

$$\begin{cases} p_{sk} = (p_{ch_{sk}} + p_{dh_{sk}})z_{sk}(1 - y_k) & (8.6) \\ SOC_{k+1} = \sum_s SOC_{sk} + \frac{T_s}{\bar{E}_s} (\eta_{ch}p_{ch_{sk}} + \eta_{dh}p_{dh_{sk}})z_{sk}(1 - y_k) & (8.7) \\ N_{k+1} = \sum_s N_{sk} + \frac{T_s(p_{ch_{sk}} - p_{dh_{sk}})}{2\bar{E}_s} z_{sk}(1 - y_k) & (8.8) \\ \forall k \in \mathcal{N}_k, s \in \mathcal{N}_s, \eta_{ch} < 1, \eta_{dh} > 1 \end{cases}$$

The dynamic ESS constraints are stated in (8.9)-(8.12). While constraints (8.9) and (8.10) define the charge and discharge powers as positive and negative power limited by the thermal limit of the MESS, constraint (8.11) limits the apparent power of the MESS to be upper bounded by the rated MESS apparent power (\bar{S}) at any time. The discrete variable ce_k guarantees that charging and discharging are mutually exclusive. If ce_k equals one, the charging limits are between rated power and zero while discharge power is zero. On the other hand, setting ce_k to zero allows discharging and limits charging power to zero. The SOC is limited in (8.12) between the desired minimum SOC \underline{SOC} and one to avoid deep discharge and overcharging that may reduce the battery life dramatically. Further, the number of cycles at the end of the day is limited by (8.13) as the battery life is a countable number of cycles.

$$0 \leq p_{ch_{sk}} \leq \bar{p}_s(ce_s) \quad (8.9)$$

$$-\bar{p}_s(1 - ce_s) \leq p_{dh_{sk}} \leq 0 \quad (8.10)$$

$$p_{sk}^2 + q_{sk}^2 \leq \bar{S} \quad (8.11)$$

$$\underline{SOC} \leq SOC_k \leq 1 \quad (8.12)$$

$$\begin{aligned} N_{\mathcal{N}} &\leq \bar{N} & (8.13) \\ \forall b \in \mathcal{N}_b, t \in \mathcal{N}_t, k \in \mathcal{N}_k \end{aligned}$$

8.2.3 Original EMS Problem

The EMS objective is maximizing the day-ahead profit for the DNO by minimizing the imported energy cost from the grid (energy arbitrage). It is assumed that the MESS is an asset owned by the DNO to provide both reactive power support and maximize net profit. RESs are

owned by different parties, and they are paid a fixed feed-in-tariff (FIT) as a motivation by the government for clean energy, such a case exists in several markets, such as Ontario, Canada [146]. RESs are operated according to the maximum power point tracking strategy; the DNO buys this energy from RESs owners with the regulated FIT (C_{FIT}). The day-ahead cost of buying RESs energy is given in (8.14). On the other hand, conventional distributed generators (DGs) owned by the DNO, such as microturbines or diesel engines, have an operating cost (C_{DG}). A quadratic cost function, as defined in (8.25), precisely represents the operation costs of DG units [90]. In (8.15), $\phi_g (\$/kWh)^2$, $\beta_g (\$/kWh)$, $\gamma_g (\$)$ are constants that depend on the generator type.

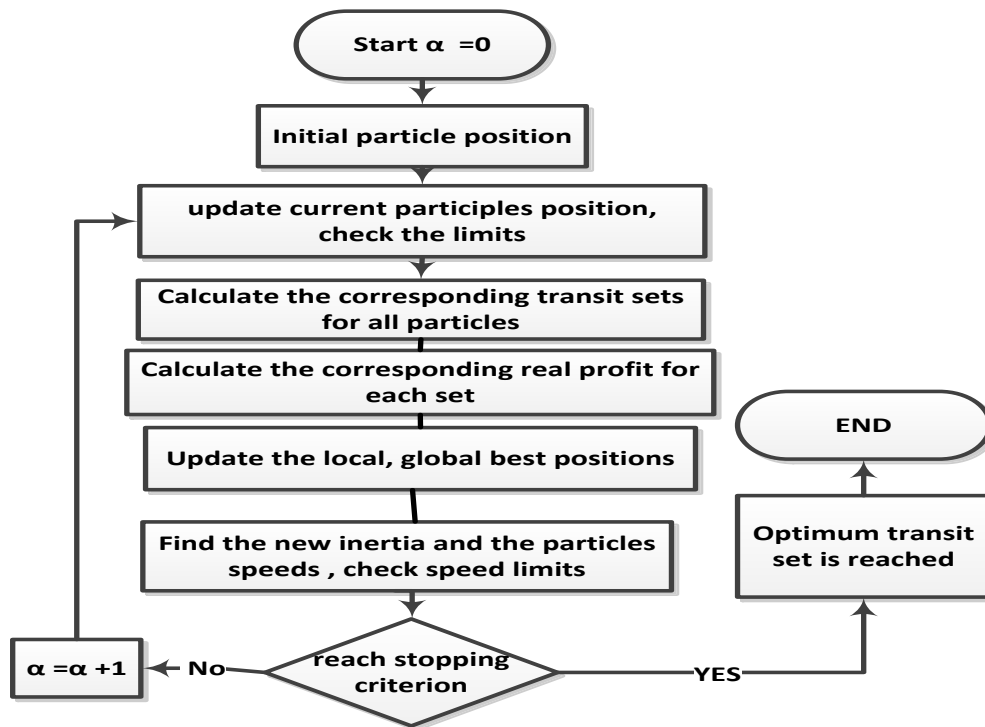


Figure 8-7 Stage 2 structure (PSO profit maximizer).

$$C_{DG} = \sum_{k=1}^{\mathcal{K}} \sum_{g=1}^{\mathcal{G}} \phi_g (p_{gk} T_s)^2 + \beta_g (p_{gk} T_s) + \gamma_g \quad (8.13)$$

$$C_{res} = \sum_{k=1}^{\mathcal{K}} \sum_{r=1}^{\mathcal{R}} p_{rk} T_s C_{FIT} \quad (8.14)$$

The MESS cost C_{mess} includes both the truck operating cost C_{truck} and the ESS cost C_{ess} as in (8.15). Firstly, the truck operating cost (8.16) includes a fuel cost and labor cost. While the fuel cost is modelled as a worst case cost (the multiplication of maximum distance (in km) by the number of the trips by the fuel consumption cost FC (\$/km)), the truck labor cost tlc includes the daily stipend of the truck driver and technicians. Secondly, (8.17) models the ESS cost as a levelized cost (C_{kwh} \$/kWh charged). This cost is adopted before for ESS in [38]. However, the capital cost is modified to include the truck capital cost and ESS maintenance cost that includes the truck maintenance cost.

$$C_{mess} = C_{truck} + C_{ess} \quad (8.15)$$

$$C_{truck} = FC \times N_{trip} \times \max(Dist) + tlc \quad (8.16)$$

$$C_{ess} = \sum_{k=1}^{\mathcal{K}} \sum_{s=1}^{\mathcal{S}} P_{ch_{sk}} T_s C_{kwh} \quad (8.17)$$

The final cost item is the grid power cost C_{grid} that is the multiplication of the expected pool price (buy price) BP_k (\$/kWh) and the grid energy $P_{gridk} T_s$ as shown in (8.18). This cost has a negative value (becomes income) in case the distribution system exports surplus energy to the grid. The income of the DNO is generated from daily selling energy to the loads with the sell price SP_k (\$/kWh) as given in (8.19). Finally, the profit is the difference between the income and the costs (MESS operating cost, DG running cost plus RES energy purchasing cost) as shown in (8.20).

$$C_{grid} = \sum_{k=1}^{\mathcal{K}} T_s B P_k P_{gridk}, P_{gridk} = P_{bk}, b = 0 \quad (8.18)$$

$$inc = \sum_{k=1}^{\mathcal{K}} \sum_{l=1}^{\mathcal{L}} T_s S P_k P_{lk} \quad (8.19)$$

$$pro = inc - C_{grid} - c_{mess} - C_{DG} - C_{res} \quad (8.20)$$

The final optimization problem is expressed as follows

$$\begin{aligned} & \max_{p_{ch_{sk}}, p_{dh_{sk}}, \mathbb{Z}, q_{sk}} (pro) \\ & S. t. (3.34) - (3.48) \& (8.3) - (8.13), \end{aligned} \quad (8.21)$$

The problem in (8.21) is a mixed integer nonconvex problem that may face a feasibility problem and does not guarantee to reach a global optimal solution in a certain time. In Section IV, this problem will be converted to a mixed integer convex problem using the proposed two-stage EMS.

8.3 Two-Stage EMS

To convert the problem in (8.21) into a mixed integer convex problem, the following suboptimal two-stage solution is proposed. Firstly, the problem is solved assuming instantaneous MESS transit; this problem calculates the MESS designated stations and its transit times (given the previous assumption). Secondly, a particle swarm algorithm optimizes the transit periods of the first stage without changing the MESS stations.

8.3.1 Stage 1 (Instantaneous Transit EMS)

The delay model \mathbb{Y} given in (8.5) is a nonlinear sophisticated Boolean expression that depends on both the truck transit time and stations \mathbb{Z} . Assuming that $\mathbb{Y} = 0$ or MESS can move instantaneously from a station to another will reduce the problem complexity on the price of sub-optimality, this part will be discussed later. The MESS model is expressed as a linear set of

equalities as in (8.22)-(8.24). This is possible after modifying the power limits constraints and adding a reactive power constraint in (8.27). This simple modification states that the MESS can charge or discharge at any station and time (s, k) if and only if it exists at this station or $z_{sk} = 1$. Otherwise, the power limits is set to zero. These limits affect all ESS dynamics as given in (8.22) - (8.24). Equation (8.22) defines the total power as a sum of charge and discharge power. Equation (8.23) represents the dynamic energy equation with the power taking into account the charging and discharging efficiencies. Equation (8.24) calculates the instanuous number of cycles. While (8.25)-(8.27) limits the active and reactive power.

$$p_{sk} = p_{ch_{sk}} + p_{dh_{sk}} \quad (8.22)$$

$$SOC_{k+1} = \sum_s SOC_{sk} + \frac{T_s}{\bar{E}_s} (\eta_{ch} p_{ch_{sk}} + \eta_{dh} p_{dh_{sk}}) \quad (8.23)$$

$$N_{k+1} = \sum_s N_{sk} + \frac{T_s (\eta_{ch} p_{ch_{sk}} - \eta_{dh} p_{dh_{sk}})}{2\bar{E}_s} \quad (8.24)$$

$$0 \leq p_{ch_{sk}} \leq \bar{p}_s z_{sk} \quad (8.25)$$

$$-\bar{p}_s z_{sk} \leq p_{dh_{sk}} \leq 0 \quad (8.26)$$

$$-\bar{s} z_{sk} \leq q_{sk} \leq \bar{s} z_{sk} \quad (8.27)$$

Now, the instantaneous EMS problem is expressed as:

$$\begin{aligned} & \max_{p_{ch_{sk}}, p_{dh_{sk}}, z_{sk}, q_{sk}} \quad (pro) \quad (8.28) \\ S. t. & \left\{ \begin{array}{l} \text{instaneous transit model: (8.3) - (8.4)} \\ \text{power flow model: (3.34) - (3.48), DG model (3.16) - (3.19)} \\ \text{ESS model: (8.9) - (8.13) \& (8.22) - (8.27)} \end{array} \right. \end{aligned}$$

Now, the problem in (8.28) is a mixed-integer convex problem that is solved efficiently using the available commercial solvers, such as GUROBI [102]. It is worth mentioning that problem (8.28) represents a finite-horizon model predictive control problem because the overall system is aggregated as a single state space dynamic model. At each sample time $0 \leq k \leq \mathcal{K}$, the model is regressively used to derive the future outputs as a function in the model expected states

and the future control action along the prediction horizon [123]. The inputs of the state-space model are the MESS power and locations $[z_{ik}, p_{sk}, q_{sk}]$, whereas the system states are the SOC and number of cycles $[SOC_{sk}, N_{sk}]$. Finally, the controlled outputs are any constrained variable in the system, such as $[SOC_k, N_k, p_{sk}, q_{sk}, \mathcal{P}_{tk}, \dots]$.

8.3.2 Stage 2 (PSO Profit Maximizer)

The resulting profit from Stage 1 is not the actual profit. In reality, the MESS transit period is not zero, and every time the MESS moves from a station i at instant λ heading to another station j , it will stay in transit for a period τ_{ijk} defined by (8.2) till it reaches its destination at instant $\lambda + \tau_{ij\lambda}$. The set of time indices that define that the MESS is at transit state is \mathcal{N}_τ :

$$\mathcal{N}_\tau = \{[\lambda, \lambda + \tau_{ij\lambda}] | z_{i\lambda} = z_{j\lambda-1} = 1 \forall i \neq j, i, j \in \mathcal{N}_s\} \quad (8.29)$$

Now, if the MESS is at transit, that means that the DNO has to buy (or sell) the MESS scheduled energy from the grid till the MESS reaches its next destination. Further, the MESS is not operating during transit periods, thus its operating cost C_{ess} should not be considered as well. The real profit $\mathcal{R}pro$ when the transit set \mathcal{N}_τ is taken into account is

$$\mathcal{R}pro = pro + \sum_{\lambda \in \mathcal{N}_\tau} \sum_{s \in \mathcal{N}_s} T_s BP_\lambda p_{s\lambda} + \sum_{\lambda \in \mathcal{N}_\tau} \sum_{s \in \mathcal{N}_s} P_{chs\lambda} T_s C_{kwh} \quad (8.30)$$

It is worth mentioning that if $p_{s\lambda} < 0$, which means the MESS is discharging at this time; however, as the MESS is in the transit state, this energy $\sum_{s \in \mathcal{N}_s} T_s p_{s\lambda}$ is exported from the grid with a price BP_λ at this time. On the contrary, if the MESS is supposed to be charged at this time, the surplus system energy is sold to the grid with this time price (or even worse, RESs energy can be curtailed in case the voltage level or thermal current levels are violated). Further, the ESS cost is excluded from the profit calculation during time periods flagged in \mathcal{N}_τ . Not

only, is the profit and power system is affected by the delay, but also the ESS dynamics as well. For instance, the real SOC (\mathcal{RSOC}) after considering the transit delay is defined as in (8.31). The SOC is normally calculated in the non-transit case, while it stays fixed during transit as the ESS is in the stand-by mode. Other ESS dynamics, such as the real number of cycles \mathcal{RN} is calculated as in (8.32).

$$\begin{cases} \mathcal{RSOC}_{k+1} = \sum_s \mathcal{RSOC}_{sk} + \frac{T_s}{\bar{E}_s} (\eta_{ch} p_{ch_{sk}} + \eta_{dh} p_{dh_{sk}}), k \in \mathcal{N}_k - \mathcal{N}_\tau \\ \mathcal{RSOC}_{k+1} = \mathcal{RSOC}_k, k \in \mathcal{N}_\tau \end{cases} \quad (8.31)$$

$$\begin{cases} \mathcal{RN}_{k+1} = \sum_s \mathcal{RN}_{sk} + \frac{T_s (\eta_{ch} p_{ch_{sk}} - \eta_{dh} p_{dh_{sk}})}{2\bar{E}_s}, k \in \mathcal{N}_k - \mathcal{N}_\tau \\ \mathcal{RN}_{k+1} = \mathcal{RN}_k, k \in \mathcal{N}_\tau \end{cases} \quad (8.32)$$

One needs to make sure that the transit set will not lead to ESS dynamic constraint violation. For instance, one transit set can move the MESS very early from discharge stations and very late from charging station, thus an overcharge may occur and vice versa. One solution to this problem is keeping a reserve in the capacity (e.g., the SOC limits are chosen from 20 to 90 %) to account for possible uncertainties.

The PSO optimizer defines optimum transit delay set \mathcal{N}_τ that maximizes the real profit without violating the ESS dynamics. Firstly, each particle x^n represents a different transit set \mathcal{N}_τ^n by changing the transit time λ_α^n , where n is the index for the particle in the population, and α is the index for the transit time. Normally, the number of transits is less than or equal N_{trips}

$$x^n = [\lambda_1^n, \lambda_2^n, \dots, \lambda_{N_{trips}}^n] \quad (8.33)$$

$$\mathcal{N}_\tau^n = \{[\lambda_1^n, \lambda_1^n + \tau_{ij} \lambda_1^n], [\lambda_2^n, \lambda_2^n + \tau_{ij} \lambda_2^n], \dots, [\lambda_{N_{trips}}^n, \lambda_{N_{trips}}^n + \tau_{ij} \lambda_{N_{trips}}^n]\} \quad (8.34)$$

$$\lambda_\alpha - M \leq \lambda_\alpha^n \leq \lambda_\alpha + M, 1 \leq \alpha \leq N_{trips} \quad (8.35)$$

As shown, the particle x^n is a randomly generated vector for the transit and is bounded by that defines the maximum shift in the transit time within a band $[-M, M]$. The swarm population \mathbb{X} is then defined with a population-size n particles, each has a corresponding transit set defined in (8.36).

$$\mathbb{X} = \{x^1, x^2 \dots x^n \dots x^n\} \quad (8.36)$$

$$\mathbb{N} = \{\mathcal{N}_\tau^1, \mathcal{N}_\tau^2 \dots \mathcal{N}_\tau^n \dots \mathcal{N}_\tau^n\} \quad (8.37)$$

The real profit is calculated for each particle, and the local and global best particle positions are allocated. At each iteration α , after the profit is calculated for all \mathbb{x} set-particles, the local and global best positions $Pbest(\alpha), G_{best}(\alpha)$ are updated and the new velocity for the next sample ($V^n(\alpha + 1)$) for each particle n is calculated as in (8.39). For solution quality, the PSO algorithm must fulfill two important criteria: first, a high exploration at the start of the search, and second, a deep exploitation to avoid trapping in a local-suboptimal later [140]. Thus, a high speed for particles exploration is gained via high initial inertia that reduces monotonically with the iterations progress in order to achieve higher exploitation later. This is possible by updating the PSO inertia $\omega(\alpha)$ as in (8.38) starting from the desired minimum value ω_{min} at the first search sample and reaching its peak ω_{max} at the maximum iteration value $Max.Iter$. Next, the particles positions are updated as in (8.40). The reader is referred to [140] for further details on the PSO algorithm. Finally, the stopping criterion is achieved in two cases. Firstly, the convergence case happens if the fitness function (real profit) settles at a certain value within the predefined tolerance zone.

$$\omega(\alpha) = \omega_{max} - \frac{\omega_{max} - \omega_{min}}{Max.Iter} \alpha \quad (8.38)$$

$$V^n(\alpha + 1) = \omega(\alpha)V^n(\alpha) + c_1r_1(Pbest - x^n(\alpha)) + c_2r_2(Gbest - x^n(\alpha)) \quad (8.39)$$

$$x^n(\alpha + 1) = V^n(\alpha + 1) + x^n(\alpha) \quad (8.40)$$

This must happen for a predefined number of iterations to guarantee convergence and avoid trapping in a local minimum. Secondly, the stopping criterion is satisfied if the number of iterations exceeds the maximum iteration numbers ($\alpha \leq \bar{\alpha}$). Figure 8-7 shows the PSO algorithm structure.

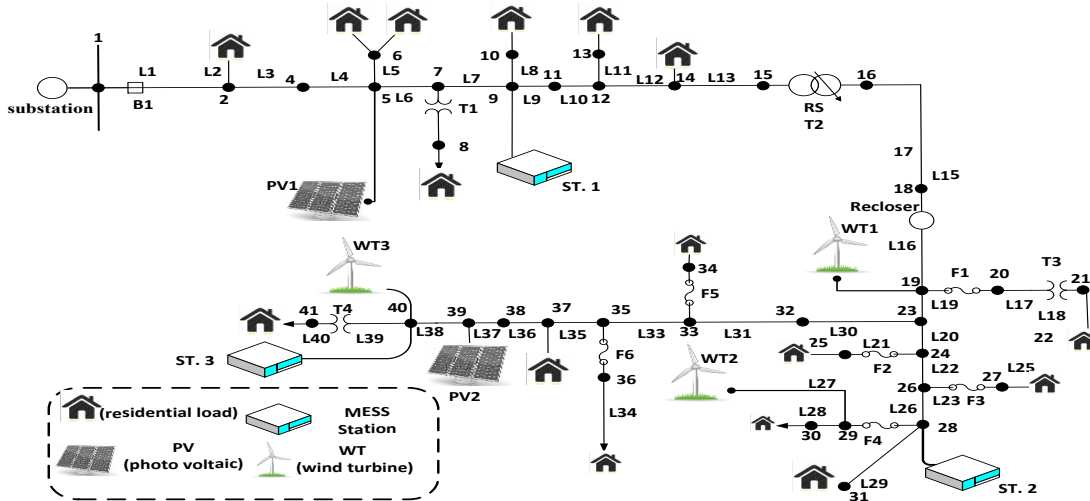


Figure 8-8 Radial feeder under study.

8.4 Case Study

To validate the proposed EMS, a detailed simulation study is conducted on a radial system described in Section 3.3. The system is owned by Hydro One, Ontario which has a fixed electricity tariff to its customers that only changes only from winter to summer [147]. The tariff adopts the time-of-use pricing policy with two peaks periods (7:11 am, 5:7 PM). Other rates, such as delivery rates, regulatory charges are considered here as well [147]. On the other hand, the DNO (here Hydro One) buys energy from Ontario independent system operator ISO (IESO) for the wholesale energy market price (deregulated market). This price is known as hourly Ontario energy price (*HOEP*) [98]. The real HOEP in February 2015 is considered here as given

in [98]. The HOEP and DNO tariff (buy and sell prices) are shown in Figure 8-9(c). RESs' owners are paid a feed-in-tariff (c_{FIT}) decided by IESO as given in [148], and it is presented in table 8-1. No utility-owned DGs exist in the system under study; however, DGs can be easily dispatched by considering their active and reactive power limits, and, power rate constraints as detailed in [90].

The MESS optimal sizing is conducted in Chapter 4. The storage cost is 600 K\$/MWh and the conversion system cost is 350K\$/MW [100], while the operation and maintenance cost for MESS are assumed to be 12k\$/year including the ESS and the truck, the truck cost is assumed to be 50K\$. After making stochastic sizing using these input data, an optimal size of the MESS is found to be 3250 kVA/6381.3 kWh which equals 4.247 Million \$. The MESS efficiency and cost parameters are stated in Table 9-1. According to [29], lithium-ion batteries have an energy density of 0.25 kWh/kg and the power density is 0.5 kW/kg. Applying that in our MESS case results in a 32-ton load which is a suitable load for a tow truck with an acceptable cost [149].

The MESS is assumed to participate 250 cycles/year with results in a 3000 cycle per its lifetime (here 12 years), Assuming more cycles makes the profit negative, and the whole investment becomes void especially when a replacement cost will be considered. The distance between different stations is given in Table 9-1. Finally, for the MESS delay model, the traffic congestion delay is used to emulate the traffic congestion pattern in freeway of a large North American city. Although the traffic events and the scheduled road maintenance are given on a real-time basis for Ontario Canada from [150], the exact transit delay data in Ontario is not available for public. As a result, this case study uses the transit delay data of Los Angeles, USA as a sample of the traffic congestion pattern in freeways in large North American cities. The data is represented in Figure 8-9(d). In case the DNO has an estimation for the transit delay,

then the EMS problem is solved as instant transition EMS problem and a suboptimal solution can be obtained.

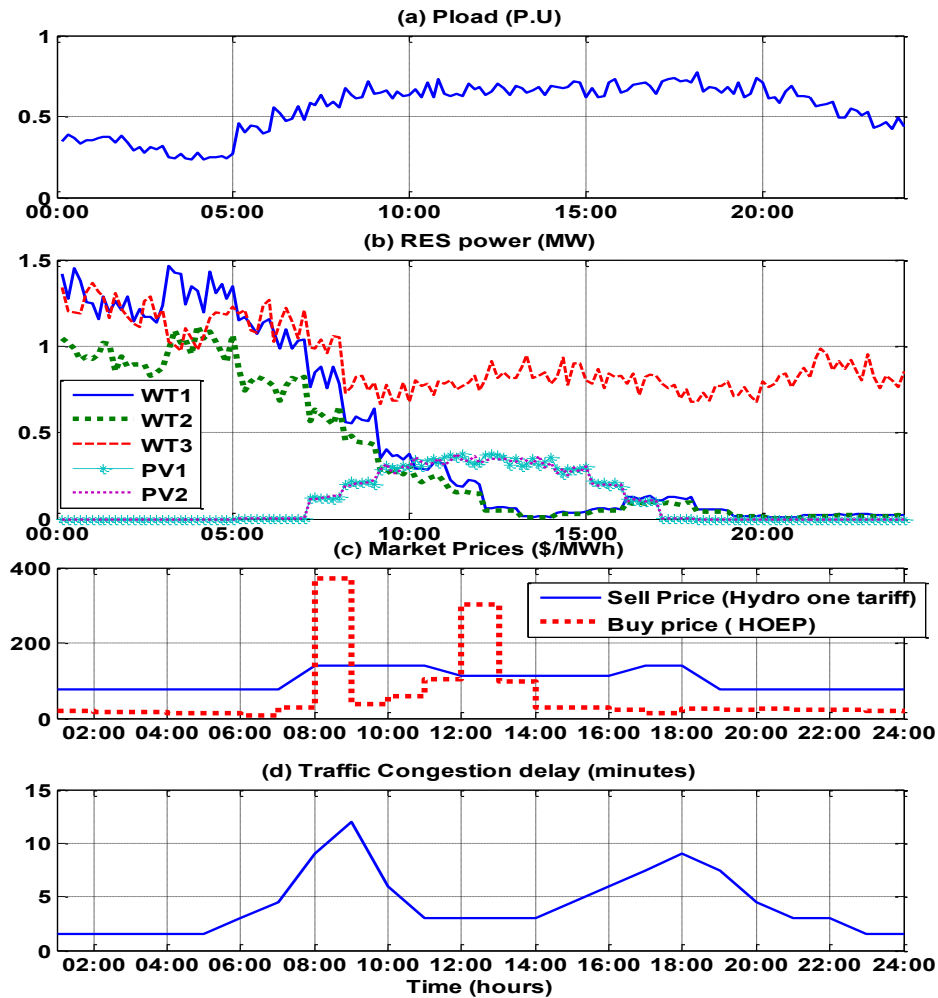


Figure 8-9 Day-ahead input data. (a) Load profile. (b) RESs profiles. (c) Wholesale market and sell prices. (d) Traffic congestion delay.

For the given system inputs shown in Figure 8-9, the EMS problem is solved as in Section 8.2, and the results are shown in Figure 8-10, whereas the voltage profile after and before using the

MESS is depicted in Figure 8-11. The main objective is maximizing the DNO profit through energy arbitrage and power loss minimization; thus as shown in Figure 8-10 (b), the MESS has been charged during the lowest buy prices times (4-6 am) till reaching full capacity.

Table 8-1 Input data for the EMS.

RES Ratings	$p_{WT1} = 2MW, p_{WT2} = 1.5MW, p_{WT3} = 1.5MW,$ $p_{pv1} = 0.5MW, p_{pv2} = 0.5MW, c_{FIT} = 128 \$/MWh$
Delay model	$d_{12} = 16.87 \text{ km}, d_{13} = 19.92 \text{ km}, d_{23} = 16.83 \text{ km}$ $V_{avg} = 40 \text{ km/hr}, t_{ins} = 5 \text{ mins.}, T_s = 10 \text{ mins.}$
EMS	$SOC_0 = 0.5, \underline{SOC} = 0.2, N_{trips} = 3, \bar{N} = 1$ $\underline{v} = 0.95, \bar{v} = 1.05, N_0 = 0, \eta_{ch} = 0.75, \eta_{dh} = 1.33$ $FC = 0.4 \$/km, C_{kwh} = 221 \$/MWh, tlc = 25 \$/hr$
PSO	$M = 30 \text{ mins.}, \omega_{max} = 0.9, \omega_{min} = 0.1, \bar{\alpha} = 2000,$ $C_1 = 2, C_2 = 2, n = 10$

The MESS is partially discharged during the first price peak at 8 am. It continues being charged at 9 am when the prices fall. It is worth mentioning that at 9 am; the battery is not charged with full power as reactive power support is needed at this time to boost the voltage to the minimum allowable level as depicted in the reactive power curve in Figure 8-10(b). Next, at noon, where the second price peak exists, the MESS is fully discharged. After that, no significant price difference exists that deserves another MESS charge and the state of charge is settled at the minimum 20% level as in Figure 8-10(d). It should be noted that the price difference should be at least greater than the charging cost C_{kwh} to make charging

economically viable (which does not happen again after 2 pm). Moreover, the number of cycles allowed in this study is one; thus the total charged energy is less than the rated capacity and the maximum number of cycle is less than one as in Figure 8-10(d). Finally, as the profit is the only objective function here (energy arbitrage strategy), charging times are driven by the energy price, unlike peak shaving whereas discharging hours are always located at peak hours. It is noticed that the grid exported power is reduced during the high energy price as depicted in Figure 8-10(c).

Regarding reactive power support, during late night, the power generated by wind turbines is very high while the line is lightly loaded (see Figure 8-9). As a result, the voltage profile increases above the limits (105%) during this time as shown in Figure 8-11, particularly in the feeder end (bus 41). As a result, the first chosen location for the MESS is near these buses (Station-3) as shown in Figure 8-10(a). During this time the energy price is minimal, and the MESS is fully charged. In the morning (7-8 am), the MESS discharge during the first peak hour, and then it changes its location to Station-1 (bus 9) where it recharges back (8-9 am). The reason behind this location change is that charging at Station-1 (the nearest to grid) provides the lowest power loss, further charging at Station-3 (bus 40) will lead to a further voltage drop at the feeder end. The second transition occurs after charging as shown in Figure 8-10(a) when the MESS goes back to Station-3 (bus 40) to discharge fully during the second peak hour (11 am-12 pm). After that, the SOC and number of cycles limits are reached as shown in Figure 8-10 (d), thus zero active power is kept until the end of the day, however; the MESS keeps providing reactive power support for keeping acceptable voltage limits. A final transition is made to Station-2 around 2 pm. As noticed from Figure 8-10, the wind power plant (WT2) near Station-2 drops to zero at the same time; thus a leading reactive power is needed at this far end feeder.

Thus, the MESS made this final transition from Station-3 into Station-2 where the voltage to reactive power sensitivity is higher than Station-3.

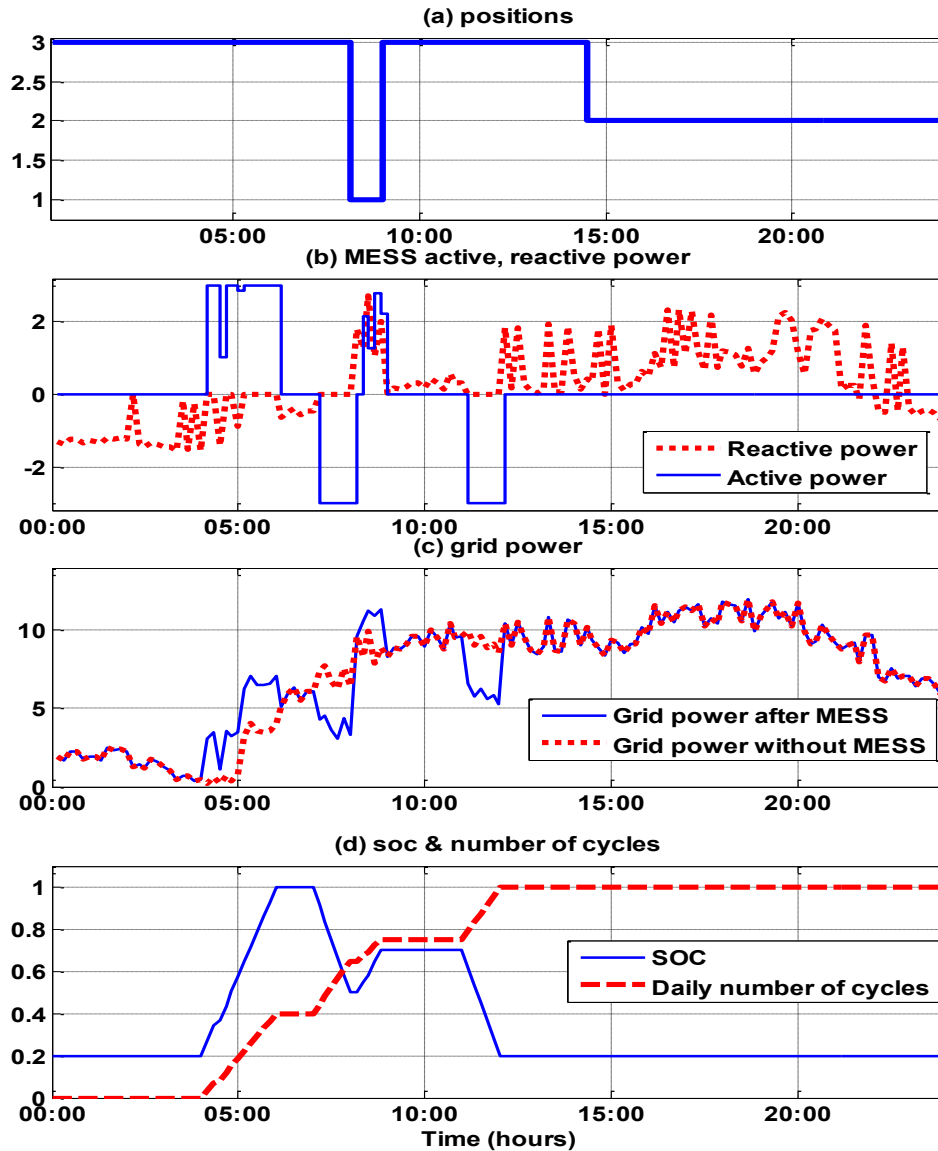


Figure 8-10 EMS results (a)MESS Position (b) MESS active power and reactive power set (c) Grid power and (e) SOC and Number of cycles.

Regarding Stage 2 (the PSO profit maximizer), the optimizer changes the transition time from (8, 9 and 14) into (8&9:30 and 13:30). For the first and second transitions, the PSO keeps

them the same as if the MESS left Station-3 earlier than 8 am, it will miss discharging during the peak hour which will result in a big profit reduction.

For the second transition, if the MESS leaves Station-1 before 9 am, it will not be fully charged which will reduce the profit in the future; however, if it stays longer at Station-1, the traffic congestion delay will reduce from its 9 am peak as depicted in Figure 8-9 (d). Finally, for the final transition (from Station-3 into Station-2), the PSO optimizer changes the transition time from (2 pm into 1:30 pm) to end the ride (approximately 30 minutes ride with delays) before the traffic congestion increases after 2 pm. It is worth mentioning that the PSO results agree with the traffic delay profile in Figure 8-9 (d); thus, the PSO optimizes the transition times to decrease the MESS delay and, therefore, maximizing its service period.

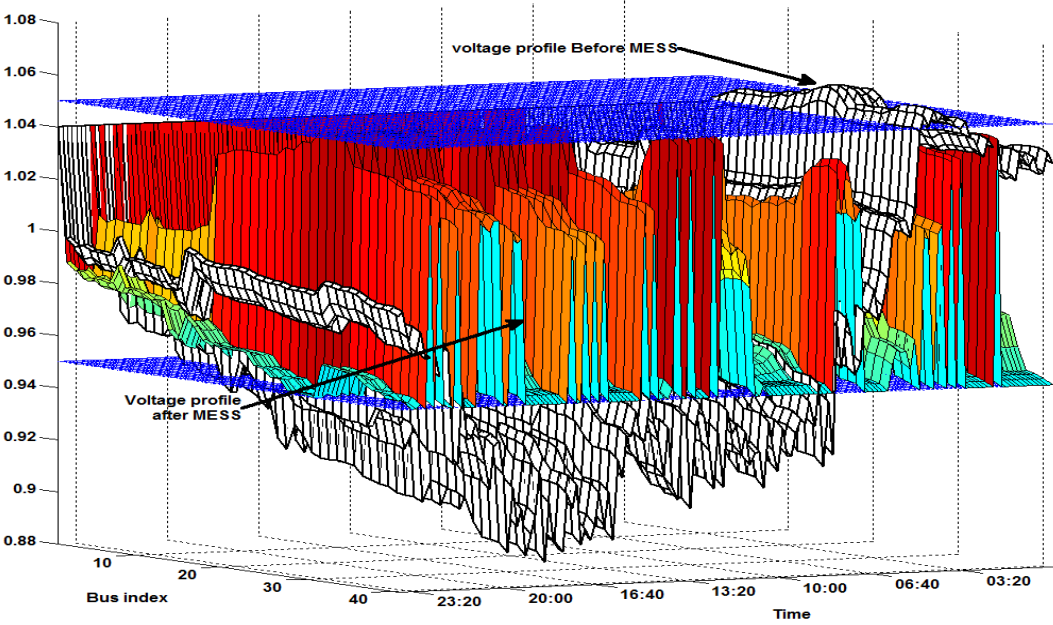


Figure 8-11 Voltage profile after and before using the MESS.

To sum up the results, Table 8-2 compares the techno-economic aspects after and before using the MESS services (system with no storage at all and system that invests in an MESS).

Firstly, the MESS managed to provide a logistic localized reactive power support to keep the voltage level within allowable limits which improves the power quality. Secondly, regarding losses, the losses has been decreased by 5.5%. It is worth mentioning that the objective function is the difference between the energy bought from the grid and that sold to loads. Thus the power loss is inherently minimized in the objective function with a weight depending on the energy prices at each instant. Thirdly, the net profit has increased by 3.1% as compared to that without including the profit from the localized reactive power support that defers adding one or two capacitor banks to this feeder.

Table 8-2 System performance comparison.

	No MESS	With MESS
Voltage level	$V_{max} = 1.062, V_{min} = 0.89$	$V_{max} = 1.04, V_{min} = 0.956$
Power loss	8.1863 MWh	7.7277 MWh
Profit	14,320\$	14,760\$

Regarding enhancing the voltage profile, a good example appears when we focus on the voltage at the worst case bus (bus-41) as shown in Figure 8-12. Bus 41 is a heavily loaded bus (2.14 MW) with a big wind farm nearby (WT3 located in bus 40). Station-3 is located at bus 41. However, the reactive power is injected at various stations according to Figure 8-10 (a).

As shown in Figure 8-12 (a), the wind power (WT3) exceeds bus-41 load till 5:00 am that results in over voltage (as shown in Figure 8-12 (c)). Because an overvoltage occurs, the MESS produces lagging reactive power from 0:00 till 4:00 (as shown in Figure 8-12 (c)) leading to reducing the voltage magnitude to the allowable margin. Moving to hours 4:00 till 6:00, the

reactive power is almost zero (limited by the converter apparent power limit), however, the MESS is full charging active power that leads to overvoltage prevention as well. From (8:20 till 22:20), the wind power is below the load and the voltage level (V_{41}) goes below the 0.95 pu as depicted in Figure 8-12 (c). Consequently, the MESS has to produce leading reactive power to keep the voltage above the minimum level and reduce the power loss as well in the whole network (which cause indirect profit increase).

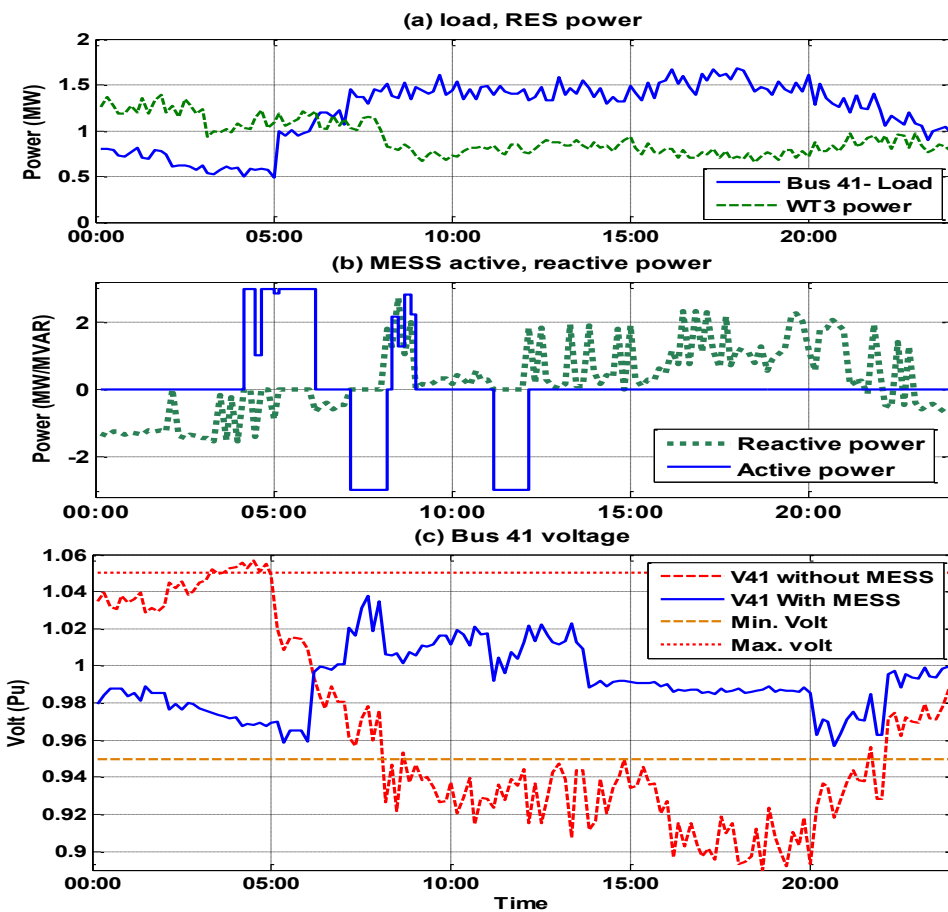


Figure 8-12 Worst case bus voltage comparison (a) Bus 41 load profile and WT3 generation (b) MESS active and reactive power (C) Bus 41 volt with and without MESS reactive power support.

The second case study discusses a crucial issue which is boosting the power system reliability by providing an on-line backup energy reservoir for sensitive loads; here the MESS

acts as an uninterruptible power supply (UPS). This is possible by solving the same economic EMS problem after imposing UPS constraints that guarantee that the MESS has enough energy (minimum SOC greater than the required energy) and the MESS is sited at the desired location. If a fault occurs, the MESS switches off into UPS mode till the service is continued again. The UPS constraints are summarized in (55-56).

$$\underline{SOC} + \frac{E_{UPS}}{\bar{E}_s} \leq SOC_k \leq 1 \quad \forall k \in [T_{ups}^{start}, T_{ups}^{end}] \quad (8.41)$$

$$z_{sk} = z_{UPS} \quad (8.42)$$

The UPS constraints assume that the MESS is required to provide a reserve energy E_{UPS} for a certain period $[T_{ups}^{start}, T_{ups}^{end}]$ while locating the MESS at the position z_{UPS} .

The main case study is repeated but with the assumption that a critical load exists at station three from hours 17 till 23. The required energy reservoir is ($E_{UPS} = 1250$ kWh) which represents 20% of the battery capacity; thus the SOC should not go below 40% at the pre-mentioned hours. A comparison between the economic MESS and the resulting UPS constrained (after imposing constraints 55-56) is shown in Figure 8-13.

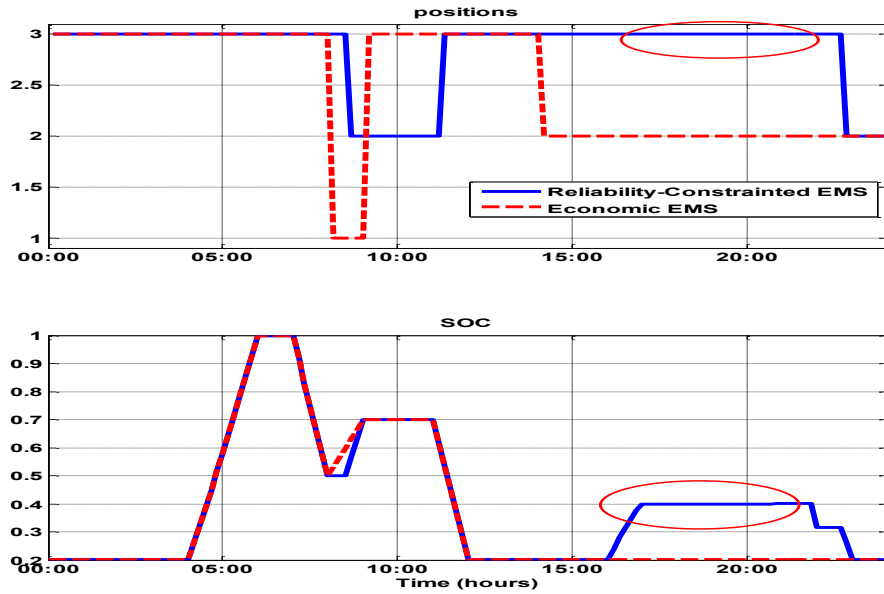


Figure 8-13 Comparison between reliability-based EMS with economic EMS. (a) Station position of MESS. (B) MESS state of charge.

In the UPS-constrained EMS, the MESS starts charging early to reach the required 40% SOC by hour 17. At time 21:50, the main supply is disconnected, and the MESS starts acting as a UPS till the service is resumed by 22:40. When the MESS returns again to the normal mode after hour 23, it discharges the whole energy to go back to the minimum SOC of 20%. The MESS has also stayed at Station-3 till hour 23; then it moved to Station-2 after (similar to the economic EMS case).

Finally, it worth noticing that these results mainly depend on the market prices, the load and RES profiles. Thus, in other days with no big market price difference, it is not economical to operate the MESS [20]. Finally, Using the MESS in voltage support is optional in case of long feeders where the transformer tap changer setting cannot guarantee an acceptable voltage at the far end.

8.5 Conclusion

A day-ahead EMS for an MESS was presented in this chapter. The EMS objective function aimed at maximizing the DNO day-ahead profit and regulating the voltage level. The proposed EMS dispatched the MESS and allocated its station in the system. A traffic delay model was developed between different stations. Using a two-stage optimization technique, firstly, the problem was solved as a mixed-integer convex problem, and secondly, a PSO-based algorithm was developed to optimize the transit times to maximize the profit. A case study on a real 41-buses radial feeder with real data of RESs and loads was used to validate the results. The proposed EMS successfully fulfilled all the optimization process objectives in an adaptive manner that fitted the time-varying nature of renewable resources in modern active distribution grids.

Chapter 9

Conclusions

9.1 Thesis Summary

This thesis discussed the optimal planning and energy management of energy storage systems in the power system. The primary objective in both the planning and operation phases was to maximize the profit of the owner (either a consumer or utility) while respecting the different system technical constraints. To achieve these objectives, various optimization techniques were utilized to guarantee feasible optimal decisions.

Different storage systems were investigated in this thesis (short and long period storage, stationary and mobile storage). The thesis began investigating stationary storage planning in Chapter 3. The planning scheme aimed at using ESSs for distribution system upgrade. ESS was intended to provide multi-services by conducting T&D deferral, energy arbitrage, power loss minimization and providing reactive power support, simultaneously. A case study using a real radial feeder data is conducted. The results showed that energy arbitrage income was vital for a viable ESS investment. Further, given the current market costs, NA-S battery was found to be a competitive system upgrade option. Results also show that ESS was an effective upgrade tool when sited at the feeder end close to big loads combined with SVCs (for reactive power support) sited at the feeder start close to both big loads and/or RESs.

Chapter 4 discusses mobile energy storage planning in active distribution systems. To achieve the same objectives as those in Chapter 3 (except for T&D deferral), a size-dependent cost for the power converter was adopted in the planning process. The study results showed that using the MESS may yield a higher profit than that yielded by stationary ESSs, due to its low bulk power conversion cost.

Regarding operation phase, Chapter 5-8 focused on the energy management of different storage systems. First, Chapter 5 presented a predictive EMS for a hybrid power system (WECS with BESS). This EMS maximized the owner's daily profit by dispatching the BESS for wind energy time-shifting. To expand the BESS lifetime, constraints on the power rating, the DOD and the number of charging cycles were included. This technique achieved the optimal profit with a minimal sacrifice in the BESS lifetime guaranteeing the maximum net profit.

Chapter 6 presented a predictive EMS for a short-term storage hybrid system. The system consisting of a FESS connected with a WECS. The EMS used an MPC-based algorithm to respect typical grid code, minimize the FESS losses, and increase the system lifetime. By comparing the proposed EMS with a traditional EMS, the case studies show that the proposed controller has managed to reduce the FESS losses up to 25%.

Chapter 7 presented a framework to define robust operating zones for multi-ESSs for day-ahead. The technical constraints included permissible voltage level and branch ampacity. This work's main contribution is to consider the power uncertainty while reducing the results conservatism. When the ROZs were tested under different uncertainty scenarios, the results showed that the proposed technique increased the ESS participation with a very low voltage and ampacity violations.

Finally, Chapter 8 proposed a novel EMS for mobile storage. This EMS minimized the cost of power imported from the grid and not only shifted renewable energy power to load peak hours but also it provided localized reactive power support. The proposed EMS managed to provide the optimal locations and dispatch power for an MESS which achieved a profit for the utility, taking into account the truck transit delay.

9.2 Future work

The following research directions can be followed as an extension out of this thesis.

- 1) The utilization of ESSs in distribution system extension. Savings in the extension cost can be achieved by reducing the feeders' sizes in futuristic expansions; moreover, ESS-multi-services enables reactive power support with the peak shaving process.
- 2) The application of the developed EMSs to hybrid systems with short and long duration ESSs.
- 3) The inclusion of a detailed transit delay model in the planning process of MESSs.
- 4) The extension of the proposed planning and operation algorithms to multiple MESSs.

Whereas the ESS cost will decrease in the future, more ESSs are expected to join the power systems for multi-services. This development will make all the suggested studies very useful for viable control and sizing strategies for ESSs.

Bibliography

- [1] S. Arefifar and Y. Mohamed, "DG Mix, Reactive Sources and Energy Storage Units for Optimizing Microgrid Reliability and Supply Security," *IEEE Transactions on smart Grid*, vol. 5, no. 4, pp. 1835-1844, 2014.
- [2] M. Arif, A. Oo and A. Ali, "Energy Storage: Applications and Advantages," in *Smart Grids: Opportunities, Developments, and Trends*, New York, Springer, 2013, pp. 77-109.
- [3] E. Jim and C. Garth, "Energy Storage for the Electricity Grid: Benefits and Market Potential Assessment Guide," SANDIA, Albuquerque, New Mexico, 2010.
- [4] R. Walawalkar and A. Jay, "Market Analysis of Emerging Electric Energy Storage Systems," NETL, 2008.
- [5] LAZARD, "LAZARD's leveled cost of storage analysis- Version 1.0," LAZARD, November 2015.
- [6] S. Chakraborty, T. Senjyu, H. Toyama, A. Saber and T. Funabashi, "Determination methodology for optimising the energy storage size for power system," *IET Generation, Transmission & Distribution*, vol. 3, no. 11, pp. 987-999, 2009.
- [7] H. Pandzic, Y. Wang, T. Qiu, Y. Dvorkin and D. Kirschen, "Near-Optimal Method for Siting and Sizing of Distributed Storage in a Transmission Network," *IEEE Trans. Power Syst.*, vol. 30, no. 5, pp. 2288-2300, 2015.
- [8] S. Wogrin and D. Gayme, "Optimizing Storage Siting, Sizing, and Technology Portfolios in Transmission-Constrained Networks," *IEEE Trans. Power Syst.*, vol. 30, no. 6, pp. 3304-3313, 2015.
- [9] M. Nick, R. Cherkaoui and M. Paolone, "Optimal Allocation of Dispersed Energy Storage Systems in Active Distribution Networks for Energy Balance and Grid Support," *IEEE Trans. Power Syst.*, vol. 29, no. 5, pp. 2300-2310, 2014.
- [10] S. Chen, H. Gooi and M. Wang, "Sizing of Energy Storage for Microgrids," *IEEE Trans. Smart Grid*, vol. 3, no. 1, pp. 142-151, Feb. 2012.
- [11] C. Abbey and G. Joos, "A Stochastic Optimization Approach to Rating of Energy Storage Systems in Wind-Diesel Isolated Grids," *IEEE trans. Power Syst.*, vol. 24, no. 1, pp. 418-426, 2009.
- [12] T. Nguyen, M. Crow and A. Elmore, "Optimal Sizing of a Vanadium Redox Battery System for Microgrid Systems," *IEEE Trans. Sust. Energy*, vol. 6, no. 3, pp. 729-737, June 2015.
- [13] Y. Makarov, P. Du, M. Meyer, C. Jin and H. Illian, "Sizing Energy Storage to Accommodate High Penetration of Variable Energy Resources," *IEEE Trans. Sust. Energy*, vol. 3, no. 1, pp. 34-40, Jan. 2012.
- [14] J. Xiao, L. Bai, F. Li, H. Liang and C. Wang, "Sizing of Energy Storage and Diesel Generators in an Isolated Microgrid Using Discrete Fourier Transform (DFT)," *IEEE Trans. Sust. Energy*, vol. 5, no. 3, pp. 907-916, 2014.
- [15] Y. Liu, W. Du, L. Xiao, H. Wang and J. Cao, "A Method for Sizing Energy Storage System to Increase Wind Penetration as Limited by Grid Frequency Deviations," *IEEE Trans. Power Syst.*, vol. pp, no. 99, pp. 1-9, 2015.
- [16] Y. Liu, W. Du, L. Xiao, H. Wang, S. Bu and J. Cao, "Sizing a Hybrid Energy Storage System for Maintaining Power Balance of an Isolated System With High Penetration of Wind Generation," *IEEE Trans. Power Syst.*, vol. PP, no. 99, pp. 1-9, 2015.
- [17] P. Li, R. Dargaville, F. Liu, J. Xia and Y. Song, "Data-Based Statistical Property Analyzing and Storage Sizing for Hybrid Renewable Energy Systems," *IEEE Trans. Indust. Electron.*, vol. 62, no. 11, pp. 6996-7008, 2015.
- [18] S. Alnaser and L. Ochoa, "Optimal Sizing and Control of Energy Storage in Wind Power-Rich Distribution Networks," *IEEE Trans. Power Syst.*, vol. pp, no. 99, pp. 1-10, August 2015.
- [19] X. Ke, N. Lu and C. Jin, "Control and Size Energy Storage Systems for Managing Energy Imbalance of Variable Generation Resources," *IEEE Trans. Sust. Energy*, vol. 6, no. 1, pp. 70-78, Dec. 2015.
- [20] H. Abdeltawab and Y. Mohamed, "Market-Oriented Energy Management of a Hybrid Wind-Battery Energy Storage System Via Model Predictive Control With Constraint Optimizer," *IEEE Trans. Indust. Electron.*, vol. 62, no. 11, pp. 6658-6670, 2015.
- [21] S. Wen, H. Lan, Q. Fu, D. Yu and L. Zhang, "Economic Allocation for Energy Storage System Considering

- Wind Power Distribution," *IEEE Trans. Power Syst.*, vol. 30, no. 2, pp. 644-652, March 2015.
- [22] H. Bludszweit and J. Navarro, "A Probabilistic Method for Energy Storage Sizing Based on Wind Power Forecast Uncertainty," *IEEE Trans. Power Syst.*, vol. 26, no. 3, pp. 1651-1658, 2011.
- [23] A. Awad, T. EL-Fouly and M. Salama, "Optimal ESS Allocation for Load Management Application," *IEEE Trans. Power Syst.*, vol. 30, no. 1, pp. 327-336, 2015.
- [24] EPRI, "Transportable Energy Storage Systems Project," Oct 2009.
- [25] D. Rastler, "Technical Specification for a Transportable Lithium-Ion Energy Storage System for Grid Support Using Commercially Available Lithium-Ion Technology," EPRI, Jul 2012.
- [26] winston-battery, "Mobile Power Storage," Winston Energy Group Limited, 2015. [Online]. Available: <http://en.winston-battery.com/index.php/products/mobile-power>. [Accessed 30 July 2015].
- [27] DOE, "Fujian Electric Power Research Institute Mobile Energy Storage Station I," Department of Energy, [Online]. Available: <http://www.energystorageexchange.org/projects/153>. [Accessed 30 July 2015].
- [28] Toshiba, "Spain's Gas Natural Fenosa and Toshiba to Demonstrate Use of Transportable Lithium-ion Battery Energy Storage System in Power Distribution Network," Toshiba, 2014. [Online]. Available: https://www.toshiba.co.jp/about/press/2014_01/pr0704.htm. [Accessed 30 July 2015].
- [29] Y. Zheng, D. Zhaoyang, S. Huang, M. Ke, L. Fengji, J. Huang and H. David, "Optimal integration of mobile battery energy storage in distribution system with renewables," *Journal of Modern Power Systems and Clean Energy*, vol. 3, no. 4, pp. 589-596, 2015.
- [30] E. Perez, H. Beltran, N. Aparicio and P. Rodriguez, "Predictive Power Control for PV Plants With Energy Storage," *IEEE Trans. Sustainable Energy*, vol. 4, no. 2, pp. 482-490, 2013.
- [31] A. Gabash and P. Li, "Flexible Optimal Operation of Battery Storage Systems for Energy Supply Networks," *IEEE Trans. Power Syst.*, vol. PP, no. 99, pp. 1-10, 2012.
- [32] S. Wang and Y. Liu, "A PSO-Based Fuzzy-Controlled Searching for the Optimal Charge Pattern of Li-Ion Batteries," *IEEE Trans. Ind. Electron.*, vol. 62, no. 5, pp. 2983- 2993, 2015.
- [33] J. Trovao, V. Santos, C. Henggeler, P. Pereirinha and H. Jorge, "A Real-Time Energy Management Architecture for Multisource Electric Vehicles," *IEEE Trans. Ind. Electron.*, vol. 62, no. 5, pp. 3223-3233, 2015.
- [34] X. Lu, K. Sun, J. Guerrero, J. Vasquez and L. Huang, "State-of-Charge Balance Using Adaptive Droop Control for Distributed Energy Storage Systems in DC Microgrid Applications," *IEEE Trans. Ind. Electron.*, vol. 61, no. 6, pp. 2804- 2815, 2014.
- [35] J. Talla, L. Streit, Z. Peroutka and P. Drabek, "Position-Based T-S Fuzzy Power Management for Tram With Energy Storage System," *IEEE Transactions on Industrial Electronics*, vol. 62, no. 5, pp. 3061- 3071 , 2015.
- [36] S. Teleke, M. Baran, S. Bhattacharya and A. Huang, "Optimal Control of Battery Energy Storage for Wind Farm Dispatching," *IEEE Trans. Energy Convers.*, vol. 25, no. 3, pp. 787-794, 2010.
- [37] W. Qi, J. Liu and P. Christofides, "Distributed Supervisory Predictive Control of Distributed Wind and Solar Energy Systems," *IEEE Trans. Control Syst. Technol.*, vol. 21, no. 2, pp. 504-512, 2013.
- [38] P. Poonpun and W. Jewell, "Analysis of the Cost per Kilowatt Hour to Store Electricity," *IEEE Trans. Energy Convers.*, vol. 23, no. 2, pp. 529-534, 2008.
- [39] L. Y and P. Flynn, "Deregulated Power prices: comparison of Volatility," *Energy Policy*, vol. 32, no. 14, pp. 1591-1601, 2004.
- [40] D. Rastle, "Electricity Energy Storage Technology Options," ELECTRIC POWER RESEARCH INSTITUTE , Palo Alto, California, 2010.
- [41] S. Vazquez, S. Lukic, E. Galvan, L. Franquelo and J. Carrasco, "Energy Storage Systems for Transport and Grid Applications," *IEEE Trans. Ind. Electron.*, vol. 57, no. 12, pp. 3881-3895, 2010.
- [42] R. Arghandeh, M. Pipattanasomporn and S. Rahman, "Flywheel Energy Storage Systems for Ride-through Applications in a Facility Microgrid," *IEEE Trans. Smart Grid*, vol. 3, no. 4, pp. 1955-1962, 2012.
- [43] Y. Suzuki, A. Koyanagi, M. Kobayashi and R. Shimada, "Novel applications of the flywheel energy storage system," *Energy*, vol. 30, no. 11-12, pp. 2128-2143, Aug. 2005.
- [44] L. H and J. J, "Flywheel energy storage—An upswing technology for energy sustainability," *Energy and buildings*, vol. 39, pp. 599-604, 2007.

- [45] S. Samineni, B. Johnson, H. Hess and J. Law, "Modeling and analysis of a flywheel energy storage system for Voltage sag correction," *IEEE Trans. Ind. Appl.*, vol. 42, no. 1, pp. 42-52, Jan. 2006.
- [46] B. power, "Beacon power," 2014. [Online]. Available: <http://beaconpower.com/>. [Accessed 30 September 2014].
- [47] X. Chang, Y. Li, W. Zhang, N. Wang and W. Xue, "Active Disturbance Rejection Control for a Flywheel Energy Storage System," *IEEE Trans. Ind. Electron.*, vol. 62, no. 2, pp. 991-1001, Feb. 2015.
- [48] C. Jin, N. Lu, S. Lu, Y. Makarov and R. Dougal, "A Coordinating Algorithm for Dispatching Regulation Services Between Slow and Fast Power Regulating Resources," *IEEE Trans. Smart Grid*, vol. 5, no. 2, pp. 1043-1050, 2014.
- [49] N. Lu, F. Rudolph and C. loutan, "THE WIDE-AREA ENERGY STORAGE AND MANAGEMENT SYSTEM PHASE II," PNNL, Richland, Washington, 2010.
- [50] G. Thijissen and J. Enslin, "Cost Comparison for a 20 MW Flywheel-based Frequency Regulation Power Plant," KEMA, Raleigh, NC, 2007.
- [51] temporal, "temporal power," 2014. [Online]. Available: <http://temporalpower.com/>. [Accessed 30 September 2014].
- [52] R. Sebastian and A. R., "Flywheel energy storage systems: Review and simulation for an isolated wind power system," *Renewable and Sustainable Energy Reviews*, vol. 16, pp. 6803-6813, Dec. 2012.
- [53] D. Francisc, S. Andreas, G. Oriol and D. Fernando, "Energy management of flywheel-based energy storage device for wind power smoothing," *Applied Energy*, vol. 110, p. 207-219, 2013.
- [54] G. Suvire, M. Molina and P. Mercado, "Improving the Integration of Wind Power Generation Into AC Microgrids Using Flywheel Energy Storage," *IEEE Trans. Smart Grid*, vol. 3, no. 4, pp. 1945-1954, 2012.
- [55] K. Z. and V. I., "Losses of flywheel energy storages and joint operation with solar cells," *Journal of Materials Processing Technology*, vol. 161, pp. 62-65, 2005.
- [56] D. Gerada, A. Mebarki, N. Brown, C. Gerada, A. Cavagnino and A. Boglietti, "High-Speed Electrical Machines: Technologies, Trends, and Developments," *IEEE Trans. Ind. Electron.*, vol. 61, no. 6, pp. 2946 - 2959, June 2014.
- [57] R. Cardenas, R. Pena, G. Asher, J. Clare and R. Blasco-Gimenez, "Control strategies for power smoothing using a flywheel driven by a sensorless vector-controlled induction machine operating in a wide speed range," *IEEE Trans. Ind. Electron.*, vol. 51, no. 3, pp. 603-614, 2004.
- [58] J. Beno, R. Thompson, M. Werst, S. Manifold and J. Zierer, "End-of-life design for composite rotors [flywheel systems]," *IEEE Trans. Magn.*, vol. 37, no. 1, pp. 284-289, 2001.
- [59] S. Arnold, A. Saleeb and N. Al-Zoubi, "Deformation and life analysis of composite flywheel disk systems," *Composites Part B: Engineering*, vol. 33, pp. 433-459, 2002.
- [60] F. Islam, A. Al-Durra and S. Muyeen, "Smoothing of Wind Farm Output by Prediction and Supervisory-Control-Unit-Based FESS," *IEEE Trans. Sust. Energy*, vol. 4, no. 4, pp. 925-933, Oct. 2013.
- [61] J. Chen and M. Goloshchapova, "Energy Storage Initiative Issue Identification," AESO, Edmonton, 2013.
- [62] A. Gabash and P. Li, "Active-Reactive Optimal Power Flow in Distribution Networks With Embedded Generation and Battery Storage," *IEEE Trans. Power Syst.*, vol. 27, no. 4, pp. 2026-2035, 2012.
- [63] D. Gayme and U. Topcu, "Optimal power flow with large-scale storage integration," *IEEE Trans. Power Syst.*, vol. 28, no. 2, pp. 709-717, 2013.
- [64] Y. Levron, J. Guerrero and Y. Beck, "Optimal Power Flow in Microgrids With Energy Storage," *IEEE Trans. Power Syst.*, vol. 28, no. 3, pp. 3226-3234, 2013.
- [65] A. Gabash and P. Li, "Flexible Optimal Operation of Battery Storage Systems for Energy Supply Networks," *IEEE Transactions on Power Systems*, vol. 28, no. 3, pp. 2788-2797, 2013.
- [66] H. Akhavan-Hejazi and H. Mohsenian-Rad, "Optimal Operation of Independent Storage Systems in Energy and Reserve Markets With High Wind Penetration," *IEEE Trans. Smart Grid*, vol. 5, no. 2, pp. 1088-1097, 2014.
- [67] S. Nykamp, M. Bosman, A. Molderink, J. Hurink and G. Smit, "Value of Storage in Distribution Grids—Competition or Cooperation of Stakeholders?," *IEEE Trans. Smart Grid*, vol. 4, no. 3, pp. 1361-1370, 2013.
- [68] A. Oudalov, D. Chartouni and C. Ohler, "Optimizing a Battery Energy Storage System for Primary Frequency Control," *IEEE Trans. Power Syst.*, vol. 22, no. 3, pp. 1259-1266, 2007.

- [69] H. Oh, "Optimal Planning to Include Storage Devices in Power Systems," *IEEE Trans. Power Syst.*, vol. 26, no. 3, pp. 1118-1128, 2011.
- [70] J. Tant, F. Geth, D. Six, P. Tant and J. Driesen, "Multiobjective Battery Storage to Improve PV Integration in Residential Distribution Grids," *IEEE Transactions on Sustainable Energy*, vol. 4, no. 1, pp. 182-191, 2013.
- [71] Z. Shu and P. Jirutitijaroen, "Optimal Operation Strategy of Energy Storage System for Grid-Connected Wind Power Plants," *IEEE Trans Sust. Energy*, vol. 5, no. 1, pp. 190-199, 2014.
- [72] C. Martinez, E. Bonvallet, R. Behnke and X.-P. Zhang, "Impacts of Energy Storage on Short Term Operation Planning Under Centralized Spot Markets," *IEEE Trans. Smart Grid*, vol. 5, no. 2, pp. 1110-1118, 2014.
- [73] M. Khodayar, L. Wu and M. Shahidehpour, "Hourly Coordination of Electric Vehicle Operation and Volatile Wind Power Generation in SCUC," *IEEE Transactions on Smart Grid*, vol. 3, no. 3, pp. 1271-1279, 2012.
- [74] D. Bertsimas, E. Litvinov, X. Sun, J. Zhao and T. Zheng, "Adaptive Robust Optimization for the Security Constrained Unit Commitment Problem," *IEEE Trans. Power Syst.*, vol. 28, no. 1, pp. 52-63, 2013.
- [75] R. Jiang, J. Wang and Y. Guan, "Robust Unit Commitment With Wind Power and Pumped Storage Hydro," *IEEE Trans. Power Syst.*, vol. 27, no. 2, pp. 800-810, 2012.
- [76] C. Zhao, J. Wang, J. Watson and Y. Guan, "Multi-Stage Robust Unit Commitment Considering Wind and Demand Response Uncertainties," *IEEE Transactions on Power Systems*, vol. 28, no. 3, pp. 2708-2717, 2013.
- [77] Y. Zhang, N. Gatsis and G. Giannakis, "Robust Energy Management for Microgrids With High-Penetration Renewables," *IEEE Trans. Sust. Energy*, vol. 4, no. 4, p. 2013, 944-953.
- [78] Q. Wang, J. Watson and Y. Guan, "Two-stage robust optimization for N-k contingency-constrained unit commitment," *IEEE Trans. Power Syst.*, vol. 28, no. 3, pp. 2366-2375, 2013.
- [79] Y. Guan and J. Wang, "Uncertainty Sets for Robust Unit Commitment," *IEEE Trans. Power Syst.*, vol. pp, no. 99, pp. 1-2, 2013.
- [80] Y. Liu, C. Yuen, N. Hassan, S. Huang, R. Yu and S. Xie, "Electricity Cost Minimization for a Microgrid With Distributed Energy Resource Under Different Information Availability," *IEEE Trans. Indust. Electron.*, vol. 62, no. 4, pp. 2571-2583, 2015.
- [81] R. Yu, W. Zhong, S. Xie, C. Yuen, S. Gjessing and Y. Zhang, "Balancing Power Demand Through EV Mobility in Vehicle-to-Grid Mobile Energy Networks," *IEEE Trans. Indust. Informat.*, vol. 12, no. 1, pp. 79-90, 2016.
- [82] K. W. Hu and C. M. Liaw, "Incorporated Operation Control of DC Microgrid and Electric Vehicle," *IEEE Trans. Ind Elect*, vol. 63, no. 1, pp. 202-215, 2016.
- [83] W. Tushar, C. Yuen, S. Huang, D. Smith and H. Poor, "Cost Minimization of Charging Stations With Photovoltaics: An Approach With EV Classification," *IEEE Trans. Intell Trans Syst*, vol. 17, no. 1, pp. 156-169, 2016.
- [84] P. Sanchez, G. Sanchez and G. Morales, "Direct Load Control Decision Model for Aggregated EV Charging Points," *IEEE Trans Power Syst.*, vol. 27, no. 3, pp. 1577-1584, 2012.
- [85] R. Bessa and M. Matos, "Optimization Models for EV Aggregator Participation in a Manual Reserve Market," *IEEE Tran Power Syst*, vol. 28, no. 3, pp. 3085-3095, 2013.
- [86] J. Eyer, "Electric Utility Transmission and Distribution Upgrade Deferral Benefits from Modular Electricity Storage," Sandia National Laboratories, Albuquerque, New Mexico, June 2009.
- [87] M. Carrion and J. Arroyo, "A Computationally Efficient Mixed-Integer Linear Formulation for the Thermal Unit Commitment Problem," *IEEE Trans. Power Syst.*, vol. 21, no. 3, pp. 1371-1378, 2006.
- [88] L. Gan, N. Li, U. Topcu and S. Low, "Exact Convex Relaxation of Optimal Power Flow in Radial Networks," *IEEE Trans. Power Syst.*, vol. 60, no. 1, pp. 72-87, 2015.
- [89] J. Lavaei, D. Tse and B. Zhang, "Geometry of Power Flows and Optimization," *IEEE Trans. Power Syst.*, vol. 29, no. 2, pp. 572-583, 2014.
- [90] W. Shi, X. Xie, C. Chu and R. Gadh, "Distributed Optimal Energy Management in Microgrids," *IEEE Trans. Smart Grid*, vol. 6, no. 3, pp. 1137-1146, 2015.
- [91] K. Christakou, J. LeBoudec, M. Paolone and D. Tomozei, "Efficient Computation of Sensitivity Coefficients of Node Voltages and Line Currents in Unbalanced Radial Electrical Distribution Networks," *IEEE Trans. Smart Grid*, vol. 4, no. 2, pp. 741-750, June 2013.
- [92] M. Hong, "An Approximate Method for Loss Sensitivity Calculation in Unbalanced Distribution Systems,"

- IEEE Trans. Power Syst.*, vol. 29, no. 3, pp. 1435-1436, May 2014.
- [93] S. Lee and S. Yang, "Derivation of P-Q Loss Sensitivities by Angle Reference Transposition and an Application to Optimal P-Q Generation for Minimum Cost," *IEEE Trans. Power Syst.*, vol. 21, no. 1, pp. 428-430, Feb. 2006.
- [94] Y. Atwa, "Distribution System Planning and Reliability Assessment under High DG Penetration," University of Waterloo, Waterloo, Ontario, Canada, 2010.
- [95] PJM, "meterd load data," 2015. [Online]. Available: <http://www.pjm.com/markets-and-operations/ops-analysis/historical-load-data.aspx>. [Accessed 1 December 2015].
- [96] SODA, "Solar Energy Services for Professionals," 2015. [Online]. Available: <http://www.soda-is.com/eng/index.html>. [Accessed 1 Dec. 2015].
- [97] A. E. S. Operator, "Wind power data," 2016. [Online]. Available: <http://www.aeso.ca/gridoperations/20544.html>. [Accessed 1 Dec. 2015].
- [98] I. E. S. Operato, "Power data of IESO," 2016. [Online]. Available: <http://www.ieso.ca/Pages/Power-Data/default.aspx#download>.
- [99] N. Pattani, "Transmission & Distribution Considerations For Distributed Generation," Hydro One, January, 2009.
- [100] S. Schoenung, "Energy Storage Systems Cost Update; A Study for the DOE Energy Storage Systems Program," Sandia National Laboratories, Albuquerque, New Mexico, April 2011.
- [101] N. Mukherjee and D. Strickland, "Second life battery energy storage systems: Converter topology and redundancy selection," in *PEMID 2014*, 2014.
- [102] Gurobi, "Gurobi Optimization," Shell, [Online]. Available: <http://www.gurobi.com/>. [Accessed 18 Aug 2015].
- [103] I. R. E. Agency, "Battery Storage For Renewables; Market Status And Technology Outlook," IRENA, 2015.
- [104] Y. Amirnasr and I. Reza, *Voltage-Sourced Converters in Power Systems*, Wiley, 2010.
- [105] D. Rastler, A. Akhil, D. Gauntlett and C. E, "Energy Storage System Costs 2011 update, Executive Summary," EPRI, Feb., 2012.
- [106] J. Kennedy and R. Eberhart, "Particle Swarm Optimization," in *IEEE International Conference on Neural Networks*, 1995.
- [107] A. E. S. Operator, "Market & System Reporting," AESO, [Online]. Available: <http://www.aeso.ca/market/8856.html>.
- [108] AESO, 2015. [Online]. Available: <http://www.aeso.ca/gridoperations/20544.html>.
- [109] AESO, 2015. [Online]. Available: <http://www.aeso.ca/market/23873.html>.
- [110] EPCOR, 2015. [Online]. Available: <http://www.epcor.com/power-natural-gas/regulated-rate-option/Pages/residential-rates.aspx>.
- [111] F. Valenciaga, P. Puleston, P. Battaiotto and R. Mantz, "Passivity/sliding mode control of a stand-alone hybrid generation system," *IEE Proceedings - Control Theory and Applications*, vol. 147, no. 6, pp. 680-686, 2000.
- [112] D. Lee and L. Wang, "Small-Signal Stability Analysis of an Autonomous Hybrid Renewable Energy Power Generation/Energy Storage System Part I: Time-Domain Simulations," *IEEE Transactions on Energy Conversion*, vol. 23, no. 1, pp. 311-320, 2008.
- [113] I. S. C. C. 2. o. S. Batteries, *IEEE Recommended Practice for Sizing Lead-Acid Batteries for Stationary Applications*, IEEE, 1997.
- [114] J. Jiang, Q. Liu, C. Zhang and W. Zhang, "Evaluation of Acceptable Charging Current of Power Li-Ion Batteries Based on Polarization Characteristics," *IEEE Trans Indust. Electron.*, vol. 61, no. 12, pp. 6844- 6851, 2014.
- [115] M. Ceraolo, "New dynamical models of lead-acid batteries," *IEEE Transactions on Power Systems*, vol. 15, no. 4, pp. 1184-1190, 2000.
- [116] M. Gholizadeh and F. Salmasi, "Estimation of State of Charge, Unknown Nonlinearities, and State of Health of a Lithium-Ion Battery Based on a Comprehensive Unobservable Model," *IEEE Trans Indust. Electron.*, vol. 61, no. 3, pp. 1335- 1344, 2014.
- [117] j. Ayoub, L. Dignard-Bailey and Y. Poissant, "exchange and dissemination of information on pv power systems," canmetENERGY, Varennes, Quebec, 2011.

- [118] Y. Li and P. Flynn, "Deregulated power prices: changes over time," *IEEE Trans Power Syst.*, vol. 20, no. 2, pp. 565-572, 2005.
- [119] AESO, "Implementation of Market & Operational Framework For Wind Integration in Alberta," 2009.
- [120] AESO, "Wind power Management Protocol for Alberta," AESO, 2008.
- [121] C. Zhou, K. Qian, M. Allan and W. Zhou, "Modeling of the Cost of EV Battery Wear Due to V2G Application in Power Systems," *IEEE Trans. Energy Convers.*, vol. 26, no. 4, pp. 1041-1050, 2011.
- [122] D. Jenkins, J. Fletcher and D. Kane, "Lifetime prediction and sizing of lead-acid batteries for microgeneration storage applications," *IET Renewable Power Generation*, vol. 2, no. 3, pp. 191-200, 2008.
- [123] L. Wang, Model control systems design and implementation Using Matlab, Springer, 2008.
- [124] S. Vazquez, J. Leon, L. Franquelo, J. Rodriguez, H. Young, A. Marquez and P. Zanchetta, "Model Predictive Control: A Review of Its Applications in Power Electronics," *IEEE Industrial Electronics Magazine*, vol. 8, no. 1, pp. 16-31, 2014.
- [125] AESO, "historical pool price for Alberta," 2000. [Online]. Available: <http://ets.aeso.ca/>. [Accessed MAY 2013].
- [126] M. Tsili and S. Papathanassiou, "A review of grid code technical requirements for wind farms," *IET Renewable Power Generation*, vol. 3, no. 3, pp. 308- 332 , 2009.
- [127] S. Kim, S. Bae, Y. Kang and J. Park, "Energy Management Based on the Photovoltaic HPCS With an Energy Storage Device," *IEEE. Trans. Ind. Electron.*, vol. 62, no. 7, pp. 4608 - 4617, July 2015.
- [128] K. Keesman, System Identification; An Introduction, Springer, 2011.
- [129] AESO, "AESO Recommendation paper (Implementation of Market & Operational Framework for Wind Integration in Alberta)," Alberta energy system operator, Edmonton, 2009.
- [130] B. Jonkman and L. Kilcher, "TurbSim User's Guide: Version 1.0600," NREL, Golden, Colorado, Sept., 2012.
- [131] R. Gagnon, B. Saulnier and A. Forcione, "mathworks," 2015. [Online]. Available: <http://www.mathworks.com/examples/simpower/105-wind-farm-dfig-phasor-model>. [Accessed 12 August 2015].
- [132] V. Marandi, L. Pak and V. Dinavahi, "Real-Time Simulation of Grid-Connected Wind Farms Using Physical Aggregation," *IEEE Trans. Indust. Electron.*, vol. 57, no. 9, pp. 3010-3021, 2010.
- [133] W. Li, G. Joos and J. Belanger, "Real-Time Simulation of a Wind Turbine Generator Coupled With a Battery Supercapacitor Energy Storage System," *IEEE Trans. Indust. Electron.*, vol. 57, no. 4, pp. 1137-1145, 2010.
- [134] J. Jung, S. Ahmed and P. Enjeti, "PEM Fuel Cell Stack Model Development for Real-Time Simulation Applications," *IEEE Trans. Indust. Electron.*, vol. 58, no. 9, pp. 4217-4231, 2011.
- [135] A. Thatte, L. Xie, D. Viassolo and S. Singh, "Risk Measure Based Robust Bidding Strategy for Arbitrage Using a Wind Farm and Energy Storage," *IEEE Trans. Smart Grid*, vol. 4, no. 4, pp. 2191-2199, 2013.
- [136] w. Pedrycz and f. Gomide, Fuzzy Systems Engineering Toward Human-Centric Computing, Wiley, 2007.
- [137] W. Li, J. Zhou, K. Xie and X. Xiong, "Power System Risk Assessment Using a Hybrid Method of Fuzzy Set and Monte Carlo Simulatio," *IEEE Transactions on Power Systems* , vol. 23, no. 2, pp. 336-343, 2008.
- [138] D. Popovic and Z. Popovic, "A risk management procedure for supply restoration in distribution networks," *IEEE Trans. Power Syst.*, vol. 19, no. 1, pp. 221-228, 2004.
- [139] A. Almeida, E. Valença de Lorenci, R. Leme, A. Zambroni de Souza, B. Lopes and K. Lo, "Probabilistic voltage stability assessment considering renewable sources with the help of the PV and QV curves," *IET Renewable Power Generation*, vol. 7, no. 5, pp. 521- 530, 2013.
- [140] M. AlRashidi and M. El-Hawary, "Hybrid Particle Swarm Optimization Approach for Solving the Discrete OPF Problem Considering the Valve Loading Effects," *IEEE Transactions on Power Systems*, vol. 22, no. 4, pp. 2030-2038, 2007.
- [141] A. Esmin, G. Torres and A. de Souza, "A hybrid particle swarm optimization applied to loss power minimization," *IEEE Trans. Power Syst.*, vol. 20, no. 2, pp. 859-866, 2005.
- [142] Y. Chakhchoukh, P. Panciatici and L. Mili, "Electric Load Forecasting Based on Statistical Robust Methods," *IEEE Trans. Power Syst.*, vol. 26, no. 3, pp. 982-991, 2011.
- [143] D. Saez, F. Avila, D. Olivares, C. Canizares and L. Marin, "Fuzzy Prediction Interval Models for Forecasting Renewable Resources and Loads in Microgrids," *IEEE Trans. Smart Grid*, vol. 6, no. 2, pp. 548-556, 2015.

- [144] "Winston Energy Group Limited," [Online]. Available: <http://en.winston-battery.com/index.php/products/mobile-power>. [Accessed 30 July 2015].
- [145] I. Cambridge Systematics, "Traffic Congestion and Reliability (Trends and Advanced Strategies for Congestion Mitigation)," Federal Highway Administration , Sept. 2005.
- [146] IESO, "feed in tariff," [Online]. Available: <http://fit.powerauthority.on.ca/>. [Accessed 8 Sept. 2015].
- [147] H. One, "electricity Rates," [Online]. Available: <http://www.hydroone.com/MyHome/MyAccount/UnderstandMyBill/Pages/ElectricityRates.aspx>. [Accessed 23 Aug. 2015].
- [148] IESO, "Price schedule," IESO, [Online]. Available: <http://fit.powerauthority.on.ca/program-resources/price-schedule>. [Accessed 08 Sept. 2015].
- [149] Alibaba, "30 ton tow truck," ALibaba.com, [Online]. Available: https://www.alibaba.com/trade/search?fsb=y&IndexArea=product_en&CatId=&SearchText=30+ton+tow+truck. [Accessed 25 May 2016].
- [150] T. G. o. Ontario, "Traveller Information Services 2015," [Online]. Available: http://www.mto.gov.on.ca/english/traveller/trip/traffic_reports.shtml. [Accessed 28 March 2016].
- [151] E. Perez, H. Beltran, N. Aparicio and P. Rodriguez, "Predictive Power Control for PV Plants With Energy Storage," *IEEE Trans. Sust. Energy*, vol. 4, no. 2, pp. 482-490, 2013.